Orhan Altan
Madhu Chandra
Filiz Sunar
Tullio Joseph Tanzi   *Editors*

Intelligent Systems for Crisis Management

Gi4DM 2018

Springer

Lecture Notes in Geoinformation and Cartography

The Lecture Notes in Geoinformation and Cartography series provides a contemporary view of current research and development in Geoinformation and Cartography, including GIS and Geographic Information Science. Publications with associated electronic media examine areas of development and current technology. Editors from multiple continents, in association with national and international organizations and societies bring together the most comprehensive forum for Geoinformation and Cartography.

The scope of Lecture Notes in Geoinformation and Cartography spans the range of interdisciplinary topics in a variety of research and application fields. The type of material published traditionally includes:

- proceedings that are peer-reviewed and published in association with a conference;
- post-proceedings consisting of thoroughly revised final papers; and
- research monographs that may be based on individual research projects.

The Lecture Notes in Geoinformation and Cartography series also includes various other publications, including:

- tutorials or collections of lectures for advanced courses;
- contemporary surveys that offer an objective summary of a current topic of interest; and
- emerging areas of research directed at a broad community of practitioners.

More information about this series at http://www.springer.com/series/7418

Orhan Altan · Madhu Chandra ·
Filiz Sunar · Tullio Joseph Tanzi
Editors

Intelligent Systems for Crisis Management

Gi4DM 2018

Springer

Editors
Orhan Altan
Department of Geomatics
Faculty of Civil Engineering
Istanbul Technical University
Istanbul, Turkey

Madhu Chandra
Microwave Engineering
and Electromagnetic Theory
Technische Universität Chemnitz
Chemnitz, Germany

Filiz Sunar
Department of Geomatics
Faculty of Civil Engineering
Istanbul Technical University
Istanbul, Turkey

Tullio Joseph Tanzi
LabSoC Laboratory, COMELEC
Department, Campus SophiaTech
Institut Mines-Telecom-Telecom ParisTech
Biot, France

Preface

Since the 1980s, the impacts of disasters have risen rapidly affecting developed and developing countries and almost all sectors of economy at local, national, and regional levels. Several hundred million people are affected annually, and losses reached over billion USD during the last years. Governments, international organizations, and research institutions worldwide have set to work to improve disaster management in all its phases: mitigation, preparedness, relief and response, and recovery and reconstruction. Many governments have put the formation of a hazard-resistant and disaster coping society on their political agenda as an important factor of sustainable economic development and better quality of civil life. In this respect, the awareness of new geospatial technologies and their successful utilization in disaster management is becoming crucial. These technologies are emerging very fast and involve different satellite systems such as meteorological and earth observation satellites, communication satellites, and satellite-based navigation and positioning systems, that may help to improve prediction and monitoring of potential hazards, risk mitigation, and disaster management, contributing in turn to reduce losses of life and property. Global navigation satellites and earth observation satellites have already demonstrated their flexibility in providing data for a broad range of applications: weather forecasting, vehicle tracking, disaster alerting, forest fire and flood monitoring, oil spill detection, desertification monitoring, and crop and forestry damage assessment. Monitoring and management of recent natural disasters have greatly benefited from satellite imagery, such as the Indian Ocean tsunami in 2004; floods (Austria, Romania, Switzerland, and Germany in 2005); hurricanes (USA in 2005); forest fires (Portugal, France, Greece, Australia in 2005, 2008 latest in Los Angeles/California—USA); earthquakes (Pakistan in 2005, Indonesia in 2006, Wenchuan/China in 2008, Haiti 2010, and many others), etc.

Systems maintaining geospatial information are becoming more elaborate and multi-functional than ever before. Many of these systems can meet requirements for early warning and real-time response and provide suitable models for elaborated predictions, simulations, and visualizations. However, the knowledge about the full range of the application potential of geospatial technologies is the domain of specialists in the geosciences.

An international effort in this direction is the Gi4DM series of conferences, which was held for the first time in 2005 in Delft after the Indian Ocean tsunami and repeated every year in almost all parts of the world. The last Gi4DM conference held on March 18–22, 2018, in Istanbul was the reflection of the intended longer-term coordination between ISPRS and URSI, two leading global scientific societies serving complementary disciplines of interest for a wide scientific community. The conference addressed diverse topics related to methodologies and technologies within a unique forum keeping participants up to date with the latest advances in disaster management.

This book includes 12 chapters organized in four parts (Earthquake Damage Assessment, Geospatial Information for Disaster Management, Landslide Monitoring, and Natural Disasters) focusing on the intelligent use of geo-information, semantics, and situation awareness. The chapters are an extended version of the presented papers selected by the Scientific Committee according to quality, significance, and originality. The Local Organizing Committee decided for the first time in the Gi4DM book series to encourage the brightest young researchers and expand the frontiers of science in their chosen fields. Therefore, the winners of the best poster award were also invited to take part in this book (Part III, Chapter "Remote Sensing Techniques in Disaster Management: Amynteon Mine Landslides, Greece"). We are earnestly thankful to all the authors for their efforts. Hence, in this book, various application-oriented 12 examples from 8 countries of different parts of the world demonstrate the potential of this technology in the Crisis Management.

Istanbul, Turkey   Orhan Altan
Munich, Germany   Madhu Chandra
Paris, France   Filiz Sunar
December 2018   Tullio Joseph Tanzi

Contents

Part I
Earthquake Damage Assessment

Synergistic Exploitation of Geoinformation Methods for Post-earthquake 3D Mapping and Damage Assessment

Nikolaos Soulakellis, Georgios Tataris, Ermioni-Eirini Papadopoulou, Stamatis Chatzistamatis, Christos Vasilakos, Dimitris Kavroudakis, Olga Roussou and Apostolos Papakonstantinou

Abstract This paper presents a methodological framework, which establishes links among the: i. 3D mapping, ii. 3D model creation and iii. damage classification grades of masonry buildings by European Macroseismic Scale-98 and the application of geoinformation methods towards 3D mapping and damage assessment after a catastrophic earthquake event. We explore the synergistic exploitation of a Real Time Kinematics system, terrestrial photogrammetry, Unmanned Aircraft Systems and terrestrial laser scanner for collecting accurate and high-resolution geospatial information. The proposed workflow was applied at the catastrophic earthquake of June 12th, 2017 on the traditional settlement of Vrisa on the island of Lesvos, Greece. The Structure from Motion method has been applied on the

N. Soulakellis (✉) · G. Tataris · E.-E. Papadopoulou · C. Vasilakos · D. Kavroudakis ·
O. Roussou · A. Papakonstantinou
Department of Geography, University of the Aegean, Mytilene, Greece
e-mail: nsoul@aegean.gr

G. Tataris
e-mail: tataris@geo.aegean.gr

E.-E. Papadopoulou
e-mail: geom17022@geao.aegean.gr

C. Vasilakos
e-mail: chvas@aegean.gr

D. Kavroudakis
e-mail: dimitrisk@aegean.gr

O. Roussou
e-mail: orousou@aegean.gr

A. Papakonstantinou
e-mail: apapak@geo.aegean.gr

S. Chatzistamatis
Department of Cultural Technology and Communication, University of the Aegean,
Mytilene, Greece
e-mail: stami@aegean.gr

3

high-resolution terrestrial and aerial photographs, for producing accurate and very detailed 3D point clouds of the damaged buildings of the Vrisa settlement. Additionally, two Orthophoto maps and two Digital Surface Models have been created, with a spatial resolution of 5 cm and 3 cm, respectively. The first orthophoto map has been created just one day after the earthquake, while the second one, a month later. The significant advantages of the proposed methodology are: (a) the production of reliable and accurate 2D and 3D information at both village and building scales, (b) the ability to support scientists during building damage assessment phase and (c) the proposed damage documentation provides all the appropriate information which can augment all experts and stakeholders, national and local organizations focusing on the post-earthquake management and reconstruction processes of the Vrisa traditional village.

1 Introduction

Natural hazards such as earthquakes have an enormous effect on populated places regarding both life-threating conditions and socio-economic impact. An earthquake is a very crucial case of natural hazards, having the following characteristics: (a) it cannot be predicted; (b) only few seconds of a strong shake can cause enormous damage in large areas; (c) it can affect all aspects of society; (d) its effects can last for many years; and (e) the correct management of an earthquake risk relies on close cooperation between different organizations at different levels.

The response phase of an earthquake regarding emergency management is extremely complicated as: (a) the buildings are highly vulnerable to aftershocks; (b) many streets are not accessible; (c) seismic activity continues to produce several strong aftershocks affecting more the most damaged buildings; (d) relief operations are in action by several organizations; and (e) most people are frightened and some in panic. The planning and the implementation of the response in a natural disaster is mainly based on the precise information provided by the assessment. Post-disaster assessment can be done in four levels: (a) rapid assessment, (b) short-term recovery and (c) long-term reconstruction and (d) recovery management.

After an earthquake, remote sensing has been widely used in rapid damage assessment to detect either region with collapsed buildings or individual damaged buildings (Olsen et al. 2013; Dong and Shan 2013). In recent decades, airborne platforms and especially Unmanned Aerial Systems (UAS) have been utilized after earthquakes and each event presented different opportunities and lessons confirming UAS's usage for imagery collection, detection and damage estimation in disaster risk and emergency management (Adams and Friedland 2011; Gomez and Purdie 2016). In Dominici et al. (2017) the authors mention that recent technological advantages make UAS-based photogrammetry highly suitable for surveys in a geo-hazard context, as in a post-earthquake scenario, and its advantages may be summarized as follows: (i) safety: no risk for operators; (ii) possibility to survey

inaccessible zones; (iii) high-resolution photographs; (iv) speed of survey and elaboration; and (v) repeatability and economic convenience. More recently, UAS data where used for automatic extraction of buildings and their facades implementing segmentation on point clouds (Chen et al. 2016; Calantropio et al. 2018). Aerial surveys are often carried out using multiple small or medium-format cameras mounted together that simultaneously capture nadir and oblique images. Oblique images capture the scene under a tilt angle, having much larger footprint than in nadir views. The tilted cameras are improving the visibility of buildings facades and other vertical structures. These non-oblique camera views have as a result scale and visibility related errors due to their scale variations (Papakonstantinou et al. 2018).

Due to the very late advances in the fields of computer vision and photogrammetry in combination with the ever-increasing data processing power, orthophoto maps and Digital Surface Models (DSM) can be produced, by terrestrial and/or aerial high-resolution 2D imagery taken after an earthquake. The Structure from Motion (SfM) algorithm has improved the quality of 3D data that can be derived from overlapping imagery by incorporating advancements in soft-copy triangulation and image-based terrain extraction algorithms (Westoby et al. 2012; Bemis et al. 2014). Many studies have been carried out using UAS-SfM pipeline, emphasizing on near real-time data acquisition and processing after an earthquake event (Xu et al. 2014; Yamazaki et al. 2015; Papakonstantinou et al. 2018). In other cases, Object-Based Image Analysis (OBIA) applied to orthophoto maps to assess damage per building (Fernandez Galarreta et al. 2015).

Additionally, Terrestrial Photogrammetry (TP) and Terrestrial Laser Scanning (TLS) are efficient tools for post-earthquake damage assessment providing accurate high-resolution dense point clouds of areas of interest. TP and/or TLS can be used to collect precise 3D information of any object need to be estimated and reconstructed, such as debris, cracks in walls, non-structural damages, volume of individual buildings etc.

The application of TLS techniques for change detection and deformation monitoring of structures is an active area of research and many methods for that purpose have been already suggested (Chang et al. 2008; Zhihua et al. 2014; Mukupa et al. 2016; Guldur and Hajjar 2016; Erkal 2017; Guldur Erkal and Hajjar 2017; Jafari et al. 2017; Zhao et al. 2018; Puente et al. 2018). Olsen et al. (2013) utilize optical techniques, such as TLS and satellite imagery, to show that recently developed change detection algorithms can quickly provide regional damage information and they investigate damaged structures from the Indonesia and American Samoa tsunamis, San Diego coastal erosion, and cracking of a historical building in Italy. Anil et al. (2013) showed that it is possible to detect as small as ∼1 mm cracks from TLS data. They identified a series of crack parameters based on the state-of-the-art damage assessment codes and standards and parameters, which affect the performance of laser scanners for detecting cracks.

Many researchers focus on the application of TLS for the damage assessment after a disaster and research using TLS data has been conducted for damage assessment after several earthquakes. TLS data have been used for change detection of seismically-induced landslides from the 2004 Parkfield, California and 2004

Niigata Ken Chuetsu, Japan, Earthquakes (Kayen et al. 2006), and for various types of detailed measurements and analyses on structures from the 2010 Chile earthquake and tsunami, with data obtained in Concepción, Constitución, Dichato, and Talcahuano (Olsen et al. 2012).

The damage assessment and modeling with TLS data are presented for a four-story masonry-infilled reinforced concrete frame building, which was severely damaged due to the 2015 Gorkha Earthquake, Nepal (Bose et al. 2016) and for a two-story reinforced concrete masonry-infilled building which was severely damaged due to the 2010 El Mayor-Cucapah, Mexico earthquake (Song et al. 2018). Olsen and Kayen (2012) argue that the use of TLS can preserve the scene digitally for post-disaster assessment after the Japanese earthquake and tsunami. Application of TLS techniques is also found in (Pesci et al. 2013) where the authors propose a data analysis strategy with application to rapidly detect deformation traces in three buildings damaged by the 2012 Emilia Romagna earthquake in Italy.

Federal Emergency Management Agency's (FEMA) current state of Preliminary Damage Assessment (PDA) in local, state and federal scale includes structure-by-structure assessment by identifying damage facilities and documenting damage, work and cost. FEMA has established four categories to describe damage to homes; Destroyed, Major, Minor, and Affected with an Inaccessible category for the homes that cannot be reached for assessment. Geospatial Damage Assessment processes (GDAP) comprises self-reporting, fly-over surveying, door-to-door assessments, geospatial analysis and GIS, modeling and lately, integration of mobile technology (Federal Emergency Management Agency (FEMA) 2016).

The classification on the EMS-98 scale (European Macroseismic Scale) of damage is based on building types. Particularly, for each type of masonry structure, depending on the employed materials and construction techniques, an empiric vulnerability class is associated (descending scale from A to E) and the level of damage is categorized observing the structure (Grünthal 1998).

Even though geoinformation is rapidly expanding to several disciplines of both human and natural sciences, there is no robust methodology to apply in urgent situations such as after an earthquake for the creation of 3D models capturing its effects at a village scale. This paper focuses on a synergistic exploitation of latest geoinformation methods (TP, TLS, UAS) proposing a methodology for gathering precise and high-resolution 3D geoinformation (dense point clouds, 3D models of buildings or debris, DSM) where the building damage documentation can be modified in order to include all the 2D and 3D information produced.

This article describes the methodology followed the strong Lesvos 12 June 2017 (Mw = 6.3) earthquake which has heavily damaged the building stock of Vrisa traditional settlement covering an area of approximately 0.3 Km^2. The damages where widespread and about 80% of settlement's buildings were affected. Most of the buildings were traditional stone masonry residential constructions built by the end of the 19th century.

2 Methodology

The present methodological framework establishes links among the: i. 3D mapping, ii. 3D model creation and iii. damage classification grades of masonry buildings by EMS-98 which involves four stages: (a) data acquisition, (b) data processing, (c) data 3D modeling and 3D visualization and (d) visual damage assessment at two different scales: i. village-scale and ii. building-scale (Fig. 1). More analytically, data acquisition refers to: (a) Real Time Kinematics (RTK) measurements, (b) very high-resolution images acquired by UAS and terrestrial cameras and (c) point clouds acquired by terrestrial laser scanner.

RTK is a differential Global Navigation Satellite System (GNSS) technique which achieves positional measurements with accuracy in the range of a few centimeters, in the vicinity of a base station. This technique is based on the use of carrier measurements and the transmission of corrections from a base station with a known location, to the rover, so that the main errors that drive stand-alone positioning to cancel out. The RTK base station covers an area extending about 10 km, and a real-time communication channel is necessary for connecting the base and the rover.

Remote sensing offers several advantages in emergency situations, the first and foremost is the investigation and information acquisition in extremely hazard-prone zones. At first, for an 'early damage assessment', the high-resolution satellite images are very useful to detect quickly the areas and structures that suffered the worst damages. For a complete and very detailed survey of structures and infrastructures, useful for the following reconstruction phase, however, UAS photogrammetry is more suitable (Xu et al. 2014).
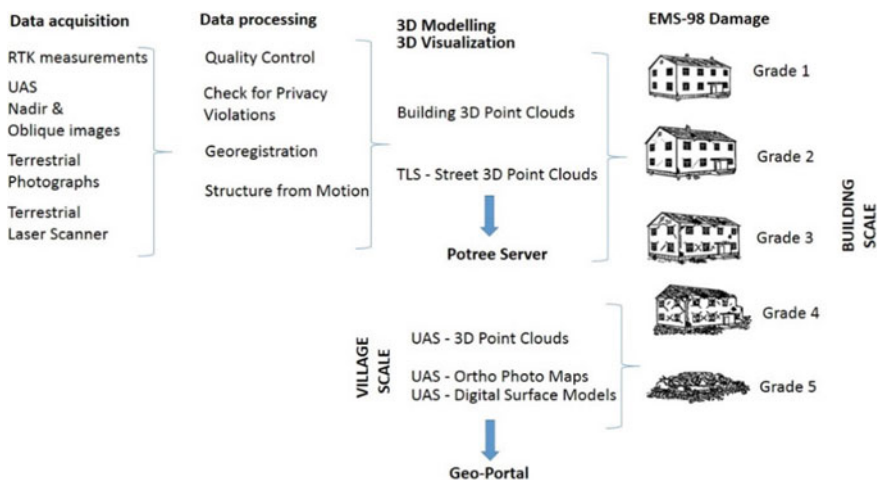
Fig. 1 Flowchart of the methodological framework for post-earthquake 3D mapping and building damage assessment of at two scales: i. village and ii. building

Photogrammetry is a cost-effective means of obtaining large-scale digital urban data. Photogrammetric techniques use 2D images without any prior data to create 3D data. Terrestrial, or ground-level, images are the most convenient data sources. Although these data provide high fidelity ground, vegetation, and building facade detail, they lack of building top information, and occlusion limits their range. The limited visible area in each image makes it difficult to construct large urban areas. In order to meet the specific goal of creating 3D models not only of the affected by the earthquake buildings (damaged) but of a whole building stock of a settlement, the photogrammetric survey planning should be based on the following criteria: i. optimize the number of the photos for each building, ii. maximize the accuracy of the information, iii. avoid privacy violations, iv. permit scale and registration of the 3D models and v. account for safety issues.

The Structure from Motion (SfM) algorithm, introduced in Computer Vision in the mid 90s, permits the automatic acquisition of the interior orientation parameters and the camera position in a relative image-space coordinate system. With SfM, scene geometry, camera position, interior and exterior orientation can all be extracted automatically, with high redundancy, using an iterative bundle adjustment (Triggs et al. 2000) on a sequence of images (multi-image approach). The principles and workflow of SfM have been described by (Snavely et al. 2008; Snavely 2011), and (Westoby et al. 2012). The Photoscan v1.3 software package was used for the SfM photogrammetric processing, which can convert many images into georeferenced DSMs, digital orthophotos and 3D models.

Terrestrial Laser Scanning has proven to be an increasingly practical technology for providing precise, accurate, timely and non-destructive estimates of human and natural objects in 3D models. Operational acquisition of TLS data, at a village scale, is possible due to the reduced instrument costs, the improved range, precision and accuracy of measurements, as well as the increased capability of software and computing infrastructure to process large datasets.

One of the main research concerns when using the above methods to acquire data is the assurance of protecting the privacy of the individuals since it is a common threat to include personal identity in this kind of data sets accidentally.

3 Application and Results

3.1 Study Area—Lesvos, June 12th, 2017 (m_w = 6.3) Earthquake

On 12 June 2017 (UTC 12:28:38.26) a magnitude Mw 6.3 earthquake occurred offshore the SE coast of Lesvos island in NE Aegean Sea, which was widely felt, caused one fatality, and partially ruined the village of Vrisa on the south-eastern coast of the island (Kiratzi 2018). Most of the traditional Vrisa buildings were damaged, several collapsed, while many were heavily damaged, reported dangerous

and/or unrepairable. Monument constructions, such as post-Byzantine churches suffered severe static effects. Fewer damages were widespread throughout the island (reported in at least 12 villages) (Papadimitriou et al. 2018).

Few days after the earthquake the Greek Earthquake Rehabilitation Organization (G-ERO) conducted first-degree inspections of the Vrisa buildings and most (not all) of the buildings were distinguished into the following three categories: i. "Green-Safe for Use", ii. "Yellow-Unsafe for Use" and iii. "Red-Dangerous for Use" according to the Earthquake Planning and Protection Organization guidelines. Typically, the last two categories, yellow and red, incorporate all degrees of damage according to the EMS-98 (Grünthal 1998), mainly from 3 (substantial-to-heavy) to 5 (destruction). Practically, the red category buildings should be demolished by their owners while the yellow category buildings could be reconstructed without being demolished.

The first-degree inspection results were marked with the appropriate signs on the buildings and mapped by means of a mobile geoinformation application. To conduct fast and collect geo-referenced data in the field, there was the need for a mobile application that could capture GPS coordinates along with some descriptive characteristics regarding the building structures of the village. For this purpose, a mobile application for Android Operating System (Nimodia and Deshmukh 2012) has been developed, that could capture the coordinates of the user along with a number of characteristics for each building. The application was based on the core code of OSMtracker application and was rebuilt with some extended functionality. The main panel of the mobile application includes button shortcuts for capturing house conditions (red cross, yellow cross, green cross). The shortcuts were used for rapid data collection in the field. Additionally, the following information of the buildings was collected: i. their geographical coordinates, ii. their constructed material (i.e., masonry R/C building) and iii. their number of stores (i.e., one, two or three floors) (Figs. 2 and 3) (see Table 1). Finally, the application includes voice notes collection, text notes collection and picture collection. All data are geo-referenced and can be processed with modern GIS systems.

3.2 Application

The synergistic exploitation of geo-information methods towards 3D mapping and damage assessment of the catastrophic earthquake of June 12th, 2017 on the traditional settlement of Vrisa on the island of Lesvos, Greece is presented in Fig. 4. One day after the earthquake a campaign started for collecting: (a) more than 150 ground control points using an RTK system, (b) more than 20.000 high-resolution terrestrial and aerial images using cameras and Unmanned Aircraft Systems and (c) 140 point clouds by a 3D Terrestrial Laser Scanner. The SfM method has been applied on the high-resolution terrestrial and aerial photographs, for producing

Fig. 2 Map presenting the distribution of first-degree inspections by the Greek ERO in combination with buildings' material
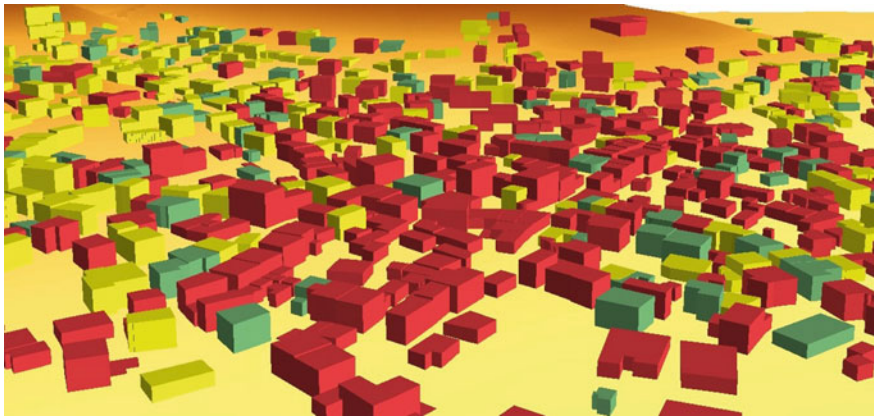
Fig. 3 3D visualization presenting the distribution of first-degree inspections by the Greek ERO in combination with buildings height. The buildings were distinguished into the following three categories: i. "Green—Safe for Use", ii. "Yellow—Unsafe for Use" and iii. "Red—Dangerous for Use" according to the Earthquake Planning and Protection Organization guidelines

Table 1 Information concerning the results after the first inspection by Greek ERO in accordance with building material and number of stories

	Number of buildings	Material			Number of Stories		
		Masonry	F/C	Mixed	1 Store	2 Store	3 Store
GREEN	218	165	46	7	125	91	2
YELLOW	314	310	8	6	122	186	6
RED	281	278	2	1	118	156	4
Uninspected	359						
Total	1162						
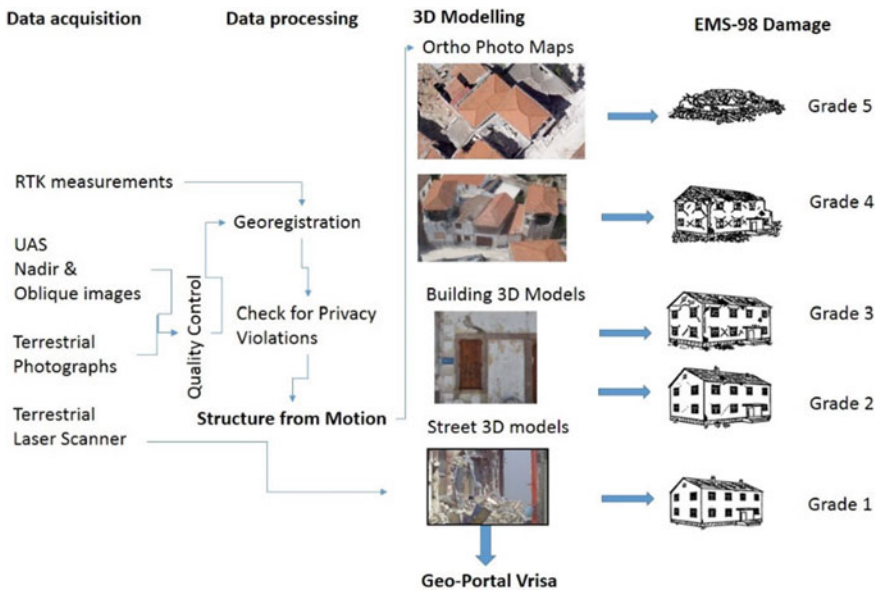
Fig. 4 Flow chart of the application of 3D mapping methods on Vrisa settlement after the catastrophic Lesvos earthquake

accurate and very detailed 3D point clouds of the damaged buildings of the Vrisa settlement. Additionally, two orthophoto maps and two DSMs have been created, with a spatial resolution of 5 cm and 3 cm, respectively.

The data acquisition campaign started on 13th June 2017, the very next day of the earthquake, under tough conditions and taking seriously into consideration the safety of the research team. During the following weeks, several very strong aftershocks occurred having magnitudes ranging from 3.5–5.0 Mw, producing more wall collapsing during the campaign.

During and following the data acquisition stage, quality control of all datasets was performed aiming to ensure the high quality of the results. Finally, the data processing and 3D modeling stages of the present methodology were carried out mainly by the application of the SfM algorithm.

3.2.1 Data Acquisition

The data acquisition stage involved several geoinformation data acquisition and processing methods and techniques: (a) RTK measurements, (b) high resolution aerial image collection by means of an UAS using an innovative multi-camera rig (Papakonstantinou et al. 2018), (c) high resolution photo collection by a DSLR camera, and (d) point clouds by a TLS and the relevant equipment.

RTK Measurements

The first important step of the campaign was the establishment of several Ground Control Points (GCPs) in Vrisa settlement with very high spatial accuracy and proper spatial distribution. These GCPs are necessary to enable georeferencing of all high-resolution aerial images as well as accurately identifying scan positions by the TLS. For this purpose, the following methodology was followed:

1. Two Base Stations (BS) were established within the village of Vrisa, depending on the base of the Greek National Trigonometric Network (NTN) located at the top of the hill named Korona, SW of the settlement of Vrisa. Due to the morphology of the settlement, as it is developed on three hills and two flat relatively low altitude surfaces, the two BSs were placed on the two hills on the outskirts of the settlement to be higher than the rest set of GCPs to achieve better and more accurate measurements.
2. One hundred fifty-seven (157) GCPs were placed within the Vrisa settlement, having very high accuracy in three dimensions (X, Y, Z), with an RTK rover, the base of which was placed at the one of the two base points, depending on the area where the GCPs were placed, to achieve better reception and a greater number of satellites, with an average horizontal error of 0.8 cm and an average elevation error of 1.3 cm. Thirty (30) of the GCPs, were used for georeferencing the orthophoto maps, resulting from the UAS images, having a suitable spatial distribution in the settlement.

UAS Nadir and Oblique High-Resolution Images

In less than 24 h after the strong earthquake, a UAS (hexacopter) flew over the Vrisa village at 160 m altitude and captured vertical images using a Sony A5100 camera with a fixed lens of 19 mm focal length. During the period 13/07/2017–6/

08/2017 several test flights was carried out with various aerial means and different sensors configuration to achieve a high-resolution mapping of the existing state of study area through the production of sub-decimeter spatial resolution orthophoto maps. The mapping of the Vrisa village was carried out with flights at different heights to explore the most efficient parameters of collecting data to record the damages of the area's buildings in an optimal way. Almost one and a half month later, on 25th July 2017, an innovative noncommercial multicamera rig attached to a UAS, flew a lower altitude (65 m), capturing high resolution images with: i. one nadir and ii. three (3) oblique cameras (angle $\theta = 45°$) having bottom, front and left-right configuration.

Terrestrial High-Resolution Images

During the period from 13th of June 2017 to 6th of July 2017, a survey for terrestrial high-resolution image acquisition took place using two Nikon D3400 cameras with 24.2 MP resolution, 23.5×15.6 mm sensor size and 6000×4000 pixel resolution, having the following standard settings: Aperture mode (f/8), Focal length: 18 mm, Production of raw JPEG images and Vibration Reduction disabled.

More specifically, the Vrisa settlement was divided into 240 road sections where each section included not more than five buildings and about 20,000 photos were taken covering all the buildings of Vrisa village, taking into serious consideration that the post-earthquake activity was in progress and many aftershocks with magnitude 4–5 were frequently occurring.

It is worth mentioning that photography on narrow-walled roads created a problem with the construction of a 3D model for tall buildings, because a large percentage of the facade was either not visible due to a balcony or was visibly tilted to the level of the camera. Note that with the specific cameras and settings the size of the visible field (field of view) at a distance of 3 m from a building is 3.92 m 2.6 m. This caused difficulty in matching images because in such a small range it was often difficult to locate uniquely distinct spots to identify in more than one photograph. The existence of a smooth pattern such as the wall without any features or rectangular rails creates a problem in identifying common features between consecutive photos. In some cases with no visible scale, measurements of distinct objects from the TLS data were used to scale the model.

Terrestrial Laser Scanning

The laser scan planning was designed with the aim of scanning not only the affected by the earthquake buildings (damaged) but the whole building stock of the Vrisa traditional settlement. Taking into consideration the TLS technical specifications and the Vrisa settlement characteristics, a network of one hundred forty scanner positions were established, that allowed maximum coverage of the settlement and guaranteed point spacing less than 1.5 cm for the whole settlement. The scan

planning was also based on the following criteria: i. optimization of the spatial distribution of the scans, ii. minimization of the number of the TLS scans, iii. minimization as possible of the occlusions, iv. avoid privacy violations (scan positions inside private property) and v. provide enough overlap (>30%) between consecutive laser scans, without using artificial targets.

Based on the criteria mentioned above, during the period from 13th June 2017 to 06th July 2017, a survey for TLS data acquisition performed by using a phase-shift laser scanner, FARO Focus[3D]. One hundred forty (140) laser scans were performed from pre-measured positions using the RTK measurements. The scans were conducted with the following settings on the laser scanner: i. scan area: 360° horizontally × 305° vertically, ii. ¼ resolution that acquires point clouds at point spacing of 6.13 mm/10 m and thus less than 1.5 cm for the whole scenario of the settlement and iii. digital compass and inclinometer measurements.

The combination of the measured scanner position with the measurements from the compass and the inclinometer offers the option of a sensor-driven method for georeferencing the laser scanner data.

3.2.2 Data Processing

Quality Control and Check for Privacy Violations

After image acquisition, quality photo scans were followed to remove those that did not meet specific criteria, such as shifted scans as well as those in which there were objects in motion. Finally, the 3D Point Model acquired the texture of the buildings through the photos to create a photo-realistic object of the entire segment.

Visual inspection of all TLS data was performed in order to assess the quality of the point clouds. Scene software package by FARO was used for the TLS data processing. The raw point clouds were cleaned from noise or undesired information such as vegetation. In cases where errors were detected (due to dust on the scanner's rotating mirror and passing vehicles), the specific scans were reshaped. Also, dozens of control distances were taken to objects in the area for comparison with digital models. These distances were taken on fixed objects (windows, doors, etc.) with a tape measure. Next, the accuracy of the scalability of the point cloud resulting from scanning with the TLS and the extent to which these measurements correspond to the actual sizes of the measured objects was determined.

Finally, a detailed and systematic review of every element of the dataset was conducted for establishing and eliminating any form of violation of citizens' privacy through their direct or indirect identification from the data used. The examined data set included: i. ground images taken with a camera, ii. 3D models produced by TLS and by terrestrial photogrammetry, and iii. photos taken by UAS flights. The methods applied for the protection of citizens' privacy were the following: (a) Removal of citizens included in the data set, (b) blurring of the parts of the images and models in cases where the specific parts could not be removed.

Geo-Registration and Accuracy Assessment

Geo-registration is a crucial step in order to provide absolute orientation and to assign the proper scale to all derivatives of the spatial data acquisition process, such as the orthorectified aerial high-resolution images, the point clouds etc. Thus, it is necessary to add an adequate number of GCPs measured, in the Greek reference system GGRS-87, using the RTK technique. Subsequently, through the bundle adjustment, the GCPs together with the tie-points allow the internal and external orientation to be refined and directly obtain the geo-referenced model. Additionally, the geo-referenced 3D models must be verified using 'ground truth' measurements, several control points (CPs) to meet the purpose of providing reliable and verified metric quantification, as required in the case of the post-earthquake damage assessment.

On the UAS surveys 20 GCP's were used with a total RMS of 2.3 cm. The products generated for Vrisa village had geo-registration accuracies (RMS) less than a half of a pixel of the derivatives' resolution. From the geo-registration accuracy achieved can be concluded that the precision of the geoinformation produced is of satisfactory accuracy for post-earthquake damage assessment.

Regarding terrestrial photogrammetry, geo-rectification of each 3D model was performed upon request in order to visualize and analyze it with other georeferenced spatial data. The GCPs were collected from the orthophoto map derived from UAS data and the resulted accuracies were less than 10 cm.

3D Modeling with the SfM Method

The Photoscan v1.3 software package was used for the SfM photogrammetric processing, which can convert many images into georeferenced DSMs, digital orthophotos and 3D models. The datasets acquired for the specific post-earthquake situation were i. DSMs; ii. Orthophoto maps; and iii. 3D models. More specifically, the final products obtained by the methodology described above, were the following: i. Orthophoto map and DSM (13th June 2017), ii. Orthophoto map and DSM (25th July 2017), iii. Digital Elevation Model (DEM) of the Vrisa area having spatial resolution 5 cm and vertical accuracy less than 1 m, iv. 240 3D models of all the buildings of Vrisa settlement.

Geoportal and 3D Point Cloud Visualization

Within the context of this application, there was also a need for sound management and visualization of a large volume of spatial information. In addition, there existed a need to visualize their spatial distribution so that they could be asynchronously and remotely studied. For this purpose, it was considered necessary to design and implement an online geoportal which is hosted on a server, accessible only by authorized users. The design considered the needs of the application to monitor the

initial data, as well as the need for online visualization of the final data from each method. The technologies used to construct the geoportal consisted of several programming languages for the construction of data structures, by server-side technologies and by client-side technologies. The technologies used included the PHP and Python programming languages. The management of the complex geo-data structures in the embedded GeoServer and the database has been achieved by using Postgresql as it offers spatial data structures management capabilities.

Geocomputation projects such as the one conducted after the Vrisa Earthquake, asks for specialized handling of the results. The type and size of results as well as the sensitivity of information included, require a fast and reliable way of visualizing data and results. Relevant stakeholders such as local authorities and property owners, need to have customized access to specific parts of the project results. Therefore, a customized web application has been developed in the following URL: https://vrisa.aegean.gr mainly for results dissemination and data management. We used an open source WebGL-based point cloud renderer (Schütz 2016) in order to present results from 3D scanning process (Fig. 5). The web application was also used for centralized data management of intermediate results of the project and allowed for multi-platform access of the visualization. Finally, one of the main advantages of this web application was the concurrent multi-role access of users based on roles. Figure 6 depicts the main view of the web application which includes a separate panel on the left part, for the configuration of the visualization panel. One of the main advantages of this work is the ability to disseminate results to a variety of stakeholders that do not necessary share the very same knowledge and perspective of the scientific results and the results of the Vrisa Project. In other words, this web application bridges the gap between experts and public as well as the gap between technical and administrative individuals.

Fig. 5 Web-application (Potree) of the "Vrisa project" showing three interconnected 3D-scans in the main square of the village

Fig. 6 Digital surface model map provided by the 13th June 2017 campaign, at a scale of 1:4.000 proved to be useful for the estimation of the collapsed and partially collapsed buildings
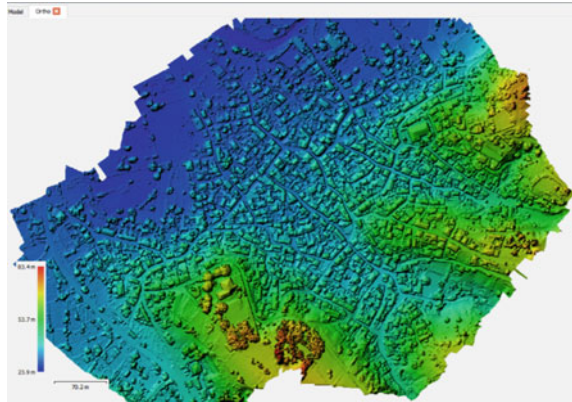
4 Discussion

4.1 Orthophoto Maps, Digital Surface Models and 3D Point Clouds by UAS Campaigns

4.1.1 UAS Campaign on June 13th, 2017

By processing the 229 nadir, high-resolution aerial images obtained the day after the earthquake, from an altitude of 160 m., an orthophoto map, a digital surface model (Fig. 7) and a 3D point cloud has been produced and proved to be very efficient in 'early damage assessment' stage. The results, required only a few hours of processing due to the small number of photos, capturing all the important information and providing a clear view of the heavily damaged areas of the Vrisa settlement, as well as those that were not essentially affected.

More analytically, the 13th June 2017 orthophoto map was visually interpreted aiming to produce an early severe-damage assessment map of the Vrisa settlement. Collapsed and partially collapsed buildings can be visually identified, showing clearly that heavy damages are concentrated on the western part of the village than on the eastern part. In parallel, blocked roads by heavily collapsed building as well as smaller debris by partial wall collapse can be clearly seen and mapped (Fig. 9). Based on the EMS-98 (Grünthal 1998) damage classification on the specific orthophoto map, damages of grade 5: destruction, e.g. partial and total collapse of buildings can be clearly visually identified giving an accurate early impact assessment in a short period of time (less than one day).
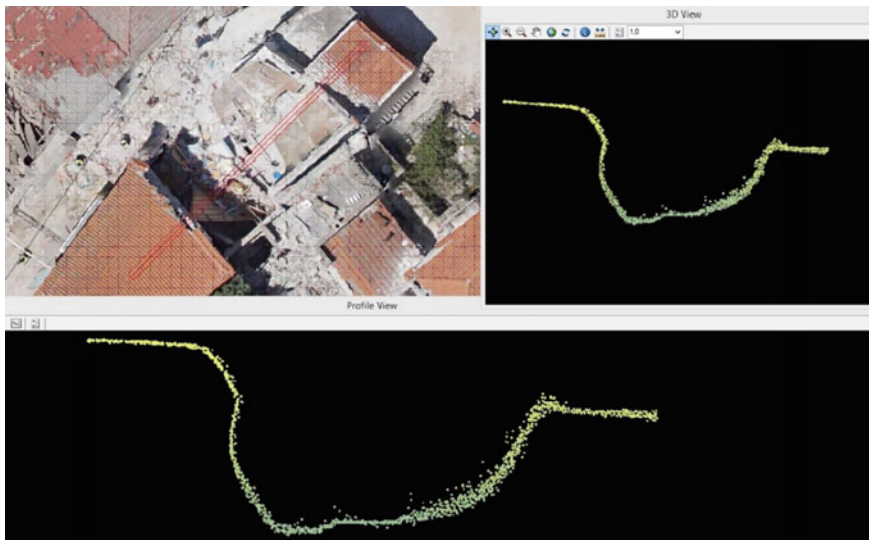
Fig. 7 3D Profile views of the 3D PointCloud (13/06/2017). Collapsed buildings can be clearly distinguished due to their smaller heights

Additionally, the DSM of Vrisa settlement (Fig. 6) derived by the processing of the 229 nadir UAS images provides a very effective mean to measure building heights after the earthquake, giving an estimation of their volume, and the possible extent of their total or partial collapse. Moreover, 3D visualization of the 3D point cloud gives the opportunity to visually explore the entirely collapsed buildings due to their smaller heights compared with the surrounding buildings (Fig. 7).

In addition, UAS high-resolution image acquisition, from medium altitudes i.e. 160 m, provides in a very short time a concise view of the earthquake affected areas. Furthermore, by visual interpretation very accurate and reliable information concerning the severity of an earthquake can be mapped, giving a very precise assessment for buildings having very heavy structural damages (grade 5), which can be taken into consideration for initiating effective emergency response and recovery actions (Fig. 8).

4.1.2 UAS Campaign on July 25th, 2017

The UAS data acquisition campaign that took place on July 25th, 2017, was implemented using an innovative Malteser cross configuration 4-camera rig. In this campaign, 1.044 nadir and 4.084 oblique high-resolution images (Fig. 9) were

Fig. 8 Orthophoto map of 13th June 2017 at a scale of 1:1.000 showing the NW part of Vrisa settlement which concentrates a large number of building of grade damages 5 e.g. partial and total collapse of buildings, the blocked roads and the areas with debris
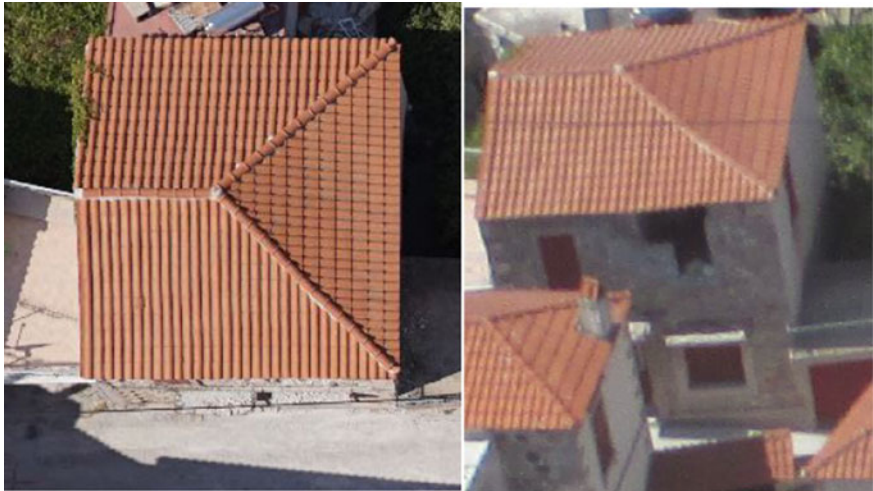
Fig. 9 Part of a nadir (left) and oblique (right) image acquired on 25th June 2017. A serious failure of the top part of a wall is captured only on the oblique image (right)

Fig. 10 Parts of the 3D point cloud derived by nadir and oblique images acquired on 25th June 2017, where building damages of grade 4 are clearly identifable

Fig. 11 Orthophoto map of 25th June 2017 at a scale of 1:1.000 showing the NW part of Vrisa settlement which concentrates a large number of building with damages of grades 4 and 5

acquired, from an altitude of 65 m and processed with the SfM method. The derivatives were the sparse and dense 3D point clouds (Fig. 10), a DSM, a 3D model (mesh), and an orthophoto map (Fig. 11).

The produced orthophoto map, having a spatial resolution of 3 cm, presents clearly: i. totally or/and partially collapsed buildings, ii. roof damages (chimney collapse, roof detachment, etc.) and iii. debris close to the buildings that are reliable indicators of wall detachments and wall collapse. As such, visual interpretation of the orthophoto map can assist damage assessment especially for damages of grades 4 and 5.

More analytically building damages of grade 4: very heavy damage (heavy structural damage, very heavy non-structural damage: serious failure of walls; partial structural failure of roofs and floors) assessment requires reliable information from the building facades and not only from the roofs. For this reason, the 4.084 oblique high-resolution images from an altitude of 65 m enrich the data into the 3D models by providing more information from the building facades. Subsequently, visual interpretation of the building facades was made to identify the differences between the 3D models that were developed only from the nadir images and those from the combination of nadir and oblique accordingly (Fig. 10). As it was expected the 3D point cloud derived only from nadir images has a large number of gaps on the building's facades giving the wrong impression of extensive wall detachments and collapse. On the other hand, the 3D point cloud derived by processing both nadir and oblique images provide a more reliable 3D information, showing clearly the severe failure of building walls.

Based on the EMS-98 damage classification, on the specific orthophoto map and 3D point cloud, building damages of grade 4-very heavy damage (heavy structural damage, very heavy non-structural damage) serious failure of walls; partial structural failure of roofs and floors, can be visually identified. Building damages of grades 1, 2 and 3 are not identifiable. These results highlight the importance of applying suitable UAS configurations and flight planning characteristics, e.g. low altitude, more than one oblique cameras on board, to achieve more detailed and reliable 3D information (Fig. 10).

3D Point Clouds by TP and TLS

Several studies reveal that two main types of visual interpretation can be performed: i. the exploitation of the images for the detection of cracks or damages on the external surfaces of the building (i.e. walls and roofs) and ii. the use of point clouds (generated by photogrammetric approach) to detect structural anomalies such as tilted or deformed surfaces. In both cases, the automated processing can only support and ease the work of the expert, who still interprets and assesses the structural integrity of the building (earthquake damage).

Fig. 12 Part of a 3D model produced by terrestrial photogrammetry

Fig. 13 Measuring the deformation of wall from a TLS point cloud

All the 240 3D Point Clouds (Fig. 12) and the 140 Point Clouds of the 3D laser scanner (Fig. 13), created by TP and TLS respectively, provide the most important 3D information for assessing building damages of: i. grade 1: negligible to slight damages of the buildings, ii. grade 2: moderate damages, e.g. cracks in many walls, detachment of small pieces of places from the walls and partial collapse of chimneys, and iii. grade 3: substantial to heavy damages e.g. large and extensive cracking of all masonry load-bearing walls, detachment of large pieces of plaster in all load-bearing walls, dislocation and fall of roof tiles, detachment of the roof from the rest of the structure and fall of gables. Their very high resolution and accuracy permit the identification of hair-line cracks in walls, fall of small pieces of plaster only, falls of loose stones from upper parts of buildings and measure their characteristics (length and width of cracks, volumes of debris from falls, etc.).
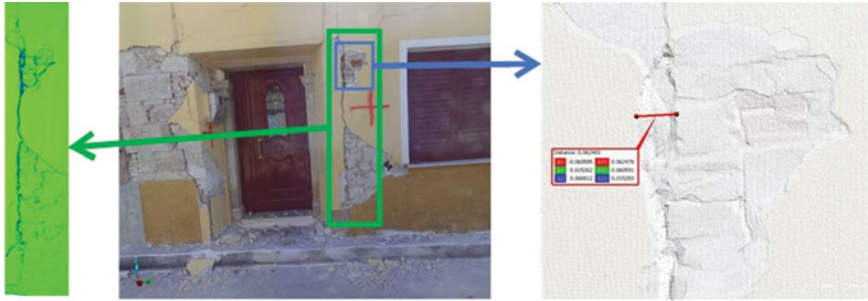
Fig. 14 Finding cracks on buildings and measuring in detail the dimension of cracks from a TLS point cloud

The ability to perform measurements is a very critical issue as post-earthquake situation is not suitable for that (Fig. 14). Especially during the first days after the disaster, it is impossible to get close enough to the buildings. Also, measurements on the upper parts of the buildings cannot be performed because it is impossible to access these parts of the buildings.

4.1.3 Building Damage Assessment Documentation

The EMS-98 presents several examples of building damage documentation, around the world, with a very comprehensive one-page document. This page provides few indicative photos, a general description of the site as well as information about the type of structure and the grade of damage of the building.

By the proposed methodology, the building damage documentation can be expanded to include all the 2D and 3D information produced and assist experts to visualize and measure building characteristics. The appropriate format is 3D-PDF because it is widely used, it permits the inclusion of 3D models and it offers: i. visualization tools (zoom-in, zoom-out, rotation etc.) and ii. a set of 2D and 3D measurement tools for measurements of lengths, areas, angles and volumes.

The proposed documentation includes four pages:

i. the first page presents all the important information concerning the building such as geographical position, type of structure, grade of damage and all the technical characteristic of the 3D point cloud produced by terrestrial photogrammetry (Fig. 15),

ii. the second page contains the 3D point cloud derived by terrestrial photogrammetry of the building, and with the 3D measurement tool it is possible to access the model and perform measurements of distances, angles and volumes (Fig. 16),

Geographical Position	Greece	DAMAGE ASSESSMENT

Geographical Position	**Greece** Lesvos earthquake Mw 6,3 12/06/2017	DAMAGE ASSESSMENT
Coordinate System: **WGS-84**		Grade of Damage (EMS-98)
Longitude: 39.040362160982 Latitude: 26.200420640525	**Lesvos island** **Village: Vrisa**	
TYPE OF STRUCTURE: Masonry		Grade of Damage (ERO)

Grade of Damage (EMS-98)

1	2	3	4	5
			X	

Grade of Damage (ERO)

Green	Yellow	Red
		X

3D Model Technical Characteristics		Comment: The extensive broken walls suggest damage of grade-4.
Number of Photos	19	
Number of Points	20.157	
Spatial Accuracy	0.004 (m)	

Indicative Photo(s)

Fig. 15 An example from the first page of the proposed documentation of building damage assessment. It contains all the important information concerning the building such as: geographical coordinates, type of structure, grade of damage and all the technical characteristic of the 3D point cloud produced by terrestrial photogrammetry

Fig. 16 An example from the second page of the proposed documentation of building damage assessment which contains the 3D point cloud obtained by the high-resolution terrestrial photos. The 3D measuring tool permits the accurate measurement of distances, angles and volumes

Fig. 17 An example from the third page of the proposed documentation of building damage assessment, which contains the 3D point cloud derived by TLS. The 3D measuring tool permits the accurate measurement of distances, angles and volumes

iii. the third page contains the 3D point cloud derived by TLS, and with the 3D measurement tool it is possible to access the model and perform measurements of distances, angles and volumes (Fig. 17),

Fig. 18 An example from
the fourth page of the
proposed documentation of
building damage assessment,
which contains the part of the
high resolution orthophoto
map presenting the damaged
building. The measuring tool
permits the accurate
measurement of distances and
surfaces

iv. finally, the fourth page contains the appropriate part of the high resolution
orthophoto map presenting the building and/or buildings, and with the 2D
measurement tool it is possible to access the map and perform measurements of
distances and areas (Fig. 18).

During the present study, a building damage assessment has been performed
based on the results obtained by the followed methodology (Fig. 19). It is worthy to
mention that the current damage assessment results should not be considered as
fully reliable because all datasets involved cover only the external parts of the
buildings. The damage evidence that can be captured from the orthophoto maps and
3D Point clouds could not consider sufficient to infer the actual damage state of the
building as it requires damages to the internal building elements (e.g., columns and
beams) that cannot be directly defined from the images and 3D point clouds.
Despite the fact that this information is limited to the external part of the buildings,
the images can provide useful information about the external condition of the
masonry buildings, showing damages and providing a first important piece of
information for structural engineers. Taking into consideration all the above, the
results obtained by the damage assessment are summarized in Table 2.

The comparison between these results with the equivalent assessment derived by
the Greek ERO shows that: i. the majority (70%) of the GREEN-buildings has been
evaluated having damages of grade-1 while only 12% having damages of grade-2,
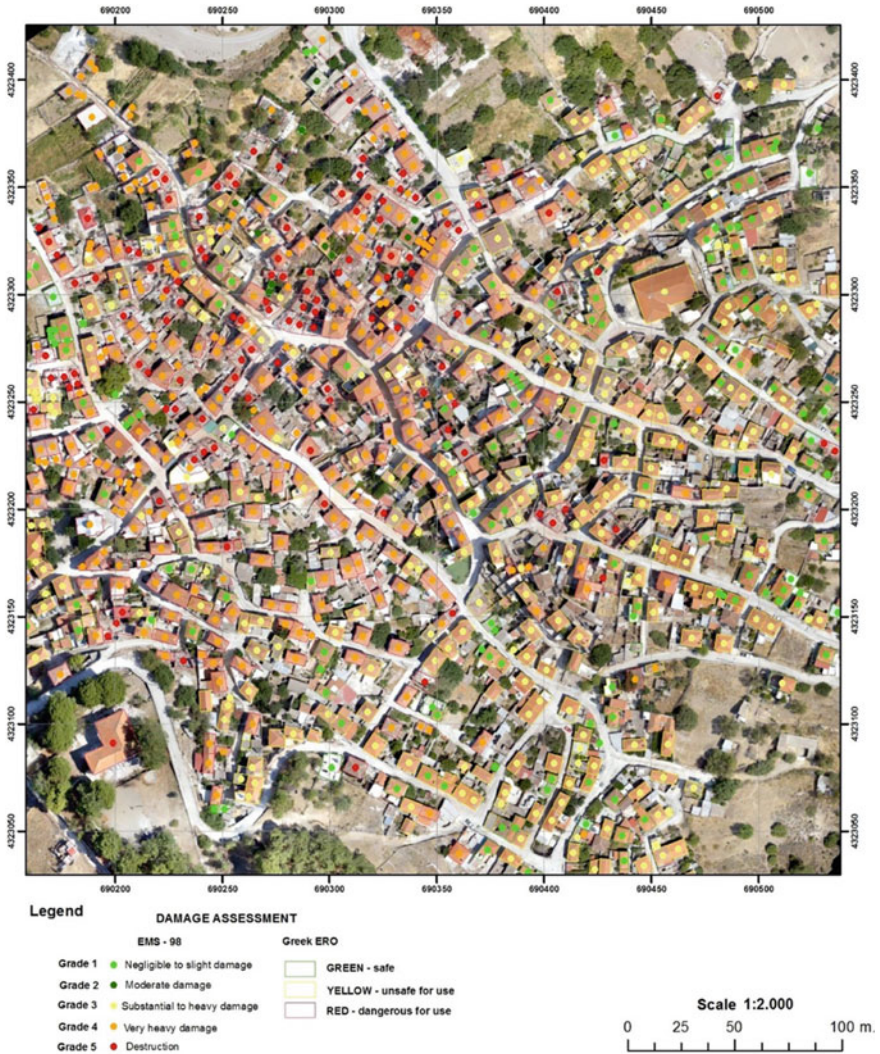
Fig. 19 Orthophoto map of 25th June 2017 at a scale of 1:2.000 presenting Vrisa settlement witch damage assessment results by: i. first inspection by Greek ERO and ii. by the use of the 3D Point Clouds produced during the present study

ii. the majority (78%) of the YELLOW-buildings has been evaluated having damages of grade-3 while only 10% of grade-4 and finally iii. the majority (64%) of the RED-buildings has been evaluated having damages of grade-4 and only 23% of grade-5 (see Table 3).

Table 2 Statistical information of the building damage assessment results obtained based on the visual interpretation and of the orthophoto maps and 3D Point clouds generated during the present study

	Number of buildings	Material			Number of Stories		
		Masonry	F/C	Mixed	1 Store	2 Store	3 Store
Grade 1	220	170	45	5	129	83	1
Grade 2	43	42	1	0	38	5	0
Grade 3	410	394	9	7	225	181	4
Grade 4	360	356	2	2	202	152	6
Grade 5	129	129	0	0	101	27	1
Total	1162						

Table 3 Comparison between damage assessment results, according to EMS-98 classification grades, based on the visual interpretation of the orthophoto maps and 3D Point clouds generated during the present study and the damage assessment results by the Greek ERO

Greek ERO	Number of build-ings	EMS 98				
		Grade 1	Grade 2	Grade 3	Grade 4	Grade 5
GREEN	218	152	27	1	4	1
YELLOW	314	2	7	246	31	3
RED	281	1	3	8	179	64

5 Conclusions

The ambitious goal of the present study was to tackle all the difficulties of a post-earthquake scenario, in order to apply 3D mapping methodologies simultaneously to two different scales: i. village, and ii. building. Both scales are important in order to document the earthquake damages occurred to the Vrisa traditional settlement, by providing metrical information to permit building damage assessment according to the five (5) EMS-98 damage classification grades.

The fact that geoinformation, in a post-earthquake scenario, provides a great spectrum of methods, techniques and algorithms to calculate and measure 3D information, in two spatial scales, their synergistic application proved to be very promising for further research and development of semi or fully automatic methodologies.

More specifically: i. the orthophoto maps and DSMs derived by UAS flights in medium heights, e.g. 160 m., proved to be a very efficient mean for providing an early impact assessment at a village scale because it permits the accurate mapping of the totally or partially collapsed buildings, as well as blocked roads and debris, ii.

the 3D point cloud provided by the nadir and oblique high-resolution images acquired by UAS low altitude flight (65 m) proved to be suitable from mapping building damages of grade 4 as it illustrates efficient information concerning the building facades, iii. The 3D point clouds provided either by TP or by TLS proved to be the most accurate for mapping building damages of grades 3, 2 and 1 because they are evidencing anomalies and damages and providing a first important piece of information for structural engineers.

Finally, all 3D models would be useful for a post-earthquake management and reconstruction processes. Also, 3D mapping of an earthquake damaged traditional settlement is of great importance because after a short period most of the heavily damaged building will be demolished, destroying all their morphological characteristics, including their construction material and morphology of a traditional house. The proposed damage documentation provides all the appropriate information which can augment all experts and stakeholders, national and local organizations focusing on the post-earthquake management and reconstruction processes of the Vrisa traditional village.

References

Adams SM, Friedland CJ (2011) A survey of unmanned aerial vehicle (UAV) usage for imagery collection in disaster research and management. In: Proceedings of the ninth international workshop on remote sensing for disaster response. Stanford, CA, USA, pp 15–16

Anil EB, Akinci B, Garrett JH, Kurc O (2013) Characterization of laser scanners for detecting cracks for post-earthquake damage inspection. In: 30th ISARC. Montreal, Canada, pp 313–320

Bemis SP, Micklethwaite S, Turner D, James MR, Akciz S, Thiele ST, Bangash HA (2014) Ground-based and UAV-Based photogrammetry: a multi-scale, high-resolution mapping tool for structural geology and paleoseismology. J Struct Geol 69:163–178. https://doi.org/10.1016/j.jsg.2014.10.007

Bose S, Nozari A, Mohammadi ME, Stavridis A, Babak M, Wood R, Gillins D, Barbosa A (2016) Structural assessment of a school building in Sankhu, Nepal damaged due to torsional response during the 2015 Gorkha earthquake. In: Pakzad S, Juan C (eds) Conference proceedings of the society for experimental mechanics series, Dynamics of civil structures. Springer, Cham, pp 31–41

Calantropio A, Chiabrando F, Sammartano G, Spanò A, Losè LT (2018) UAV strategies validation and remote sensing data for damage assessment in post-disaster scenarios. Int Arch Photogramm Remote Sens Spat Inf Sci XLII-3/W4:121–128. https://doi.org/10.5194/isprs-archives-xlii-3-w4-121-2018

Chang KT, Wang EH, Chang YM, Cheng HK (2008) Post-disaster structural evaluation using a terrestrial laser scanner. Integrating generations FIG working week 2008. Stockholm, Sweden, pp 1–15

Chen J, Liu H, Zheng J, Lv M, Yan B, Hu X, Gao Y (2016) Damage degree evaluation of earthquake area using UAV aerial image. Int J Aerosp Eng 2016:1–10. https://doi.org/10.1155/2016/2052603

Dominici D, Alicandro M, Massimi V (2017) UAV photogrammetry in the post-earthquake scenario: case studies in L'Aquila. Geomat Nat Hazards Risk 8:87–103. https://doi.org/10.1080/19475705.2016.1176605

Dong L, Shan J (2013) A comprehensive review of earthquake-induced building damage detection with remote sensing techniques. ISPRS J Photogramm Remote Sens 84:85–99. https://doi.org/10.1016/j.isprsjprs.2013.06.011

Erkal BG (2017) The prototype of a software application for laser and image-based surface damage detection. In: Proceedings of the 2nd world congress on civil, structural, and environmental engineering (CSEE'17), pp 1–7

Federal Emergency Management Agency (FEMA) (2016) Damage assessment operations manual-A guide to assessing damage and impact

Fernandez Galarreta J, Kerle N, Gerke M (2015) UAV-based urban structural damage assessment using object-based image analysis and semantic reasoning. Nat Hazards Earth Syst Sci 15:1087–1101. https://doi.org/10.5194/nhess-15-1087-2015

Gomez C, Purdie H (2016) UAV-based photogrammetry and geocomputing for hazards and disaster risk monitoring–A review. Geoenvironmental Disasters 3:23. https://doi.org/10.1186/s40677-016-0060-y

Grünthal G (1998) European Macroseismic Scale 1998. Chaiers du Centre Européen de Géodynamique et de Séismologie, Luxembourg

Guldur B, Hajjar J (2016) Automated classification of detected surface damage from point clouds with supervised learning. In: Proceedings of the 33rd ISARC. Auburn, AL, USA, pp 307–313

Guldur Erkal B, Hajjar JF (2017) Laser-based surface damage detection and quantification using predicted surface properties. Autom Constr 83:285–302. https://doi.org/10.1016/j.autcon.2017.08.004

Jafari B, Khaloo A, Lattanzi D (2017) Deformation tracking in 3D point clouds via statistical sampling of direct cloud-to-cloud distances. J Nondestruct Eval 36:65. https://doi.org/10.1007/s10921-017-0444-2

Kayen R, Collins BD, Bawden G, Pack RT (2006) Earthquake deformation analysis using terrestrial scanning Laser-LIDAR technology. In: 8th US national conference on earthquake engineering. San Francisco, California, USA

Kiratzi A (2018) The 12 June 2017 Mw 6.3 Lesvos Island (Aegean Sea) earthquake: slip model and directivity estimated with finite-fault inversion. Tectonophysics 724–725:1–10. https://doi.org/10.1016/j.tecto.2018.01.003

Mukupa W, Roberts GW, Hancock CM, Al-Manasir K (2016) A review of the use of terrestrial laser scanning application for change detection and deformation monitoring of structures. Surv Rev 49:99–116. https://doi.org/10.1080/00396265.2015.1133039

Nimodia C, Deshmukh HR (2012) Android operating system. Softw Eng 3:10–13

Olsen MJ, Chen Z, Hutchinson T, Kuester F (2013) Optical techniques for multiscale damage assessment. Geomat Nat Hazards Risk 4:49–70. https://doi.org/10.1080/19475705.2012.670668

Olsen MJ, Cheung KF, YamazakI Y, Butcher S, Garlock M, Yim S, McGarity S, Robertson I, Burgos L, Young YL (2012) Damage assessment of the 2010 Chile earthquake and tsunami using terrestrial laser scanning. Earthq Spectra 28:S179–S197. https://doi.org/10.1193/1.4000021

Olsen MJ, Kayen R (2012) Post-earthquake and tsunami 3D laser scanning forensic investigations. Forensic engineering 2012. American Society of Civil Engineers, Reston, VA, pp 477–486

Papadimitriou P, Kassaras I, Kaviris G, Tselentis G-A, Voulgaris N, Lekkas E, Chouliaras G, Evangelidis C, Pavlou K, Kapetanidis V, Karakonstantis A, Kazantzidou-Firtinidou D,

Fountoulakis I, Millas C, Spingos I, Aspiotis T, Moumoulidou A, Skourtsos E, Antoniou V, Andreadakis E, Mavroulis S, Kleanthi M (2018) The 12th June 2017 Mw = 6.3 Lesvos earthquake from detailed seismological observations. J Geodyn 115:23–42. https://doi.org/10.1016/j.jog.2018.01.009

Papakonstantinou A, Doukari M, Moustakas A, Chrisovalantis D, Chaidas K, Roussou O, Athanasis N, Topouzelis K, Soulakellis N (2018) UAS multi-camera rig for post-earthquake damage 3D geovisualization of Vrisa village. In: Themistocleous K, Hadjimitsis DG, Michaelides S, Ambrosia V, Papadavid G (eds) Sixth international conference on remote sensing and geoinformation of the environment (RSCy2018). SPIE, p 52

Pesci A, Teza G, Bonali E, Casula G, Boschi E (2013) A laser scanning-based method for fast estimation of seismic-induced building deformations. ISPRS J Photogramm Remote Sens 79:185–198. https://doi.org/10.1016/j.isprsjprs.2013.02.021

Puente I, Lindenbergh R, Van Natijne A, Esposito R, Schipper R (2018) Monitoring of progressive damage in buildings using laser scan data. In: ISPRS Int Arch Photogramm Remote Sens Spat Inf Sci XLII-2:923–929. https://doi.org/10.5194/isprs-archives-xlii-2-923-2018

Schütz M (2016) Potree: rendering large point clouds in web. Master Thesis, Vienna University of Technology

Snavely N (2011) Scene reconstruction and visualization from internet photo collections: a survey. IPSJ Trans Comput Vis Appl 3:44–66. https://doi.org/10.2197/ipsjtcva.3.44

Snavely N, Seitz SM, Szeliski R (2008) Modeling the world from internet photo collections. Int J Comput Vis 80:189–210. https://doi.org/10.1007/s11263-007-0107-3

Song M, Yousefianmoghadam S, Mohammadi M-E, Moaveni B, Stavridis A, Wood RL (2018) An application of finite element model updating for damage assessment of a two-story reinforced concrete building and comparison with lidar. Struct Heal Monit 17:1129–1150. https://doi.org/10.1177/1475921717737970

Triggs B, McLauchlan PF, Hartley RI, Fitzgibbon AW (2000) Bundle adjustment—a modern synthesis. In: Lecture Notes in Computer Science, pp 298–372

Westoby MJ, Brasington J, Glasser NF, Hambrey MJ, Reynolds JM (2012) 'Structure-from-Motion' photogrammetry: a low-cost, effective tool for geoscience applications. Geomorphology 179:300–314. https://doi.org/10.1016/j.geomorph.2012.08.021

Xu Z, Yang J, Peng C, Wu Y, Jiang X, Li R, Zheng Y, Gao Y, Liu S, Tian B (2014) Development of an UAS for post-earthquake disaster surveying and its application in Ms7.0 Lushan Earthquake, Sichuan, China. Comput Geosci 68:22–30. https://doi.org/10.1016/j.cageo.2014.04.001

Yamazaki F, Matsuda T, Denda S, Liu W (2015) Construction of 3D models of buildings damaged by earthquakes using UAV aerial images. In: Proceedings of the tenth pacific conference earthquake engineering building an earthquake-resilient pacific

Zhao X, Kargoll B, Omidalizarandi M, Xu X, Alkhatib H (2018) Model selection for parametric surfaces approximating 3D point clouds for deformation analysis. Remote Sens 10:634. https://doi.org/10.3390/rs10040634

Zhihua X, Lixin W, Yonglin S, Qiuling W, Ran W, Fashuai L (2014) Extraction of damaged building's geometric features from multi-source point clouds. In: 2014 IEEE geoscience and remote sensing symposium, IEEE, pp 4764–4767

Comparison of Terrestrial Photogrammetry and Terrestrial Laser Scanning for Earthquake Response Management

Christos Vasilakos, Stamatis Chatzistamatis, Olga Roussou and Nikolaos Soulakellis

Abstract Response management is the first and very critical phase of the disaster management cycle on the post-earthquake reconnaissance efforts. After an earthquake, a rapid damage assessment is vital for emergency response actions. Various types of devices and methods were used in a post-earthquake situation to estimate damages such as deformation of structures. However, standardized procedures during emergency surveys often could not be followed due to restrictions of outdoor operations because of debris or decrepit buildings, the high human presence of civil protection agencies, expedited deployment of survey team and cost of operations. Terrestrial photogrammetry and laser scanning are two of the recently emerging technologies, which became even more preferable in hazard areas, due to there is no need for direct contact with the structure to be assessed. This research aims to discuss the challenges and benefits for the use of the technologies above, focusing on the comparison of the processed models derived from data acquired with these technologies. An evaluation is undertaken whether terrestrial photogrammetry and laser scanning provide high precision and spatial resolution data suitable for post-earthquake building damage assessment. Furthermore, the extracted models are valuable components that help engineering to understand the seismic behavior in a more comprehensible way.

C. Vasilakos (✉) · O. Roussou · N. Soulakellis
Department of Geography, University of the Aegean, 81100 Mytilene, Greece
e-mail: chvas@aegean.gr

O. Roussou
e-mail: orousou@aegean.gr

N. Soulakellis
e-mail: nsoul@aegean.gr

S. Chatzistamatis
Department of Cultural Technology and Communication, University of the Aegean, 81100 Mytilene, Greece
e-mail: stami@aegean.gr

1 Introduction

1.1 *Earthquake Response and Recovery*

Disaster management is characterized as encompassing mitigation, preparedness (pre-disaster hazard research), response and recovery strategies (post-disaster research) undertaken to lessen the vulnerability and assess the impact of a disaster (Alexander 1991; Baird 2010; Van Westen 2013). The emergency disaster management encloses multi-criterial decision analysis based on increasing demand for up-to-date and accurate spatial information of the current situation during all the phases of the disaster management cycle (Fig. 1). This information is essential to plan a rapid response allocating a huge number of first responders, volunteer teams, technicians and experts to the affected areas in time (Alexander 2005).

Geographic information systems (GIS) is a powerful tool in natural disaster assessment and management. Spatial referenced data, regarding buildings, streets, services, population, positions of hazardous facilities and topography, enter into a GIS by converting to shapefiles and geodatabases (Erden and Karaman 2012). Analysis and visualization of the spatial information can help in risk identification, development of preparedness and response scenarios, estimation of building damage, relief operations, socio-economic impacts assessment, simulation of disaster effects and generally in decision making before, during and after a natural disaster (Cutter 2003; Altan 2005; Goodchild 2006).

Geo-informatics has the important role of connecting the technology acquisition and identification of information resources with the methodologies and previous experiences in handling natural disasters, mainly earthquakes (Altan et al. 2001; Yang and Zhang 2013; Sivakumar and Ghosh 2017). A variety of earthquake damage assessment methodologies developed and applied in the research

Fig. 1 Disaster management cycle

community worldwide focusing on either physical or socio-economic vulnerability decrease (Hashemi and Alesheikh 2011).

However, the sudden strike, with little or no warning, of an earthquake has a significant effect on human life and property. After an earthquake, a rapid damage assessment is vital for emergency response actions, rescue operations and post-disaster reconstructions (Tu et al. 2016). Building damage is one of the major issues that civil protection agencies should cope within the crisis management of an earthquake. Various types of remote sensing data (aerial or satellite images, SAR, LiDAR) and different techniques are utilized in building damage detection and assessment, that either evaluate the changes using data before and after a disaster or interpret only data after a disaster for initial building damage evaluation and rapid response (Dong and Shan 2013; Rastiveis et al. 2015; Tu et al. 2016). Tong et al. (2012) detected both individual collapsed buildings and region of buildings based on building height change using IKONOS stereo image pairs before and after the Wenchuan earthquake. Gerke and Kerle (2011) developed a building damaged classifier based on airborne oblique, multi-perspective pictometry data. The application of oblique images assessed except roof and facade building information that would not be visible from traditional image-based methods. Aerial imagery, UAVs and LiDAR system appeared as alternative sources of building damage information in earthquake-damaged areas (Yamazaki et al. 2015; Fernandez Galarreta et al. 2015; Vetrivel et al. 2015).

All aforementioned methods assess the damage information without taking into consideration some parts of the building that are ready to be collapsed. Detailed building damage information is crucial for stakeholders regarding response and rescue operations, as accurate damage recognition of individual parts of the building can activate experts at the right place the appropriate time (Vetrivel et al. 2015).

Nowadays, 3D modeling is becoming very popular in documenting building environment. The texturized photorealistic 3D models can exceptionally describe the shape and size of an object with all details and high level of features' accuracy. These models were widely acquired with three different survey methods: (i) aerial photogrammetry; (ii) terrestrial photogrammetry (TP); or (iii) terrestrial laser scanning (TLS). Fusion of the above methods has also been explored (Lerma et al. 2010).

1.2 Terrestrial Photogrammetry and Terrestrial Laser Scanning 3D Modeling

Photogrammetry is the scientific methodology for the definition of the 3D geometry of a target by analyzing its 2D images and is divided into two categories: aerial and terrestrial photogrammetry. When the images are acquired by a camera located on or near the earth surface, then, photogrammetry is called terrestrial, while a distance

between the camera and the target less than 100 m defines the close-range photogrammetry. A photogrammetric project includes all the steps from data acquisition until the construction of a 3D virtual model. The most common representations of a 3D model are a point cloud and a textured triangulated network surface called a polygon mesh.

In the previous years, an analytical photogrammetry workflow was applied in order to establish a relationship between a measuring system, several photo coordinate systems and target coordinate systems. This workflow includes several procedures such as the interior orientation, the exterior orientation, and the bundle adjustment while the user's interaction with the digital photogrammetric workstation was intense. However, the recent trends in processing algorithms and the low-cost software provide to the users a complete digital workflow (Jiang et al. 2008). One of the main advantages of the close-range terrestrial applications is the usage of inexpensive non-metric cameras. Laboratory calibration is not recommended for off-the-shelf cameras because the calibration is rarely valid due to the long period between calibration and data acquisition.

Aerial and terrestrial photogrammetry ranks among the methods that can be used to survey building structures and assess 3D models. This approach became more popular when photogrammetry algorithms were enhanced by computer vision techniques leading to the well-known methodology of Structure from Motion (SfM) (Ullman 1979). The SfM became popular due to the Scale Invariant Feature Transform (SIFT) algorithm (Lowe 1999; Snavely et al. 2006, 2008).

The evolution of technology in the imaging sciences in recent years has introduced new measurement techniques for objects and whole areas. The introduction of LASER (Light Amplification by Stimulated Emission of Radiation) technology in the early 1960s and the understanding of the advantages of its radiation characteristics such as monochromaticity, proper alignment, and ease of laser beam formation, led to its initial application among other things to the manufacturing of distance and imaging instruments. The first applications wherein military instruments and over the years, the use of the laser has been transferred and established at the geodetic stations that are the precursors of terrestrial laser scanners. The primary differentiation of TLSs from geodetic stations is found in the absence of the optical sighting device and the ability to center and level as it is replaced using special sensors.

The data obtained by measuring with the TLS is the scanner-object-point distance, the polar coordinates of the points of the scanned surface (two steering angles and the distance) and the intensity value of the return laser beam. The cartesian coordinates (x, y, z) are automatically calculated by the polar coordinates of the points of the object being measured. Thus, at each point, the information (x, y, z, I) corresponds to its position. During scanning, the TLS also collects photos of each scanned point with its embedded camera (RGB values) in order to define the color and texture of the surface. The points of the scanned object are presented uniformly, after appropriate processing, in the form of a set of points with seven values defined as a point cloud that accurately forms and delivers its three-dimensional model.

The acquired point cloud represents in detail the geometry of the object without inaccuracies, which was impossible for conventional geodetic stations, and it forms the raw data ready for measurement and processing. However, because modern TLSs acquire millions of points per second, the point cloud is huge in volume. TLSs are nowadays used to measure objects in a wide range of applications such as civil engineering, archaeology, industrial facilities, and their potential enables them to acquire geometric data of an object or a larger area which later can be used to create representations of their 3D models.

Based on their principle of operation, TLSs systems can be categorized into three main categories: (a) Triangulation, (b) Time of Flight and (c) Phase Shift (Vosselman and Maas 2010).

On the triangulation principle, the instrument generates a laser beam that is deflected across the object by a rotating mirror. The beam is then reflected by the surface of the object and focused onto the sensor by the lens. The location of the laser beam on the sensor, plus the known distance between it and the mirror is combined with the recorded angle of the mirror to determine a point coordinate by triangulation. Triangulation scanners find application only at measuring at close distances and small objects as the accuracy of the distance between an instrument and an object depend on the square of the distance.

TLSs using the Time-of-Flight (ToF) principle emit a laser beam and calculate the travel time of the signal between transmission and reception. As the speed of light is known, by recording the time of transmission and reception of the beam to the detector, the distance traveled is calculated which is twice the distance between the device and the object. The measurements are made separately for each point, and so the laser beam should change direction each time, which is achieved by using mirrors deflecting the beam direction.

Phase-Shift (or Phase-Comparison) TLSs operate on the principle of comparing the phase difference between the transmitted light wave and the return wave. In this case, the transmitted beam is converted into a harmonic wave and the distance is calculated by the phase difference between the transmitted and received wave.

Various types of devices and methods were used in a post-earthquake scenario in order to estimate damages such as deformation of structures. TLS is one of the recently emerging technologies, which becomes even more preferable in hazard areas, because there is no need for direct contact with the object or the structure to be scanned. Researchers in the past years argue that TLS data can provide high precision and spatial resolution data suitable for damage assessment generally and especially after a natural disaster such as an earthquake.

Kayen et al. (2006) were ones of the first that investigated the potential of TLS data for the rapid assessment of damaged terrain, by presenting examples of geometric measurement and change detection of seismically-induced landslides. Devilat (2014) presents the methodology to build color and accurate 3D model from TLS of a heritage area which was hit by an earthquake, which can be used for assessment and further design. Olsen and Kayen (2012) discuss the challenges and benefits for the use of a TLS on post-disaster reconnaissance efforts and argue that the use of TLS can preserve the scene digitally for post-disaster assessment.

Many researchers proved that it is possible to detect deformations in buildings from TLS data proposing various automated and semi-automated methods (Olsen et al. 2013; Pesci et al. 2013; Jafari et al. 2017; Zhao et al. 2018; Puente et al. 2018; Xu et al. 2018). Erkal (2017) utilizes previously developed surface damage detection algorithms implemented in a software application, which extracts damage features from imported texture-mapped point clouds such as shape and size, determining condition ratings and producing damage reports.

Olsen et al. (2013) utilize optical techniques to show that recently developed change detection algorithms can quickly provide regional damage information with application on damaged structures from tsunamis, coastal erosion, and cracking of a historical building. Chang et al. (2008) investigate the use of TLS data to acquire the displacement information of columns and beams for safety evaluations, while Anil et al. (2013) showed that it is possible to detect as small as $\sim$1 mm cracks from TLS data.

Oppose to TLS, the TP has been rarely used for damage assessment while the Unmanned Aerial Vehicles (UAV) are the most common platform for image acquisition. The 3D dense point clouds and the 3D building models generated from TP are used to recognized cracks, holes, horizontal drifts, debris or other detailed damages in building facades after an earthquake (Dai et al. 2011; Papakonstantinou et al. 2018).

Images for rapid 3D reconstruction for post-earthquake damage assessment can also be taken with tablets (Dabove et al. 2018). In this study, the extracted point clouds from tablet cameras compared with the 3D model retrieved from a professional camera and the differences were less than 2 cm. At the same time, the georeferencing process resulted in approximately 5 cm error at the control points. For a specific building the total time for data acquisition was 30 min which is sufficient for rapid mapping during emergency response.

Many researchers propose to combine and integrate both TLS and photogrammetric methods as they are capable of collecting precise and dense 3D point clouds (Lerma et al. 2010; Moussa et al. 2013; Zhihua et al. 2014). Li et al. (2008) proposed a 3D model and high-resolution imagery fusion for reconstructing 3D building models. LiDAR data, before and after an earthquake, were also proposed for detecting building changes by measuring the rate of destroyed rooftops of building models. Galarreta et al. (2015) demonstrated that the combination of 3D point clouds with damage features extracted from oblique images can be useful for intermediate damage assessment at building level. Yamatzaki et al. (2015) highlighted the usefulness of SfM technique to depict damage situation of buildings due to the 2011 Tohoku earthquake. Following the 24 August 2014 Napa earthquake, Morelan et al. (2015) used SfM to produce extremely high-resolution 3D point clouds with an mm-scale resolution of surface rupture through anthropogenic features. Nowadays, research interest focuses on the comparison of the 3D accuracy between measurements of high-resolution TLS and TP, so as to examine point cloud characteristics for accuracy assessment and suitability for different 3D applications (Widyaningrum and Gorte 2017; Selvaggi et al. 2018).

2 Methodology

2.1 Data Acquisition

The complexity of building structures, especially after an earthquake event, requires a large number of photographs because a stereo pair of images cannot provide the necessary details. Therefore, a convergent horizontally, vertically and oblique bundle of images generally pointing towards the center of the building are required (Hanke et al. 2002). The user, also, should ensure that each point of interest should be visible by at least two images taken with an adequate intersection angle.

Among with the off-the-shelf cameras, a typical survey requires additional elements, i.e. scale objects (Fig. 2) (Jiang et al. 2008). Moreover, retro-reflective targets can be established, if the project requires high accuracy measurements. During the survey, camera settings should be configured appropriately. Photo quality should be in RAW or a high-quality JPEG format with a typical f-stop between f/8 and f/16. For outdoor surveys a maximum ISO 400 and a minimum shutter speed 1/30 can provide qualitative photo images. Furthermore, cameras and lenses use to have some image stabilization features. The user should set to "off" any vibration reduction settings because settings that aim to reduce the vibrations and stabilize the images can reduce the potential accuracy (Rieke-Zapp and Peipe 2006).

The methodology used for the acquisition process using a TLS differs from that of conventional methods. In the applications of classical techniques, the correlation of the points to be captured with the instrument position, whose coordinates are known, plays a key role. On the other hand, scanning with a TLS makes the data correlated with each other and not with the position of the instrument. The main factors to be taken into consideration for the positioning of the scanner are to cover the 3D space or object to be scanned fully. In particular, positioning stations should

Fig. 2 Scale objects, i.e. objects with known dimensions

be well distributed to cover the entire desired area and no obstructions should be placed between them and the scanned object. It is also necessary to control the range of the scanner concerning the accuracy, since the farthest the distance from the object, the lower the resolution and the accuracy of the final product will be, or for the same resolution and accuracy, the more considerable amount of time will be needed.

After selecting the acquisition stations, an essential step in the measurement methodology is to determine the location of control points used to merge the scans and/or the georeference of the 3D model. These points are usually circular or spherical targets and high reflectivity stickers, which are automatically recognized by point cloud processing software. There must be at least three points well distributed in each scan, for the optimal definition of its reference system relative to the previous one. It should be noted that the merging of the scans can also be achieved with the features of the 3D space visible in the scan, without using artificial targets.

2.2 Data Processing

The SfM and multiview stereo (MVS) approach are the most popular for the generation of the 3D point cloud (Fig. 3). This approach has been extensively implemented the last decade in 3D mapping in different scales. For example, Westoby et al. (2012) used terrestrial images for 3D modeling of meso- and micro-scale landforms while Gallo et al. (2014) applied SfM for the 3D reconstruction on objects with a bounding box diagonal ranging from 13.5 to 41 mm. The combination of SfM and MVS has been employed in some commercial and free software packages in different variations (Snavely et al. 2006; Wu et al. 2011).

The first step of the SfM approach is the identification of common points between the images and the generation of a descriptor for each of these points. The most popular algorithms are the SIFT (Lowe 1999) and the Speeded Up Robust Features (SURF) (Bay et al. 2006). The advantage of these methods is that the corresponding points of more than one images can be matched regardless of the scale of the images, i.e. the distance between the camera and the target. Within the software, the user also can specify a set of points to aid the image matching, create scale bars, and check the accuracy of the procedure. The above algorithms require images that meet specific qualitative standards for the appropriate distinction of
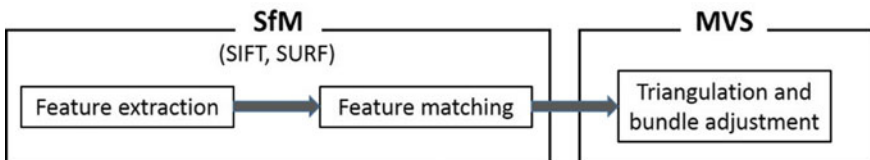
Fig. 3 Pipeline for generation of dense point cloud

textures appearing in the images (Wu et al. 2013). Therefore, quality control of the images should be applied, assuring that no blurred images will be included in the process. Furthermore, moving and other undesirable objects (i.e. sky, humans, moving trees by the wind, reflections to windowpanes, shadowed or sun glinted areas) should be masked. Another problem that the user can meet during a survey, is the homogeneous surfaces i.e. walls and railings, and due to the available small distance between stations and objects, matching algorithms quite often are unable to match adjacent images. The output of the SIFT and SURF, is the list of the common points forming a sparse point cloud. These points are also used for the estimation of the camera intrinsic and extrinsic orientation parameters based on a bundle-adjustment algorithm (Triggs et al. 2000). Next step is the generation of the final dense point cloud based on the MVS algorithm and the camera locations and the sparse point cloud generated from the feature extraction and matching algorithm. Moreover, the surface normal for each point can be estimated (Furukawa and Ponce 2010). However, MVS performs well on Lambertian surfaces and often fail on non-Lambertian objects (Wu et al. 2011).

The acquired raw data of the TLS consist of individual point clouds, where their position and orientation should be changed so that each point cloud uses a universal coordinate system. This process is characterized as cloud alignment or registration, where the point clouds resulting from the different scans of the object are "joined" together using common points. The process is differentiated according to the software but generally uses three techniques. The first method is called target-to-target registration and performs the clouds' alignment with the help of commonly-labeled artificial targets (targets come in a variety of forms such as physical objects like spheres and paper targets with a recognizable pattern printed on them) that have been captured at each scan or physical feature-specific points visible in two consecutive scans. The second method is called cloud-to-cloud registration and attempts to align scans based on common areas, with the constraint that there is enough overlap (>30%) between two consecutive scans. The latest method is surface-to-surface registration, where the alignment of the scans is based on the geometry of their surfaces.

At this stage, the georeference of the 3D model can be made by aligning the individual clouds of points in a particular coordinate system. The georeferencing process can use the targets used to register the scans, as their coordinates are known. Another method of registering the point clouds is to georeference them. Following this method, each point cloud is oriented based on the known points whose coordinates are determined by the topographic mapping. That way all the point clouds refer to a universal reference system.

During the scanning process, the TLS captures points which do not represent correct information as to the geometry of the object being scanned. The TLS point clouds are affected by a disorder generally referred to as "noise". The noise depends on the scanning method and the surface characteristics of the object. The process at this stage consists of the "cleaning" of these points, which allows a significant

reduction in the data, resulting in better point cloud management. The effect of noise dramatically affects the quality of models resulting from the scans. Noise reduction is made either automatically using special software and specialized algorithms or manually. The automatic noise reduction is achieved by applying filters which are capable of analyzing statistical indicators (maximum distance, mean distance and mean square deviation) based on the calculations that have been carried out. Finally, it is necessary to detect and remove points that do not belong to the object such as vegetation or any obstacles between the scanner and the object.

A lot of research is ongoing in analyzing an object or an area directly from the point clouds, but still, sometimes there is a need to "connect" the points and construct the final 3D model. This can be achieved through the triangulation process. It is a triangular irregular network (TIN), a polygon mesh created by the point cloud. In the first step, polygons are processed. Initially, the cleansing of the polygons that do not intersect with the main object or that are tangled are first cleared. Gaps created after this process need to be filled. The number of gaps to be displayed, lies in the integrity of the data and the number of truncated polygons. The principle of filling the gaps in software is based on the curvature surrounding it. After all the gaps are filled, the polygons are cleaned again. However, when filling the gaps, new fragmented polygons are created, so the process is repeated until there are no other gaps. Then the surface adaptation stage follows, where the construction of the sectors takes place, e.g. the segmentation based on the surface analysis. After the construction of sectors is completed, the next step is to construct the networks. Networks can be made symmetrical and coherent artificially. In general, the denser the networks are, the more accurate the surface they describe. The last step is to apply texture to the final model from the photographs taken the same time with the scanning process.

The quality of TLSs and therefore the data they acquire depends on a variety of parameters not only related to the precision of the instrument. Factors such as the environment, the features of the object to be scanned, the specifications of the TLS, and the methodology followed in each survey can cause significant errors and affect the final scan result. These factors can be distinguished from those related to the operation of the instrument, the shape and nature of the object, the environmental conditions and the choice of methodology for the measurement process (Boehler et al. 2003).

The laser beam diameter affects the resolution of the point cloud. The larger the diameter, the more likely there are deviations in the coordinates of the scanned points. Also, in the same way, the laser beam divergence (the angular measure of the increase in beam diameter or radius) can cause significant errors. Another factor that can cause errors is the "edge effect". This error is observed at the edges of the objects being scanned. When the laser beam reaches a point on the edge of the desired object, only a part of it is reflected and returned to the scanner. The rest may be reflected by a surface behind the edge, if it exists, from an adjacent point or not

at all. So, the scanner returns signals from different regions. Most TLSs use mirrors to deflect the laser beam in a particular direction. Any deviations occur in the angle generated by the laser beam and the surface of the mirror may lead to the calculation of wrong coordinates.

The various surface characteristics of the objects to be scanned can affect the accuracy of the distance measurements, which is dependent on the reflection of the laser beam (Ingensand et al. 2003). Depending on the material, color, roughness, temperature and humidity of the surfaces of the object being scanned, the reflected beam is varied. Corresponding error results also arise in the case of surfaces of translucent materials in which the laser beam is refracted, and it reflects on the surface itself. Other features of the objects that affect the results of the distance measurements are size, curvature, and orientation.

Environmental factors such as atmospheric temperature, pressure, humidity, vibrations affect the accuracy of the measurements of a TLS. Potential radiation interference from external light sources such as a projector or sunlight can alter the measurement results because they affect the power of the laser beam. Methodological factors can also affect the accuracy of the measurements. Such errors may result from a wrong selection of settings such as the desired sampling resolution and the distance from the scanned object. Additionally, some errors may result from the wrong approach to the georeference of the point cloud.

Various software packages have been developed and are available for TLS and TP data processing. Most of them, implement the same algorithms presented above applying a similar pipeline. In Table 1 we present a list of software packages that are available under different licenses and operating systems.

2.3 Point Cloud Comparison

Various methods have been developed for the comparison of two 3D models. The most common is the Multiscale Model to Model Cloud Comparison (M3C2) algorithm (Lague et al. 2013). The method requires that both of the 3D models are in raw point cloud format oppose to the methods that require meshes or grids. Furthermore, M3C2 is proposed for high accuracy distance measurements while other methods i.e. Cloud to Cloud (C2C) are applied for rapid change detection on very dense point clouds (Girardeau-Montaut et al. 2005). M3C2 computation is based on local normal direction rather than only on the vertical direction between points. The user defines a radius based on objects roughness and the algorithm creates a cylinder oriented along the normal vector. The intersection between the cylinder and the point clouds defines two-point subsets for which the mean distance is computed.

Table 1 List of software packages implementing photogrammetry techniques for image-based creation of 3D point clouds and meshes and/or processing of laser scanning point clouds

Application	Vendor	TP	TLS	OS	License
3DF Zephyr	3DFlow	Yes	No	Windows	Commercial, 14 days trial, limited free version,
COLMAP	ETH Zurich and UNC Chapel Hill	Yes	No	Windows, Mac, Linux	BSD license
ContextCapture	Bentley systems	Yes	Yes	Windows	Commercial, 30-day trial
CYCLONE	Leica	No	Yes	Windows	Commercial, demo version
Descartes	Bentley systems	No	Yes	Windows	Commercial
Drone2Map for ArcGIS	ESRI	Yes	No	Windows, Web	Commercial, 15-day trial
DroneDeploy	DroneDeploy	Yes	No	iOS, Android	Commercial, 14-day trial
Geomagic wrap	3D systems	No	Yes	Windows	Commercial, 15-day trial
Inpho	Trimble	Yes	Yes	Windows	Commercial
iWitness	DeChant consulting services	Yes	No	Windows	Commercial, 30-day trial
Maps made easy	Maps made easy	Yes	No	Web	Commercial
MicMac	IGN and ENSG	Yes	No	Command line	Open source
Multi-View environment	TU Darmstadt	Yes	No	Windows, Mac, Linux	BSD 3-Clause License
OpenDroneMap	–	Yes	No	Web, CLI	Open source
PhotoModeler	PhotoModeler	Yes	No	Windows	Commercial,15-day trial
Photoscan	Agisoft	Yes	No	Win, Mac, Linux	Commercial, 30-day trial
Pix4Dmapper	Pix4D	Yes	Yes	Win, Mac, Linux	Commercial, 25-day trial
Pointools	Bentley systems	No	Yes	Windows	Commercial
RealityCapture	Capturing reality	Yes	Yes	Windows	Commercial, limited free ver
RealWorks	Trimble	No	Yes	Windows	Commercial
ReCap	Autodesk	Yes	Yes	Windows	Commercial, 30-day trial
Regard3D	–	Yes	No	Win, Mac, Linux	Open source
SCENE	Faro technologies	No	Yes	Windows	Commercial, demo version
SOCET SET	BAE systems	Yes	No	Windows	Commercial
SURE	nFrames GmbH	Yes	No	Windows, Linux	Commercial, 14-day trial
VisualSFM	Changchang Wu	Yes	No	Win, Mac, Linux	Free
Voxxlr	Voxxlr	No	Yes	Web	Commercial

3 Application

3.1 Study Area

On 12th June of 2017 a Mw 6.3 earthquake occurred offshore Lesvos Island in SE Aegean Sea, Greece (Kiratzi 2018). Heaviest damage was reported in the village of Vrisa, where the majority of buildings constructed by stone masonry (Papadimitriou et al. 2018). According to the official nomenclature, engineers inspected all the 788 buildings. Nearly, 35% of the buildings suffered from very heavy damages or destruction and they characterized as beyond repair, about 39% are reported as moderate to heavy non-structural damage buildings, while 26% are characterized as buildings with negligible to slight damage.

For this research, the Vrisa village was divided into sectors, and each sector included several road sections. TP and TLS data were acquired for the entire settlement immediately after the earthquake. All surveys were conducted under real conditions with extended debris and decrepit buildings (Fig. 4-upper left and right). The weather conditions were quite extreme in some cases. For the month following the earthquake and during the working hours, the maximum air temperature was 39° and the maximum wind speed was 27.5 m/sec. In this research, we selected a road section including four buildings. Two of them were damaged beyond repair, one was damaged and needs restoration and one was undamaged (Fig. 4-down left and right).

3.2 Results and Discussion

All images were acquired by two NIKON D3400 using an 18–55 mm and an 18–105 mm lens respectively. This 24.2-megapixel DSLR camera is equipped with a 23.5 mm × 15.6 mm CMOS sensor. The acquisitions performed with 18 mm focal length, therefore, the dimension of each pixel of the 6000×4000 pixel image was 4×4 μm. A total of 189 images were shot for this roadside section. The approximate distance between the stations and the facades were 4 m which was also the width of the road. Images were shot perpendicular to facades and at an angle of approximately 45° to the X and Z axes. A hand-held mounting pole also was used to shoot photos from higher stations (Fig. 5).

In order to scale the model to the ground units, we used two artificial scale objects with known distances. A 2-sided wooden bar with sides 21 cm and 51 cm respectively and a 2×2 chessboard sized 18×18 cm. In the present road section, only the first scale object was identified and used.

The laser scanning process was performed using the terrestrial laser scanner Focus[3D], manufactured by FARO. This scanner features a full 360° x 305° field-of-view, with high scan speed (976 k pts/sec) and the distance measurement is realized by the phase-shift measurement principle.

Fig. 4 Street conditions during surveys (up) and two damaged beyond repair buildings of the study area (down)

Fig. 5 Projection centers at street level (blue) and by using mounting pole (pink)

The first step was to determine the positions and the appropriate parameters setup of the scanner. The fundamental element to be taken into consideration for the positioning of the scanner is to fully cover the desired 3D area, so the chosen positions should be well distributed. A single scan was not sufficient, because of occlusions and possible danger of the physical safety of the team members (near ready-to-collapse walls), thus three positions were chosen (Fig. 6). Three partial scans with 120° x 305° field-of-view were captured using the Focus³ᴰ laser scanner. The selected resolution was at ¼, translated at a spatial resolution (point
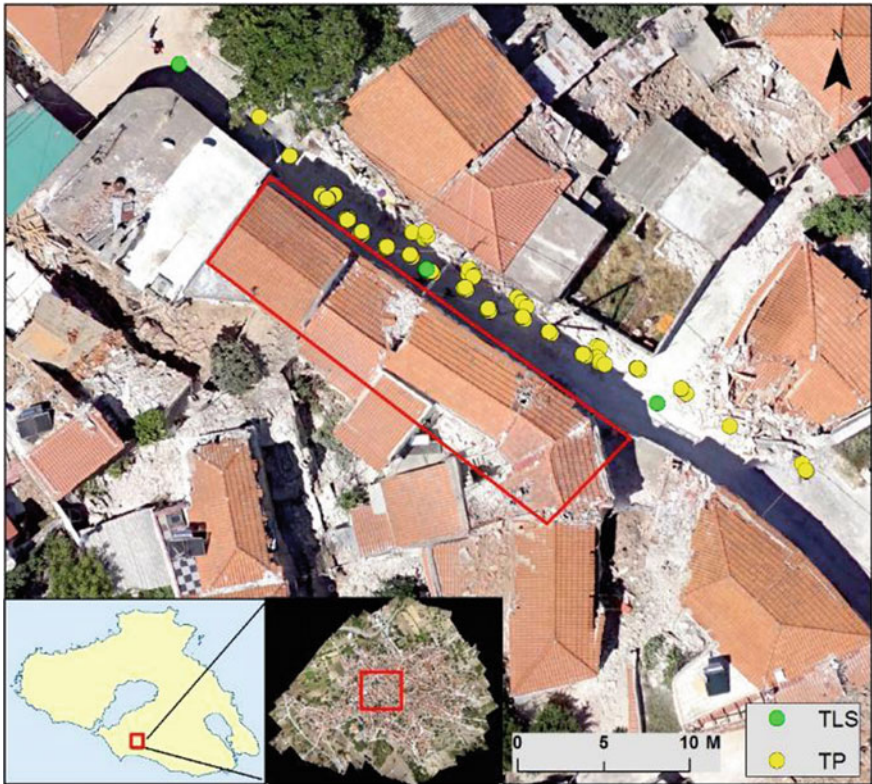
Fig. 6 The study area, the TLS positions and the TP projection centers

distance) of 6.13 mm/10 m and the selected quality was 2x, meaning that every point was fired two times by a laser beam for more accurate distance-value. During data collection, digital photos were captured by the integrated digital camera of the scanner. Also, measurements were taken from the two integrated sensors of the scanner, the digital compass and inclinometer, which is useful information for the later registration of the scans.

During the survey presented in this paper, artificial targets were not used, because it is time and effort consuming and not suitable for a post-earthquake rapid response. SCENE software by FARO (2018) was used for the process of the scans, and the registration process took place using the cloud-to-cloud method. It is an automated registration approach which uses distinctive features extracted from point clouds, and these features have to be matched between pairwise scans in order to estimate an initial approximation for the six-parameter rigid-body transformation, followed by an error minimization step using a surface matching algorithm like the Iterative Closest Point (ICP).

Two filters were applied to the registered point cloud: (a) an outlier removal filter to eliminate isolated and undesired points such as noise and (b) the point cloud was cropped to the study area. The next step was to apply the texture on the segmented point cloud by using the acquired photos from the scanner which were automatically mapped to the corresponding point measurements. The final step was the quality assurance of the point cloud. This was done by comparing a number of control distances that were taken on fixed objects like windows and doors with the corresponding measurements on the point cloud, resulting to a deviation of less than 2 mm.

Comparison between two point clouds requires that both datasets must be co-registered. Observation stations of the laser scanner were georeferenced to the Greek Geodetic Reference System (GGRS87-EPSG: 2100) with the use of Real Time Kinematics (RTK) measurements. Georeferencing of all cameras' stations was not feasible because more than 20,000 images were acquired for the whole settlement. Furthermore, a set of ground control points was not used for the terrestrial photogrammetry as a result of the rapid deployment of the survey immediately after the earthquake. Finally, georeferencing to GGRS87 was accomplished by identifying common points between the images and an orthomosaic that was created during a UAV survey that took place at the same time.

For the present study a fine registration of the two datasets was required. The main methods usually applied for this task are: (a) alignment by picking an adequate number of point pairs in both point clouds; and (b) the ICP (Besl and McKay 1992). It should be noticed that ICP has been extensively used in co-registration of point clouds not only on its primary form but also with hundreds of variations (Pomerleau et al. 2013). ICP was finally chosen for this research because its robustness and the better performance especially when the two datasets have small differences and overlap in a large extent. After the co-registration, the two datasets were clipped with the same bounding box, ensuring that the comparison will take place to the same spatial extent.

The alignment of the 189 images required 48,409 tie points that were automatically identified by the SIFT algorithm implemented in the Agisoft Photoscan (Agisoft 2018). Due to available processing power, the large dataset and the limited time, original images were downscaled to 25%. Thirteen checkpoints were required in order to assist the alignment. The reprojection error was 1.81 pixel and the final ground resolution of the images given the distance between the camera stations and the houses was 0.763 mm/pixel. Finally, 3 control points were used for the georeferencing resulting in Root Mean Square (RMS) error 7.57 cm while the error at the scale bars was 1.02 cm. The area covered by the facades of the four houses of this road section was 130 m^2.

Regarding TLS methodology, the mean registration error of the three scans was 2.3715 mm. A percentage of 66.3 and 66.7% had an error less than 4 mm on pairwise registered point clouds. That error represents the distance where a specific point has been calculated between two consecutive scans. The point density of the registered point cloud was very high (41 M points) due to the massive overlap of the consecutive scans pairwise (53.4 and 40.9%).

Next step was the fine co-registration of both datasets with the ICP algorithm. Registration was based on 50,000 random sampling points and the process would stop either if the computation would exceed the 20 iterations or the RMS error would drop more than 10^{-5} between two consecutive iterations. The theoretical overlap between the two datasets was set to 90%. The RMS error from this procedure was 3.58 cm. Figure 7 shows the final point clouds of the 2 methodologies cropped to the same extent. It can be seen that both methodologies capture the facades in a similar way. Blind spots are created (a) at the second floor due to balconies; and (b) at doors or windows that are installed in a niche (Fig. 8). These spots are quite often at TLS approach due to fewer scanning positions (Fig. 6).

Concerning the point density of the generated clouds, TLS produced locally a higher density point cloud with higher mean value equal to 142,458 points per 0.0314 m². However, the density of the TP point clouds is uniformed throughout the facades with a mean value of 121,399 points per 0.314 m². On the other hand, TLS present the higher density at the center of the scene (Fig. 9). The nature of TLS approach resulted to the convergence of the sight beams to the center of the study area and the irregular distribution of the point density.

The implementation of the M3C2 algorithm reveals that the point clouds produced by the two methodologies can similarly describe the facades and the roughness of the buildings (Fig. 10). Usually, the user defines a point cloud as a

Fig. 7 Point cloud based on terrestrial photogrammetry (up) and laser scanning (down)

reference, however we would like to examine the areas that can be seen by TLS and not from TP and vice versa. Thus, we estimated both distances by assigning as a reference point cloud, the point clouds from both methodologies. When using the TLS point cloud as a reference, the mean absolute difference is 3.8 cm while the 94.9% of the computed differences are lower than 10 cm (Fig. 11). The higher differences are observed at the right side of the study area even though differences are still less than 10 cm. This is due to the fact that fewer camera stations locate at this area. The 5% of points that are in the distance greater than 10 cm are detected mainly in two areas. At the left side of the study area the damaged door of a building exposes the inner house which can be scanned by the TLS approach but cannot be photographed because of the light conditions. Another subset of points that seems to be misplaced between the 2 point clouds is an area that is behind glass windows. Optical properties of materials such as glass windows is a common error source of TLS and the distance measurement is affected and limited by the physical laws of reflection, including refraction and inner reflection effects (Ingensand et al. 2003). Thus, the surface reflection on glass of a laser beam normally causes reflected beams in many directions.

When using the TP point cloud as a reference, results are quite similar. The mean absolute difference is 5.6 cm while the 91.4% of the computed differences are lower than 10 cm. By using as referencing both point clouds during distance estimation, we see that the 94.9% of the point cloud generated by TP overlaps the point cloud of TLS within a distance of 10 cm while the 86.9% of the TLS point cloud overlaps the dataset from TP within the same distance. Both ICP and M3C2 algorithms applied through the open source software CloudCompare (2018).

Fig. 8 Facade extensions (i.e. balconies) creating blind spots
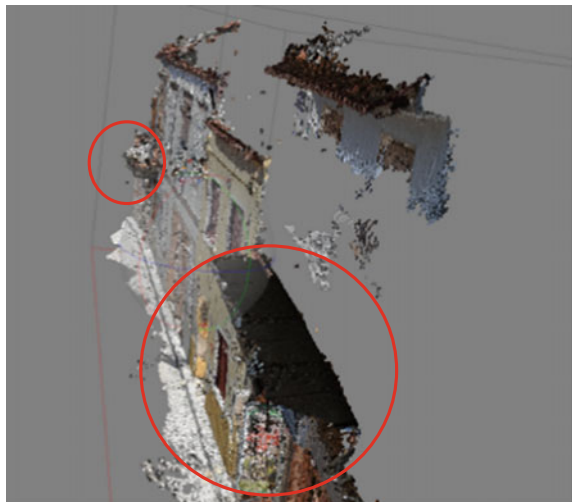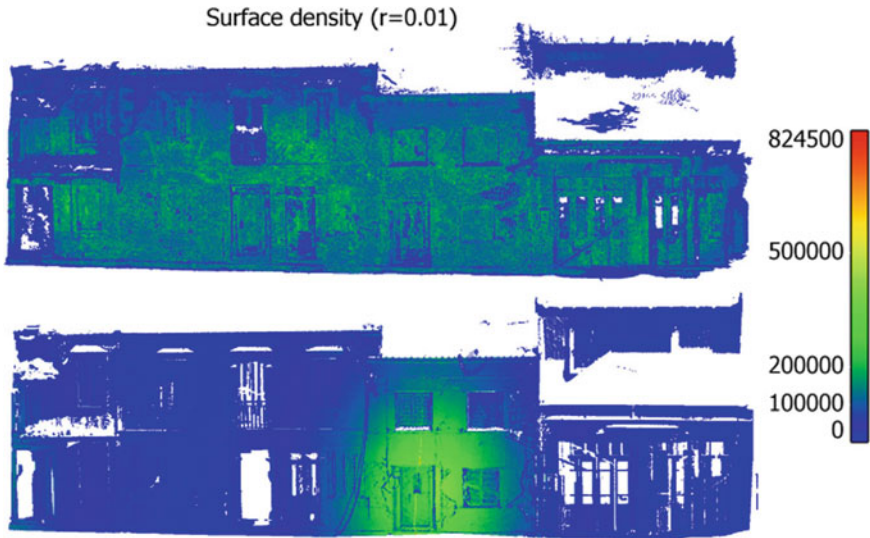
Fig. 9 Cloud point density based on terrestrial photogrammetry (up) and laser scanning (down)
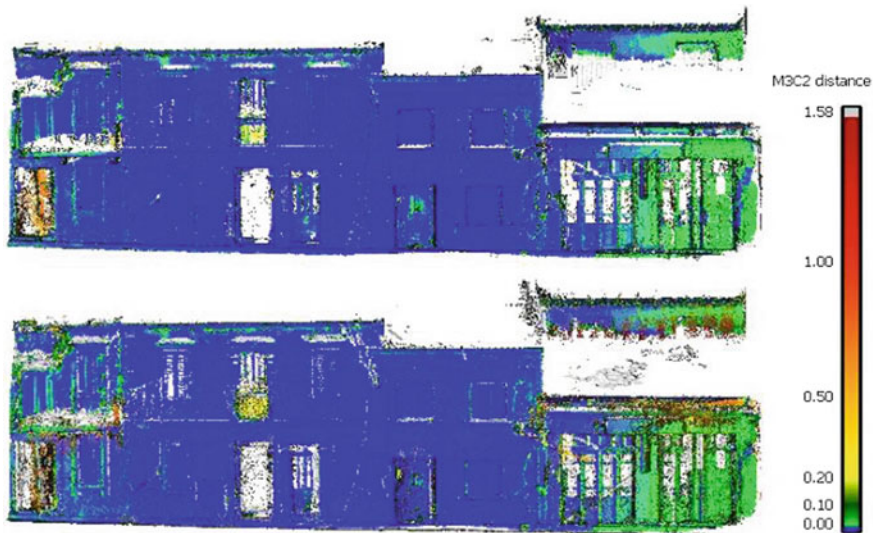
Fig. 10 Absolute difference between TP and TLS point clouds setting the TLS dataset as reference (up) and TP dataset as reference (down)

Gauss: mean = 0.037794 / std.dev. = 0.117004 [551 classes]   Gauss: mean = 0.056355 / std.dev. = 0.157573 [1126 classes]
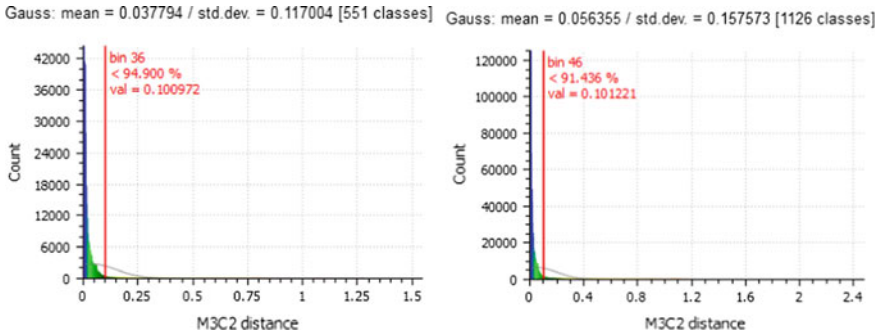
Fig. 11 Histograms of the absolute differences between TP and TLS point clouds setting the TLS dataset as reference (left) and TP dataset as reference (right)

4   Conclusions and Future Work

Before and after an earthquake occurs, geo-information technologies can be utilized rapidly in hazard area for building damage assessment. A significant number of studies have shown that TP and TLS can assist in the response phase for gathering metric and qualitative information on a building scale. Both TP based on DSLR images and TLS lead to 3D building models which are geometrically accurate and high-quality textured. An important issue regarding assessed data in a hazard area is their reliability and credibility. After a natural disaster took place, data acquisition by agencies using different techniques needs to crosscheck or compare from different sources. 3D models including 3D spatial information can become a valuable tool in deep communication and development planning between engineers, constructors and citizens, during the recovery phase of an earthquake.

Within this research it is evaluated whether terrestrial photogrammetry is a reliable methodology to create a 3D model with acceptable accuracy. Comparing to laser scanners, terrestrial photogrammetry is based on low-cost equipment such as DSLR cameras and smartphones. The SfM processing approach and the supporting software, are more user-friendly to non-expert users although a basic background of analytic photogrammetry is critical for survey planning and results in the evaluation.

The exploitation of the 3D output models from the above processing was succeeded as embedded 3D objects in pdf files. The civil protection agencies of Greece used these models for a complete representation of the post-physical state of the Vrisa's buildings. Based on the measurements that can be retrieved from the 3D model within the pdf file, agencies recognized and measured cracks, holes, volumes of debris and other detailed damages in building facades and estimated the compensation for the property loss. As the three-dimensional depiction tends to realism, stakeholders and civil protection agencies can use 3D models geometric information for post-earthquake reconstructions and gain knowledge for pre-earthquake

hazard research. The extracted models are valuable components that assist engineers to understand the seismic behavior in a more comprehensible way.

Recently, Unmanned Aerial Systems appear as an alternative source for both less time-consumed spatial data acquisition in emergency situations, and cost-effective 3D documentation, even in areas with limited access by civil protection agencies, TP or TLS experts. New UAS are smaller, more flexible in terms of flight parameters and among with the cameras' optimization, their use can replace TP. More specifically, the use of multi-view oblique images among with the vertical can support more efficient the damage assessment, because very high spatial resolution images of roofs and facades can be investigated for cracks, deformations and collapses (Gerke and Kerle 2011; Fernandez Galarreta et al. 2015). One of the most promising methodologies for this task is the Convolutional Neural Networks (CNNs) that have been applied in object classification and segmentation in remote sensing applications (Karpathy et al. 2014; Hu et al. 2015; Kampffmeyer et al. 2016). The usefulness of point clouds has been started to be investigated through CNNs for object classification, part segmentation and semantic labeling (Qi et al. 2017; Maltezos et al. 2017; Hackel et al. 2018) with some efforts to focus on earthquake damage assessment (Vetrivel et al. 2018). The transferability of the learning of CNNs is an important aspect of these methodologies that should be taken into consideration for future studies. The integration of a common database including training data (i.e. images and point clouds) from various earthquake events can further assist the damage assessment in different landscapes.

References

Agisoft LLC (2018) Agisoft Photoscan. http://www.agisoft.com. Accessed 20 Oct 2018

Alexander D (1991) Information technology in real-time for monitoring and managing natural disasters. Prog Phys Geogr 15:238–260. https://doi.org/10.1177/030913339101500302

Alexander D (2005) Towards the development of a standard in emergency planning. Disaster Prev Manag An Int J 14:158–175. https://doi.org/10.1108/09653560510595164

Altan O (2005) Use of photogrammetry, remote sensing and spatial information technologies in disaster management, especially earthquakes. In: van Oosterom P, Zlatanova S, Fendel EM (eds) Geo-information for disaster management. Springer, Berlin, p 311

Altan O, Toz G, Kulur S, Seker D, Volz S, Fritsch D, Sester M (2001) Photogrammetry and geographic information systems for quick assessment, documentation and analysis of earthquakes. ISPRS J Photogramm Remote Sens 55:359–372. https://doi.org/10.1016/S0924-2716(01)00025-9

Anil EB, Akinci B, Garrett JH, Kurc O (2013) Characterization of laser scanners for detecting cracks for post-earthquake damage inspection. In: 30th ISARC, Montreal, Canada, pp 313–320

Baird ME (2010) The "phases" of emergency management. Intermodal Freight Transportation Institute, p 50

Bay H, Tuytelaars T, Van Gool L (2006) SURF: speeded up robust features. In: Lecture Notes in Computer Science (including subseries Lecture Notes in Artificial Intelligence and Lecture Notes in Bioinformatics), pp 404–417

Besl PJ, McKay ND (1992) A method for registration of 3-D shapes. IEEE Trans Pattern Anal Mach Intell 14:239–256. https://doi.org/10.1109/34.121791

Boehler W, Bordas Vicent M, Marbs A (2003) Investigating laser scanner accuracy. In: Altan O (ed) Proceedings of XIXth CIPA symposium. ISPRS/CIPA, vol 34. Antalya, Turkey, pp 696–701

Chang KT, Wang EH, Chang YM, Cheng HK (2008) Post-disaster structural evaluation using a terrestrial laser scanner. Paper presented at the international federation of surveyors (FIG) Working Week 2008, Stockholm, Sweden, 14–19 June 2008

CloudCompare (2018) CloudCompare v 2.6.X user documentation. http://www.danielgm.net/cc. Accessed 20 Oct 2018

Cutter SL (2003) GI science, disasters, and emergency management. Trans GIS 7:439–446. https://doi.org/10.1111/1467-9671.00157

Dabove P, Di Pietra V, Lingua AM (2018) Close range photogrammetry with tablet technology in post-earthquake scenario: Sant'Agostino church in Amatrice. Geoinformatica 22:463–477. https://doi.org/10.1007/s10707-018-0316-7

Dai F, Dong S, Kamat VR, Lu M (2011) Photogrammetry assisted measurement of interstory drift for rapid post-disaster building damage reconnaissance. J Nondestruct Eval 30:201–212. https://doi.org/10.1007/s10921-011-0108-6

Devilat BM (2014) 3D laser scanning of heritage areas after earthquakes: San Lorenzo de Tarapacá, Chile. Opticon1826 12. https://doi.org/10.5334/opt.cc

Dong L, Shan J (2013) A comprehensive review of earthquake-induced building damage detection with remote sensing techniques. ISPRS J Photogramm Remote Sens 84:85–99. https://doi.org/10.1016/j.isprsjprs.2013.06.011

Erden T, Karaman H (2012) Analysis of earthquake parameters to generate hazard maps by integrating AHP and GIS for Küçükçekmece region. Nat Hazards Earth Syst Sci 12:475–483. https://doi.org/10.5194/nhess-12-475-2012

Erkal BG (2017) the prototype of a software application for laser and image-based surface damage detection. Paper presented at the 2nd world congress on civil, structural, and environmental engineering (CSEE 2017), Barcelona, Spain, 2–4 April 2017

FARO Technologies, Inc (2018) FARO scene. https://www.faro.com. Accessed 20 Oct 2018

Fernandez Galarreta J, Kerle N, Gerke M (2015) UAV-based urban structural damage assessment using object-based image analysis and semantic reasoning. Nat Hazards Earth Syst Sci 15:1087–1101. https://doi.org/10.5194/nhess-15-1087-2015

Furukawa Y, Ponce J (2010) Accurate, dense, and robust multiview stereopsis. IEEE Trans Pattern Anal Mach Intell 32:1362–1376. https://doi.org/10.1109/TPAMI.2009.161

Gallo A, Muzzupappa M, Bruno F (2014) 3D reconstruction of small sized objects from a sequence of multi-focused images. J Cult Herit 15:173–182. https://doi.org/10.1016/j.culher.2013.04.009

Gerke M, Kerle N (2011) Automatic structural seismic damage assessment with airborne oblique pictometry© imagery. Photogramm Eng Remote Sens 77:885–898. https://doi.org/10.14358/PERS.77.9.885

Girardeau-Montaut D, Roux M, Marc R, Thibault G (2005) Change detection on points cloud data acquired with a ground laser scanner. In: International archives of the photogrammetry, remote sensing and spatial information sciences-ISPRS archives, vol 36, pp 30–35

Goodchild MF (2006) GIS and disasters: planning for catastrophe. Comput Environ Urban Syst 30:227–229. https://doi.org/10.1016/j.compenvurbsys.2005.10.004

Hackel T, Wegner JD, Savinov N, Ladicky L, Schindler K, Pollefeys M (2018) Large-scale supervised learning For 3D point cloud labeling: Semantic3d.Net. Photogramm Eng Remote Sens 84:297–308. https://doi.org/10.14358/PERS.84.5.297

Hanke K, Grussenmeyer P, Streilein A (2002) Architectural photogrammetry: basic theory, procedures, tools. In: Kasser M, Egels Y (eds) Digital photogrammetry. Taylor & Francis, pp 300–339

Hashemi M, Alesheikh AA (2011) A GIS-based earthquake damage assessment and settlement methodology. Soil Dyn Earthq Eng 31:1607–1617. https://doi.org/10.1016/j.soildyn.2011.07.003

Hu F, Xia G-S, Hu J, Zhang L (2015) transferring deep convolutional neural networks for the scene classification of high-resolution remote sensing imagery. Remote Sens 7:14680–14707. https://doi.org/10.3390/rs71114680

Ingensand H, Ryf A, Schulz T (2003) Performances and experiences in terrestrial laser scanning. In: Proceedings of the 6th conference on optical 3D measurement techniques. Zurich, pp 1–8

Jafari B, Khaloo A, Lattanzi D (2017) Deformation tracking in 3D point clouds via statistical sampling of direct cloud-to-cloud distances. J Nondestruct Eval 36:65. https://doi.org/10.1007/s10921-017-0444-2

Jiang R, Jáuregui DV, White KR (2008) Close-range photogrammetry applications in bridge measurement: literature review. Measurement 41:823–834. https://doi.org/10.1016/j.measurement.2007.12.005

Kampffmeyer M, Salberg A-B, Jenssen R (2016) Semantic segmentation of small objects and modeling of uncertainty in urban remote sensing images using deep convolutional neural networks. In: 2016 IEEE conference on computer vision and pattern recognition workshops (CVPRW). IEEE, pp 680–688

Karpathy A, Toderici G, Shetty S, Leung T, Sukthankar R, Fei-Fei L (2014) Large-scale video classification with convolutional neural networks. In: 2014 IEEE conference on computer vision and pattern recognition. IEEE, pp 1725–1732

Kayen R, Collins B, Bawden G, Pack R (2006) Earthquake deformation analysis using terrestrial scanning laser-lidar technology. In: 8th U.S. national conference on earthquake engineering. San Francisco, California, USA

Kiratzi A (2018) The 12 June 2017 Mw 6.3 Lesvos Island (Aegean Sea) earthquake: slip model and directivity estimated with finite-fault inversion. Tectonophysics 724–725:1–10. https://doi.org/10.1016/j.tecto.2018.01.003

Lague D, Brodu N, Leroux J (2013) Accurate 3D comparison of complex topography with terrestrial laser scanner: application to the Rangitikei canyon (N-Z). ISPRS J Photogramm Remote Sens 82:10–26. https://doi.org/10.1016/j.isprsjprs.2013.04.009

Lerma JL, Navarro S, Cabrelles M, Villaverde V (2010) Terrestrial laser scanning and close range photogrammetry for 3D archaeological documentation: the Upper Palaeolithic Cave of Parpalló as a case study. J Archaeol Sci 37:499–507. https://doi.org/10.1016/j.jas.2009.10.011

Li M, Cheng L, Gong J, Liu Y, Chen Z, Li F, Chen G, Chen D, Song X (2008) Post-earthquake assessment of building damage degree using LiDAR data and imagery. Sci China Ser E: Technol Sci 51:133–143. https://doi.org/10.1007/s11431-008-6014-1

Lowe DG (1999) Object recognition from local scale-invariant features. In: Proceedings of the IEEE international conference on computer vision, pp 1150–1157

Maltezos E, Doulamis N, Doulamis A, Ioannidis C (2017) Deep convolutional neural networks for building extraction from orthoimages and dense image matching point clouds. J Appl Remote Sens 11:1. https://doi.org/10.1117/1.JRS.11.042620

Morelan AE, Trexler CC, Oskin ME (2015) Surface-rupture and slip observations on the day of the 24 August 2014 South Napa earthquake. Seismol Res Lett 86:1119–1127

Moussa W, Wenzel K, Rothermel M, Abdel-Wahab M, Fritsch D (2013) Complementing TLS point clouds by dense image matching. Int J Herit Digit Era 2:453–470. https://doi.org/10.1260/2047-4970.2.3.453

Olsen MJ, Kayen R (2012) Post-earthquake and tsunami 3D laser scanning forensic investigations. Forensic Engineering 2012. American Society of Civil Engineers, Reston, VA, pp 477–486

Olsen MJ, Chen Z, Hutchinson T, Kuester F (2013) Optical techniques for multiscale damage assessment. Geomat Nat Hazards Risk 4:49–70. https://doi.org/10.1080/19475705.2012.670668

Papadimitriou P, Kassaras I, Kaviris G, Tselentis G-A, Voulgaris N, Lekkas E, Chouliaras G, Evangelidis C, Pavlou K, Kapetanidis V, Karakonstantis A, Kazantzidou-Firtinidou D, Fountoulakis I, Millas C, Spingos I, Aspiotis T, Moumoulidou A, Skourtsos E, Antoniou V, Andreadakis E, Mavroulis S, Kleanthi M (2018) The 12th June 2017 M w = 6.3 Lesvos earthquake from detailed seismological observations. J Geodyn 115:23–42. https://doi.org/10.1016/j.jog.2018.01.009

Papakonstantinou A, Doukari M, Moustakas A, Chrisovalantis D, Chaidas K, Roussou O, Athanasis N, Topouzelis K, Soulakellis N (2018) UAS multi-camera rig for post-earthquake damage 3D geovisualization of Vrisa village. In: Themistocleous K, Hadjimitsis DG, Michaelides S, Ambrosia V, Papadavid G (eds) Sixth international conference on remote sensing and geoinformation of the environment (RSCy2018). SPIE, p 52

Pesci A, Teza G, Bonali E, Casula G, Boschi E (2013) A laser scanning-based method for fast estimation of seismic-induced building deformations. ISPRS J Photogramm Remote Sens 79:185–198. https://doi.org/10.1016/j.isprsjprs.2013.02.021

Pomerleau F, Colas F, Siegwart R, Magnenat S (2013) Comparing ICP variants on real-world data sets. Auton Robots 34:133–148. https://doi.org/10.1007/s10514-013-9327-2

Puente I, Lindenbergh R, Van Natijne A, Esposito R, Schipper R (2018) Monitoring of progressive damage in buildings using laser scan data. In: International archives of the photogrammetry, remote sensing and spatial information sciences-ISPRS archives, vol 42, no 2, pp 923–929

Qi CR, Su H, Kaichun M, Guibas LJ (2017) PointNet: deep learning on point sets for 3D classification and segmentation. In: 2017 IEEE conference on computer vision and pattern recognition (CVPR). IEEE, pp 77–85

Rastiveis H, Eslamizade F, Hosseini-Zirdoo E (2015) Building damage assessment after earthquake using post-event LiDAR data. In: International archives of the photogrammetry, remote sensing and spatial information sciences-ISPRS archives, vol 40, no 1W5, pp 595–600

Rieke-Zapp DH, Peipe J (2006) Performance evaluation of a 33 megapixel alpa 12 medium format camera for digital close range photogrammetry. In: International archives of the photogrammetry, remote sensing and spatial information sciences-ISPRS archives, vol 36, p 4

Selvaggi I, Dellapasqua M, Franci F, Spangher A, Visintini D, Bitelli G (2018) 3D comparison towards a comprehensive analysis of a building in cultural heritage. In: International archives of the photogrammetry, remote sensing and spatial information sciences-ISPRS archives, vol 42, no 2, pp 1061–1066

Sivakumar R, Ghosh S (2017) Earthquake hazard assessment through geospatial model and development of EaHaAsTo tool for visualization: an integrated geological and geoinformatics approach. Environ Earth Sci 76:442. https://doi.org/10.1007/s12665-017-6777-4

Snavely N, Seitz SM, Szeliski R (2006) Photo tourism: exploring photo collections in 3D. ACM Trans Graph 25:835–846. https://doi.org/10.1145/1141911.1141964

Snavely N, Seitz SM, Szeliski R (2008) Modeling the world from Internet photo collections. Int J Comput Vis 80:189–210. https://doi.org/10.1007/s11263-007-0107-3

Tong X, Hong Z, Liu S, Zhang X, Xie H, Li Z, Yang S, Wang W, Bao F (2012) Building-damage detection using pre- and post-seismic high-resolution satellite stereo imagery: a case study of the May 2008 Wenchuan earthquake. ISPRS J Photogramm Remote Sens 68:13–27. https://doi.org/10.1016/j.isprsjprs.2011.12.004

Triggs B, McLauchlan PF, Hartley RI, Fitzgibbon AW (2000) Bundle adjustment—a modern synthesis. In: Lecture Notes in Computer Science, pp 298–372

Tu J, Sui H, Feng W, Song Z (2016) Automatic building damage detection method using high-resolution remote sensing images and 3D GIS model. ISPRS Ann Photogramm Remote Sens Spat Inf Sci III-8:43–50. https://doi.org/10.5194/isprs-annals-iii-8-43-2016

Ullman S (1979) The interpretation of structure from motion. In: Proceedings of the royal society B: biological sciences, pp 405–426

Van Westen CJ (2013) Remote sensing and GIS for natural hazards assessment and disaster risk management. In: Schroder JF, Bishop MP (eds) Treatise on geomorphology. Academic Press, San Diego, pp 259–298

Vetrivel A, Gerke M, Kerle N, Vosselman G (2015) Identification of damage in buildings based on gaps in 3D point clouds from very high resolution oblique airborne images. ISPRS J Photogramm Remote Sens 105:61–78. https://doi.org/10.1016/j.isprsjprs.2015.03.016

Vetrivel A, Gerke M, Kerle N, Nex F, Vosselman G (2018) Disaster damage detection through synergistic use of deep learning and 3D point cloud features derived from very high resolution oblique aerial images, and multiple-kernel-learning. ISPRS J Photogramm Remote Sens 140:45–59. https://doi.org/10.1016/j.isprsjprs.2017.03.001

Vosselman G, Maas H-G (2010) Airborne and terrestrial laser scanning. Whittles Publishing, Scotland, UK

Westoby MJ, Brasington J, Glasser NF, Hambrey MJ, Reynolds JM (2012) 'Structure-from-Motion' photogrammetry: a low-cost, effective tool for geoscience applications. Geomorphology 179:300–314. https://doi.org/10.1016/j.geomorph.2012.08.021

Widyaningrum E, Gorte BGH (2017) Comprehensive comparison of two image-based point clouds from aerial photos with airborne LiDAR for large-scale mapping. In: International archives of the photogrammetry, remote sensing and spatial information sciences-ISPRS archives, vol 42, no 2W7, pp 557–565

Wu C, Liu Y, Dai Q, Wilburn B (2011) Fusing multiview and photometric stereo for 3D reconstruction under uncalibrated illumination. IEEE Trans Vis Comput Graph 17:1082–1095. https://doi.org/10.1109/TVCG.2010.224

Wu J, Cui Z, Sheng VS, Zhao P, Su D, Gong S (2013) A comparative study of SIFT and its variants. Meas Sci Rev 13:122–131. https://doi.org/10.2478/msr-2013-0021

Xu X, Bureick J, Yang H, Neumann I (2018) TLS-based composite structure deformation analysis validated with laser tracker. Compos Struct 202:60–65. https://doi.org/10.1016/j.compstruct.2017.10.015

Yamazaki F, Matsuda T, Denda S, Liu W (2015) Construction of 3D models of buildings damaged by earthquakes using UAV aerial images. In: Proceedings of the tenth Pacific conference on earthquake engineering. Sydney, Australia

Yang X, Zhang Q (2013) Seismic spatial information grid: applications of geo-informatics in earthquake disaster management. In: Bian F, Xie Y, Cui X, Zeng Y (eds) Communications in computer and information science. Springer, Berlin, pp 397–406

Zhao X, Kargoll B, Omidalizarandi M, Xu X, Alkhatib H (2018) Model selection for parametric surfaces approximating 3D point clouds for deformation analysis. Remote Sens 10:634. https://doi.org/10.3390/rs10040634

Zhihua X, Lixin W, Yonglin S, Qiuling W, Ran W, Fashuai L (2014) Extraction of damaged building's geometric features from multi-source point clouds. In: 2014 IEEE geoscience and remote sensing symposium. IEEE, pp 4764–4767

Part II
Geospatial Information for Disaster Management

AYDES: An All-in-One Solution for Geospatial Information Technology Based Disaster Management and Decision Support

Irfan Keskin, Nihan Karacameydan, Murat Tosun,
Mustafa Kemal Tüfekci, Dogus Bulut, Fatih Avci and Oktay Gökce

Abstract The Disaster Management and Decision Support System (AYDES) is a software, data and analysis platform that provide accurate and current disaster and emergency data, reports, statistics, job inspections, queries, analyses etc. at every stages before and after the disaster. AYDES is a holistic platform integrated with many internal and external systems and services, including desktop, mobile and web-based applications that utilize GIS and RS technologies. It has been developed according to the content of the National Disaster Response Plan of Turkey and designed to be easily used by the National Disaster and Emergency Management Agency of Turkey (AFAD), collaborative Ministries, private institutions and provincial organizations. AYDES consists of three core components with their sub components, namely "Incident Command System", "Spatial Information System" and "Recovery Information System". Mobile software tools that can deliver real-time information to the web-based core components of AYDES that consists of applications used for mapping during both post-disaster damage detection and pre-disaster risk reduction. Additionally, in case of a need to disaster event

I. Keskin (✉) · N. Karacameydan · M. Tosun · M. K. Tüfekci · D. Bulut · F. Avci · O. Gökce
Department of Information Systems and Communication,
National Disaster and Emergency Management Agency of Turkey (AFAD),
Universiteler Mah., Dumlupinar Bulvari No: 159 Cankaya, Ankara, Turkey
e-mail: irfan.keskin@afad.gov.tr

N. Karacameydan
e-mail: nihan.karacameydan@afad.gov.tr

M. Tosun
e-mail: murat.tosun@afad.gov.tr

M. K. Tüfekci
e-mail: mkemal.tufekci@afad.gov.tr

D. Bulut
e-mail: dogus.bulut@afad.gov.tr

F. Avci
e-mail: fatih.avci@afad.gov.tr

O. Gökce
e-mail: oktay.gokce@afad.gov.tr

inventories, potentially vulnerable assets, hazard—risk data, affected areas of probable or actual disasters, damage detection results and such data and analyses, two software tools have been developed, namely AYDES-RS, a desktop image processing and analysis software and AYDES-CS, a web-based crowdsourcing software tool whereas two of them enable to allow the use of imagery acquired by remote (space/aerial) technologies for various analyses before and after a disaster. In this chapter, we introduce AYDES and related literature survey about similar disaster management platforms and systems in the world.

1   Introduction

IT based disaster management is one of the specific fields of Industry 4.0 consisting of hardware, software, services, data, personnel and methodology components. If one needs to pay more attention to one of these components, data seems to be self-evident as in the all IT based systems. And the satellite/areal images are primary data sources to process and analyse in order to extract for and disseminate to the disaster community, institutions, academia and public. Although the online web map services such as "Google Maps, Yahoo Maps, Bing Maps, etc". support the disaster community with a large amount of satellite imagery, they are not data-distribution platforms for disaster responders, since they are closed system which don't allow to download the original images which are required for processing and analyzing with GIS and remote sensing tools within an IT based disaster management system.

Geographical Information Technologies (Geo-ITs) constitute geo-spatial components of the IT based disaster management systems in addition to the non-spatial parts, rather say infrastructure components such as computer, communication, internet, software, database and other technologies. Regarding the usage of Geo-ITs (especially GIS and Remote Sensing technologies) in disaster management, there have been a number projects and studies worldwide. These projects and studies can be evaluated in five aspects: system architecture, geographical area of interest, type of disaster, phase of disaster and target users. In terms of the system architecture, some of them are limited to stand-alone tools, web portals or mobile applications whereas some others are combinations of them. In regard to the geographical area of interest of those projects and studies, some of them are confined to a small region (as in some case studies), some deal with a city, country, continent or the whole world. As the type of disaster regards, the majority of these studies and projects are based on a specific type of disaster such as earthquake, flood, tsunamis, wildfires, mass-migration, etc. The fourth aspect is the phase of disaster: prevention/mitigation, preparedness, response, recovery which is/are the working area of the projects and studies. As for the target users, some of them aim at academia only and the target users of some others are public or institutions. It's really hard to find an "all-in-one" system covering all scopes of those four aspects of the evaluation.

Apart from region based projects, one of the well-known example of the projects at national and international level is the "HAZUS" (FEMA 2018) which is a desktop software on earthquakes, floods, hurricanes and tsunamis in the USA for public to be used during respond phase of disaster (to estimate potential losses).

An example for the Disaster Management at national level is "National Database for Emergency Management portal (NDEM 2018) which is hosted at Indian Geo-Platform of ISRO (NRSC 2017). Having the all phases and types of disaster, serving to the public, integrated with two mobile applications (Geo-spatial database on emergency facilities, disaster relief management), NDEM system (NDEM User Manual 2017) seems near to an all-in-one solution (with lack of desktop tools) for disaster management.

The inventory of resources that enlists equipment and human resources for disasters is managed by a separate non-spatial web portal "India Disaster Resource Network-IDRN" (IDRN 2018) which is not public and not integrated to NDEM portal.

UNOSAT LIVE Map (UNOSAT 2018) is a web portal which shows only damage assessments after a disaster (Fig. 1) and Disaster AWARE Platform (DAP 2017) developed by Pacific Disaster Center (PDC) is another web portal which displays active hazards in the world.
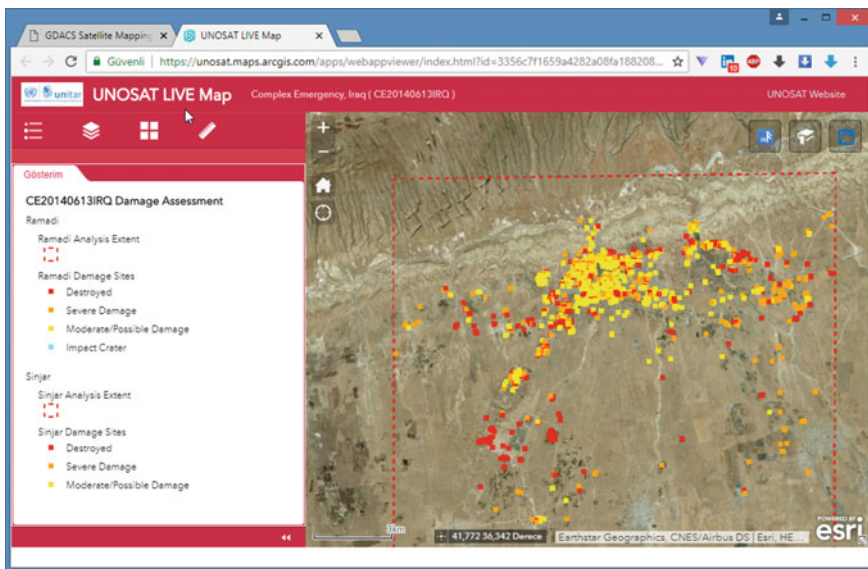
Fig. 1 Screenshot of *UNOSAT LIVE Map* Web Portal (© 2018 UNOSAT Team) (The screenshot of *UNOSAT LIVE Map* web portal (© 2018 UNOSAT Team) at the URL https://unosat.maps.arcgis.com/apps/webappviewer/index.html?id=3356c7f1659a4282a08fa188208036d7 is used with the permission from "*UNOSAT Team*".)
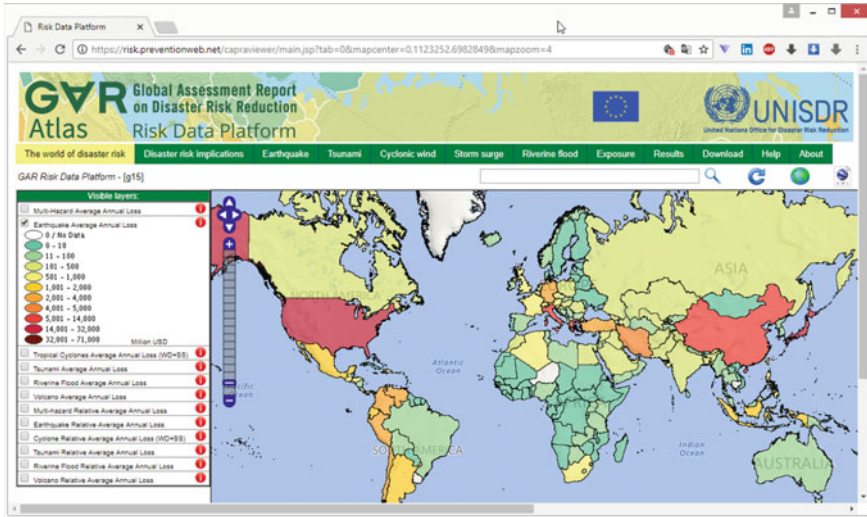
Fig. 2 Screenshot of *GAR-ATLAS Risk Data Platform* (© 2018 UNISDR) (The screenshot of *GAR-ATLAS Risk Data Platform* (© 2018 UNISDR) at the URL https://risk.preventionweb.net/capraviewer is used with the permission from "*Mr. Ricardo Mena, Chief of Supporting and Monitoring Sendai Framework Implementation Branch at United Nations Office for Disaster Risk Reduction (UNISDR)*".)
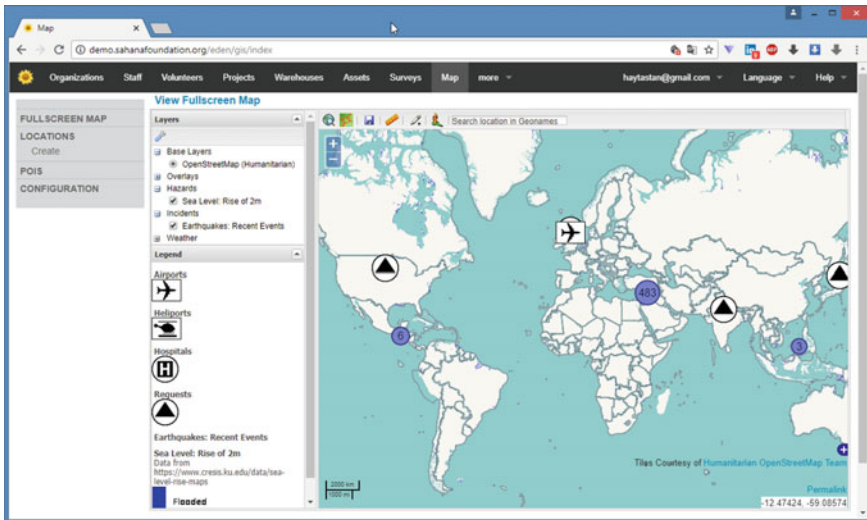
Fig. 3 Screenshot of *Sahana-Eden Humanitarian Management Platform* at the remote server (© SAHANA Software Foundation) (The screenshot of *Sahana-Eden Humanitarian Management Platform* at the remote server at http://demo.sahanafoundation.org/eden/gis/index is used with the permission from "*Dr. Devin Balkind, President at SAHANA Software Foundation*".)

Global Disaster Alert and Coordination System (GDACS) web portal (GDACS 2018) developed by UN&EU, "Reliefweb" web portal (RELIEFWEB 2018) developed by OCHA are web portals which have been broadcasting about the disasters in real time in the world, as a list and on a map, respectively. GAR-ATLAS Risk Data Platform (GAR-ATLAS 2018) developed by UNISDR (United Nations Office for Disaster Risk Reduction) shows the average annual loss numbers for each type of disaster together with the disaster risk implications and disasters in the past in the world (Fig. 2).

Sahana-Eden is the world's most popular open-source information management system for disaster and humanitarian aid management (SAHANA-EDEN 2018). It can support all phases of the emergency cycle *out of the box* (SAHANA-EDEN Demo 2018) at the remote server (Fig. 3) or be customized at the local server after setup (Fig. 4) to meet the specific needs of agencies and organizations.

Ushahidi is an open source collaborative web mapping platform used also for crises response (USHAHIDI Software 2018). This web platform can be used at "ushahidi.io" domain with a payment plan (mapper for free, surveyor with 9/month, responder with $499/month, solutions with negotiation) (Fig. 5) or can be downloaded (USHAHIDI Platform 2018), installed and used with a GPL license at local WAMP/XAMPP server.
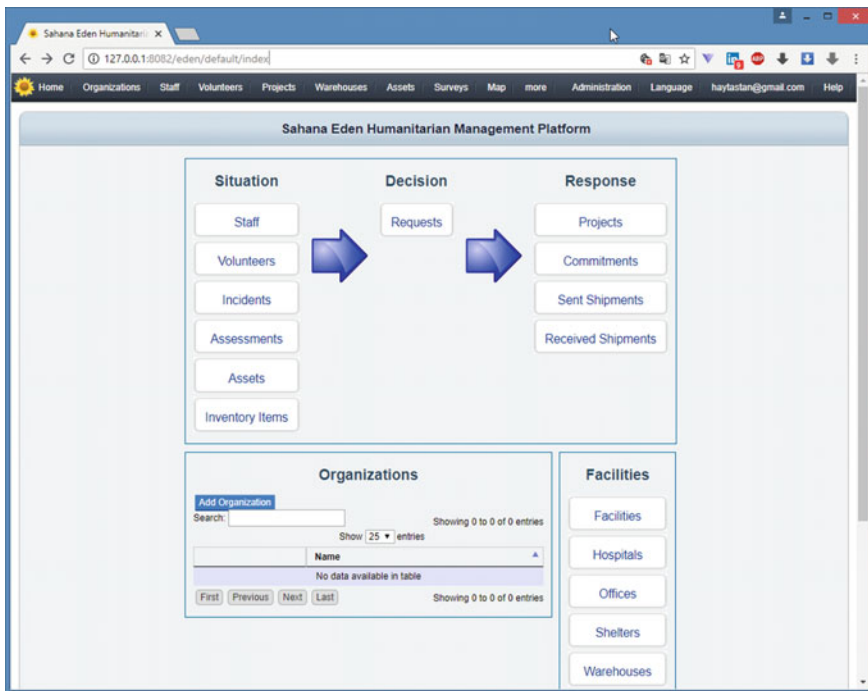
Fig. 4 Screenshot of *Sahana-Eden Humanitarian Management Platform* at the local server (© SAHANA Software Foundation) (The screenshot of *Sahana-Eden Humanitarian Management Platform* at the local server at https://hayatitastan.ushahidi.io/views/map is used with the permission from "*Dr. Devin Balkind, President at SAHANA Software Foundation*".)
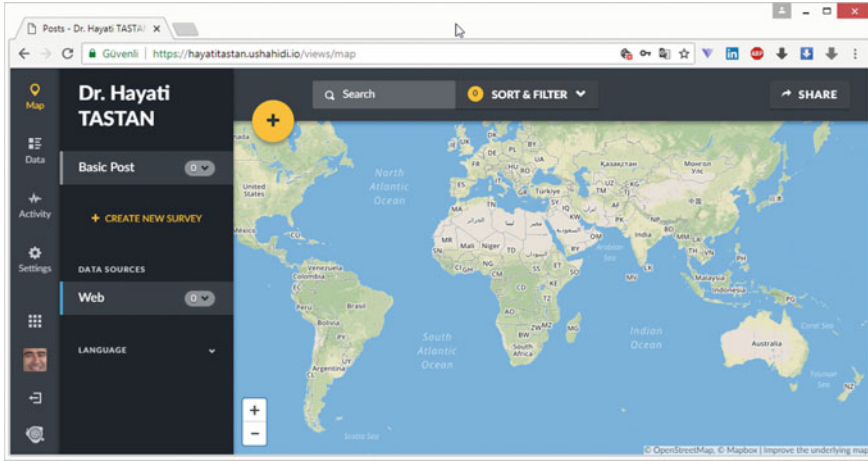
Fig. 5 Screenshot of the free *Ushahidi web platform* at *ushahidi.io* domain (© 2018 USHAHIDI) (The screenshot of the free *Ushahidi web platform* (© 2018 USHAHIDI) at *ushahidi.io* domain at the URL https://hayatitastan.ushahidi.io/views/map is used with the permission from "*Staicy Gitau, Innovation Engagement Officer at USHAHIDI*".)
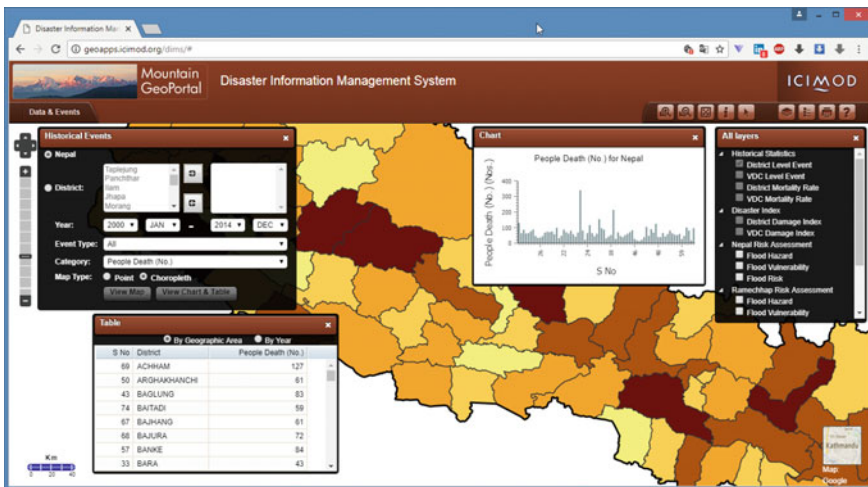
**Fig. 6** Screenshot of the *Nepal Mountain GeoPortal—Disaster Information Management System* (© 2018 ICIMOD) (This application was developed as part of the SERVIR Hindu Kush Himalaya (SERVIR-HKH) initiative. SERVIR is a joint development initiative of the United States Agency for International Development (USAID) and the National Aeronautics and Space Administration (NASA). SERVIR-HKH is implemented by the International Centre for Integrated Mountain Development (ICIMOD) in its regional member countries, prioritizing activities in Afghanistan, Bangladesh, Myanmar, Nepal, and Pakistan. The screenshot of this application is used with the permission from "*Birendra Bajracharya, Regional Program Manager at ICIMOD*".)

Mountain Geoportal—Disaster Information Management System (DIMS 2017) is a web portal developed by the International Centre for Integrated Mountain Development (ICIMOD 2018) which gives map based statistics about disasters in Hindu Kush Himalaya—Afghanistan, Bangladesh, Bhutan, China, India, Myanmar, Nepal, and Pakistan in the past years (Fig. 6).

2 Methodology

Disaster Management and Decision Support System (AYDES) is an information system which is developed for performing the processes of disaster and emergency management efficiently. The system is an integral platform connected to other internal and external systems and applications and composed of desktop software, GIS based web applications (2D and 3D) and mobile applications. AYDES is prepared properly to the content of Turkey Disaster Response Plan (TAMP). The system presents a holistic approach for effective and easy usage in disaster management processes and is designed to be used by Disaster and Emergency Management Presidency (AFAD), relevant ministries and provincial organizations.

AYDES consists of three main components as "Incident Command System", "Spatial Information System", "Recovery Information System" and subcomponents belong to these (Fig. 7). Mobile software tools that can deliver real-time information to the web-based main modules are developed in accordance with the field data collection and consist of applications used in mapping studies within the scope of risk mitigation as well as post-disaster damage detection. In addition, disaster event inventories, potentially vulnerable assets, hazard—risk data, areas of probable or actual disasters, etc. AYDES-RS "desktop image processing and analysis software and AYDES—Crowd Sourcing software have been developed for the use of
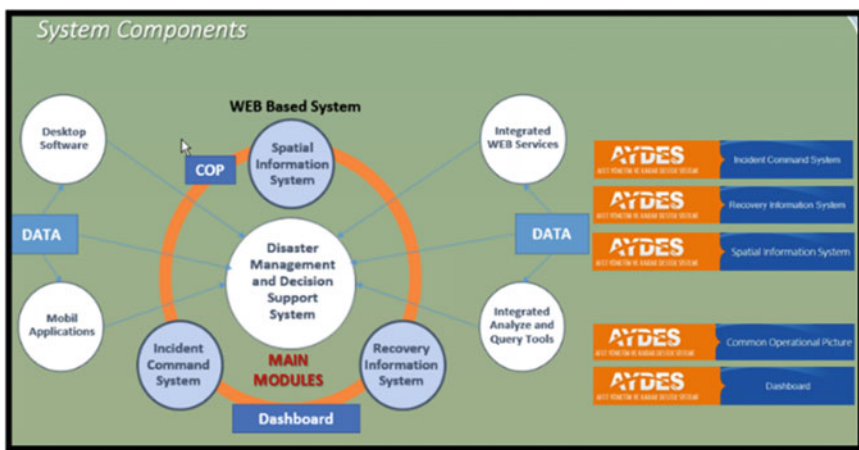
Fig. 7 System components of AYDES

remote (space/air) sensing technologies in various analyses before and after disasters. AYDES is a software and data platform that provide accurate and current disaster and emergency data, reports, statistics, job inspections, queries, analyses etc. at every stages before and after the disaster.

3 Main Components

3.1 Incident Command System

Incident Command System (ICS) is an AYDES component which allows the holistic management of the processes of disaster preparation, planning and response phases that are described in TAMP. Software based management model supports disaster and emergency preparedness and response activities at the local and national level through the main management processes (resource management, transport, demand management) flexibly and effectively. When a disaster event occurs at national or local level, event notifications can be sent to teams by SMS and e-mail so that via the instant messaging and e-mail, service groups (defined as part of TAMP) can remain in continuous interaction and communication.

Data pool and data analysis framework was set up so that 28 service groups could process the processes related to their own specialization fields and data that could be needed in the management of service groups could be entered into the system during various stages of disaster.

Sub-menus in ICS are as follows: (1) Incident identification and listing, (2) Organization structure, (3) Address book, (4) Facility management, (5) TAMP documentation, (6) Service Group Recovery procedures, (7) Resource management,
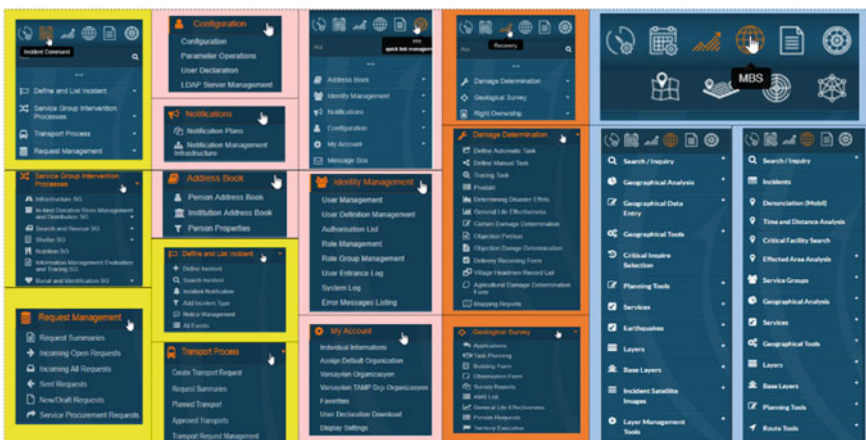
Fig. 8 Menus and sub-menus of AYDES

(8) Demand management, (9) Transportation and transfer operations, (10) Scenario panel, (11) Identity management, (12) Message box, (13) Notifications, (14) Reports, (16) My Account. Figure 8 shows the menus and sub-menus of AYDES.

ICS is designed according to the content of TAMP. A post-disaster use of ICS can be summarized as follows. After a disaster, the need estimate is automatically calculated by AYDES ICS using the information obtained from the disaster area. Search and rescue teams demand the equipment they need from the system.

The tasks and transactions of service groups carried out within the scope of the tasks and responsibilities, what requests are made, whether they are met or not and all response operations are monitored and can be monitored and reported in real time from the system. Figure 9 shows the ICS and Fig. 10 shows the dashboards of ICS for the number of total evacuated, identity status and injured information.
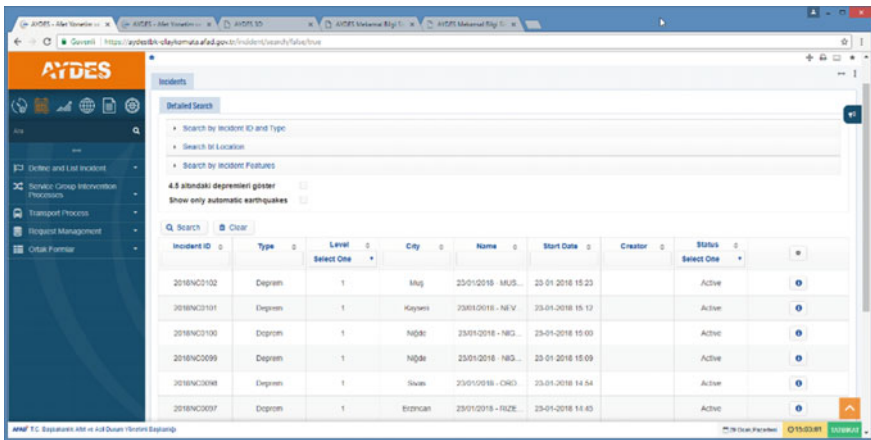
Fig. 9 Incident management system of AYDES

Fig. 10 Dashboards of incident management system
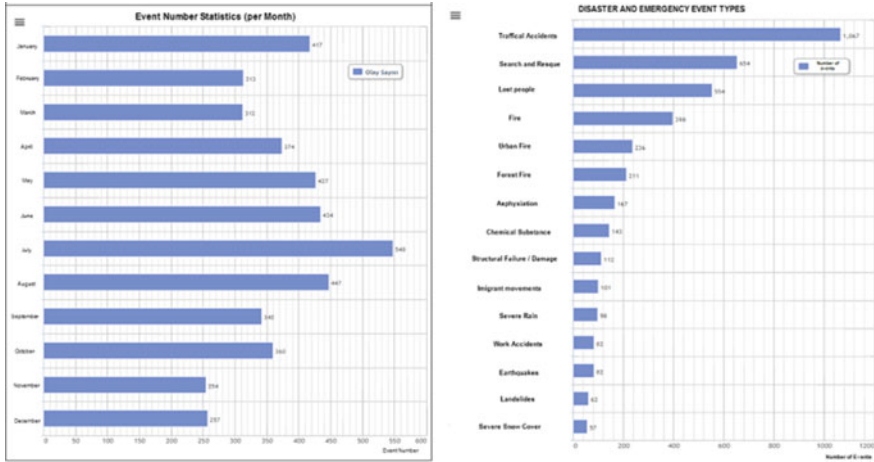
Fig. 11 The monthly numbers of incidents and most disaster and emergency types in 2017

A total of 4442 events were entered in AYDES using Incident Command System in 2017. This shows that AFAD responds on an average of more than 12 disasters every day. Figure 11 shows the monthly numbers of incidents and the most disaster and emergency types recorded in 2017.

3.2 Recovery Information System

Sub modules of the RIS developed already are as follows:

- Damage Assessment
- Geological Hazard Survey
- Beneficiary Management.

The other sub modules of the RIS to be developed are as follows:

- Resettlement Site Selection
- Investment Program
- National Emergency Assistance and Tracking.

The outputs the "Damage Assessment" sub module are used as input to the Beneficiary Management sub module of RIS.

Recovery Information System (RIS) aims to realize post disaster recovery activities in electronic environment with GIS support. Thus, consistency between the different recovery stages (damage determination, geological surveys, right ownership and debiting, resettlement site selection, investment program and national emergency assistance and tracking) that produce input for other stages will
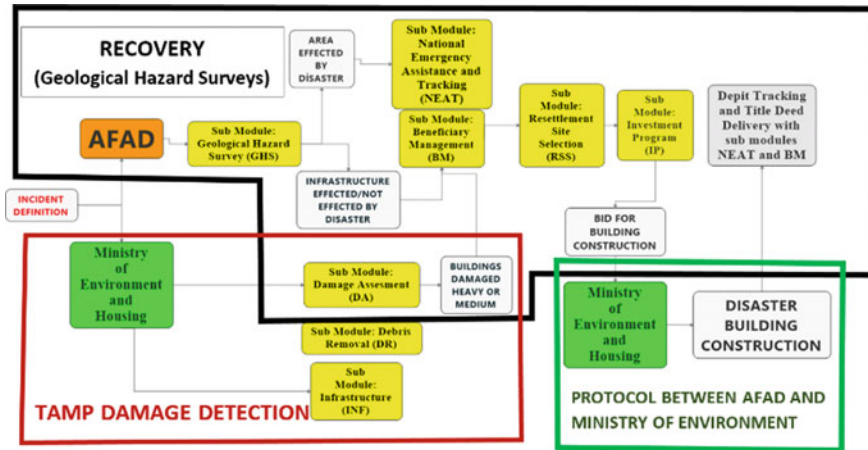
Fig. 12 Relationships between submodules of RIS and TAMP damage detection

be ensured and incorrect operations—caused by repeated or wrong data records-will be prevented. Also, system allows the collection of data by mobile applications from field and near real time location based post disaster data are presented for decision makers and other users of the system. Figure 12 shows the relationships between RIS sub modules and TAMP damage detection sub module.

3.2.1 Damage Assessment Sub Module

With this module, after the earthquake, flood and fire disaster events are defined, the technical teams are assigned to the site and the damage level of the structures (houses, barns, etc.), information about location, owners and tenants of these structures are acquired via web and mobile applications. The owners of heavy and moderately damaged structures are considered to be victims of disaster (possible beneficiary candidates). This information provides input data to the entitlement and beneficiary management module. This information is also used in permanent settlement construction, housing and rent aids (Fig. 13).

3.2.2 Resettlement Site Selection Sub Module

For the victims of disasters, it is the module where the safe residential areas are searched, identified and selected for settlement planning and construction. In the determination of new settlement areas, General Directorate of State Hydraulic Works, General Directorate of Forestry, institutional remarks are collected. The settlement zoning plans, cadastral plans and land registries of the possible settlement areas to be selected are evaluated. If there is no zoning plan in new settlement
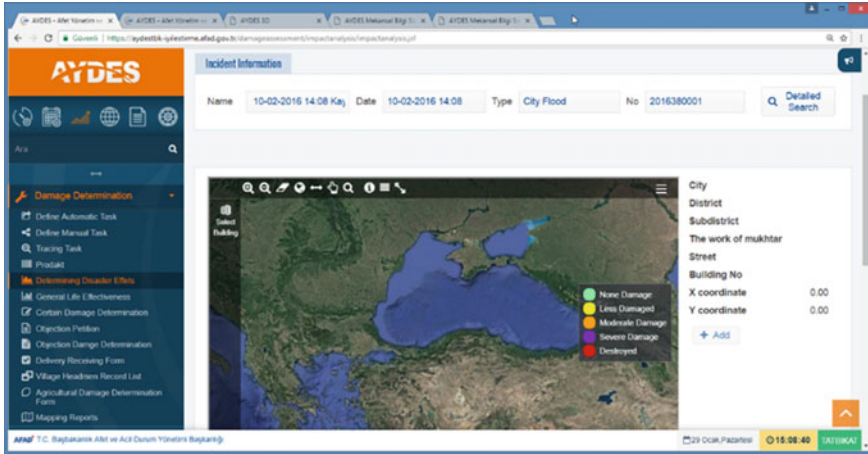
Fig. 13 AYDES-RIS damage determination sub module

areas, zoning plans will be created by taking geological and geotechnical survey studies after mapping the current situation. Site selection report is prepared after technical studies.

3.2.3 Geological Hazard Survey Sub Module

With this module, the ground and building conditions are analyzed together after identifying any disaster events. After the event is defined, all insensitivities in the field caused by landslide, avalanche, flood, earthquake, fire etc. are mapped and areas affected by disaster are marked on the map using web and mobile applications. The location, the owner and the tenant information of the buildings in the areas affected by disaster are collected via the interfaces of this module. This information provides input data to the entitlement and debit module. This information also provides input data to the entitlement and debit module. This information is also used in housing, housing and rent aids.

3.2.4 Investment Program Sub Module

The entitlements to be placed in the new settlement areas where the site selection report is prepared are taken to the investment program list. This list also includes methods of housing construction (e.g. household assistance, tender, TOKI, etc.). Allocation is requested from the Ministry of Development for the beneficiaries of the investment program. It is the module of the works done up to the delivery of the houses made by the above mentioned housing construction methods. In addition, this module is used to list the excess land and houses.

3.2.5 National Emergency Assistance and Tracking Sub Module

Using this module, in accordance with Law No. 4123 on the Execution of Services Related to Natural Disasters Due to Natural Disasters, carrying out are the services that will provide the normal life for the areas affected by the disaster and the requests made in the Governor's offices for the removal of damage and destruction were followed.

3.2.6 Beneficiary Sub Module

With this module, Beneficiary Management commission, created by AFAD's provincial directorate, evaluates the beneficiary management of the disaster victims using the outputs of damage assessment and geological hazard survey modules. After evaluation, they prepare and approve the name lists of the beneficiary disaster victims. Disaster victims who are deemed as beneficiary shall be debited for no interest for a period of 20 years. With this module, repayment of debits is also followed.

3.3 Spatial Information System

Spatial Information System (SIS) is the supplementary part of the whole work to build a sustainable disaster management and decision support system by using geographical information system (GIS) technologies. Spatial data—which can be used in disaster and emergency management—were collected in physical environment or by web services from different governmental or non-governmental agencies to create a geodatabase as part of SIS. It is designed for accurate and quick decision making by spatial queries and analysis with existing and contemporaneously added data pre-disaster, during disaster and post-disaster activities. Subcomponents and menus of the application provide to update, edit and query of the spatial data as real time and allow to view and report the final results. The *Common Operation Picture* (COP), which has basically the same design and common features as the SIS (MBS in Turkish), is an additional component that displays and reports on work and results, especially with respect to the stage of the response to the disaster. Under COP, real-time information from AYDES components is planned to be generated instantaneously by means of this information.

3.3.1 Layers of Geographic Database that Have Been Created Through SIS

Inspire Layers:
(1) Land use cover, (2) Buildings, (3) Geographical grid systems and map indexes, (4) Geographical structures, (5) Energy resources, (6) Hydrography,

(7) Administrative units, settlements, addresses, (8) Geology, (9) Public services, (10) Protected private areas, (11) Population distribution and demography, (12) Agriculture, (13) Transportation Networks, (14) Industrial areas, (15) Topography.

Facility Layers:
(1) Finance, shopping and trade, (2) Sheltering and accommodation, (3) Educational institutions, (4) Critical substructure and superstructure, (5) Public institutions, (6) Health facilities, (7) Industrial and manufactural points, (8) Non-governmental organizations, (9) Socio-cultural facilities, (10) Historical and touristic structures, (11) Telecommunication, (12) Transportation facilities, (13) Food, drink and amusement places, (14) Green zones.

AFAD Layers:

Disaster Prevention and Response Sub Layers:
(1) AFAD and AADYM units, (2) Sheltering, (3) Food production units and facilities, (4) Distribution points, (5) Burial service areas, (6) Warehouses, (7) Debris removal, (8) Food, agricultural and farming, (9) Security and traffic, (10) Communication, (11) Service groups and logistic, (12) Health cares, (13) Technical support and supply, (14) Assembly areas, (15) Warn and alarm points, (16) Fires, (17) Routes to AFAD logistic warehouses of city centers.

Disaster Inventory–Danger—Risk Zones Sub Layers:
(1) Earthquake (2) Faults, (3) Landslides, (4) Rock fall, (5) Floods, (6) Risk Maps, (7) Technological disasters, (8) All disaster inventories (point), (9) Avalanches.

3.3.2   Main Components of the SIS Sublayer

- *Map Tools*: with map tools you can use functions such as get info, zoom in, zoom out, clear map, layer control, active layer, go to coordinate, preview window, scale tool, coordinate system selection tool.
- *Address Search Bar*: provides an option to search for an address or facility on the map.
- *Search and Query Menu*: provides an option to make an inquiry from disaster preparation data, structural data, inspire data and also from the events that occurred.
- *Geographic Analysis Menu*: makes an inquiry by creating a buffer zone for disaster preparation and some analysis processes such as proximity analysis, linear proximity analysis, buffer zone analysis and analysis by drawing areas.
- *Geographical Data Entry Menu*: provides an option to entry geographical data to layer of buildings, disaster inventory risk zones, also primary damage and primary influence area risk analyses.
- *Geographical Tool Menu*: provides an option to load and view kml, shp files.

- *Services Menus*: provides an option to reach services such as YAHOO meteorology, EUMSTAT, KGM, YUVAM, TRAFFIC WFS, AFKEN tent areas and AFAD logistic warehouses.
- *Earthquakes Menu*: provides an option to view all earthquake information on the map which have been supplied by Earthquake Department of AFAD.
- *Layers Menu:* provides an option to reach layers of Ortho-photo, vector tile, Google earth, Bing aerial, TURKSAT Satellite, World imagery, Landsat 2000.
- *Event Dependent Layer Menus*: provides an option to matchup event dependent layers and to view layers that matchup depending on events.
- *Layer Management Tools*: provide an option to view the metadata of layers.
- *Events Menu*: provides an option to search for disaster and emergency situations and locate them on map.
- *Service Groups Menu*: provides an option to view the special info of data that have been entered by command module of COP module.
- *Planning Tools Menu*: provides an option to make geographical planning on map and record it.
- *Route Tools*: provide an option to determine and draw the route between two locations by selecting start and finish points on the map.
- *Preliminary Impact Analysis/Preliminary Damage Locating Menus*: provide an option to view the estimated distribution of earthquake damage made by AFAD-RED, the remote sensing analysis results, the analysis of damaged buildings.

3.3.3 Main Components of the SIS Sublayer

- REGISTRY and CADASTER (integrates spatial land/parcels data to SIS by using title parcels services and land registry)
- KGM (displays the roads that are closed or under construction with the help of web services supplied by the General Directorate of Roads)
- GEZGIN (connects to services that shows metadata and coverage service Ares of RASAT satellite images)
- TRAFIK WFS (integrates up-to-date data of traffic situation, roads, real-time speeds and speed limits in Turkey that have been acquired by Başarsoft web services by using 4 different colors according to the traffic density)
- NVI-UAVT (connects National Address Database (UAVT) to SIS to locate the address of the user)
- METEOROLOJI (integrates weather forecast acquired by meteorology to SIS)
- YAHOO (integrates YAHOO weather forecasts data to SIS)
- EUMETSAT (integrates EUMETSAAT weather forecasts data to SIS)
- GOOGLE (integrates Google satellite, Google Street, Google physical data)
- BING (integrates BING satellite maps)
- TÜRKSAT (integrates TURKSATMAPS satellite, physical, land data)

- VECTOR TILE, VECTOR LAYERS (integrates vector layers and tiles to SIS.)
- ORTHO-PHOTO (integrates raster data that have been acquired by General Directorate of Registry and Cadaster (TKGM) in 2009, 2010, 2011, 2011, 2013)
- LANDSAT 2000 (integrates Landsat satellite images)
- SETTLEMENT SUITABILITY SERVICE (integrates the data of settlement sustainability areas that acquired by settlement sustainability service which were created by settlement sustainability (YUVAM) project)
- DISASTER AFFECTED ZONES SERVICE (integrates the data of disaster affected zones that have created by settlement sustainability (YUVAM) project)
- AFKEN TENT POINTS (integrates the data of tent points that acquired by AFKEN web application)
- CONTAINER TRACKING (integrates the data of container tracking that have been acquired by logistic warehouse systems applications)
- AFAD LOGOSTIC WAREHOUSES (integrates the spatial data of AFAD logistic warehouse layers with their attributes).

Although SIS and COP menus look alike, they differ in purpose of use and user profiles. COP is a supplementary component for disaster response. Disaster and emergency events that have happened in our country can be viewed by these component. Both components have analysis and query modules. Flood domains, real-time estimations of seismic intensities of earthquakes that happened, inter-pretation, analyses and queries can be made by these components. Screenshots of components of SIS and COP are shown in Figs. 14 and 15.

3.4 Mobile Applications

After the disaster, damage detection data related to the disaster area and disaster event inventory (landslide, rock fall, avalanche) data can be gathered by mobile applications quickly and efficiently as well as offline while offline data can be transferred to AYDES as soon as the Internet connection is available. The mobile applications developed in this context are as follows.

3.4.1 Disaster Event Inventory Data Collection Mobile Application

Spatial data related to disaster events such as landslide, rock fall and avalanche (landslide area, rock fall source-spread area, falling blocks, avalanche areas etc.) and descriptive data (feature attribute values) can be collected on-line and off-line by this mobile application. The roads, points of interest (parks, public institutions, shopping centers, industrial areas, etc.), topographic maps, geological maps and satellite images (in on-line mode) as well as provincial, district and neighborhood border data can be used as base layers. The collected data can be displayed in the
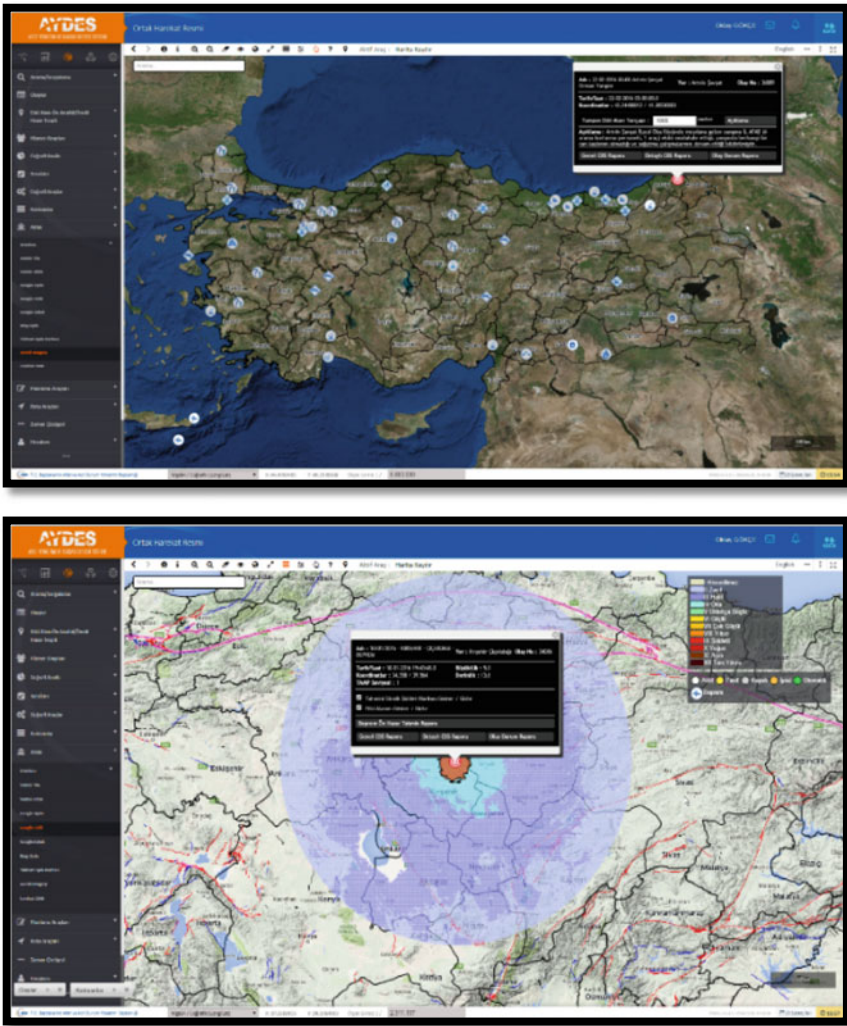
Fig. 14 SIS and COP components (1) of AYDES

main component of the SIS in real time. Figure 16 shows screenshots of this Disaster Event Inventory Data Collection Mobile Application.

3.4.2 Damage Assessment Mobile Application

Spatial On-line and off-line, geo-located damage detection data can be collected using damage detection forms in different detail. Unauthorized transactions are
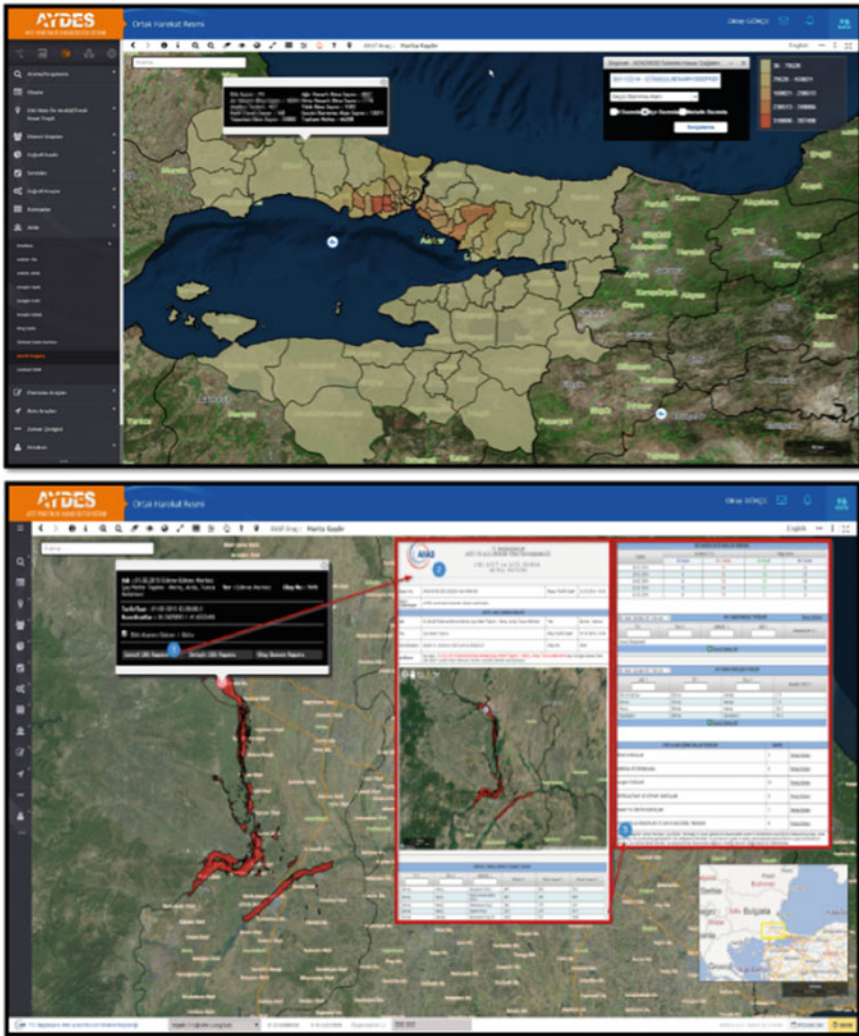
Fig. 15 SIS and COP components (2) of AYDES

prevented by interrogating the personnel information to be assigned to the damage assessment studies during the data entry. In practice, it can be used as a base by taking the roads, important points (parks, public institutions, shopping centers, etc.), topographic maps and satellite images—on-line—on the mobile device memory as well as provincial, district and neighborhood data. The collected data can be displayed in real-time on the relevant screens of SIS and Recovery components.
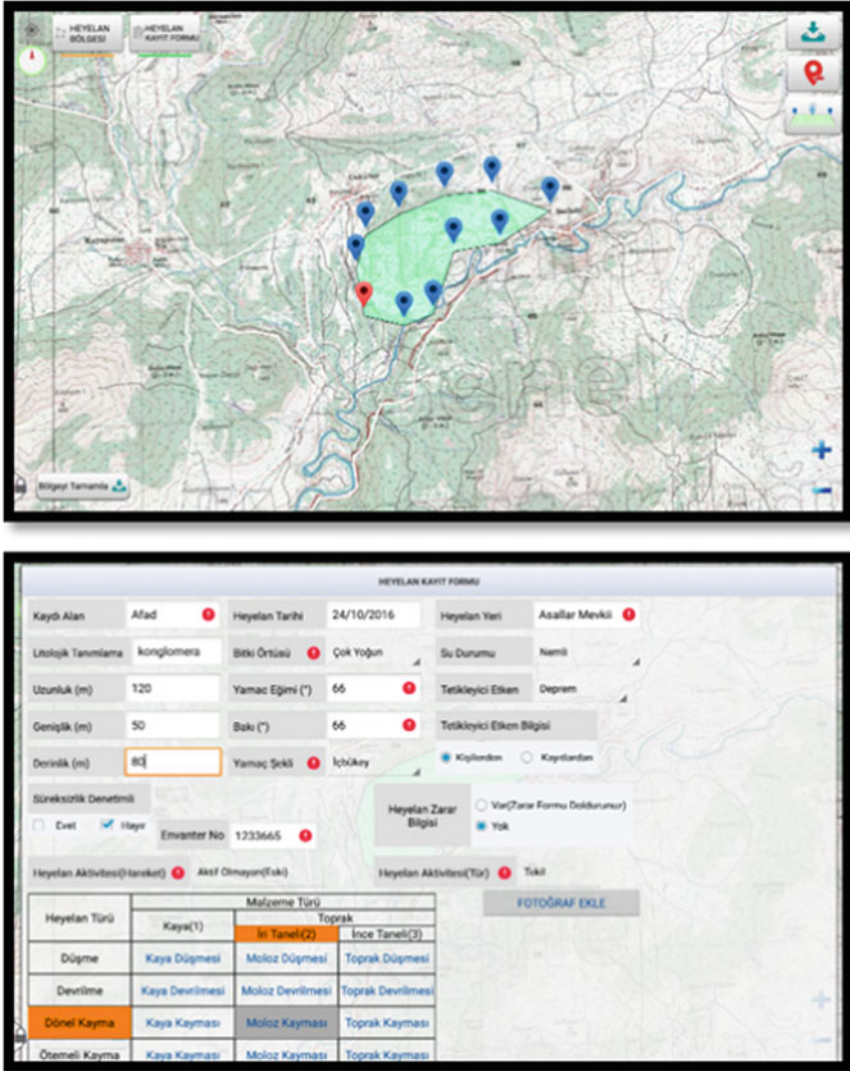
Fig. 16 Disaster event inventory data collection mobile application

3.4.3 Geological Hazard Survey Reports Mobile Application

Spatial data (survey area, landslide area, area exposed to hazard etc.) determined in geological hazard survey reports and related descriptive data (disaster victim list, disaster situation etc.) will be collected on-line and off-line. The collected data can be displayed on the relevant screens of the SIS and Recovery components in real time (to be developed).

3.4.4   Resettlement Site Selection Mobile Application

This software will allow the collection of spatial data (parcel, area, etc. determined for site selection) and relevant descriptive data (feature attribute values) specified in the site selection protocols and works. The collected data can be displayed on the relevant screens of the SIS and Recovery components in real time (to be developed).

4   Image Processing and Analysis Tools of AYDES

Remote sensing technology provides an important data source that can be used in disaster management. A lot and various data and evaluations related with disaster event inventory, vulnerable assets, hazard-risk, disaster prone areas, and damage assessment results etc. are needed in context of disaster management and decision support systems. For this purpose, AYDES-RS software and AYDES-CS platform have been developed to use in processing and evaluating the images provided by remote sensing (space/aerial) technology for several disaster managements related analyses in terms of Disaster and Emergency Management Authority (AFAD)'s needs. Evaluation results are integrated directly to AYDES and shared publicly by AFAD web site.

4.1   AYDES-RS (Remote Sensing) Software

AYDES-RS (AYDES-UZAL in Turkish) is a desktop software that process and analyze synthetic aperture radar (SAR) electro-optic (EO) satellite images/aerial photos. It is developed in Java by using ESA's open source libraries and contains specific applications for identifying preliminary affected area and hazard/damage assessment caused by disasters like earthquake, flood and forest fire. Different applications and algorithms also provide change detection, supervised/unsupervised classification, object based image analysis and fabric analysis. The primary aim of AYDES-RS is to offer an integrated software solution of visualizing, processing, analyzing remote sensed data, presenting and exporting results into disaster management and decision support systems (Fig. 17).

4.2   AYDES-CS (Crowd-Sourcing) Platform

AYDES-CS (AYDES-KITLEKAYNAK in Turkish) is a web based crowd—sourcing platform. In order to eliminate the deficiency of automatic image processing algorithms or to confirm their results, manual assessment of post-disaster
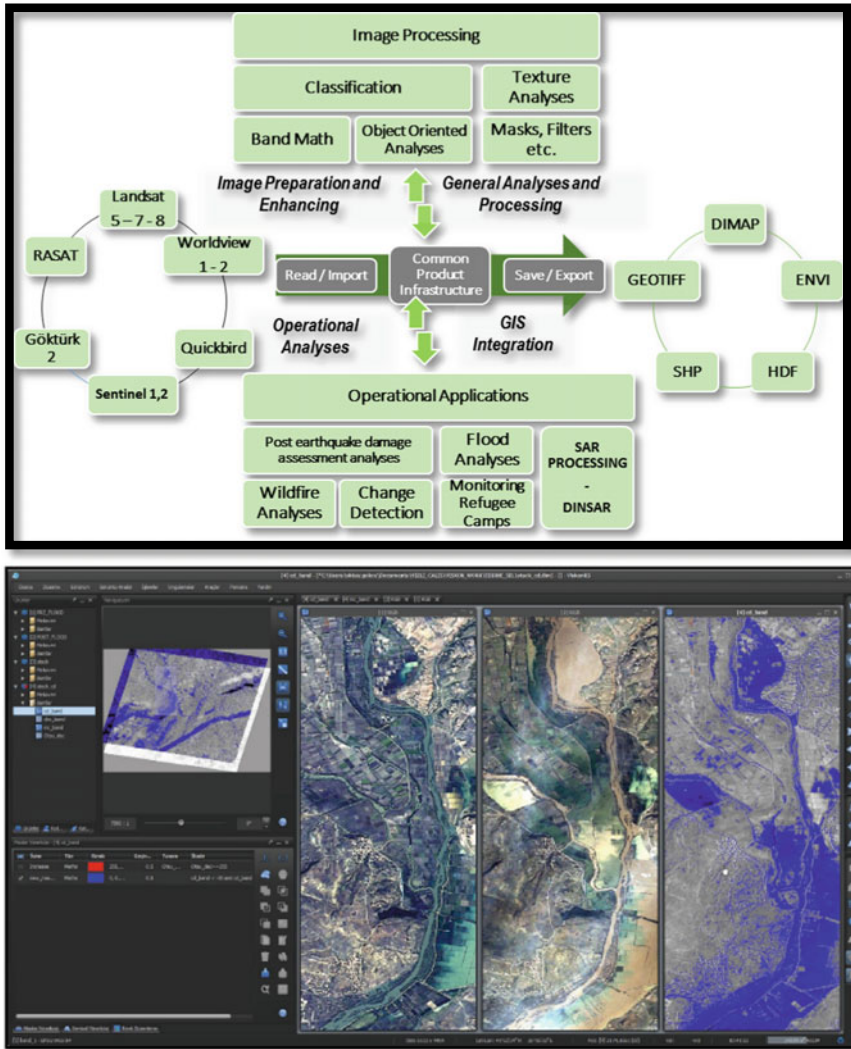
Fig. 17 Main functions and simple analyses with AYDES-RS

images is required. For this purpose, post disaster images are divided into little pieces, tiled and then sent to previously identified users called as crowd through the web. They fulfil their duties by examining the images and marking on them according to type of operation. Same image tile can be sent more than one user. Consequently, the system evaluates the markings of users and produce a final report automatically by using statistical algorithms. The results about the number and location of damaged buildings, location of closed roads, wrecks and landslide flood prone areas etc. are available in minutes (Fig. 18).
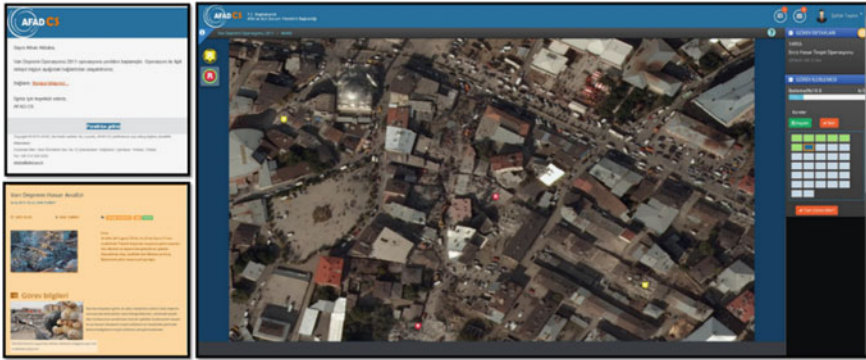
Fig. 18 AYDES-CS platform

The crowd of experts or volunteers are informed that they are being tasked with a manual disaster assessment by SMS or e-mail sent automatically to them. They enter the system via their computers or mobile devices. For example, the buildings destroyed after an earthquake are quickly marked by the crowd. Each user is given a limited size and number of satellite/aerial image tiles. The same image tile can be evaluated by more than one user. Once users complete the marking, the system
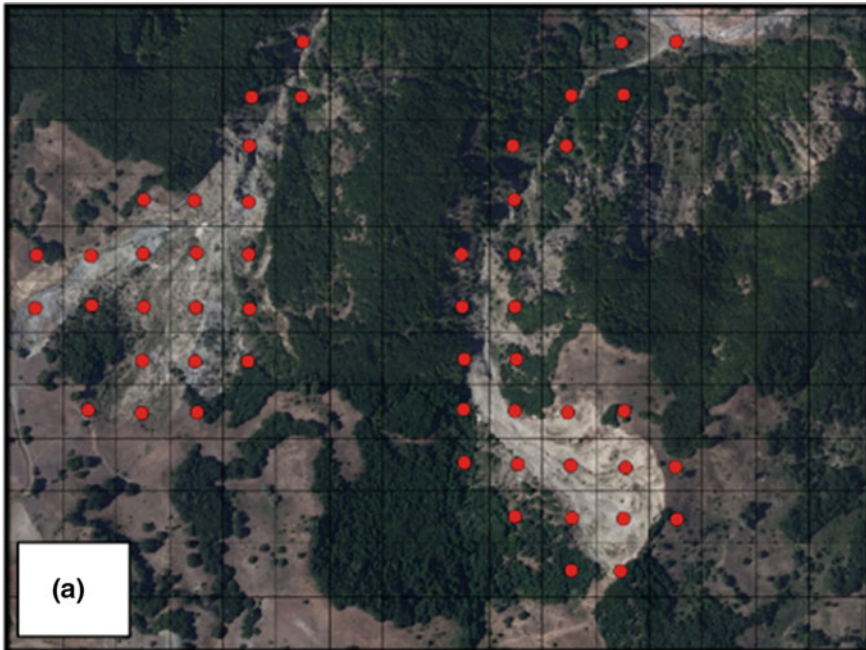
Fig. 19 Digitizing the landslide areas at AYDES-CS platform

Fig. 20 Marking buildings damaged by earthquake at AYDES-CS platform
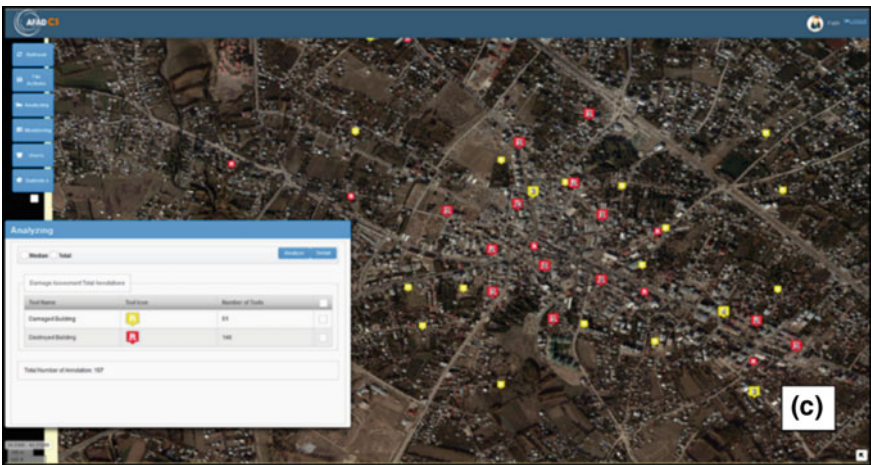
Fig. 21 Integration of AYDES-CS results into AYDES

evaluates the markings with its own algorithms and provides optimal results. When the results are obtained, the user's assessment scores from previous disaster events, stable markings made by different users in the same image tile, etc. are taken into consideration. Figures 19 and 20 show the markings to identify landslide inventory collection (using image tiles with a size 50 × 50 m) and the inventory of buildings damaged by post-disaster floods, respectively whereas Fig. 21 shows their results integrated to AYDES.

AYDES-RS and AYDES_CS have been developed with the cooperation of AFAD and TUBITAK (The Scientific and Technological Research Council of Turkey).

5 Discussion

We have developed an integrated infrastructure with desktop tools, a web platform and mobile applications to support collaboration efforts for all types and phases of disaster in any part of the world and for everybody (i.e. an all-in-one solution for IT based disaster management). Using the web-GIS based technology, we built AYDES web platform to combine vector and raster geographical datasets as the base data layers; using Java technology, we developed desktop tools AYDES-RS and AYDES-Crowd Sourcing to extract information from satellite images for AYDES web platform; and using GNSS & GSM and mobile programming technologies, we developed mobile applications to feed AYDES web platform with up-to-date disaster information and vice versa. Serving AYDES web platform and AYDES-Crowd Sourcing as an "Infrastructure as a service (IaaS)" and serving AYDES-RS as a "Software as a Service (SaaS)" are among our future plans. As compared with the disaster systems/portals/software tools discussed in the introduction section, AYDES is an all-in-one system whereas the others are not or lack of some components of AYDES.

6 Conclusion

Through the Disaster Management and Decision Support System (AYDES) project, efforts are being made to establish and sustain an information infrastructure and decision support system centered management model required for the effective management of disaster and emergency management processes. AYDES, including desktop, mobile and web-based applications based on GIS and RS technologies, is an integrated platform connected to many internal and external systems.

This platform, especially Turkey Disaster Response Plan coverage prepared in accordance with AFAD, relevant Ministries, designed to be used by private organizations and provincial organizations, processes active, care is taken to be an

Before Disaster	Disaster Event	After Disaster
• Mapping the areas at disaster risk • Mapping the entities at disaster risk	• Where? • How? • How big? • Haw many buildings?	• Image Acquisition & Analysis • Effected Area • Damaged Structures

Fig. 22 The procedure at AYDES

integrated framework that allows quick execution. Figure 22 summarizes the procedure at AYDES which is trying to answer briefly about any disaster event.

As a result; within the context of disaster management and decision support system, AYDES is an integrated Geospatial IT based platform comprising procedures, human resources, data, hardware and software tools which provide accurate and current disaster and emergency data and information, various reports, statistics, task monitoring, queries and analysis, etc. at all stages before and after a disaster. As for the future development of AYDES, we plan to update existing modules and add new functionalities according to the feedbacks of the users.

References

DAP (2017) Disaster Alert Platform. https://disasteralert.pdc.org/disasteralert/. Accessed 29 Oct 2017

DIMS (2017) Nepal Geoportal. http://geoapps.icimod.org/dims/. Accessed 27 Dec 2017

FEMA (2018) Hazus Software. https://msc.fema.gov/portal/resources/hazus. Accessed 18 March 2018

GAR-ATLAS (2018) Risk Data Platform of UNISDR. https://risk.preventionweb.net/capraviewer. Accessed 23 Apr 2018

GDACS (2018) Global Disaster Alert and Coordination System. https://vosocc.unocha.org/VODiscussions.aspx#t5546. Accessed 19 May 2018

ICIMOD (2018) The International Centre for Integrated Mountain Development. http://geoapps.icimod.org/dims/. Accessed 29 May 2018

IDRN (2018) Indian Disaster Resources Network. http://www.idrn.gov.in/. Accessed 30 Aug 2018

NDEM (2018) National Database for Emergency Management (NDEM Version 2.0) Portal of Indian Space Research Organization. http://bhuvan.nrsc.gov.in/governance/bhuvandisaster/. Accessed 13 Oct 2018

NDEM User Manual (2017) National Database for Emergency Management (NDEM Version 2.0) System's User Manual. http://bhuvan-noeda.nrsc.gov.in/disaster/disaster/get/ndem_vpn_user_manual.pdf. Accessed 29 Oct 2017

NRSC (2017) National Remote Sensing Center of Indian Space Research Organization. http://
    bhuvan.nrsc.gov.in/, Accessed 27 Dec 2017
RELIEFWEB (2018) Reliefweb of UN Office for the Coordination of Humanitarian
    Affairs (OCHA), https://reliefweb.int/disasters. Accessed 18 March 2018
SAHANA-EDEN (2018) Open Source Disaster Management Solutions of Sahana Foundation.
    https://sahanafoundation.org/eden/. 23 Apr 2018
SAHANA-EDEN Demo (2018) Sahana-Eden Remote Demo Server. http://demo.sahanafoundation.
    org/eden/gis/index. Accessed 19 May 2018
UNOSAT (2018) UNOSAT LIVE Map of UNITAR (United Nations Institute for Training and
    Research) Operational Satellite Application Programme. https://unosat.maps.arcgis.com/apps/
    webappviewer/index.html?id=3356c7f1659a4282a08fa188208036d7. Accessed 29 May 2018
USHAHIDI Platform (2018) Source Code of USHAHIDI platform. https://github.com/ushahidi/
    Ushahidi_Web/. Accessed 30 Aug 2018
USHAHIDI Software (2018) https://www.ushahidi.com/. Accessed 13 Oct 2018

Detecting Influenza Outbreaks Based on Spatiotemporal Information from Urban Systems

Lars Ole Grottenberg, Ove Njå, Erlend Tøssebro, Geir Sverre Braut, Karoline Bragstad and Gry Marysol Grøneng

Abstract This paper explores the application of real-time spatial information from urban transport systems to understand the outbreak, severity and spread of seasonal and pandemic influenza outbreaks from a spatiotemporal perspective. We believe that combining travel data with epidemiological data is the first step to develop a tool to predict future epidemics and better understand the effects that these outbreaks have on societal functions over time. Real-time data-streams provide a powerful, yet underutilised tool when it comes to monitoring and detecting changes to the daily behaviour of inhabitants. Historical datasets from public transport and road traffic serves as an initial indication of whether changes in daily transport patterns corresponds to seasonal influenza data. It is expected that changes in daily transportation habits corresponds to swings in daily and weekly influenza activity and that these differences can be measured through geostatistical analysis. Conceptually one could be able to monitor changes in human behaviour and activity in nearly true time by using indicators derived from outside the clinical

L. O. Grottenberg (✉) · O. Njå
Department of Safety, Economics and Planning, University of Stavanger, Stavanger, Norway
e-mail: lars.grottenberg@uis.no

O. Njå
e-mail: ove.njaa@uis.no

E. Tøssebro
Department of Electrical Engineering and Computer Science, University of Stavanger, Stavanger, Norway
e-mail: erlend.tossebro@uis.no

G. S. Braut
Stavanger University Hospital, Stavanger, Norway
e-mail: geir.sverre.braut@sus.no

K. Bragstad
Department of Influenza, Norwegian Institute of Public Health, Oslo, Norway
e-mail: karoline.bragstad@fhi.no

G. M. Grøneng
Department of Infectious Diseases Epidemiology and Modelling,
Norwegian Institute of Public Health, Oslo, Norway
e-mail: grymarysol.groneng@fhi.no

health services. This type of more up-to-date and geographically precise information could contribute to earlier detection of influenza outbreaks and serve as background for implementing tailor-made emergency response measures over the course of the outbreaks.

1 Introduction

Influenza is one of few diseases that have a major impact on public health and cause regular epidemics, re-occurring every winter in the Northern hemisphere. Influenza is also the only disease that have caused several pandemics. An estimate based on the 1998–2006 period in Norway show that the direct cost of seasonal influenza totalled US$22 million annually. Loss of working days resulting in an estimated productivity loss of US$231 million. Self-reported sick leave accounted for approximately one-third of the total indirect cost. During a pandemic, the total cost could rise to over US$800 million (Xue et al. 2010). Worldwide, influenza outbreaks carry an enormous societal cost in human and monetary terms, and are one of the few crises with a global reach and sub-yearly temporal frequencies. The seasonal variants see significant loss of life, with the Norwegian Institute for Public Health (NIPH) estimating the 2016/2017 epidemic to have caused an excess of 1700 deaths (NIPH 2017c). This is mirrored at the global scale, with the World Health Organization (WHO) estimating 5–15% of the world's population being infected with the seasonal influenza each year (WHO 2013), resulting in 300,000 to 650,000 deaths per year (Iuliano et al. 2017). The Spanish flu in 1918–1919 presents a dire example of the human costs of major influenza outbreaks, with 20–50 million deaths, equal to 3–5% of the world's population at the time (Guan et al. 2010). While recent outbreaks have not seen the same impact, the risk for severe epidemic or pandemic influenza outbreaks remain, pandemic influenza is rated as one of the top 10 threats to global health in 2018 by the WHO.

The societal ability to respond to major influenza outbreaks is heavily dependent on successful interactions between a wide series of participants, components, and processes (Wolf 2017). Essential components are early detection and monitoring of the influenza outbreak, reporting to responsible health authorities and to the general public, public health action by increased awareness, proper vaccination and general public personal protective measures such as improved personal hygiene and increased social distancing (i.e. avoiding mass gatherings and public transporting). Accomplishing this requires a major emphasis on having robust technological and organisational tools and methods available to manage information flow and decision support between stakeholders at all levels of the hierarchy (WHO 2018). Urban societies present a series of complex and dynamic systems, with many interacting subsystems and processes that change fluidly depending on time of day, societal trends, and a host of other influencing factors. Efficient preventive measures and management procedures is reliant on contextual knowledge of societal functions, as spread of influenza within a population is strongly driven by human social patterns

at the individual and societal levels. Surveillance systems are used to acquire and maintain situational awareness of ongoing and emerging trends which is fundamental for all stages of the influenza management process.

The emergence of urban information initiatives has vastly increased the access to data streams that measure the use and integrity of critical societal systems. Real-time use metrics is increasingly feasible and integrated across a variety of societal systems. Transportation systems, critical infrastructure and distribution networks collects statistics in near real-time, allowing for a continuous understanding of how these systems are used in spatial and temporal contexts within an urban area. Conceptually one could be able to monitor changes in human behaviour and activity in close to real-time by using indicators derived from outside the clinical health services. Combining the spatial components of existing data streams with GIS-based data from additional sources adds to the spatial and temporal quality of produced information, and can be a significant addition to the public health surveillance and early detection of disease by geographic understanding of the evolving risk picture.

This article describes the design of an initiative that seeks to examine the viability of monitoring real-time data from urban systems to improve the public health surveillance by earlier detection and monitoring of influenza outbreaks in urban societies. This type of more up-to-date and geographically precise information could be a helping tool in the day-to-day planning and management of the public health services related to outbreaks. The earlier detection and a better geographic overview of areas with influenza spread could make public health action more efficient by for instance relocation of staffing and scarce resources related to medical equipment as e.g. respirators and equipment for extracorporeal membrane oxygenation.

1.1 Impact of the Seasonal and Pandemic Influenza

The Pandemic Influenza Severity Assessment (PISA) initiative (WHO 2017) describes the following key metrics to assess influenza severity: *Transmissibility, Seriousness of disease, Impact*. These metrics describes the spread of influenza within a population, the virus effect on the individual person, as well as the effect of the epidemic and pandemic on health-care services and societal systems. It can be used as a tool for global and national risk assessment of influenza outbreaks. Recent outbreaks provide an avenue to understand the impact and societal effects of influenza outbreaks. The 2009 A(H1N1) pandemic was notable as the first pandemic since the Hong Kong influenza in 1968. The saw the mobilisation of major cross-sectoral epidemic efforts (WHO 2013). The global mortality has been estimated between 201,200 (Simonsen et al. 2013), to 284,000 (Dawood et al. 2012). In Norway, the 2016–2017 seasonal influenza outbreak was estimated to have caused 1,700 deaths (NIPH 2017c).

The Norwegian Directorate for Civil Protection (DSB) claims the effects of a severe influenza outbreak to be severe, implying a large to very large impact on the Norwegian society (DSB 2015). The National Risk Analysis (NRA) from the quantifies the costs of a major pandemic in Norway, based on the influenza metrics developed by the NIPH and the WHO. The likelihood is estimated to be high, based on historical pandemics such as the 1918 Spanish influenza, the 1957 Asian influenza, the 1968 Hong Kong influenza, and the 2009 Swine influenza (Guan et al. 2010). The direct impact on life and health is estimated to 1.2 million people infected (25% of the Norwegian population), with a mortality rate of 0.5% (6,125), and 3% (35,000) requiring hospitalization. The socioeconomic effects primarily stem from disruptions to production, with large numbers of the work force out at any given time over the course of the outbreak. The knock-on effect caused by the disruption to societal functions and health services in the event of a pandemic outbreak is expected to lead to an increase in mortality, resulting in an overall death toll of around 8,000 persons.

The NRA case is exploratory, and has as such not explored the societal effects of a pandemic outbreak in detail. The limited scope of the assessments must be taken into consideration, and we believe that further analyses should be initiated. The epidemic and pandemic risk assessments are limited by a lack of mechanisms to acquire updated information on societal functions and integrity over the course of an outbreak. Without a way to assess the impact of influenza outbreaks on society, these calculations will remain coarse. Our proposed framework and research methodology must be seen as a contribution to better understanding of factors and mechanisms in influenza patterns. Hence, it would present a way to map and monitor the societal effects of influenza outbreaks at earlier stages, where knowledge is scarce. We think this could significantly improve the quality of information used in risk assessments of epidemic and pandemic influenza. Mapping the effects of societal systems over time will provide valuable information on how societal behaviour changes during outbreaks, and may improve the understanding of the societal impact of influenza outbreaks, and to give us quantifiable indicators of the societal cost of these outbreaks.

1.2 Influenza Management and the Norwegian Health Sector

The 2014 national pandemic influenza preparedness plan (Ministry of Health and Care Services 2014) outlines the roles and responsibilities of the various components of the Norwegian health management structure, as well as the contributions of auxiliary parts of the national emergency management domain. A recent examination of the risk and vulnerability within the Norwegian health sector (Norwegian Directorate of Health 2017) outlines the main challenges facing the public health emergency management domain in Norway. Seasonal and pandemic influenza are

the main concerns, with major accidents and disasters as the secondary and tertiary focus areas. An emphasis is placed on issues relating to information security and systems integrity, with comparatively little focus placed on management of information. Issues arising from the lack of clear routines and responsibilities relating to flow of information in major health-related disasters is only briefly mentioned.

One of the main future challenges of the Norwegian health sector is to manage the impact of influenza outbreaks, both of seasonal and non-seasonal variants. A influenza pandemic is stated to be one of the main societal threats facing the Norwegian society (DSB 2015), while the seasonal influenza each year affects the entire society during the winter months. Rapid response to influenza outbreaks requires a major mobilisation of societal resources and depends on the activation of large parts of the national and international disease management structures. The NIPH publishes annual risk assessments of seasonal influenza at the beginning of each influenza season (NIPH 2017b). NIPH also produce weekly influenza reports during the Norwegian influenza season (NIPH 2017d), as well as end-of-season summaries (Bragstad et al. 2018; Norwegian Institute of Public Health 2017b) and reports to guide WHO in vaccine composition meetings (National Influenza Centre 2018). To manage seasonal influenza outbreaks, virologists, public health officials and epidemiologists use information compiled from the national surveillance system for influenza. The Norwegian Syndromic Surveillance System (NorSySS) is one of the data sources used in this system. NorSySS collects diagnosis data from general practitioners (GPs) and out-of-hours primary care facilities. A network of GPs and national microbiological laboratories contribute to the surveillance program with clinical samples and reports weekly lab confirmed influenza cases with denominator. In addition, surveillance of severe influenza is carried out at hospitals and intensive care facilities.

2 Connecting Influenza to Societal Behaviour

Spread of infections within a societal system cannot be assumed to be static or uniform but is rather a continuously changing process based on local factors, such as time of day, occupation, access to services and information patterns. The dynamic nature of these types of events makes rapid intelligence capabilities a necessity, as situational awareness is highly dependent on information with a high temporal resolution (Yan et al. 2017). Analyses based on a single point of time will rapidly be outdated, given the rapid changes in number of afflicted and their effect on the integrity and functions of the key societal systems (Gao et al. 2018; Wang and Ye 2018). Behavioral changes caused by influenza outbreaks have been observable in how people interact with societal functions, such as how they move throughout a cityscape or make use of urban medical services. Symptomatic individuals see an increase in societal contact patterns at home, while the average number and duration of social contacts drops drastically for travel, work and leisure while symptomatic (Van Kerckhove et al. 2013). Some measures of population

self-control can also be expected to be applied for asymptomatic individuals (Durham et al. 2012; Kleczkowski et al. 2015). Furthermore, the gradual spread of disease throughout a society acts as a catalyst for further behavioural changes, as people adapt their behaviour because of infection, or through adopting preventative measures to avoid illness (Aleman et al. 2009; Fierro and Liccardo 2013).

2.1 Influenza Spread Within an Urban System

To accurately model the spread of disease in urban areas, it is necessary to understand the structure and dynamics within these societies. Urban systems are composed through interactions of numerous networks and processes, which are driven by the behaviour of inhabitants at the individual and group levels (Batty 2009). Cities exists at various states of a dynamic scale, with subsystems that continuously react and adapt to ongoing events and trends (Batty 2012; Kitchin 2014). Sudden or gradual changes to inhabitant behaviour causes changes in the dynamic subsystems that builds up urban societies (Kitchin et al. 2015). Time of day, occupation, and access to services are strong influencing factors of human mobility patterns, while access to information, socioeconomic background and age are examples of factors that influence population behaviour. The complex and dynamic nature of these factors means that the spread of infections within a societal system cannot be assumed to be static or uniform but should rather be viewed as a continuously changing process based on a variety of local factors.

The spread of infectious diseases within an urban area can be predicted and modelled by the use of epidemiological tools. There have been multiple examinations that draw the link between human mobility and spread of diseases (Timpka et al. 2009), with development of complex models to account for urban and rural population patterns (Aleman et al. 2009; Poletto et al. 2013). The link between environment and health has been debated by multiple authors (Robertson 2017), demonstrating importance of modelling spatial environmental factors to accurately assess the spread of infectious diseases. Lal et al. (2018) presents a case for real-time surveillance of non-clinical indicators to map the societal factors that directs the spread of influenza. Yang et al. (2017) propose a framework to model the spatiotemporal characteristics of an outbreak, showcasing an approach to infer a dynamic social contact structure based on demographic data, heterogeneous surveillance data and epidemiological models. Yao et al. (2017) shows an application of multi-source geospatial data for modelling population distributions. Lewis and White (2017) demonstrates an approach that integrates multi-source surveillance information based on spatial components to model the incidence and prevalence rates of Chlamydia within a local population.

3   Influenza Surveillance

Public health surveillance is defined as "The ongoing systematic collection, analysis, interpretation and dissemination of data regarding a health-related event for use in public health action to reduce morbidity and mortality and to improve health" (German et al. 2001). The public health surveillance traditionally only included infectious diseases, but later also other public health issues were includes such as poisonings, disabilities, risk factors and health practices (Thacker and Berkelman 1988). One of the important public health surveillance functions is detection of outbreaks such as the start of the influenza season. This is identified by an increase of cases above the baseline value. Most European countries have an influenza surveillance system in place and are reporting to the infectious disease indicator-based surveillance system at the European level (TESSy) (ECDC 2014) or at WHO. The surveillance systems can include only one or several data sources, and as automated electronic tools are getting broadly available, the systems tend to be more complex. Traditionally, influenza surveillance has been accomplished through clinical indicator-based surveillance systems. These methods are based on collection and aggregation of patient diagnosis data of influenza-like illness (ILI) from physicians and laboratories. In addition, laboratory confirmed influenza reported from laboratories and through the sentinel system of GPs ensures all year-round reporting of influenza viruses and virus characterisation data. The high reliability, broad sampling and relatively high temporal accuracy provides a powerful dataset that describes the spread of influenza in the society with a time delay ranging from 0–28 days, depending on the characteristics of the national systems (Dailey et al. 2007).

The last decade has seen further development of the clinically-based surveillance approaches, often coupled with the development of other indicator-based approaches, where they make use of non-clinical indicators such as pharmaceutical sales, absenteeism reports and website access to trace the spread of influenza throughout a society. One of the focal points of this research has been to make use of web-based indicators, and a series of approaches has been developed to integrate the wealth of data found in online search patterns and social media behaviour. Google Flu Trends (Carneiro and Mylonakis 2009; Cook et al. 2011) offered an example of multi-indicator surveillance of online trends, and published influenza models in the 2008–2014 period through aggregation of time series of online search patterns relating to ILI tied to location (IP-address) (Vanja et al. 2012). While the efficiency of influenza detection based on social media monitoring varied from year to year relative to ILI-measurements (Lazer et al. 2014), they demonstrated the potential of monitoring social media feeds for the detection of key phrases. Santillana et al. (2015) demonstrates a fusion approach, which integrates real-time multi-indicator measurements based on an ensemble consisting of ILI-data, Google Trends data on search queries, Twitter trends, FluNearYou and Google Flu Trends weekly ILI estimates. The multi-indicator approach improves the accuracy of the data relative to analysis based on single indicators and provides a broader set of mechanisms to understand and predict the spread of influenza (Santillana et al. 2015; Timpka et al. 2009; Yan et al. 2017).

3.1 Norwegian Influenza Surveillance Structure

The NIPH carries the overall responsibility for monitoring influenza in Norway. The institute has a mandate to collect and manage information to monitor the occurrence and progress of influenza outbreaks (MSIS 2003), as well as to advice on public health matters resulting from effects of the seasonal influenza. The influenza monitoring system consists of six components (Table 1).

The virological part of the surveillance gathers information on laboratory confirmed influenza cases with in depth characterisation of circulating viruses all year round. The severity of the influenza season is assessed by hospital and ICU ward surveillance of laboratory confirmed cases as well as all-cause mortality numbers. In addition, the immunity of the population is assessed by yearly seroepidemiology studies. The NIPH generate weekly reports on influenza surveillance during the influenza season (week 40 to week 20). These reports provide the public, health care workers and decision-makers with an understanding of the week-by-week development of the influenza outbreak. The laboratory-confirmed influenza is most often reported one week after the sample was collected from the patient. The surveillance system covers nearly all laboratory confirmed cases diagnosed in Norway. The test activity in Norway is high, exceeding 190 000 samples tested during the 2017/18 season (Bragstad et al. 2018; Norwegian Institute of Public Health 2017c).

NorSySS (NIPH 2017a) receives data about the patient's age group, gender and the municipality of residence, the municipality where the consultation was performed, date and ICPC-2 diagnosis code (WICC 1998). The overall structure of

Table 1 The Norwegian surveillance system for influenza

System	Function
NorSySS	Indicator-based surveillance of influenza-like illness in primary health care
Hospital (all ward) surveillance	Laboratory-based surveillance of hospitalised influenza cases
ICU surveillance	ICU treated flu patients. Data collected by the Norwegian Intensive Care Registry (pilot project since 2016/17)
Virological surveillance	(1) Submission of data and samples from Norwegian laboratories testing for influenza. (2) Sentinel system, GP-based virological surveillance
Norwegian mortality monitoring system (NorMOMO)	Surveillance of weekly all-cause excess mortality
Seroepidemiological analysis	Annual survey of flu immunity in the population

Fig. 1 The Norwegian Syndromic Surveillance System (NIPH 2017a)
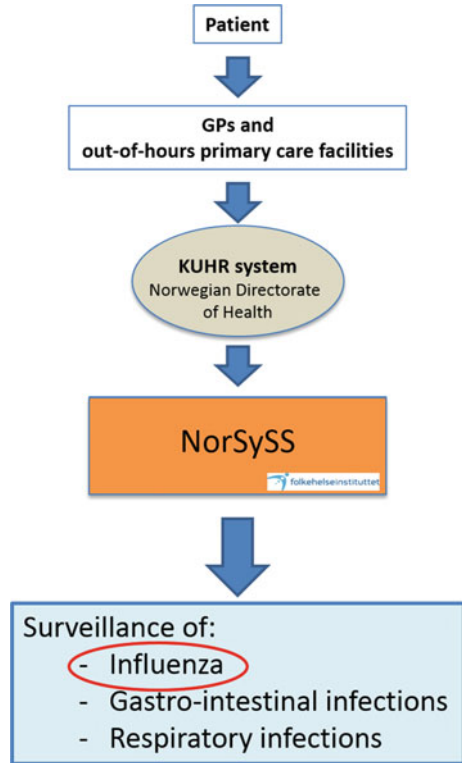
NorSySS and other component systems can be seen in Fig. 1. The datasets are compiled and anonymized through the KUHR system, before being passed on to NIPH and NorSySS for further analysis. ILI, ICPC-2 code R80, is used as an indicator for influenza activity. The NIPH compiles weekly reports on influenza surveillance during flu season (week 40 to week 20), where ILI % is used to describe the occurrence of flu and the intensity of the outbreak compared with the intensity of previous outbreaks. The epidemic threshold for seasonal influenza (ILI %) is based on the Moving Epidemic Method (MEM) (Vega et al. 2013). These reports provide the public, health care workers and decision-makers with an understanding of the week-by-week development of the outbreak. The data provided through the NorSySS has a high reliability, with data from nearly all GPs and out-of-hours primary care facilities in Norway and a firmly established routine and reporting methodology. The timeliness of the data is on the other hand lower, as most GPs accumulate the diagnosis data for a week or two before submitting to the KUHR system. This creates a situation where the datasets are not temporarily consistent, with some reports being submitted within a few days, while others lag by weeks. The lack of completeness is taken into account in the influenza surveillance by using the ratio of influenza consultations to the total number of consultations.

4 Building Societal Indicators for Detection of Influenza Patterns

To augment the existing influenza surveillance systems, it is of interest to establish a monitoring system that enables immediate detection of emerging trends and patterns of influenza outbreaks, whether epidemic or pandemic. One possible way to build this understanding is to use data produced within existing non-clinical surveillance systems. Data streams from infrastructures provides interesting data that combines a high spatiotemporal resolution with frequent update schedules. Public transport, power utilisation, distribution of goods, and data traffic can be used as indicators of the day-to-day and hour-to-hour functioning of the societal systems that make up urban societies. The hypothesised interdependencies between usage of critical infrastructures and increased influenza activity is illustrated in Figs. 2 and 3. These interdependencies should be measurable in historic datasets on use patterns and influenza activity, with increased influenza activity being reflected in a decrease in daily use of public transport networks in major cities.

Indicators from multiple systems can be collected and monitored, giving an understanding of the level of functionality and the ability of inhabitants to make use of these functions. Differences between expected and actual use of these systems based on spatial and temporal factors allows for a contextual understanding of the current societal state, and to understand emerging trends in relation to systems that are a critical part of the day-to-day urban life. Composite indicators based on these datastreams can be used to monitor the development of societal behaviour over
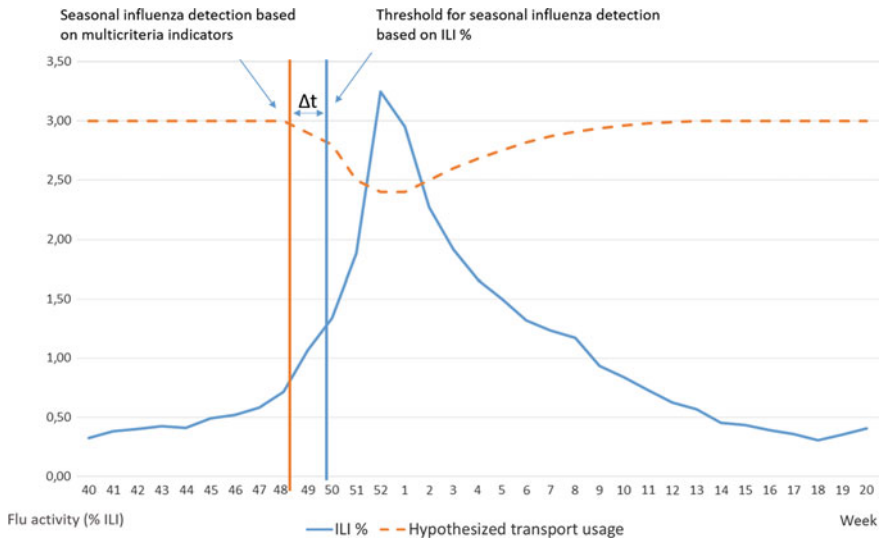
Fig. 2 Theoretical correlation between weekly public transport utilization and influenza activity (ILI %) in an urban population
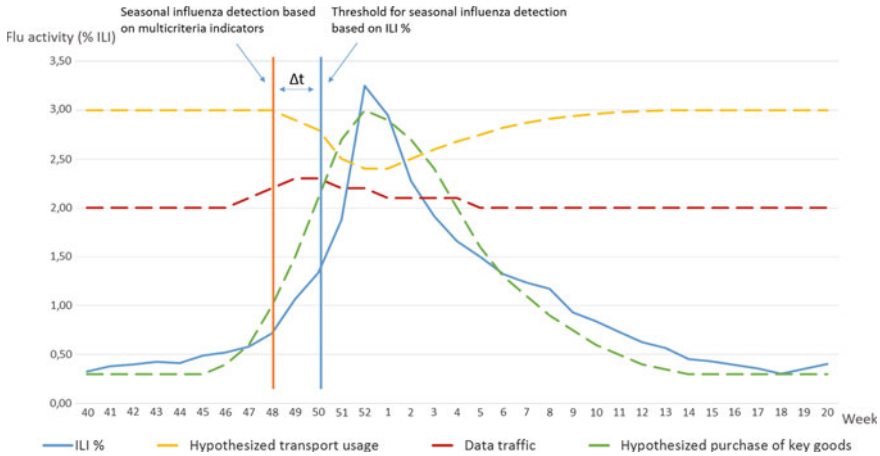
Fig. 3 Multicriteria pattern detection based on indicator surveillance

time, with deviations from expected patterns across multiple systems, combined in a manner that minimises indicator interdependency outside the specific target domains.

4.1 Study Approach

Our goal is to augment the existing influenza surveillance system with an approach that monitors trends in society for indicators of influenza activity. A search for similar works in the scientific literature at the thematic crossroads between epidemiological intelligence, spatial epidemiology and outbreak management has revealed limited results.

The initial concept of an indicator-based seasonal influenza monitoring system is presented to explore the role that spatial information and GIS can play in epidemiological intelligence. We believe that disruptions to the social patterns can be detected through spatial analysis on key metrics, such as daily travel patterns, consumption statistics and sales of key indicator goods.

4.2 Preliminary Hypotheses

We need a research design that can reveal metrics, which are somehow interrelated with occurrence of seasonal influenza. In order to improve abilities for influenza management we hypothesize that we will be able to become aware of the influenza outbreak Δt prior to the normal identification of an influenza outbreak, Fig. 2 shows

our hypothesized transport usage curve in a region combined with the actual clinically diagnosed influenza (ILI%) curve in the 2016/2017 and 2017/2018. The first step of the study will focus on investigating and testing the two main hypotheses:

Hypothesis 1: A significant drop in commuting habits predicts seasonal influenza outbreak.

Travel at specific times of day signifies ability to move between residential areas, work places, and leisure activities, and major disruptions to this ability should be traceable at daily level. To account for this, the transport-based monitoring systems will serve as a primary indicator for detecting changes in social patterns. Transport data will be augmented by other data sources, to strengthen the signal strength of patterns and eliminate sources of statistical noise that may falsely indicate pulses in influenza impact. The idea in this hypothesis is that changes in commuting habits fairly momentarily will detect seasonal influenza. Such drops might be followed up with a more detailed investigation system. However, the rate and absolute change will be interesting quantities to follow up in the study. We will also prepare the research on geospatial commuting data to explore severity levels and other characteristics of the seasonal influenza.

Hypothesis 2: A significant increase in sales data on painkillers/antipyretics and antivirals predicts seasonal influenza outbreaks.

In order to have a more robust system and even compare information we will investigate significant local changes in sales data of relevant pharmaceutical products, such as painkillers/antipyretics and antivirals. If sales metrics for these goods can be tied to pulses of the seasonal influenza, this provides a powerful and readily available indicator that can be applied throughout the country.

We start with two fairly independent societal systems in which geospatial data is easy to retrieve and analyse. Further studies could implement other quantities, which could be historical datasets from public transport, road traffic data, as well as consumption-based metrics such as key indicator goods, utility usage and other available information sources from the city of Oslo. These data will be analysed for change patterns against the daily and weekly influenza data delivered from NorSySS at the NIPH. The presence of detailed epidemiological datasets for Norwegian influenza outbreaks will provide the necessary historical backdrop to demonstrate whether corresponding patterns and correlations between use of urban services and the presence of seasonal influenza exist. We believe that it is possible to identify Δt when seen the data in retrospect and throughout some years develop a framework for seasonal influenza surveillance.

4.3 Proposed Metrics

The seasonal influenza management within societies is relatively well-understood (Wolf 2017), with clearly defined roles for the various actors in the civil society. For the outbreak management hierarchy, one of the key requirements is the availability of information that indicates the prevalence and impact of the influenza outbreak in local societies. The dynamic nature of these phenomena lessens the role of static information sources, as the ground situation develops quickly over time. Applying these concepts to an information management perspective indicates a need for relevant information throughout all phases of an outbreak, to ensure that the stakeholders have the sufficient situational awareness.

To fill the present in the current-day intelligence networks, we propose an indicator-structure that integrates information from a variety of urban systems and critical infrastructure to maintain an up-to-date awareness of changes in patterns and trends within these systems. Table 2 highlights an initial set of indicators, based on the urban information systems available within major Norwegian cities. We believe that these indicators provide a way to detect possible trends at an early stage and provides a capability to compare daily and sub-daily disturbance against historical and current influenza data. Use patterns of utilities, sales of key indicator goods (such as painkillers/antipyretics and antivirals), commercial activity and data traffic in residential areas provides powerful auxiliary information sources that are not mutually affected by events or incidents.

Changes in use patterns may be the result of a variety of reason—Public holidays, cold weather, or fluctuations in the gas price may drastically change the weekly and daily statistics from public transport. Similarly, the other indicators are influenced by internal and external factors that affects the day-to-day use of the monitored systems. To combat these uncertainties, specific indicator profiles must be developed by exploiting the spatial components inherent in all the measured data. Combined, the set of indicators provide a statistical foundation for further epidemic analysis, as well as the necessary data for implementation of analytical models for epidemiological work. The data-driven approach further will allow for rapid development of new indicator profiles and can be adapted to the varying

Table 2 Urban systems indicators

No	Indicator description
1	Public transport utilisation (Subway, trains, buses, light rail, etc.)
2	Toll road activations
3	Data traffic (internet traffic, cell phone networks)
4	Consumption of key indicator goods (Painkillers, Tamiflu, coughing medicine, etc.)
5	Utility use patterns in residential and commercial areas (Electricity, water, gas, etc.)
6	Use of key urban services (pharmacies, schools, GP offices, etc.)
7	Activity information from commercial stakeholders (convenience stores, restaurants, etc.)

information needs over the course of an outbreak. An example of applying trends from multiple urban indicators can be seen in Fig. 3. By monitoring changes in multiple systems, in this case transport usage, purchase of key goods, and data traffic, it may be possible to detect changes to regular use patterns an earlier stage than in existing surveillance systems. This would move the Δt for influenza detection forward, increasing the time and situational awareness to support planning and management efforts in influenza outbreaks.

5 Integrating Spatiotemporal Information into a Systems-Based Management Structure

The societal ability to respond to influenza outbreaks in an urban setting requires successful execution of processes at every hierarchical level of governance, ranging from the city district to national-level stakeholders and intergovernmental organizations (Wolf 2017). However, communication between hierarchical levels have often proved to be a serious obstacle to effective societal safety management, in which actors are more concerned with own responsibilities and tasks than being able to holistically combat the health related disease (Grottenberg and Njå 2017). Access to updated information is a fundamental requirement to accomplish a multisector and multidisciplinary approach to health disaster management, as outlined in the Pandemic Influenza Risk Management guidelines (WHO 2013). The proposed system would offer a method for integrating information from urban systems into decision-making processes in health-based disasters. A spatiotemporal model for analyzing and presenting data on an ongoing outbreak should be regarded as an instrument for structured and standardized communication between decision makers and managers from different societal sectors. A systematic approach to demonstrating spatiotemporal dimensions of an outbreak tend to be under-communicated or even lacking in cross sectoral, traditional risk analyses used when planning for and dealing with epidemics.

The role of the proposed system within the broader Norwegian influenza management system can be illustrated through a perspective founded in systems safety (Leveson 2011). The multi-indicator monitoring system provides a set of normal operating constraints. When threshold-values from the indicators are exceeded, this provides the information needed to assess whether the changes in use within the monitored systems correspond to influenza-related changes to public behaviour. The basic control loop for a societal indicator structure can be seen in Fig. 4. Influenza-related changes to public behavioural patterns are monitored through sensors emplaced within the urban system indicators from Table 2. These data streams are compiled and contextualized by an automated controller, to ensure that epidemic management specialists have access to timely and accurate information. This provides access to an up-to-date understanding necessary for the influenza management apparatus to implement targeted measures to manage and control societal processes related to influenza outbreaks.
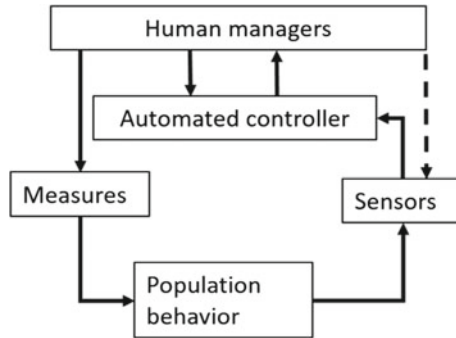
Fig. 4 Basic operating process for societal indicators (based on systems safety models (Leveson 2015)
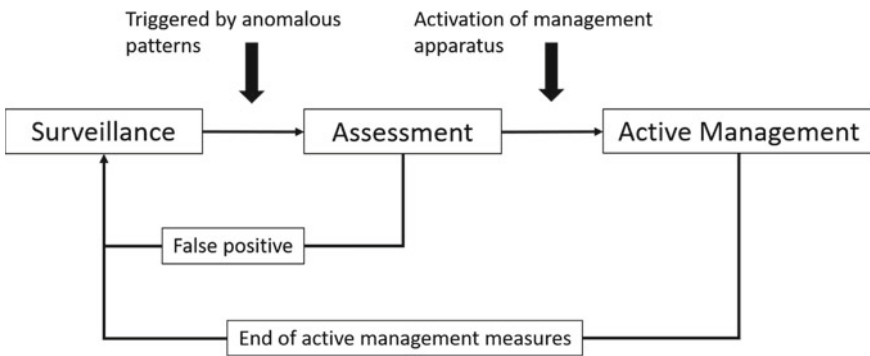
Fig. 5 Process structure for indicator-based monitoring system

The data streams feeds into a broader process structure (Fig. 5) which consists of different processes depending on the overall state of an outbreak—The routine surveillance gives a continuous awareness of the state of societal indicators that may indicate the presence of influenza within a society. When the observed values indicate a potential need for intervention, the system moves to an assessment stage. This process enables analytical capabilities to assess the state of the societal functions, and whether there is a need to activating the larger management system. This might be in the form mobilizing a surge capacity within the local and regional health services, or through controlling the spread of an outbreak through closure of societal functions like transportation systems or school networks. Table 3 showcase the initial stages of a conceptual management structure that is built upon continual surveillance of societal indicators. The system implements the processes structure found in Fig. 5 and seeks to provide a continuous systemic ability from routine

Table 3 Outbreak process structure

	Monitoring assessment		Initiation of management efforts	
Outbreak status	Discrepancy in use patterns	Outbreak suspected	Outbreak confirmed	Outbreak ongoing
Information collection methods	Continuous automated monitoring of use patterns	Automated information collected augmented by manual collection	Automated information collected augmented by manual collection	Continuous impact assessment
Activation of analytical capacity	Automated analytical process	Activation of manual epidemic intelligence capabilities	Deployment of field-based epidemic intelligence resources	Participation of national/ transnational analytical resources
Epidemiological work	Mitigation and monitoring	Monitoring and notification of key stakeholders	Activation of response apparatus	Epidemiological response Containment Care/treatment
Societal activation	No activation of resources, day-to-day activity	Mobilisation of top-level analytical resources	Mobilisation of specialist domain	Mobilisation of surge capacity within health services and governance

surveillance to active management. The system would provide the know for escalation and de-escalation of management efforts, through giving access to data describing the severity and potential of ongoing outbreaks.

6 Conclusion

This paper outlines the design of an ongoing project to assess the suitability of data-streams from urban systems and critical infrastructures for epidemiological surveillance of influenza outbreaks. It is our belief that real-time information from urban systems can fill an important role in improving the understanding of societal functions during major disasters and crises, and that multisource spatial information from urban systems, critical infrastructure and sector authorities can be combined with epidemiological information to provide actionable intelligence for use in influenza management efforts.

Influenza outbreaks have a major impact on public health. Seasonal influenza is a re-occurring event every winter in the northern hemisphere, with significant loss of life and major societal losses. The regularity of these outbreaks produces a rich

dataset of historical observations which can be used to test and validate the proposed indicator structure. We believe that pulses of seasonal influenza should be directly traceable in historical data on public transport utilisation in major urban areas, with increases in influenza activity corresponding to a drop in the utilisation of these service. Similar trends should also be present in data from other urban systems, providing a broad data-driven understanding of societal functions relating to management of infectious diseases.

By extending and formalising the information available to public health officials and decision-makers, the situational awareness of the impact and development of the seasonal influenza can be maintained over time. The initial step of this process is to build the tools needed to maintain a data-driven awareness of societal functions in urban areas, based on the integration of data-sources with a high spatiotemporal quality. The benefits of such an approach is threefold—(1) Models of influenza spread can be developed based on a broader set of information, (2) Secured access to information across the hierarchies of management organisations allows for increasingly collaborative systems and workspaces, (3) The societal effects of a seasonal or pandemic influenza can be mapped in near real-time.

References

Aleman DM, Wibisono TG, Schwartz B (2009) Accounting for individual behaviors in a pandemic disease spread model. In: Proceedings of the 2009 winter simulation conference (WSC), 1977–1985

Batty M (2009) Cities as complex systems: scaling, interaction, networks, dynamics and urban morphologies. Springer

Batty M (2012) Build Sci Cities Cities 29:S9-S16

Bragstad K, Hungnes O, Waalen K, Aune T, Tønnessen R, Rydland KM, Klüwer B, Hauge S (2018) Influensasesongen i Norge 2017–18 [Influenza season in Norway 2017–18]. Norwegian Institute of Public Health

Carneiro HA, Mylonakis E (2009) Google trends: a web-based tool for real-time surveillance of disease outbreaks. Clin Infectious Dis 49:1557–1564

Cook S, Conrad C, Fowlkes AL, Mohebbi MH (2011) Assessing google flu trends performance in the United States during the 2009 Influenza Virus A (H1N1) Pandemic PLOS ONE 6:e23610

Dailey L, Watkins RE, Plant AJ (2007) Timeliness of data sources used for influenza surveillance. J Am Med Inform Assoc 14:626–631

Dawood FS, Iuliano AD, Reed C, Meltzer MI, Shay DK, Cheng P-Y, Bandaranayake D, Breiman RF, Brooks WA, Buchy P, Feikin DR, Fowler KB, Gordon A, Hien NT, Horby P, Huang QS, Katz MA, Krishnan A, Lal R, Montgomery JM, Mølbak K, Pebody R, Presanis AM, Razuri H, Steens A, Tinoco YO, Wallinga J, Yu H, Vong S, Bresee J, Widdowson M-A (2012) Estimated global mortality associated with the first 12 months of 2009 pandemic influenza A H1N1 virus circulation: a modelling study The Lancet Infectious Diseases 12:687–695

Durham DP, Casman EA, Albert SM (2012) Deriving behavior model parameters from survey data: self-protective behavior adoption during the 2009–2010 influenza A(H1N1) pandemic Risk Analysis: an official publication of the society for risk analysis 32:2020–2031

ECDC (2014) The European Surveillance System (TESSy). European Centre for Disease Prevention and Control. https://ecdc.europa.eu/en/home

Fierro A, Liccardo A (2013) Lattice model for influenza spreading with spontaneous behavioral changes. PLoS ONE 8:1–12

Gao Y, Wang S, Padmanabhan A, Yin J, Cao G (2018) Mapping spatiotemporal patterns of events using social media: a case study of influenza trends. Int J Geographical Inf Sci 32:425–449

German RR, Lee L, Horan J, Milstein R, Pertowski C, Waller M (2001) Updated guidelines for evaluating public health surveillance systems MMWR Recomm Rep 50

Grottenberg LO, Njå O (2017) Applying a systems safety approach to the development of GIS in the Norwegian emergency management domain. In: Safety and reliability—theory and applications. CRC Press, pp 484–484

Guan Y, Vijaykrishna D, Bahl J, Zhu H, Wang J, Smith GJD (2010) The emergence of pandemic influenza viruses Protein & Cell 1:9–13

Iuliano AD, Roguski KM, Chang HH, Muscatello DJ, Palekar R, Tempia S, Cohen C, Gran JM, Schanzer D, Cowling BJ, Wu P, Kyncl J, Ang LW, Park M, Redlberger-Fritz M, Yu H, Espenhain L, Krishnan A, Emukule G, van Asten L, Pereira da Silva S, Aungkulanon S, Buchholz U, Widdowson M-A, Bresee JS, Azziz-Baumgartner E, Cheng P-Y, Dawood F, Foppa I, Olsen S, Haber M, Jeffers C, MacIntyre CR, Newall AT, Wood JG, Kundi M, Popow-Kraupp T, Ahmed M, Rahman M, Marinho F, Sotomayor Proschle CV, Vergara Mallegas N, Luzhao F, Sa L, Barbosa-Ramírez J, Sanchez DM, Gomez LA, Vargas XB, Acosta Herrera a, Llanés MJ, Fischer TK, Krause TG, Mølbak K, Nielsen J, Trebbien R, Bruno A, Ojeda J, Ramos H, an der Heiden M, del Carmen Castillo Signor L, Serrano CE, Bhardwaj R, Chadha M, Narayan V, Kosen S, Bromberg M, Glatman-Freedman A, Kaufman Z, Arima Y, Oishi K, Chaves S, Nyawanda B, Al-Jarallah RA, Kuri-Morales PA, Matus CR, Corona MEJ, Burmaa A, Darmaa O, Obtel M, Cherkaoui I, van den Wijngaard CC, van der Hoek W, Baker M, Bandaranayake D, Bissielo A, Huang S, Lopez L, Newbern C, Flem E, Grøneng GM, Hauge S, de Cosío FG, de Moltó Y, Castillo LM, Cabello MA, von Horoch M, Medina Osis J, Machado A, Nunes B, Rodrigues AP, Rodrigues E, Calomfirescu C, Lupulescu E, Popescu R, Popovici O, Bogdanovic D, Kostic M, Lazarevic K, Milosevic Z, Tiodorovic B, Chen M, Cutter J, Lee V, Lin R, Ma S, Cohen AL, Treurnicht F, Kim WJ, Delgado-Sanz C, de mateo Ontañón S, Larrauri A, León IL, Vallejo F, Born R, Junker C, Koch D, Chuang J-H, Huang W-T, Kuo H-W, Tsai Y-C, Bundhamcharoen K, Chittaganpitch M, Green HK, Pebody R, Goñi N, Chiparelli H, Brammer L, Mustaquim D (2017) Estimates of global seasonal influenza-associated respiratory mortality: a modelling study. The Lancet 391(10127):1285–1300

Kitchin R (2014) The real-time city? Big data and smart urbanism GeoJournal 79:1–14

Kitchin R, Lauriault TP, McArdle G (2015) Knowing and governing cities through urban indicators, city benchmarking and real-time dashboards Regional Studies. Reg Sci 2:6–28

Kleczkowski A, Maharaj S, Rasmussen S, Williams L, Cairns N (2015) Spontaneous social distancing in response to a simulated epidemic: a virtual experiment. BMC Public Health 15:1–13

Lal A, Marshall J, Benschop J, Brock A, Hales S, Baker MG, French NP (2018) A Bayesian spatio-temporal framework to identify outbreaks and examine environmental and social risk factors for infectious diseases monitored by routine surveillance Spatial and Spatio-temporal Epidemiology 25:39–48

Lazer D, Kennedy R, King G, Vespignani A (2014) The parable of google flu: traps in big data analysis. Science 343:1203–1205

Leveson N (2011) Engineering a safer world : systems thinking applied to safety. Engineering systems. Cambridge, Mass. MIT Press, cop

Lewis J, White PJ (2017) Estimating local chlamydia incidence and prevalence using surveillance data epidemiology (Cambridge, Mass) 28:492–502

Ministry of Health and Care Services (2014) National management plan for pandemic flu. The Norwegian Government

MSIS (2003) Forskrift om Meldingssystem for smittsomme sykdommer (MSIS-forskriften). Ministry of Health and Care Services

National Influenza Centre (2018) Influenza epidemiological information prepared for WHO informal meeting on strain composition for inactivated influenza vaccines for use in season 2018–19 Geneva, Feb 2018. Norwegian Institute for Public Health

Norwegian Directorate for Civil Protection (2015) National Risk Analysis 2014. Norwegian Directorate for Civil Protection

Norwegian Directorate of Health (2017) Overall risk and vulnerability routines in the healthcare sector

Norwegian Institute of Public Health (2017a) About the Norwegian Syndromic Surveillance System. Norwegian Institute of Public Health. https://www.fhi.no/en/hn/statistics/NorSySS/about-the-norwegian-syndromic-surveillance-system/. Accessed 03 Oct 2018

Norwegian Institute of Public Health (2017b) Early risk assessment: What to expect of the 2017/18 influenza season in Norway. https://www.fhi.no/en/publ/2017/what-to-expect-of-the-201718-influenza-season-in-norway/. Accessed 03 October 2018

Norwegian Institute of Public Health (2017c) Influensasesongen i Norge 2016–17 [Influenza season in Norway 2016-17]. Norwegian Institute of Public Health

Norwegian Institute of Public Health (2017d) Influenza surveillance. Norwegian Institute of Public Health. https://www.fhi.no/sv/influensa/influensaovervaking/. Accessed 03 October 2018

Poletto C, Tizzoni M, Colizza V (2013) Human mobility and time spent at destination: Impact on spatial epidemic spreading. J Theor Biol 7(338):41–58. https://doi.org/10.1016/j.jtbi.2013.08.032

Robertson C (2017) Towards a geocomputational landscape epidemiology: surveillance, modelling, and interventions GeoJournal 82:397–414

Santillana M, Nguyen AT, Dredze M, Paul MJ, Nsoesie EO, Brownstein JS (2015) Combining search, social media, and traditional data sources to improve influenza surveillance PLOS computational biology 11:e1004513

Simonsen L, Spreeuwenberg P, Lustig R, Taylor RJ, Fleming DM, Kroneman M, Van Kerkhove MD, Mounts AW, Paget WJ, the GCT (2013) Global Mortality Estimates for the 2009 Influenza Pandemic from the GLaMOR Project: A Modeling Study PLOS Medicine 10: e1001558

Thacker SB, Berkelman RL (1988) Public health surveillance in the United States Epidemiologic reviews 10:164–190

Timpka T, Eriksson H, Gursky EA, Nyce JM, Morin M, Jenvald J, Strömgren M, Holm E, Ekberg J (2009) Population-based simulations of influenza pandemics: validity and significance for public health policy. Bull World Health Organ 87:305–311

Van Kerckhove K, Hens N, Edmunds WJ, Eames KTD (2013) The Impact of Illness on Social Networks: Implications for Transmission and Control of Influenza. Am J Epidemiol 178:1655–1662

Vanja D, Hedibert FL, Nicholas GP (2012) Tracking epidemics with google flu trends data and a state-space SEIR model. J Am Statist Assoc, 1410

Vega T, Lozano JE, Meerhoff T, Snacken R, Mott J, Ortiz de Lejarazu R, Nunes B (2013) Influenza surveillance in Europe: establishing epidemic thresholds by the moving epidemic method influenza and other respiratory viruses 7:546–558

Wang Z, Ye X (2018) Social media analytics for natural disaster management. Int J Geograph Inf Sci 32:49–72

WICC (1998) International Classification of Primary Care, ICPC-2 Oxford University Press, Oxford

Wolf M (2017) Knowing pandemics: an investigation into the enactment of pandemic influenza preparedness in urban environments science & technology studies 30:8–29

World Health Organization (2013) Pandemic influenza risk management: WHO interim guidance

World Health Organization (2017) Pandemic influenza severity assessment (PISA): a WHO guide to assess the severity of influenza in seasonal epidemics and pandemics

World Health Organization (2018) Essential steps for developing or updating a national pandemic influenza preparedness plan

Xue Y, Kristiansen IS, de Blasio BF (2010) Modeling the cost of influenza: the impact of missing costs of unreported complications and sick leave. BMC Public Health 10:724

Yan SJ, Chughtai AA, Macintyre CR (2017) Utility and potential of rapid epidemic intelligence from internet-based sources. Int J Infectious Dis 63:77–87

Yang B, Pei H, Chen H, Liu J, Xia S (2017) Characterizing and discovering spatiotemporal social contact patterns for healthcare. IEEE Trans Pattern Anal Mach Intell 39:1532–1546

Yao Y, Liu X, Li X, Zhang J, Liang Z, Mai K, Zhang Y (2017) Mapping fine-scale population distributions at the building level by integrating multisource geospatial big data. Int J Geogr Inf Sci 31:1220–1244

Complex Geoinformation Analysis of Multiple Natural Hazards Using Fuzzy Logic

Valentina Nikolova and Plamena Zlateva

Abstract Natural hazards are existence of natural components and processes, which create a situation that could negatively affect people, the economy and the environment. Rising public awareness about natural hazards could improve the quality of life, save financial resources and even save lives. The complicated essence of natural hazards and the interrelations between natural components require a complex analysis of natural hazard factors. In the current research, the factors are analysed by application of analytic hierarchy process. Spatial overlay analysis is done in GIS environment and as a result, landslide susceptibility and flood susceptibility maps are created. Single hazard maps are overlaid in order to receive a complex hazard level. A fuzzy logic with four inputs and one output is designed. This model is used to determine the complex level of hazard considering the factors interaction. The results of the current research and suggested approach could support decision makers in civil protection, territorial planning and management.

1 Introduction

In recent years, an increase is observed in the adverse effects of natural hazards on social relations, economic growth and sustainable development of the countries (Prevention Web 2018; Tzvetkova 2017; UNISDR 2018). Generally, natural hazards can be determined as natural phenomena, which could have adverse impact on life and human activity. These phenomena occur as a result of development of natural processes but in many cases they are triggered by human activity. The largest

V. Nikolova
Department of Geology and Geoinformatics, University of Mining and Geology, Sofia, Bulgaria
e-mail: v.nikolova@mgu.bg

P. Zlateva (✉)
Institute of Robotics, Bulgarian Academy of Sciences, Sofia, Bulgaria
e-mail: plamzlateva@abv.bg

number of environmental hazardous event in global scale and the significant number of people living in risk areas call for extending researches in the field of the hazard and risk, and show the growing need to include natural hazard management issues in integrated territorial development and planning. The complex essence of the natural hazards requires that they to be investigated and evaluated within the scope of the overall natural/natural-anthropogenic complex, taking into account the interaction between the factors causing the hazards as well as between the possible hazards. Actually the problem is not new and there are many publications considering single natural hazards and risks, but the publications considering multiple hazards and risk are still less.

The geomorphological properties of the area in regional scale are analyzed by Karagiozi et al. (2011) as a base for creating a flood hazard map. A probabilistic approach is proposed for assessment of landslide hazard in Lari et al. (2014). The authors consider the particularities and relevance of the methodology for different methodologies of landslides. They determine two main categories: slow moving landslides and fast long-runout landslides (rock avalanches, debris flows, rock falls). Although the identity and properties of occurrence of rock falls are different from sliding, the authors consider them as a type of landslide (a common approach in many publications) and present the methodology for rock fall hazard assessment based on geostatistics application. Hazard curves, representing the probability of exceeding a certain level of landslide intensity within a defined time period, accounting for uncertainty and integrating different magnitude scenarios are created.

The complex nature of single natural hazards is usually investigated by multi-criteria evaluation and GIS application. This approach in landslide investigations is applied in the publications of Grozavu et al. (2010), Ilanloo (2011), Costanzo et al. (2012), Pandey and Shahbodaghlou (2014), Feizizadeh et al. (2014). For example, Costanzo et al. (2012) determine 15 controlling or determining landslides considering topographic, geologic, geomorphologic and pedologic data. In particular, the matrix method in GIS is applied. The analysis show that slope angle is among the more effective instability factors as well as roughness, land use and topographic wetness index. Ilanloo (2011) presents a method for making a landslide susceptibility map of a landslide prone area by fuzzy relations in GIS environment. He uses the fuzzy function to analyse landslide factors and assign fuzzy membership values to the determined classes of each one of the landslide factors (lithology, distance from faults, slop angle, slope aspect, altitude, land cover, distance from road, distance from rivers and wells. In this way, non-quantity data is turned in quantity values and all layers entered in GIS are in the same format. The resulted maps are created using fuzzy sum, product, and gamma operators.

Some authors (Liu et al. 2016b) determine hazards as the presence of potentially damaging physical events in an area. According to Di Mauro et al. (2006) multi-hazard is considered in three dimensions: (1) different sources of hazard on one territory; (2) one hazardous event can trigger another hazardous event; and (3) two hazardous event without relation between them can appear simultaneously on one territory. Multi-criteria index approach and GIS application in flood hazard is applied by Zheng et al. (2008), Kourgialas et al. (2011), Kazakis et al. (2015) etc.

Many of papers analyse multiple hazards as a part of multi hazards risk assessment (Di Mauro et al. 2006; Kreibich et al. 2014; Eshrati et al. 2015; Liu et al. 2016b). For example, Gill and Malamud (2016) consider the differences between multi-layer single-hazard approaches and multi-hazard approaches that integrate all aspects of hazard interactions. The authors consider multi-hazard methodologies based on the hazard interactions and interaction networks, outlining of three types of interaction relationship (triggering, increased probability, and catalysis/ impedance). According to papers of Gill and Malamud (2014, 2016) the progress from multi-layer single hazard to multi-hazard pass through the following steps: hazard identification and comparison; hazard interactions; hazard coincidence (spatial aspect); and dynamic vulnerability.

The interactions between hazards are analysed by Liu et al. (2016a) who present a comprehensive approach for classifying hazard interactions based on analysis of the hazard-forming environment. Regarding hazard-forming environment they determine stable factors for hazard identification—actors that act as a precondition for major natural hazards; and trigger factors—these in which substantial changes are the main reason that hazards are induced. Liu et al. (2016a) consider the relationship between some specific major hazards and their hazard-forming environments. The authors present four types relationships between different natural hazards: independent, mixed, parallel and series.

Fuzzy logic and analytic hierarchy process (AHP) are used by Tazik et al. (2014) in landslide susceptibility assessment. The authors determined the weights of each landslide factor on the base of questionnaire and AHP method, and fuzzy map of each factor was multiplied to its weight. Ilanloo (2011) and Kayastha et al. (2013) use fuzzy logic for landslide susceptibility mapping and evaluation of landslide factors. The method is also used for flood susceptibility and risk assessment Jiang et al. (2009), Fotis et al. (2012), Yeganeh and Sabri (2014), Perera et al. (2015), etc.

The approaches for multiple risk assessment using fuzzy logic are proposed by (Zlateva and Velev 2013; Velev and Zlateva 2018). Spatial analyzes in the GIS environment and fuzzy logic are applied in the analysis of the several factors influencing to the natural hazards (Nikolova and Zlateva 2017).

The essence of the natural hazards and the complexity of the environment require collecting and processing of large volume of information about hazards and hazards factors and modelling for the aim of the multi-hazard risk assessment. Theoretical approach and mathematical methods and modelling are applied in most of the researches (Rosso et al. 2006; Eshrati et al. 2015; Harab and Dell'Acqua 2017). The review of the publications about multi hazard risk assessment and mapping shows that multiple hazard assessment and mapping is not only overlay of single hazard maps but a special attention should be given on the interaction between hazard factors as well as between hazards themselves.

The aim of the current research is to present some aspects of the geoinformation technology in complex assessment of natural hazards on the example of floods and landslides events. This assessment is done by applying GIS and fuzzy logic in order to analyse interaction of multiple natural hazard factors. The hazards factors are analyses and estimated by AHP (Saaty 1987).

The main idea is to propose a fuzzy logic model for risk assessment based on the complex analysis of the multiple interaction between natural hazards (Floods and Landslide) and related factors (Rainfall duration, Rainfall amount, Riverbank altitude above the water level). In particular, it is calculated the complex natural hazard level (Fuzzy logic system output) of the study area.

This article is limited to analyse the susceptibility of the study area to floods and landslides. The article does not explore the essence of the two hazardous events and does not address the genetic link between them. However, the possible interrelationships between floods and landslides are taken into account in the analysis and as a result a map of the complex hazard level is created.

2 Data and Methodology

2.1 Data and Factors for Floods and Landslides

In the current research, the multiple hazard is analysed considering the floods and landslides. These events are possible to occur independently, but in many cases because of the intensive water erosion or rising the groundwater level floods can trigger landslides. On the other side, the landslides can influence to the watercourses by increasing the solid runoff and/or blocking the rivers and this could trigger the floods. In this regard, the complex assessment is needed, taking into account the properties of the hazards and the possible interactions between them.

The research is done in the following steps: identifying the hazardous events, determining hazards factors; analyzing the factors and determining weights of influence; analyzing the available data and entering in GIS environment; data processing and making a spatial overlay analysis; building fuzzy model to rate the possible hazard in relation to hazard triggering factors.

For the aim of the research, a GIS database is built in ArcGIS (ESRI Inc.) environment consisting of the following layers:

- Digital elevation model (DEM)—The raster image was projected in projected coordinate system (UTM) in order to transform angular geographic co-ordinates in Cartesian ones and to make spatial analyses and calculations. 30 m SRTM DEM (Reuter et al. 2007) is used for generating slope map and analysing the spatial distribution of slopes. On the base of DEM the area of the investigated river catchment is determined as well as the drainage network is delineated.
- Drainage network—raster layer determined on the DEM and converted in vector polyline layer;
- Precipitation data—taken from a climate model (https://en.climate-data.org). Monthly average amount and average annual amount of precipitation—entered as a point data (at 9 rain gauging stations) in GIS layer;

- Lithology data—taken of Geological map of Bulgaria, sheets Sliven and Sungurlare (Kanchev 1995a, b). The data is entered as a polygon layer and is converted in raster format for the aim of spatial overlay analysis.
- The land use/land cover (LULC) data—polygon layer, taken from CORINE Land Cover 2012 Project. A raster of LULC is generated for the aim of the analysis.
- Observed landslides—point data about active landslides taken of the web-site of Geoprotection Ltd.—Varna, Bulgaria (http://varna.geozashtita.bg/).

The complex analysis of multiple natural hazard is done on the base of the susceptibility of the investigated area to single hazardous event (floods and landslides). For this purpose single maps (for each one of the factors) presenting the flood and landslide triggering factors (rainfall intensity, rocks type, slope, flow accumulation, distance from stream and land cover types) are created. These factors are rated according to their role for flood or landslide occurrence and weighted overlay analysis of the layers of different factors is done.

The rainfall intensity is presented by modified Fournier index (MFI) (Arnoldus 1980). The monthly average amount and average annual amount of precipitation at nine rain gauging stations were used for calculating the rainfall intensity. The point data received for each one of the station is presented continuously by inverse distance weighted (IDW) interpolation.

The rocks are grouped regarding their physical—mechanical and chemical properties that influence the rocks permeability and in this relation determine the susceptibility of the territory to landslides and floods.

The slopes are determined on the base of DEM using Slope tool of ArcGIS. On the base of DEM a flow accumulation map is elaborated. This represents a flow accumulation in each cell in the elevation raster and is an indicator for the areas water. Hydrology tools of ArcGIS Spatial Analyst is applied for this purpose.

The distance from stream is considered as a factor influencing the flood and landslide occurrence. It is assessed regarding to the possibility the high waters to flood adjacent areas and also to the time for which the surface (slope) flows reach the river beds. Although the importance of this factor it should be considered and evaluated in relation to the altitude of the adjacent areas above water level, particularly when we talk about floods. The intensive stream erosion is often a reason for landslide occurrence. In this relation, the slope areas near to the streams/ rivers are more prone to sliding.

The type of land cover influences on the time to drain the slope runoff. In relation to this, the land cover influence on the stream runoff and distribution of the precipitation in the surface and underground flows. The land cover influences also on the possibility for landslide occurrence. Usually the forest vegetation holds the earth masses while the deforested areas are more prone to sliding. In this regard, we analyzed the land use/land cover (LULC) as flood and landslide factors.

After determining and analyzing the floods and landslides factors, the next step of the research is to rate, each one according to its importance for occurrence of hazardous event as follow: 1—Very low, 2—Low, 3—Moderate, 4—High,

5—Very high. These rates are assigned by reclassifying the raster layers presenting the factors. Weighted sum overlay in ArcGIS environment is applied for making a complex evaluation of the area susceptibility to single hazard. The weights are determined by AHP (Tables 1 and 2).

The values in rows of the tables show the importance of the given factor to the factor in the column. For example if we consider the rainfall we determined that the rainfall is 5 times more important for flood occurrence than rocks type, and the rocks type is evaluated reciprocally to the rainfall with weight of 1/5 (0.2).

The results of AHP show that rainfall and water capacity of the area have the greatest importance for floods and landslides occurrence, while the rocks type and slope of the topographic surface are more significant in landslides than in floods. Applying the AHP for the purpose of the assessment of the influence of different factors gives good results and minimize the personal view on the importance of one or other factor, although each one of the factors is rated regarding to the other factors by expert evaluation.

Table 1 Floods factors and factor weights

Factors	Rocks type	Slope	Rainfall	Flow accumulation	Distance from streams	Land cover	Total	Weight (%)
Rocks type	1.00	3.00	0.20	0.25	0.25	2.00	6.70	10.23
Slope	0.33	1.00	0.25	0.25	0.50	2.00	4.33	6.61
Rainfall	5.00	4.00	1.00	4.00	3.00	4.00	21.0	32.05
Flow accumulation	4.00	4.00	0.25	1.00	5.00	5.00	19.25	29.38
Distance from streams	4.00	2.00	0.33	0.20	1.00	4.00	11.53	17.60
Land cover	0.50	0.50	0.25	0.20	0.25	1.00	2.70	4.12
							65.52	100.00

Table 2 Landslides factors and factor weights

Factors	Rocks type	Slope	Rainfall	Flow accumulation	Distance from streams	Land cover	Total	Weight (%)
Rocks type	1.00	2.00	0.50	0.33	0.50	0.50	4.83	9.02
Slope	0.50	1.00	0.50	0.50	0.50	5.00	8.00	14.93
Rainfall	2.00	2.00	1.00	3.00	5.00	5.00	18.00	33.58
Flow accumulation	3.00	2.00	0.33	1.00	1.00	3.00	10.33	19.28
Distance from streams	2.00	2.00	0.20	1.00	1.00	2.00	8.20	15.30
Land cover	2.00	0.20	0.20	0.33	0.50	1.00	4.23	7.90
							53.60	100.00

The layers presenting the single hazard susceptibility of each one of the factors are overlaid, taking into account the above weights, and a complex map presenting flood susceptibility as well as a map of landslide susceptibility were developed.

For determining the complex assessment of multiple hazard, a weighted sum overlay is applied to the single hazard susceptibility maps. In this case and considering that floods more often cause landslides than vice versa we accepted that the layers of flood susceptibility has 30% importance for the complex hazard level. The layer representing landslide susceptibility has 20% and the layer of frequency of floods occurrence is evaluated of 50% of importance.

2.2 Design of Fuzzy Logic Model for Complex Analysis of Multiple Natural Hazards and Factor Interactions

In this research, a fuzzy logic model for complex risk analysis of the multiple natural hazards (floods and landslide) and three natural factor interactions is designed as a three-level hierarchical system with four inputs and one output. Each level of the system is consisted from one fuzzy logical subsystem with two inputs. The fuzzy logic system output gives the complex assessment for hazard degree of study area regarding to the multiple natural hazards and three related factors.

A scheme of this three-level hierarchical fuzzy system is presented on Fig. 1.

The fuzzy system inputs are defined on the basis of expert knowledge and current research of study area, as follow:

- Input 1 "*Rainfall duration*", hours;
- Input 2 "*Rainfall amount*", mm;
- Input 3 "*Riverbank altitude above the water level*", m;
- Input 4 "*Multiple hazard (landslides + floods) level*".
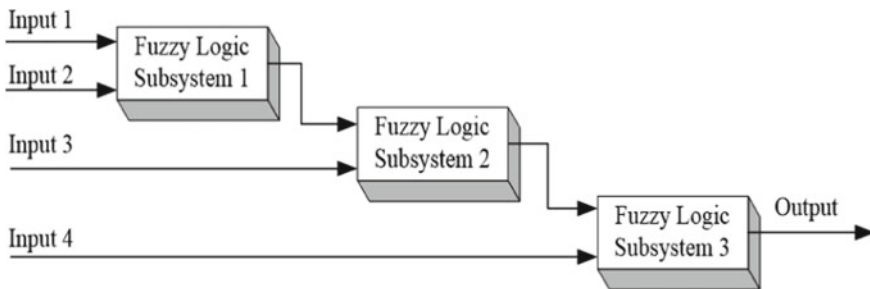

Fig. 1 Three-level hierarchical fuzzy system with four inputs

Two intermediate linguistic variables are defined in the design of the model:

- Intermediate variable 1 "*Rainfall intensity*";
- Intermediate variable 2 "*Rainfall-topographic characteristics*".

Here, the inputs of the first fuzzy logic subsystem are Input 1 "*Rainfall duration*" and Input 2 "*Rainfall amount*", and the output variable is the Intermediate variable 1 "*Rainfall intensity*".

The inputs of the second fuzzy logic subsystem are Intermediate variable 1 "*Rainfall intensity*" and Input 3 "*Riverbank altitude above the water level*", the output variable is the Intermediate variable 2 "*Rainfall-topographic characteristics*".

The inputs of the third fuzzy logic subsystem are Intermediate variable 2 "*Rainfall-topographic characteristics*" and Input 4 "*Multiple hazard (land-slides + floods) level*". The output of third fuzzy logic subsystem is output of the proposed fuzzy logic system. The value of the complex assessment is a criterion for final decision making about the risk degree about multiple hazards for the study area. The higher value corresponds to the higher risk degree.

In the proposed fuzzy logic model, the all input linguistic variables, corresponding to the defined four inputs, are represented by five fuzzy membership functions, as follow: "*Very low* (VL)", "*Low* (L)", "*Moderate* (M)", "*High* (H)", and "*Very high* (VH)". The all input variables are assessed in the interval [0, 5] using trapezoidal membership functions.

The output of the fuzzy logic model (Complex assessment of the multiple natural hazards) is described by five fuzzy membership functions: "*Very low* (VL)", "*Low* (L)", "*Moderate* (M)", "*High* (H)", and "*Very high* (VH)". The output variables is assessed in the interval [0, 100] using trapezoidal membership functions.

The inference rules in the three fuzzy logic subsystem are defined as "If—then"—clause. The number of rules in the knowledge base for each of the fuzzy logic subsystems is 25. Some of the inference rules are defined as follow:

- If *Rainfall duration* is VL and *Rainfall amount* is M and *Riverbank altitude above the water level* is L and *Multiple hazards (floods and landslide)* is L then complex natural hazard level is M;
- If *Rainfall duration* is VL and *Rainfall amount* is VH and *Riverbank altitude above the water level* is VL and *Multiple hazards (floods and landslide)* is H then complex natural hazard level is VH;
- If *Rainfall duration* is L and *Rainfall amount* is H and *Riverbank altitude above the water level* is M and *Multiple hazards (floods and landslide)* is VL then complex natural hazard level is M;
- If *Rainfall duration* is M and *Rainfall amount* is L and *Riverbank altitude above the water level* is VH and *Multiple hazards (floods and landslide)* is VH then complex natural hazard level is M;
- If *Rainfall duration* is H and *Rainfall amount* is VL and *Riverbank altitude above the water level* is VH and *Multiple hazards (floods and landslide)* is VL then complex natural hazard level is VL;

- If *Rainfall duration* is VH and *Rainfall amount* is VH and *Riverbank altitude above the water level* is VL and *Multiple hazards (floods and landslide)* is M then complex natural hazard level is H;
- If *Rainfall duration* is VH and *Rainfall amount* is VH and *Riverbank altitude above the water level* is VH and *Multiple hazards (floods and landslide)* is VH then complex natural hazard level is M.

The logic matrix with inference rules of one fuzzy logic system with two linguistic input variable can be expressed also in the form of table.

The logic matrices corresponding to each one of the three fuzzy logic subsystem are represented respectively in Tables 3, 4 and 5.

Here, the fuzzy logic hierarchical system is designed in MATLAB computer environment using Fuzzy Logic Toolbox.

The outputs of the three fuzzy logic subsystems are calculated as an average weighted of all the inference rules, included in the fuzzy logic matrix. The three fuzzy logic models are based on Mamdani's inference machines, max/min operations and center of gravity defuzzification (Gilat 2011).

The inference surfaces in 3D for the three fuzzy logic subsystems are shown on Figs. 2, 3 and 4, respectively as follow: (Input 1, Input 2, Intermediate variable 1), (Intermediate variable 1, Input 3, Intermediate variable 2), (Intermediate variable 2, Input 4, Fuzzy logic system output).

Table 3 The logic matrix of the first fuzzy logic subsystem

Input 1	Input 2	Intermediate variable 1
Rainfall duration	Rainfall amount	Rainfall intensity
VL	M	H
VL	H	VH
VL	VH	VH
L	L	M
L	M	H
L	H	H
M	L	L
M	H	H
M	VH	H
H	VL	VL
H	M	M
H	VH	H
VH	VL	VL
VH	M	L
VH	VH	M

Table 4 The logic matrix of the second fuzzy logic subsystem

Intermediate variable 1	Input 3	Intermediate variable 2
Rainfall intensity	Riverbank altitude above the water level, m	Rainfall-topographic characteristics
VL	VL	L
VL	M	L
VL	VH	VL
L	L	L
L	M	L
L	VH	VL
M	VL	H
M	L	M
M	VH	L
H	VL	VH
H	M	H
H	VH	M
VH	VL	VH
VH	L	VH
VH	VH	M

Table 5 The logic matrix of the third fuzzy logic subsystem

Intermediate variable 2	Input 4	System output
Rainfall-topographic characteristics	Multiple hazard (landslides + floods)	Complex natural hazard level
VL	VL	VL
VL	M	L
VL	VH	M
L	VL	L
L	M	L
L	VH	M
M	VL	L
M	L	M
M	VH	H
H	VL	M
H	M	H
H	VH	H
VH	VL	M
VH	M	H
VH	VH	VH
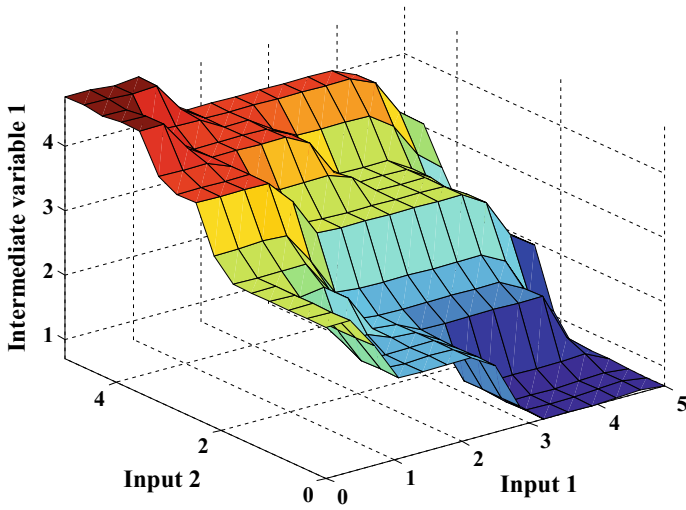
Fig. 2 Inference surfaces of the first fuzzy logic subsystem
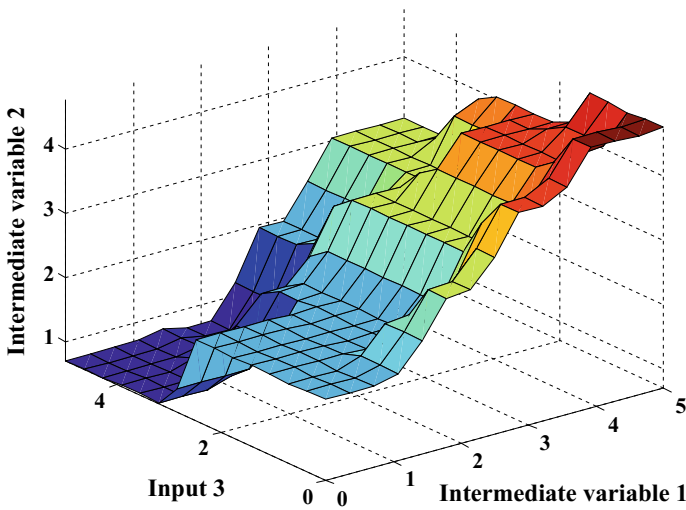
Fig. 3 Inference surfaces of the second fuzzy logic subsystem

2.3 Study Area of the Current Research

The area subject of the current research is the upper part of the river Luda Kamchia catchment (Fig. 5). It is a part of the river Kamchia basin, which is the largest Bulgarian river that flows into the Black Sea. Regarding the whole area of the river
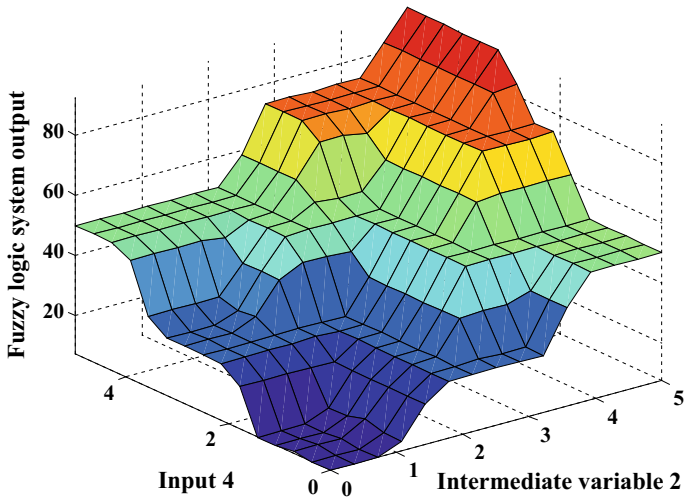
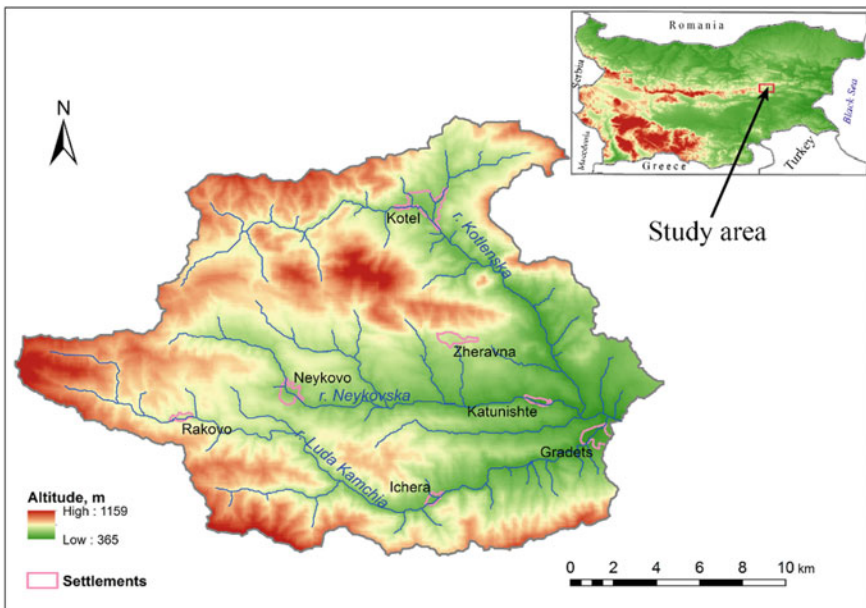**Fig. 4** Inference surfaces of the third fuzzy logic subsystem

Fig. 5 Study area of the current research

Luda Kamchia basin there are two big dams constructed in the middle and low part of the basin, which regulate the river runoff and minimize the flood risk.

However, the small mountain valleys are vulnerable to floods in the zones of transition from the mountain slope to the less sloping area of the mountain foothills and valley extension.

The slope of the topographic surface together with the rainfall and erosion processes is a prerequisite for landslide development in areas covered by non-consolidated weathered rock materials. In this regards we choose the upper part of the river Luda Kamchia as a study area for complex analysis of natural hazards.

The relief is presented by mountainous river valleys, hilly to low mountainous, the average altitude is around 750 m and the highest point is 1180 m. Besides the main drainage axis—the river Luda Kamchia, two other relatively large rivers—Kotlenska and Neykovska can be defined. The total many-years precipitation amount is moderate but intensive rain of 40 mm per 24 h can be observed in 75% probability (Climate reference book—Precipitation in Bulgaria 1990). The most part of the investigated area is built of alternation of carbonate and non-carbonate rocks. Nearly 70% of the studied area are occupied by forest and around 5% are with transitional shrubs and sparsely vegetated areas. The last ones are more prone to sliding and floods in comparison to other areas with hydro-climatological and geomorphological conditions. Agricultural lands with significant areas of natural vegetation take nearly 9% are also prone to sliding and flooding depending on the behavior of other environmental factors. The dense river network and variety of the topographic surface combined with the lithological substrate and the land use types influence the drainage of the surface water and the infiltration of the waters in the soils, and in this relation influence the occurrence of floods and landslides.

2.4 Environmental Prerequisites for Floods and Landslides in the Study Area

The first step in the investigation of nature hazards and risk reduction is to analysis of the hazard factors and determining the hazard susceptibility of the given area. On the other side factor analysis, require good knowledge about the identity of the hazardous event as well as about the possible interaction between factors. Floods are complex natural phenomena caused by heavy rainfalls or intense snowmelt. The development and intensity of floods depend also on the other environmental components (lithological composition, physical-mechanical properties of soils, character of the topography, vegetation) as well as on the way of land use. The landslides as a natural phenomenon are more closely related to the geological—geomorphological conditions of the area but they are usually triggered by intensive rainfall and snowmelt or occur in case of saturation of soils and weathered non-consolidated materials, or in case of rising the groundwater level.

The geological-geomorphological characteristics of the site influence the flow of surface runoff and the redistribution of the runoff into the underground and surface component, and thus influence the occurrence and characteristics of the floods, and also could impact on the landslides development. The grain-size composition of the deposits and physical-chemical properties of the rocks determine the water permeability of the rocks, which is of great importance for occurrence of the flood and landslide events. Highly permeable rocks favor the penetration of water and the underground flow, while less permeable rocks determine higher values of surface flow. In this case high flood sensitivity is identified at horizontal or low slope areas. However, when assessing the flood and landslide hazard, the water permeability of the rocks should be considered in a complex with other environmental characteristics such as water retention capacity, groundwater level, elevation of the site above the river water level, etc. For example, despite the high permeability of sands and gravel, they have a high degree of flood sensitivity due to the fact that, in most cases, these deposits occupy areas with high groundwater levels and or are located near to the river bed.

The altitude and slope of the catchment area impact on the hydro-climatic conditions. Usually, high areas have higher rainfall, which is a prerequisite for higher river flow, but on the other side valleys and low lands (less than 200 m above sea level) are more susceptible to flooding, as they facilitate the overflowing the river at high waters. Altitude and slope affect the amount of water and, in most cases, the velocity of water flow and the development of erosion processes. Low and flat areas are a more frequent prerequisite for floods than higher and steeper territories, while high and steep slopes are more prone to sliding than to floods.

In regards to the above, we considered the following environmental components as a hazard triggering factors: rocks type, slope, rainfall, flow accumulation and distance from streams. In addition, LULC is analysed as a hazard factor and the land cover type are rated to their impact on the floods and landslides occurrence.

In the selection of factors, we were limited by the availability of the data and some factors like groundwater level and distance from faults were not considered. However, we accept that in assessing natural hazards, simultaneous occurrence and the interaction of factors is of greater importance than the impact of the single factor. Taking into account the identity of the floods and landslides as natural phenomenon each one of the factors is analysed and rated according to its role for hazard occurrence (Table 6).

On the base of the information from geological map quoted above, the following lithological groups are determined in the investigated area: unconsolidated non-carbonate; alternation of carbonate and non-carbonate; consolidated carbonate; and consolidated non-carbonate. The susceptibility rates are determined on expert assessment and regarding the specific geological-geomorphological conditions of the environment. For example, sands and gravels have the highest water permeability, they can keep a significant part of the slope runoff, transform it into an underground, and thus minimize the flood hazard, but already saturated, these unconsolidated materials can help to form greater surface runoff.

Table 6 Natural hazards factors and susceptibility rates

Factors	Susceptibility to flooding	Susceptibility to sliding
Rocks/ deposits		
Unconsolidated non-carbonate	4	5
Alternation of carbonate and non-carbonate	4	4
Consolidated carbonate	2	2
Consolidated non-carbonate	5	2
Slope (degree)		
0 ÷ 3	5	1
3 ÷ 6	4	3
6 ÷ 12	3	4
12 ÷ 25	2	4
>25	1	5
Modified Fournier index (MFI), mm		
56 ÷ 58.9	2	2
59 ÷ 63	3	3
Distance from streams (m)		
0 ÷ 50	5	5
50 ÷ 50	4	4
150 ÷ 300	3	3
300 ÷ 500	2	2
More than 500	1	2
Flow accumulation—raster classified by natural breaks method	1 to 5	1 to 5
LULC		
Urban areas	Not evaluated	Not evaluated
Industrial or commercial units	Not evaluated	Not evaluated
Mineral extraction sites	Not evaluated	Not evaluated
Non-irrigated arable land	3	2
Pastures	3	3
Complex cultivation patterns	3	3
Land principally occupied by agriculture with significant areas of natural vegetation	3	3
Broad-leaved forest	1	1
Coniferous forest	2	1
Mixed forest	1	1
Natural grassland	3	3
Transitional woodland/shrub	3	2
Sparsely vegetated areas	4	4

Considering this and the fact that these deposits are usually associated with a higher level of groundwater, the unconsolidated non-carbonate group is estimated with a high susceptibility to flooding and very high to sliding.

Slopes influence the time for which surface runoff approach the stream/river bed. They are also of importance for the infiltration and underground flows. In this relation, they are evaluated at floods. The slope of the topographic surface determines the intensity of sliding. Even small slopes can trigger landslides in case of rain if unconsolidated materials and sparsely vegetation cover the study area. The slope surface calculated in ArcGIS on the base of DEM is reclassified into the five classes (Table 6) and these classes are rated according to their susceptibility to floods and landslides. We defined the limits of the slope intervals considering that areas with a slope less than 3° are flat areas, 12° are accepted as the limit of delineating mountain areas, and 25° are the a limit above which areas are considered as very steep.

Flat areas are estimated as very high susceptible to floods and very low susceptible to sliding, while the steepest slopes are less prone to floods and much prone to sliding.

The modified Fournier index (MFI) in the investigated part of the river Luda Kamchia basin is between 56 and 63 mm and this shows low rainfall aggressiveness (Costea 2012).

Distance from streams influence mainly on the possibility the areas near to streams to be flooded. This indicator is also related to the groundwater level and in this regard could impact on landslides development. We considered 5 distance zones which are rated to flood and landslides susceptibility (Table 6).

Flow accumulation is considered as an indicator for water quantity of the area. It is presented as a raster layer in GIS environment, generated on the base of DEM. The values of flow accumulation in the investigated area are from 0 to 2 294 333 and show the number of cells from which the given cells collect surface flows. Taking into account the relief of the catchment, we accepted that the threshold area to create a stream is 5 km². In this relation, cells with a value less than 5600 (at 30 m cell size of DEM) are excluded from the assessment. The resulted raster is classified in ArcGIS environment using natural breaks method in 5 classes, indicating the susceptibility rates. The larger the number flow accumulation, as the greater is the susceptibility of flooding or sliding.

Floods and landslides are considered as natural hazardous phenomena but in many cases, human activity has high impact on their occurrence and behavior. In this regard, we considered LULC as a hazard triggering factor and rated the LULC types according to their impact on the floods and landslides occurrence (Table 6).

The above considered factors are presented as ArcGIS layers and the susceptibility rates given in Table 3 are assigned to this layers. The integrated impact of the above mentioned factors is evaluated and spatially presented by weighted overlay in ArcGIS environment. The weights of each one of the factors are determined using Analytic Hierarchy Process, AHP, (Saaty 1987), according to Tables 1 and 2.

The analysis of the landslide and flood factors and their weights show that rainfall and flow accumulation (presenting the water content of the area) are the most important factors for hazard occurrence but this should be considered in

relation to the other environmental component and the particular features of the study area. This group of factors normally have greater influence on floods than on landslides while the total weight of the influence of rocks type and slope is greater on landslides. For example, unconsolidated non-carbonate rocks (gravel and sand) are usually susceptible to sliding on slope surface but under the same wet conditions, the susceptibility increases if the materials are deposited on clay or other waterproof layer and it is greater at steeper slopes. On the other side the surface layer can start to slide even at small slopes (a bit steeper than 3°) in case of intensive rain and high level of groundwater, and it is relatively stable if there is no rain and the groundwater level is low, even on steeper slopes. In this regard, when we talk about a complex phenomenon like natural hazard, interaction between the hazard triggering factors should be taken into account. Though the values of the importance of each one of the factors are determined by using expert knowledge, the AHP minimizes the subjectivity of judgment when determining the weighting coefficients.

3 Research Results and Discussion

Single hazard susceptibility maps (for floods and for landslides) are created by weighted overlay of floods and landslides factors (Figs. 6 and 7). The results show that the investigated part of the river Luda Kamchia catchment is very low to moderately susceptible to floods and landslides. There is a moderate probability of landslides occurring in larger areas of the investigated territory, while floods are possible in limited areas around the rivers. The created models are validated to the data of observed landslides (Geoprotection Ltd.—Varna, http://varna.geozashtita.bg/) and to flooded areas determined in Flood Risk Management Plan, FRMP, (Black Sea Directorate—Varna, https://www.bsbd.org/uk/FR_mplans.html).

The results of validation are better at landslide susceptibility model. Floods susceptibility model shows better results at the river Kotlenska and at the Gradets region, and future researches are needed to clarify the model in the other upper parts of the catchment.

At equal rainfall intensity, the moderate rate of flood susceptibility in the river Neykovska basin (the central part of the investigated area) could be explained with the relatively low slope of the topographic surface and sparsely vegetated areas. The form of the river basin affects the time for which the surface runoff flows into the main river, which in turn influences the amount of river flow. Regarding to the landslide susceptibility map areas near to rivers are more susceptible to sliding, where the calculated rates of susceptibility are moderate.

Comparison with the registered cases of active landslides in the region (Geoprotection Ltd.—Varna) shows that 10 of 15 registered cases are located in the determined by the model area of moderate landslide susceptibility and 5 cases fall in the low landslide susceptibility area according to the model (Fig. 7). Two of
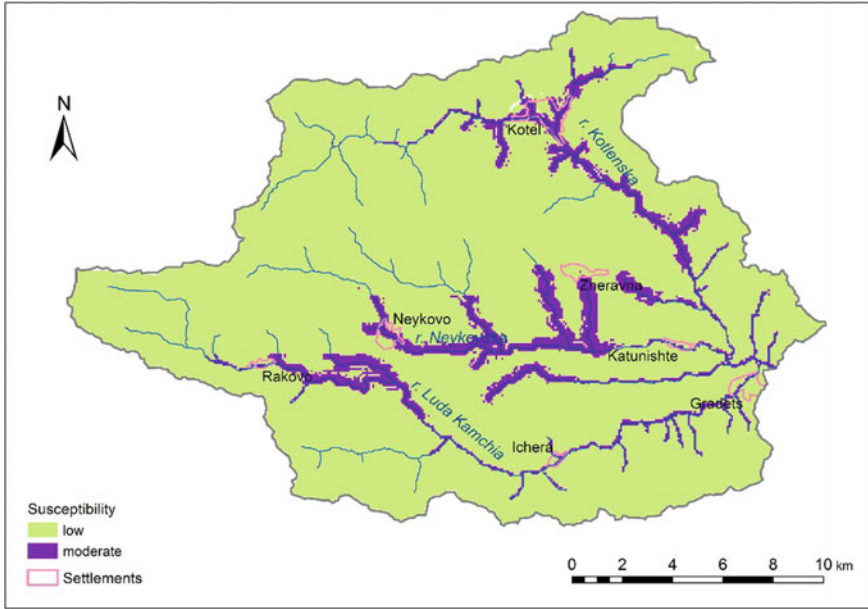
Fig. 6 Flood susceptibility map
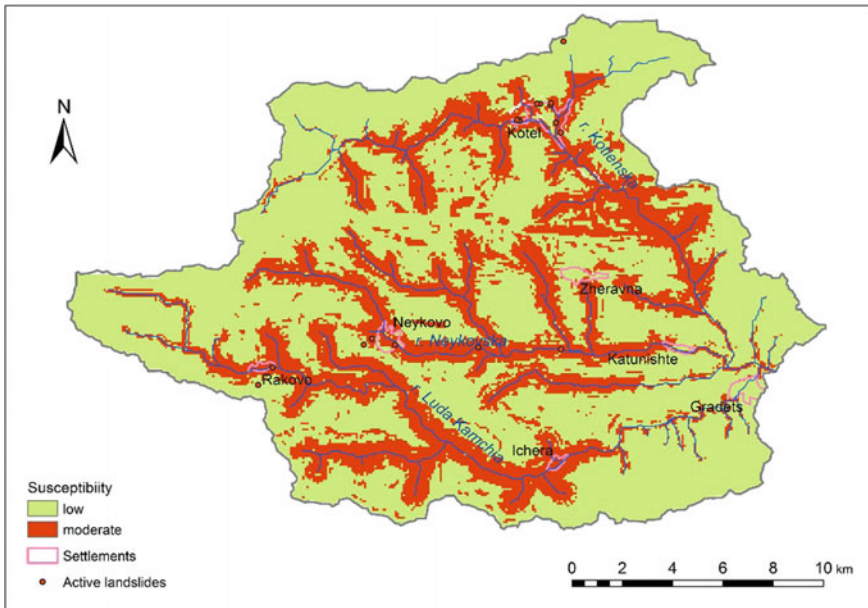
Fig. 7 Landslide susceptibility map

these 5 cases are in the area of Kotel town and the reason for their occurrence is more probably human activity than environmental processes.

Despite some imperfection in the models, we consider that they are enough reliable to direct attention of decision makers in planning preventive activities.

To evaluate the complex hazard level we used weighted sum overlay of layers of flood and landslide susceptibilities, observed landslides and flooded areas (according to the above FRMP) with a repeat period of 20 years.

Applying the weighted sum overlay and taking into account that floods can trigger landslides we accepted that the layers of modelled flood susceptibility has 30% importance, modelled landslides layer is weighted by 20% and the layer of active landslides and flooded areas with a repeat period of 20 years is set to 50% of importance.

The complex assessment, given on Fig. 8, shows slightly higher values in comparison of the single hazard layers.

In this research, in order to carry out the complex hazard analysis with proposed fuzzy logic model the numeral values of the linguistic variables of the multiple natural hazards (floods and landslide) and three natural factor interactions (Rainfall duration, Rainfall amount, Riverbank altitude above the water level) are chosen. The particular numeral values for the trapezoidal membership functions of the four factors (Input 1, Input 2, Input 3) are given in Tables 7, 8 and 9, respectively. These values are obtained from real monitoring (experimental data) and expert knowledge.
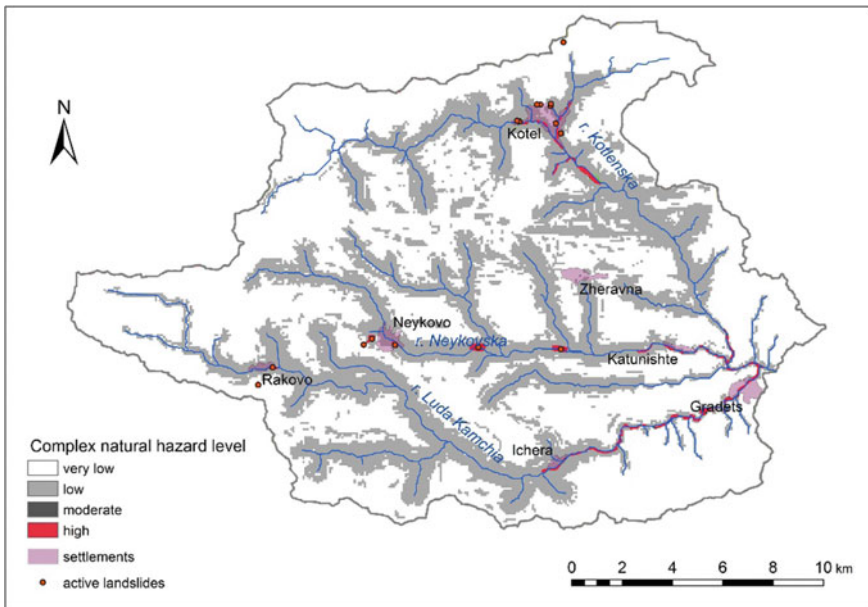
Fig. 8 Complex hazard assessment map

Table 7 Numeral values of trapezoidal membership functions and relative linguistic variables of the Input 1—Rainfall duration, h

Rainfall duration h	Trapezoidal membership functions	Rated trapezoidal membership functions	Linguistic variables
<9	[0, 0, 6, 9]	[0, 0, 0.6, 0.9]	Very low (VL)
6 ÷ 18	[6, 9, 12, 18]	[0.6, 0.9, 1.2, 1.8]	Low (L)
12 ÷ 30	[12, 18, 24, 30]	[1.2, 1.8, 2.4, 3.0]	Moderate (M)
24 ÷ 48	[24, 30, 42, 48]	[2.4, 3.0, 4.2, 4.8]	High (H)
>42	[42, 48, 50, 50]	[4.2, 4.8, 5, 5]	Very high (VH)

Table 8 Numeral values of trapezoidal membership functions and relative linguistic variables of the Input 2—Rainfall amount, mm

Rainfall amount mm	Trapezoidal membership functions	Rated trapezoidal membership functions	Linguistic variables
<15	[0, 0, 10, 15]	[0, 0, 1.0, 1.5]	Very low (VL)
10 ÷ 25	[10, 15, 20, 25]	[1.0, 1.5, 2.0, 2.5]	Low (L)
20 ÷ 35	[20, 25, 30, 35]	[2.0, 2.5, 3.0, 3.5]	Moderate (M)
30 ÷ 45	[30, 35, 40, 45]	[3.0, 3.5, 4.0, 4.5]	High (H)
>40	[40, 45, 50, 50]	[4.0, 4.5, 5.0, 5.0]	Very high (VH)

Table 9 Numeral values of trapezoidal membership functions and relative linguistic variables of the Input 3—Riverbank altitude above the water level, m

Riverbank altitude above the water level, m	Trapezoidal membership functions	Rated trapezoidal membership functions	Linguistic variables
<0.5	[0, 0, 0.25, 0.5]	[0, 0, 0.5, 1.0]	Very low (VL)
0.25 ÷ 1	[0.25, 0.5, 0.75, 1.0]	[0.5, 1.0, 1.5, 2.0]	Low (L)
0.75 ÷ 1.5	[0.75, 1.0, 1.25, 1.5]	[1.5, 2.0, 2.5, 3.0]	Moderate (M)
1.25 ÷ 2	[1.25, 1.5, 1.75, 2.0]	[2.5, 3.0, 3.5, 4.0]	High (H)
>1.75	[1.75, 2.0, 2.5, 2.5]	[3.5, 4.0, 5.0, 5.0]	Very high (VH)

The values of Input 4 is taken from Complex hazard assessment map (Table 10). The defined output values of the fuzzy logic system are presented in Table 11.

Here, several simulations with proposed fuzzy logic model were done using particular input values in order to calculate the complex natural hazard level (Fuzzy logic system output) of the study area. The simulation results for complex risk analysis of the multiple natural hazards (floods and landslide) and three natural factor interactions are show in Table 12.

The obtained output values (crisp values) from the fuzzy logic model after the defuzyfication belong to one of the five sub-intervals of the interval [0, 100].

Table 10 Numeral values for trapezoidal membership functions and relative linguistic variables of the Input 4—Multiple hazard (landslides + floods)

Multiple hazard (landslides + floods)	Trapezoidal membership functions	Linguistic variables
<1.25	[0, 0, 0.75, 1.25]	Very low (VL)
0.75 ÷ 3.25	[0.75, 1.25, 1.75, 2.25]	Low (L)
1.75 ÷ 3.25	[1.75, 2.25, 2.75, 3.25]	Moderate (M)
2.75 ÷ 4.25	[2.75, 3.25, 3.75, 4.25]	High (H)
>3.75	[3.75, 4.25, 5.0, 5.0]	Very high (VH)

Table 11 Numeral values for trapezoidal membership functions and relative linguistic variables of the fuzzy logic system output—Complex natural hazard level

Multiple hazard (landslides + floods)	Trapezoidal membership functions	Linguistic variables
<25	[0, 0, 15, 25]	Very low (VL)
25 ÷ 45	[15, 25, 35, 45]	Low (L)
35 ÷ 65	[35, 45, 55, 65]	Moderate (M)
55 ÷ 85	[55, 65, 75, 85]	High (H)
>75	[75, 85, 100, 100]	Very high (VH)

Table 12 Simulation results for complex natural hazard level from the fuzzy logic model

Input 1	Input 2	Input 3	Input 4	Output
Rainfall duration h	Rainfall amount mm	Riverbank altitude above the water level, m	Multiple hazard (landslides + floods)	Complex natural hazard of study area
6	28	0.3	2.2	High
6	28	1.8	3.3	Moderate
6	40	2.4	2.8	Moderate
6	40	0.3	2.5	Very High
10	22	1.9	4.2	Moderate
18	22	1.2	1.8	Low
24	32	1.2	1.5	Moderate
24	10	0.4	2.8	Moderate
24	10	0.4	1.2	Low
28	15	1.5	1.7	Low
28	15	1.5	3.5	Low
36	10	0.9	0.9	Very Low
36	22	0.9	3.8	Moderate
42	48	0.4	2.8	High
42	48	2.1	3.1	Moderate

These five sub-intervals are used to determine the *Complex natural hazard level* of the study region on the four hazard factors (inputs) as shown in Table 12.

The sub-intervals are defined as follows:

If the value of *Complex natural hazard level* ∈ [0, 20) then *Complex natural hazard* has *Very low* level;

If the value of *Complex natural hazard level* ∈ [20, 40) then *Complex natural hazard* has *Low* level;

If the value of *Complex natural hazard level* ∈ [40, 60) then *Complex natural hazard* has *Moderate* level;

If the value of *Complex natural hazard level* ∈ [60, 80) then *Complex natural hazard* has *High* level;

If the value of *Complex natural hazard level* ∈ [80, 100] then *Complex natural hazard* has *Very high* level.

In evaluation of complex hazard level, the interaction between hazard factors should be considered of high importance. Particularly the rainfall duration should be assessed taking into account the amount of precipitation. For example, we have 6 h rain but the amount is less than 20 mm the hazard level determined by rain is low, but if we have 40 mm rain at the same duration of 6 h than the hazard will be evaluated as very high. On the other side if we have 48 mm precipitation but for 42 h the rain hazard will be low or moderate depending on the retention capacity of soils and rocks and because of the longer time for which this amount of precipitation is collected that means less intensity of the rain. Adding the other factors in the model modify the complex hazard level. If we consider the same rainy conditions—Rainfall intensity (rain duration 42 h and amount 48 mm) the complex hazard could be higher in case of low riverbank and moderate if the riverbank is higher. On the other hand if we have the same rainfall duration (for example 24 h) but different amount of rainfall (32 and 10 mm) then it could be expected that the hazard would be higher in case of higher rainfall amount but taking into account the riverbank altitude above the river level (respectively 1.2 m and 0.4 m) and modeled multiple hazard level (1.5 and 2.8) the complex natural hazard level in evaluated as moderate in the both cases.

The current study of the natural hazard and analysis of the hazard factors shows that the altitude of the riverbank and adjusted areas above the river level has the most noticeable influence in the complex natural hazard assessment, however the complex character of natural hazard requires all hazard factors to be considered in interaction.

The obtained results from fuzzy logic model for the complex natural hazard level of study area about the multiple natural hazards (floods and landslide) and three natural factor interactions (Rainfall duration, Rainfall amount, Riverbank altitude above the water level) could successfully help stakeholders to make informed decisions about effective activities in risk reduction.

4   Conclusions

The analysis of the multiple hazard is done on the example of floods and landslides susceptibility assessment and taking into account the data about active landslides and possible floods in the upper part of the river Luda Kamchia catchment. The lack of historical observations is considered as a limiting factor of the research. The results of overlay analysis show that under moderate and high level of hazard are around 0.5% of the investigated area. Nearly 34% of the area are estimated with low level of hazard and around 65%—with very low. Adding additional factors in fuzzy model and considering the relation between these factors and their role in hazard occurrence could modify the previously received values of hazard level.

The interaction between hazards factors is analyzed by AHP. The analysis shows the main role of rainfall and flow accumulation, better expressed at floods hazards than at landslides.

The advantages of the presented methodology for complex analysis of multiple natural hazard by application spatial analyses in GIS environment is that it gives an information about the total hazard rate as well as for each one of the observed hazards. It also allows to consider the factors triggering the particular hazardous event and this can be used by decision makers to take the relevant action in the particular situation.

A fuzzy logic is applied in order to determine the total level of natural hazards and to analyze the interaction between factors and their reflectance on the hazard. The results of fuzzy logic approach strongly depend on the way of setting the hazard factors in the different inputs, the chosen membership functions and defined inference rules. In this regard, we could say that fuzzy logic is a subjective method and depends on the expert's knowledge and view on the modelled phenomena. Future researches are needed in expanding the scope of hazard factors and investigating the interactions between them as well as to finding the best way for emphasizing the single hazards in the complex multiple hazards.

The GIS data base built as a result of the research can be easily updated and allows adding new factors of hazard which enable expanding the analyses. The suggested models of hazard susceptibility and common hazard level can be used as a first stage of multiple risk assessment and are tools to support decision makers and planning experts in the process of mitigating the impact of hazardous event and better territorial development.

References

Arnoldus HML (1980) An approximation of rainfall factor in the Universal Soil Loss Equation. In: De Boodt M, Gabriels D (eds) Assessment of erosion. Wiley, Chichester, pp 127–132

Climate data for cities worldwide (2018) Climate data. https://en.climate-data.org. Accessed 22 Nov 2017

CORINE Land Cover project (2012). http://eea.government.bg/bg/projects/korine-14/index. Accessed 25 Apr 2016

Costanzo D, Rotigliano E, Irigaray C, Jimenez-Peralvarez JD, Chacon J (2012) Factors selection in landslide susceptibility modelling on large scale following the gis matrix method: application to the river Beiro basin (Spain). Nat Hazards Earth Syst Sci, 12:327–340. https://doi.org/10.5194/nhess-12-327-2012

Costea M (2012) Using the Fournier indexes in estimating rainfall erosivity. Case study-the Secasul Mare Basin. Aerul si Apa. Componente ale Mediului, pp 313–320

Di Mauro C, Bouchon S, Carpignano A, Golia E, Peressin S (2006) Definition of multi-risk maps at regional level as management tool: Experience gained by civil protection authorities of Piemonte region. In: Proceedings of the 5th Conference on risk assessment and management in the civil and industrial settlements. http://conference.ing.unipi.it/vgr2006/archivio/Archivio/2006/Articoli/700196.pdf. Accessed 17 Sept 2017

Eshrati L, Mahmoudzadeh M, Taghvaei M (2015) Multi hazards risk assessment, a new methodology. Int J Health Syst Disaster Manag 3(2):79–88

Feizizadeh B, Roodposhti MS, Jankowski P, Blaschke T (2014) A GIS-based extended fuzzy multi-criteria evaluation for landslide susceptibility mapping. Comput Geosci 73:208–221

Flood Risk Management Plan, Black Sea Directorate—Varna (2018) BSBD. https://www.bsbd.org/uk/FR_mplans.html. Accessed 5 Feb 2018

Fotis M, Georgia M, Apostolos V (2012) Estimation of the Prefecture of Evros vulnerability in flood cases using GIS and fuzzy set algebra. Paper presented at the 16th international water technology conference, Istanbul, Turkey, 7–10 May 2012

Gilat, A. (2011) MATLAB—An Introduction with Applications. 4-th ed., Wiley, New York

Gill JC, Malamud BD (2014) Reviewing and visualizing the interactions of natural hazards. Rev Geophys 52:680–722

Gill J C, Malamud BD (2016) Hazard interactions and interaction networks (cascades) within multi-hazard methodologies. Earth Syst. Dynam. 7:659–679. https://doi.org/10.5194/esd-7-659-2016, www.earth-syst-dynam.net/7/659/2016

Grozavu A, Margarint MC, Patriche CV (2010) GIS applications for landslide susceptibility assessment: a case study in Iaşi County (Moldavian Plateau, Romania). Trans Inf Commun Technol 43:393–404. https://doi.org/10.2495/RISK100341

Harab MM, Dell'Acqua F (2017) Remote Sensing in Multi-Risk Assessment: Improving disaster preparedness. IEEE Geosc Remote Sens Mag 5(1):53–65. https://doi.org/10.1109/MGRS.2016.2625100

Ilanloo M (2011) A comparative study of fuzzy logic approach for landslide susceptibility mapping using GIS: An experience of Karaj dam basin in Iran. Proced Soc Behav Sci 19:668–676

Jiang W, Deng L, Chen L, Wu J, Li J (2009) Risk assessment and validation of flood disaster based on fuzzy mathematics. Prog Nat Sci 19:1419–1425

Kanchev I (1995a) Geological map of Bulgaria, Map sheet Sliven. Scale 1:100000. Geology and Geophysics JSC

Kanchev I (1995b) Geological map of Bulgaria, map sheet Sungurlare. Scale 1:100000. Geology and Geophysics JSC

Karagiozi E, Fountoulis I, Konstantinidis A, Andreadakis E, Ntouros K (2011) Flood hazard assessment based on geomorphological analysis with GIS tools—the case of Laconia (Peloponnesus, Greece). In: Proceedings of the 8th international symposium on GIS, Ostrava 2011, pp 201–216

Kazakis N, Kougias I, Patsialis T (2015) Assessment of flood hazard areas at a regional scale using an index-based approach and Analytical Hierarchy Process: Application in Rhodope-Evros region. Greece Sci Total Environ 538:555–563

Kayastha P, Bijukchhen SM, Dhital MR, De Smedt F (2013) GIS based landslide susceptibility mapping using a fuzzy logic approach: A case study from Ghurmi-Dhad Khola Area, Eastern Nepal. J Geol Soc India 82:249–261

Kourgialas NN, George P, Karatzas GP (2011) Flood management and a GIS modelling method to assess flood-hazard areas—a case study. Hydrol Sci J 56(2):212–225. https://doi.org/10.1080/02626667.2011.555836

Kreibich H, Bubeck P, Kunz M, Mahlke H, Parolai S, Khazai B, Daniell J, Lakes T, Schroter K (2014) A review of multiple natural hazards and risks in Germany. Nat Hazards 74:2279–2304

Lari S, Frattini P, Crosta GB (2014) A probabilistic approach for landslide hazard analysis. Eng Geol 182:3–14

Liu B, Siu Y L, Mitchell G (2016a) Hazard interaction analysis for multi-hazard risk assessment: a systematic classification based on hazard-forming environment. Nat Hazards Earth Syst Sci 16:629–642. https://doi.org/10.5194/nhess-16-629-2016

Liu B, Siu YL, Mitchell G, Xu W (2016b) The danger of mapping risk from multiple natural hazards. Nat Hazard 82:139–153. https://doi.org/10.1007/s11069-016-2184-5

Nikolova V, Zlateva P (2017) Assessment of flood vulnerability using fuzzy logic and geographical information systems. In: Murayama Y, Velev D, Zlateva P et al (eds) Information technology in disaster risk reduction 2016, IFIP Advances in information and communication technology, vol 501. Springer, Cham, pp 254–265. https://doi.org/10.1007/978-3-319-68486-4_20

Pandey AR, Shahbodaghlou F (2014) Landslide hazard mapping of Nagadhunga-Naubise section of the Tribhuvan highway in Nepal with GIS application. J Geogr Inf Syst 6:723–732

Perera EDP, Lahat L (2015) Fuzzy logic based on flood forecasting model for the Kelantan river basin, Malaysia. J Hydro-environ Res 9:542–553

Prevention Web (2018) Strengthening climate change adaptation through effective disaster risk reduction. http://www.preventionweb.net. Accessed 6 Sept 2018

Reuter HI, Nelson A, Jarvis A (2007) An evaluation of void filling interpolation methods for SRTM data. Int J Geogr Inf Sci 21(9):983–1008

Rosso R, Rulli M C, Vannucchi G (2006) A physically based model for the hydrologic control on shallow landsliding. Water Resource Research 42, W 06410. https://doi.org/10.1029/2005wr004369

Saaty RW (1987) The analytic hierarchy process—what it is and how it is used. Math Model 9(3–5):161–176

Tazik E, Jahantab Z, Bakhtiari M, Rezaei A, Alavipanah S K (2014) Landslide susceptibility mapping by combining the three methods: Fuzzy logic, Frequency ratio and Analytical hierarchy process in Dozain basin. Paper presented at the 1st ISPRS International Conference on Geospatial Information Research, 15–17 November 2014, Tehran, Iran. The International Archives of the Photogrammetry, Remote Sensing and Spatial Information Sciences, vol XL-2/W3. https://doi.org/10.5194/isprsarchives-XL-2-W3-267-2014

Tzvetkova S (2017) Ecological aspects of the management of transport enterprises. Scientific Journal Mechanics. Transport and Communications 15 (3/3): IX-19—IX-25

United National Office for Disaster Risk Reduction (2018) UNISDR Annual report 2017. https://www.unisdr.org/files/58158_unisdr2017annualreport.pdf. Accessed 6 Sept 2018

Velev D, Zlateva P (2018) Information system framework for integrated risk assessment from natural disasters. International Archives of the Photogrammetry, Remote Sensing and Spatial Information Sciences—ISPRS Archives 42 (3W4): 535–541

Yeganeh N, Sabri S (2014) Flood vulnerability assessment in Iskandar Malaysia using multi-criteria evaluation and fuzzy logic. Res J Appl Sci Eng Technol 8(16):1794–1806

Zheng N, Tachikawa Y, Takara K (2008) A Distributed flood inundation model integrating with rainfall-runoff processes using GIS and remote sensing data. The International Archives of the Photogrammetry, Remote Sensing and Spatial Information Sciences. vol XXXVII, Part B4. Beijing, pp 1513–1518

Zlateva P, Velev D (2013) Complex risk analysis of natural hazards through fuzzy logic. J Adv Manag Sci 1(4):395–400

Developing a Multi-agent Based Modeling for Smart Search and Rescue Operation

Sanaz Azimi, Mahmoud Reza Delavar and Abbas Rajabifard

Abstract One important issue aftermath of disasters is the optimum allocation of the medical assistance to the demanded locations. In this paper, the optimum allocation of the medical assistance to the injured according to a multi-criteria decision making is performed by Multiplicatively Weighted Network Voronoi Diagram (MWNVD). Particle Swarm Optimization (PSO) is applied to optimize the MWNVDs. In this paper, two types of multi-agent rescue models for incorporating the allocation of the medical supplies to the injured locations according to the generated PSO-MWNVDs, wayfinding of emergency vehicles as well as using smart city facilities were proposed. In one of the proposed model, the priority of the injured for receiving the medical assistance, information transfer about the condition of the injured to the hospitals prior to ambulance arrival and updating of ambulance route were considered. Another proposed model has facilities of coordination of emergency vehicles with traffic lights in the intersection and updating of fire engine route compared to the facilities of the first one. The partial difference between the estimated and expected population for receiving the medical assistance in MWNVDs is computed as 37%, while the PSO-MWNVD decreased the mentioned difference to 6%. Also, the time evaluation of the mentioned proposed models and another multi-agent rescue operation model, which uses MWNVD and does not have the studied smart facilities was performed. The results show that the response time of ambulances to the injured and the ambulance mission duration in the proposed model, that has more smart facilities, is improved to other models.

S. Azimi · M. R. Delavar (✉)
School of Surveying and Geospatial Engineering, College of Engineering,
Center of Excellence in Geomatic Engineering in Disaster Management,
University of Tehran, Tehran, Iran
e-mail: mdelavar@ut.ac.ir

S. Azimi
e-mail: sanazazimi@ut.ac.ir

A. Rajabifard
Department of Infrastructure Engineering, Centre for Spatial Data Infrastructures
and Land Administration, The University of Melbourne, Melbourne, VIC, Australia
e-mail: abbas.r@unimelb.edu.au

1 Introduction

Disasters can have highly destructive effects on society. The high density of the population, buildings, and infrastructure in cities cause them vulnerable to disasters (Zhuang and Bier 2007; Li et al. 2011). Tabas, Rudbar and Bam earthquakes are the worst and deadliest earthquake disasters in the last 100 years in Iran (Ibrion et al. 2015). During the 208 natural disasters from 1900–2015 in Iran, 156332 people have been died and a number of people injured (Ghomian and Yousefian 2017). Providing the quick assistance to the wounded is a significant factor for increasing their survival probability.

There is the main requirement to the better assignment of the available medical assistance to the disaster sites in order to increase the survival chance of victims and improve the performance of the relief operation (Bostick et al. 2008). Therefore, the optimum allocation of ambulances to the emergency victims as fast as possible is essential where optimum routing of the ambulances to the emergency victims' locations is important at the same time. The optimum allocation of the victims to the appropriate emergency centers would require consideration of traffic conditions for transferring of the medical assistance to the wounded locations. Reducing the travel time of the ambulances to the emergency victims is one way to decrease the emergency vehicle response time (Billhardt et al. 2014).

Medical resource assignment has not been much considered in disaster management (Fiedrich et al. 2000; Gong and Batta 2007). There has been few research that explicitly study patients allocation problems to their most appropriate hospitals for receiving the medical assistance. In most of the studies, allocation of the nearest available ambulances to the emergency victims' location is performed. Bandara et al. (2014) showed that dispatching the nearest vehicle has not been applied in an optimum manner.

In some studies, the priority of the victims has been analyzed with regard to the severity of their injuries in order to receive the first aid. (Andersson and Värbrand 2007) illustrated that the vehicle with the shortest travel time route is dispatched to the patient with the highest priority location. López et al. (2008) proposed a multi-agent system for ambulances allocation that is considered the priority of patients. Bandara et al. (2014) showed that considering the severity level of patients leads to an increase in the average survival probability of patients.

In some research, the response time for emergency medical services is analysed. Haghani et al. (2003) proposed an optimization model for developing the flexible dispatching of the medical services by considering the ambulances available in the real-time.

On the other hand, the Voronoi Diagram (VD) can be used to determine the service area for urban facilities. Karimi et al. (2009) investigated the Ordinary Voronoi Diagram and multiplicatively weighted Voronoi Diagram for determining the space allocation of the educational centers. Rezayan and Najian (2008) studied Adaptive Multiplicatively Weighted Voronoi Diagram to determine service areas of the primary schools. The population density, proximity and safety of access rules

parameters are investigated in order to minimize the proportional difference of the estimated and expected level of service in their proposed model. After applying the linear programming and simulated annealing optimizations algorithms, it was concluded that the linear optimization generates better results.

After occurring of disasters due to the blockage of many streets, investigating the access of relief groups to the street network and navigating the relief group in the disaster site are crucial. Yue et al. (2012) proposed an efficient approach for allocating and transferring ambulance dynamically. The purpose of this approach was ambulance navigation to the demand site in order to maximize the level of services of the emergency medical services system. Talarico et al. (2015) studied ambulance routing problem in order to find ambulances routes to serve a large number of injured people at the same time. Also, the effect of the number of ambulances, hospitals, and the priority of slightly and seriously injured patient's parameters was considered in the proposed model.

Search and rescue operation is a good application for agent-based modelling. Because the agent-based modelling is a natural way to model the complexity of disaster relief and relief groups interactions during an emergency situation. According to Rusell and Norvig (2003), the agent perceives its environment through sensors and acts upon them through its effectors. Multi-Agent Systems (MAS) are composed of multiple agents interacting with each other and with objects in a single simulation environment, for complying a common goal (Roozemond 2001). In some studies, the issue of the multi-agent rescue operation is concerned. Chavoshi et al. (2008) proposed a novel agent-based model of wayfinding for rescue operation based on landmarks remained after the earthquake. Sang (2013) modelled the multi-criteria decision making and dynamic tasks allocation to simulate the rescue process in multi-agent environments. In the proposed multi agent-based rescue model, the volunteer helping a disabled person in an emergency situation was considered. Wang et al. (2014) proposed a multi-agent cooperative coverage control model for the resource assignment to provide a distributed convergent approach to the ambulance position. The Voronoi set for each ambulance was determined based on keeping track of its neighbours. As Hawe et al. (2015) have indicated the agent-based modelling of the best allocation of resources for a hypothetical two-site incidents in order to minimize transportation time of the injured to the appropriate hospital was performed. Wang and Zlatanova (2016) proposed a multi-agent system for navigation of the first responders to emergency situations due to moving obstacles such as fires, plumes, and floods. Hooshangi and Alesheikh (2018) investigated a dynamic agent-based simulation model for urban search and rescue operation after occurring of the earthquake by the employment of geospatial information system and multi agent systems. Also, the dynamic task allocation and interaction between agents in the search and rescue operation were studied. Bae et al. (2018) proposed an agent-based model for coordinating the interaction between the disaster responders in order to manage a large number of victims by considering the limitation of the resources and facilities around the disaster site.

Smart health and transportation facilities can expedite the rescue operation. In the smart city, the real-time routing of the vehicles by considering traffic flow information, street status and traffic incidents are performed that can assist decreasing the emergency vehicle response time (Li et al. 2013).

The ambulances during their tasks have strengthened their communication with the related hospitals. On the other hand, ambulances transfer information about the condition of the injured to the hospitals prior to their arrival in order to provide appropriate treatment which can improve the survival probability of the patients. Also, the ambulance can get patient's medical reports in real time (Alami-Kamouri et al. 2017).

There have been a number of studies on the rescue operations in the smart city. Alazawi et al. (2014) have developed responsive systems to deal with accidents at different scales focusing on the smart transportation systems. Information from various sources such as the network of sensors and social networks has been gathered and information aggregation and decision making have been done accordingly. Billhardt et al. (2014) proposed a dynamic coordination model for ambulances fleet that combines ambulances redeployment mechanism with the optimal assignment of ambulances to victim locations at each moment. Djahel et al. (2015a) proposed a mechanism to leverage the communication between vehicles and traffic light controllers to prevent traffic congestions and ensuring the notable reduction of commuters' travel times in most large cities worldwide. Hirokawa and Osaragi (2016) investigated the accessibility of firefighters to the location of fire immediately after an earthquake by A* algorithm. When volunteers gathered information on street blockage, the arrival time of the firefighters to the location of fire have been reduced. Alami-Kamouri et al. (2017) presented a mobile agent-based model in order to transfer the information on patient conditions from smart ambulance to a hospital and getting a patient's medical report from the hospital to the smart ambulance in real time. Azimi et al. (2017) proposed a multi-agent model for aggregating the optimal allocation of service area to emergency centers based on population density, supply, demand and distance in the street network by applying the simulated annealing optimization algorithm to the constrained network Voronoi diagrams, ambulance routing under the travel distance and time and use of smart city facilities to improve rescue operations.

In this paper, we are faced with the situation how to expedite the allocation of medical assistance to the emergency victims after some disasters or accidents, based on the facilities of smart city and modeling of the multi-agent system.

The hypothesis of this paper is that optimum allocation of the medical services to the emergency victims' locations according to the priority of emergency victims, optimum wayfinding of ambulances by considering the blockage of streets and the smart city facilities can accelerate the rescue operation.

In this paper, the coordination among the agents in the model for ambulance fleets that provide the allocation of ambulances to the injured locations based on particle swarm optimization-Multiplicatively Weighted Network Voronoi Diagram (PSO-MWNVD) is proposed. In the proposed multi agent-based model, the urban street network, population density, and the ambulances of the emergency

centers, optimum wayfinding of emergency vehicles to the injured location by considering travel distance, travel time, the street blockage and smart city facilities to improve the rescue operation are considered. The coordination center, emergency centers, ambulances, fire stations, fire engines and the wounded are modelled as agents.

In the proposed model it is assumed that the wounded delivered their locations by mobile global positioning system (GPS) and their initial symptoms to the coordination center agent.

The allocated Voronoi Diagram is determined for each emergency center. The number of ambulances are considered as the weight of the emergency centers. The Bi-label Dijkstra algorithm is used for wayfinding of ambulances in order to minimize travel length and travel time of the ambulances in the street network. Three types of multi-agent rescue operation models are implemented and their results are compared.

In the first type of the multi-agent rescue operation, the MWNVD is determined for each emergency center. The ambulances from proper emergency center based on the MWNVD that include the location of the wounded, according to the priority of the wounded and the ambulance numbers which are dispatched from the emergency center to the wounded sites are considered. This process is performed simultaneously for all the injured in different Voronoi diagrams. In the case that the ambulance capacity of each emergency center became zero, the response time to the new demand is delayed until the return of the first ambulance to the emergency center. In the case of the reported blocked street, the fire engine dispatched to the reported location.

In the second type of the multi-agent rescue operation, the PSO-MWNVD and the optimum weight for each of the emergency centers are computed. The ambulance from proper emergency center based on PSO-MWNVD according to the severity level of the wounded and the optimum ambulance numbers of the emergency center is transferred to the wounded site. The ambulances routes are updated according to blocked streets, if it is possible. Also, the ambulances are able to transfer information about the condition of the injured to the hospitals prior to their arrival in order to provide appropriate treatment. In case that all the ambulances of each emergency center are already dispatched, PSO-MWNVD for other emergency centers are activated and the rescue process is continued.

The third type of the multi-agent rescue operation model is similar to the second one with the difference that has more smart facilities. In the case of the reported blocked street, the proper fire engine dispatched to the reported location and the initial path of the fire engine is updated by considering the blocked streets. At each intersection, the traffic light phase becomes green during the passage of the emergency vehicles. After the passage of the emergency vehicles, the traffic light phase becomes red.

Finally, these three types of multi-agent rescue operation models are compared according to the optimum generated Voronoi diagrams, the arrival time of ambulances to the patient location and the length of time of ambulance's mission.

The outline of the rest of the paper is as follows. Section 2 provides the fundamental concepts for the proposed multi agent-based model. Section 3 explains the methodology of the allocation of the wounded to the emergency centers, the wayfinding of the ambulances in the disaster situation and the facilities of the smart city for accelerating the rescue operation in three types of the multi-agent rescue operation models. Section 4 explains the implementation and results of the proposed multi-agent rescue operation models. The results of the proposed models are discussed in Sect. 5. Finally, Sect. 6 presents conclusions and directions for future research.

2 Fundamental Concepts

2.1 Voronoi Diagram

The Voronoi Diagram (VD) represents the partitioning of the given space into the regions based on a set of generators such that for each generator a corresponding region is determined (Okabe et al. 1992). In our application, the two-dimensional VD is considered. Network Voronoi Diagram (NVD) is the street network based VD that is utilized for allocating service areas to each emergency centers (Okabe et al. 1992; Aurenhammer and Klein 2000). The NVD partitions the nodes and the arcs of the network. In principle there are three types of NVDs including the Node Network Voronoi Diagram, the Arc Network Voronoi Diagram and the Area Network Voronoi Diagram (Okabe et al. 1992).

The Bi-Label Dijkstra shortest path algorithm is used for the construction of the NVD.

2.1.1 Multiplicatively Weighted Network Voronoi Diagram

In Weighted Network Voronoi Diagram (WNVD), a weight is considered for all points. The weight of each generator is dissimilar in a Multiplicatively Weighted Network Voronoi Diagram (MWNVD).

By MWNVD, the demand nodes are assigned to the nearest emergency center which may cause an overloaded or underloaded problem in many VDs. The iteration process is applied to the MWNVDs in order to reduce the difference between the expected population in each MWNVD for using the services and the estimated population in the same MWNVD.

2.1.2 Particle Swarm Optimization—Multiplicatively Weighted Network Voronoi Diagram

Particle Swarm Optimization algorithms (PSO) (Yang 2010; Santosa 2006) is a metaheuristic and stochastic optimization algorithm that searches an objective spaces for attaining the best solution. Two major components of the movement of a swarming particle are a stochastic component and a deterministic component. Each particle is attracted toward the best position of their neighbourhood called global best (*gBest*) and its own best location called local best (*lBest*) in history. The position of particles is affected by velocity of the particles (Bai 2010; Engelbrecht 2006; Santosa 2006). The velocity and position of the particles are computing using Eqs. 1 and 2, respectively (Santosa 2006; Engelbrecht 2006). The $v_i(t+1)$ is the velocity of the particle i in the time step t+1, $x_i(t+1)$ denotes the position of particle i in time step t+1 and t is discrete time steps.

$$v_i(t+1) = av_i(t) + c_1r_1[lBest(t) - x_i(t)] + c_2r_2[gBest(t) - x_i(t)] \qquad (1)$$

$$x_i(t+1) = x_i(t) + v_i(t+1) \qquad (2)$$

a promotes local exploitation. c_1 and c_2 coefficients are learning rates for individual influence (cognitive component) and social influence (social component) that usually considered as 2. r_1 and r_2 are the random vectors in the range [0,1].

The procedure of PSO can be summarized as the following steps. At first, the size of the group of particles (M), the coefficients of c_1, c_2 and a are specified. Then a random swarm is generated. After selecting the objective function, the value of the objective function is computed for each particle. The initial velocity of all the particles are assumed to be zero. All of the particles move towards the optimum point with a velocity. In each iteration, the *lBest* for each particle with the lowest value of an objective function in the minimization case, *gBest*, the velocity and position of each particle are calculated.

Also, the aim of this optimization is to find the *gBest* among all the current local best solutions after a certain number of iterations (N_{max}) or until the objective improves. This process is repeated until the termination criteria is met (Rini et al. 2011).

In Particle Swarm Optimization-Multiplicatively Weighted Network Voronoi Diagram (PSO-MWNVD), the PSO algorithm is applied to MWNVD to determine optimum service areas for each emergency center.

In this paper, the number of ambulances of each emergency center is regarded as an emergency center weight. In the PSO-MWNVD algorithm, the initial position of each particle within the search space is determined by the initial weight of the emergency centers. The weight of the emergency centers is updated for each particle per iteration using Eq. 2. The process of the PSO-MWNVD continues until the difference between the demand and supply in the MWNVDs become minimum.

In the PSO-MWNVD algorithm, the mean proportional absolute error (Er) is regarded as the termination criteria to determine optimum service area for each emergency center. The error metric, Er, can be used for assessing partitioning method which is presented in Eq. 3 (Reitsma et al. 2007; Wood 1974).

$$Er = \frac{1}{N} \sum_{i=1}^{N} \frac{P_j - p_{i,j}}{P_j}$$

(3)

where $p_{i,j}$ is the estimated population of the service areas of emergency center j in iteration i as proportion of the total population. $p_{i,j}$ is get from the sum of the population in service areas of emergency center j. P_j is the expected population for receiving the medical assistance in service areas of emergency center j as proportion of the total population. N is the total number of emergency centers, respectively.

The performance of Bi-Label Dijkstra shortest path algorithm for wayfinding the ambulances to the wounded location is explained in the next section.

2.2   Bi-Label Dijkstra Algorithm

In this paper, the Bi-label Dijkstra shortest path algorithm is used for the construction of the MWNVD. Each node in the network is assigned to singular emergency center by calculating the Bi-label Dijkstra shortest path algorithm based on the minimum travel time and the travel length from the emergency center to the node in the street network.

The bi-objective shortest path problem is a development of the classical shortest path problem that is related to the class of multi-objective optimization problems. In the specific network, the Bi-objective Shortest Path Problem uses for specifying the set of non-dominated paths between nodes by optimizing the two objective functions (Ticha et al. 2017; Serafini 1987).

In the Bi-label Dijkstra algorithm, each label represents a sub path from a source node v_0 to a certain node u that is represented as $L = (u, d(L), t(L))$ where u is the ending node of the sub path L. In addition, $d(L)$ and $t(L)$ represent the total distance and the total travel time associated with the sub path, respectively.

In this paper, lexicographic order is used for comparing the labels to determine the optimum path. A vector $a = (a_1, a_2)$ is lexicographically smaller than a vector $b = (b_1, b_2)$, denoted by $a < b$ if either $a_1 < b_1$ or both $a_1 = b_1$ and $a_2 < b_2$. A path p_1 lexicographically smaller than path p_2 if and only if $(t(p_1), d(p_1)) <_{lex} (t(p_2), d(p_2))$. $d(p)$ and $t(p)$ represent the total distance and the total travel time associated with the path p, respectively (Pyrga et al. 2008).

2.3 Smart Transportation and Smart Health

In the smart city (Li et al. 2013; Bakıcı et al. 2013), better and safer living conditions for citizens, including lack of restrictions on transportation and medical care, city administration, crisis management and so on are established.

In a smart city, the real-time routing of vehicles according to traffic density information, street condition, temperature and traffic accidents are recorded by sensors (Li et al. 2013).

Intelligent transportation systems (ITS) are a symbol of smart cities. ITS centers collect and reserve real-time road traffic data from various sources to reduce traffic congestion problems (Imawan et al. 2016).

In the emergency situation, accomplishing of actions at dispatch time of the emergency vehicles for ensuring the quick possible response to an emergency is essential. Two of the emergency actions are discussed below.

The effective coordination between the emergency vehicle and the traffic light controller at each intersection is the first one. When the emergency vehicle reaches a new road segment, the current traffic light phase can be changed or its duration extended to ensure that the emergency vehicle meets green light only (Djahel et al. 2015a, b). After the passage of the emergency vehicle, the traffic light becomes red for preventing the passage of others vehicles. So, the traffic congestion at the next intersection for passage of the emergency vehicle reduced (Fig. 1).

The second action is the rerouting of the emergency vehicles in faced with some blocked streets and traffic congestion situation toward emergency situations (Djahel et al. 2015b).

To make closer a city to the smart city, improving the different areas that are part of the city such as the health sector is necessary (Alami-Kamouri et al. 2017).

In disaster response situation, if information about condition of the wounded persons are announced to hospitals prior to their arrival, the hospitals can prepare pre-arrival support to the wounded persons. So, the relevant actions about the appropriate treatment or operation can be performed in the hospitals. Also, the ambulance team can get additional information about special patients from the

Fig. 1 Coordination of emergency vehicles with lights for crossing the intersection
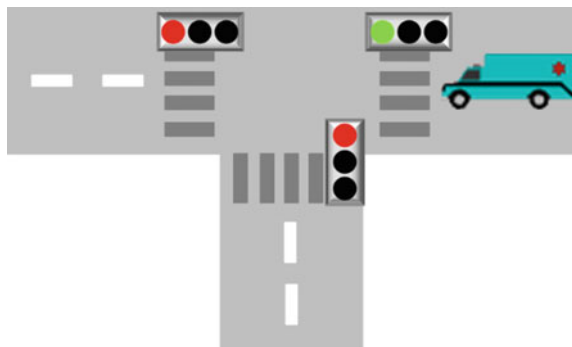
hospitals and perform proper actions. So, the ambulance team and the hospital team can more adequately response, quickly provide services to the wounded and avoid delay in commencing patient treatment (Alami-Kamouri et al. 2017; Mustafa 2013).

3 Methodology

After the occurrence of a natural disaster, the locations and initial symptoms of the wounded are delivered to the coordination center. The priority of the wounded according to their severity level is specified. The wounded with severe injuries more quickly receive the medical assistance. The service areas of emergency centers for delivering medical assistance to the wounded according to the population, supply, and the street network are determined by MWNVD and PSO-MWNVD. The number of ambulances in each emergency center is considered as an emergency center weight. The Bi-label Dijkstra algorithm is applied for wayfinding of ambulances in order to minimize the ambulances travel time and the route length in the street network.

In this study, the three types of the rescue operation models are considered. Agent-based simulation (ABS) is able to provide a natural description of the rescue operation situations. The multi agent-based rescue operation for modeling the allocation of ambulances to the injured location, reallocation of ambulances and the facilities of the smart city in order to improve the relief operation for these three types of the rescue operation models is performed.

As shown in Fig. 2, the coordination center, the emergency centers, ambulances, fire stations, fire engines and the wounded are modeled as agents in Anylogic simulation software with specific attributes and behaviours.
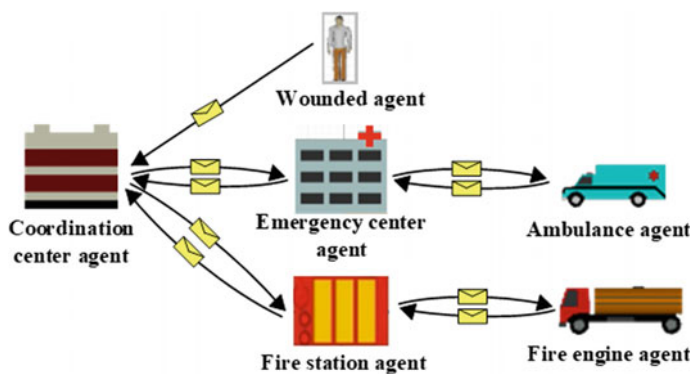

Fig. 2 The communication of agents in the proposed models (Azimi et al. 2018)

The emergency management is usually controlled by an emergency operation center. In this study, the «coordination center agent» implement the role of the emergency operation center.

The task of this agent is determination and assignment of tasks to other agents of the proposed models. The coordination center agent communicates with other agents and updates its database. The wounded agent delivers help demand to the coordination center agent. The coordination center agent determines the appropriate emergency center and assigns the task of providing medical assistance for the injured based on the information received from the injured person and according to the VDs. The coordination center agent will share reports on road blockage and the location of the wounded with other agents for considering these reports during their navigation. The coordination center agent will determine the appropriate firefighting organization according to the location of the blocked streets, the location of firefighting organizations, the number of available fire engines, and the distance as well as time of accessing the fire engines to the blocked street. Then, this agent will send the blocked street information to the determined firefighting organization.

The emergency center agent receives the information and status of the injured, updates its information and dispatches an ambulance without a mission to the injured location.

The ambulance agent receives the injured person information from the emergency center agent, is delivered to the wounded location and communicates with the emergency center agent during its mission. When the ambulance reaches a new intersection, the traffic light phase becomes green and after its passage becomes red. Also, the ambulance agent will report the coordination center agent when faced with the new blocked street that is faced and update its route accordingly. Figure 3a explains the ambulance agent responsibilities and performance from the emergency center to the injured location.

The fire station agent receives the location of the blocked street from the coordination center agent and updates its database based on new information. This agent dispatches a fire engine agent to the reported blocked street. The fire station agent continuously communicates with the fire engine agent during its mission. This agent delivers the fire engine reports about the new blocked street and the location of the new wounded to the coordination center agent. The fire station agent after the completion of the fire engine mission, will inform the coordination center agent about its preparation for accepting the new mission.

The fire engine agent actions from the fire station to the blocked street are shown in Fig. 3b. The fire engine agent, after receiving the message from the fire station agent, will dispatch to the reported blocked location. The fire engine agent is responsible for shutting down the fire and removing the related obstacles. During its mission, the initial path of the fire engine is updated in order to minimize travel time and distance. During the mission, the fire engine agent is communicated with the fire station agent and reports the performance of its mission and its preparedness for initiating a new mission. These agents inform the fire station agent in the event of encountering the blocked streets or the injured. Traffic light phase becomes green in the event of passage of the fire engine and after that becomes red.
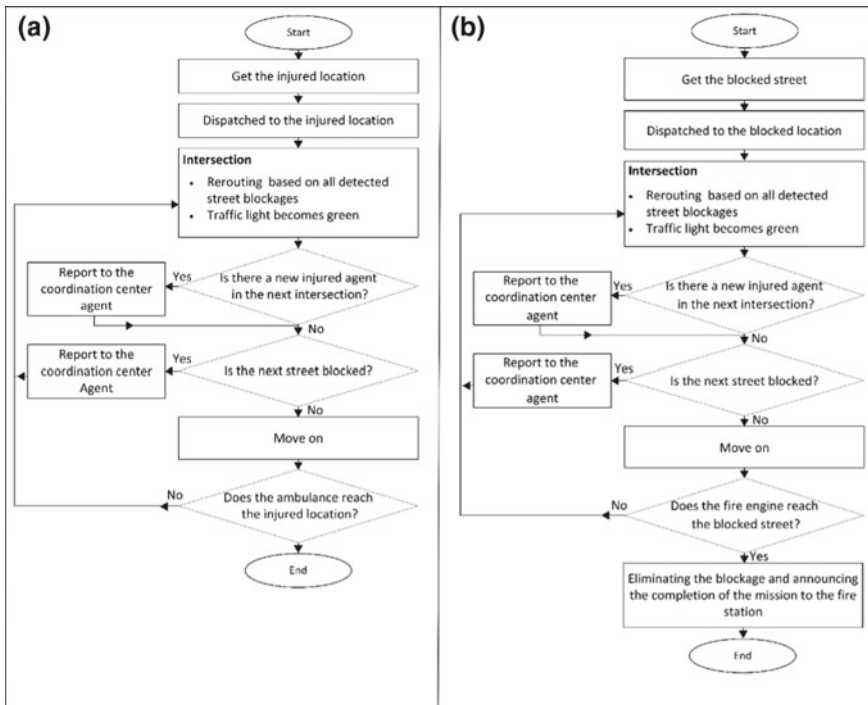
Fig. 3 **a** The ambulance agent performance from the emergency center to the injured location,
b The fire engine agent performance to complete one mission

The three types of the rescue operation models were implemented in the multi
agent-based simulation environment.

In the first type of the rescue operation model, after determining the MWNVD
for each emergency center, the proper emergency center according to the generated
MWNVDs is allocated to the demand location. The emergency center due to the
priority of the demand is delivered the ambulance to the demand location. The
ambulance route is determined according to the goals of minimizing the route
length and travel time at the beginning of its movement which is unable to update
when faced with the blocked street. So, the ambulance will be delayed until the fire
engine resolved the blockage of the street. The initial ambulance number of the
emergency center is considered in the computation. In the case that ambulance
capacity of each emergency center is fully employed, a new demand will not be
delivered to the related emergency center until at least one of the ambulances of this
emergency center completes its mission and returns to the emergency center. In this
case, the wounded demand for receiving the first aid will be answered late and the
injured survival probability reduced.

In the second type of the rescue operation model, the PSO iterative mechanism decreases the difference between the supply (the expected population lives in the region for using the services) and the demand (the estimated population lives in the region) in the MWNVD. So, the optimum PSO-MWNVD and optimum ambulance number for each emergency center are determined. The ambulance from proper emergency center that is located in PSO-MWNVD including the location of the wounded, according to the severity level of the wounded and the existing ambulances of the emergency center is dispatched to the wounded location. During the mission, the ambulance can benefit from the smart city facilities that are explained below. The optimum ambulance route is specified in order to minimize the route length and the travel time at the beginning of its movement. If the ambulance is faced with some blocked streets, the optimum route from the current location to the destination is re-calculated. The ambulance on the way back from the injured location to the emergency center, is able to send the name and the current state (such as heart rate, body temperature, blood pressure and blood type) of the injured to the hospital. Figure 4 shows[1] the list of some relevant information about the condition of the patients en route to the hospital[2]. Figure 5 shows the two-way communication between the hospital and the ambulance. In the case that the ambulances of many emergency centers during the mission are fully employed, responding to the new demand is different form the first type of the multi-agent rescue operation model. In this case, PSO-MWNVD is re-calculated for the emergency centers that have free ambulances and the rescue operation process is continued.

The third type of the rescue operation model is similar to the second one with the difference that it has more smart facilities. When the emergency vehicle arrives at each intersection during its mission, the traffic light phase becomes green until the emergency vehicle passes. After the passage of the emergency vehicle, the traffic

Identification			
Name:	Time:	Date:	Chief complaint:
SSN[1]:	Age:	Gender:	Phone number:
Vital Signs			
Pulse Rate:	Blood Type:	Right Pupil:	Blood Pressure:
Body Temprature:	Respiration:	Left Pupil:	SPO2[2]:
Status			
Perfusion:	Burns:	Skin Condition:	Wounds:
Mental State:	Bleeding:	Skin Color:	Fractures:

Fig. 4 List of information about condition of the wounded by the ambulance to the hospital (Azimi et al. 2018) (Social Security Number) (Blood Oxygen Saturation Level)

---

[1]Social Security Number

[2]Blood Oxygen Saturation Level

Fig. 5 The two-way communication between the ambulance and the hospital (Azimi et al. 2018)
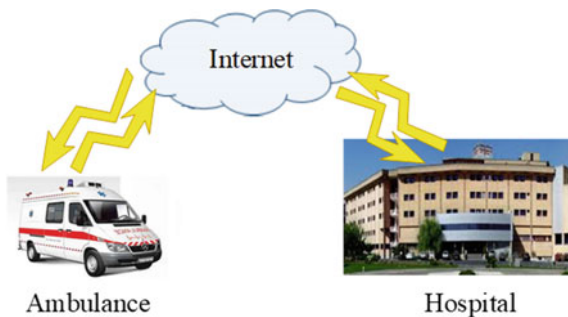
light phase becomes red. Therefore the traffic congestion at the next intersection for passage of the emergency vehicle will reduce and the chance of saving the lives of the injured increase. Also, after the detection of the new blocked street, the appropriate fire engine is dispatched to the reported location and the initial path of the fire engine is updated by considering the blocked streets.

4 Implementation

The proposed multi-agent rescue operation models are implemented in a part of Tehran municipal District 5. Figure 6 represents the study area that is limited to the Hakim highway from North, the Sanaye Havapeymayi Street and Sattari highway from West, the Lashkari highway from South and the Jenah highway from East.

The topographic map of National Cartographic Center (NCC) at the scale of 1:2000 was used in this study. The emergency center part of the Sarem Specialist hospital, Ebne Sina hospital, Fatemeh Zahra health center and Payambaran hospital
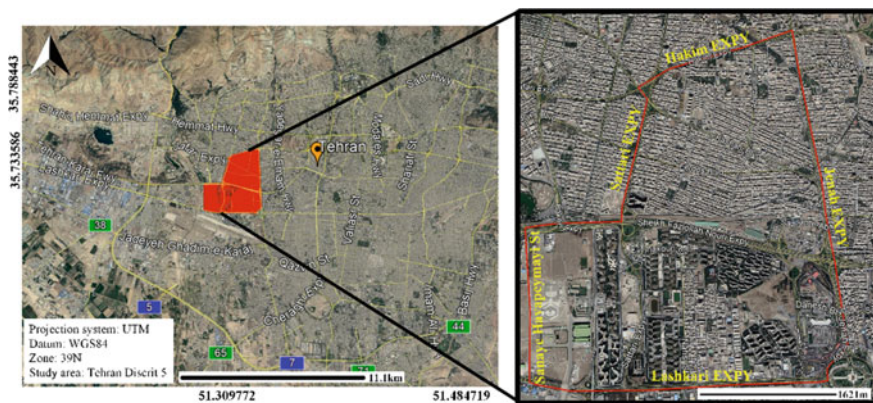
Fig. 6 The study area
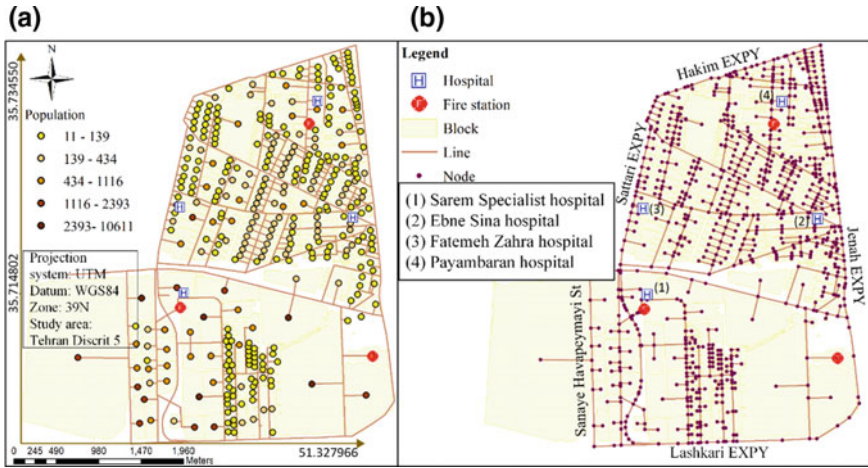
Fig. 7 **a** The population density in the study area, **b** The study area

are located in Tehran municipal District 5 that have 3, 4, 1, and 5 ambulances which are shown in Fig. 7.

The locations of emergency centers were acquired from Tehran municipality District 5. Also, the studied fire stations and population density of the study area are represented in Fig. 7. The travel time of the vehicles on the urban street network of Tehran municipal District 5 in 2017 is obtained from Municipality of Tehran Transport and Traffic Company.

In this paper, MWNVD and PSO-MWNVD allocation for the emergency center are investigated. The generated MWNVDs and PSO-MWNVDs for the studied
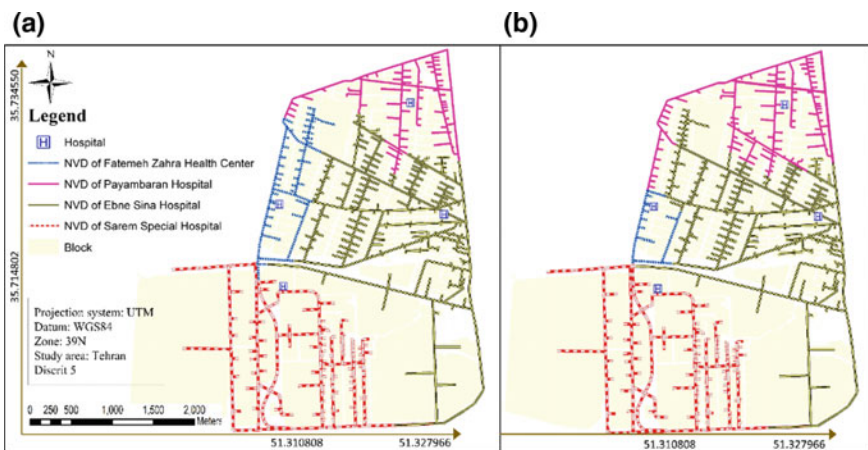
Fig. 8 **a** The generated PSO-MWNVDs, **b** The generated MWNVDs

Fig. 9 Diagram of the PSO optimization of the MWNVD
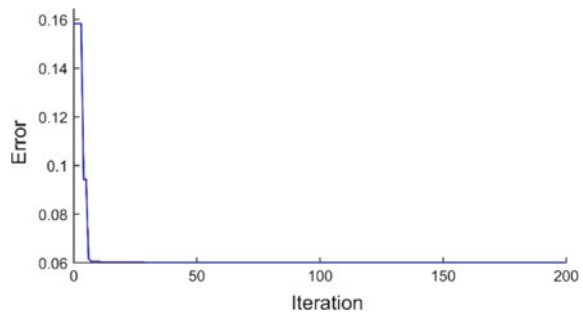
emergency centers are presented in Fig. 8. The optimum values for the parameters of PSO are determined in order to minimize Er for the VDs. The optimum values of c_1, c_2, a and population size are selected to be 2, 2, 0.7 and 200, respectively. PSO is reached to the optimal mode of MWNVD in 200 iterations.

The changing of mean partial absolute error of PSO-MWNVD in 200 iterations is presented in Fig. 9. As shown in Fig. 9, the PSO algorithm with a relatively high speed in 12 iterations has achieved value of 6% error. While the Er error of MWNVD allocation is computed about 37%.
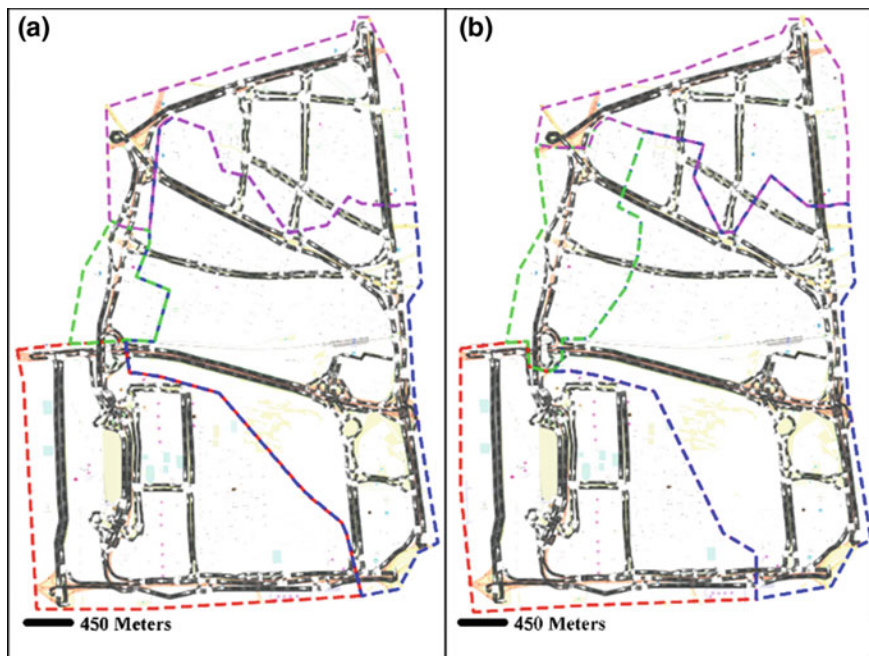
Fig. 10 a The generated MWNVDs in Anylogic software, **b** The generated PSO-MWNVDs in Anylogic software

In this study, seventeen wounded with varying level of injuries and the random position were considered. The four above mentioned hospitals must be assigned to these wounded. The process of implementation is explained in the methodology section. The generated MWNVDs and PSO-MWNVDs in Anylogic are shown in Fig. 10. The initial VDs allocated to Sarem Specialist hospital, Ebne Sina hospital, Fatemeh Zahra health center and Payambaran hospital are called "VD$_1$", "VD$_2$", "VD$_3$" and "VD$_4$", respectively.

In the first type of the multi-agent rescue operation model, the six wounded are located in VD$_1$, the two wounded are located in VD$_2$, the three wounded are located in VD$_3$ and one wounded is located in VD$_4$. After delivering the help demand messages to the coordination center agent, the necessary actions are undertaken and

Fig. 11 The generated PSO-MWNVD for the emergency centers that have the free ambulances when **a** the ambulances of the Sarem Specialist hospital, **b** the ambulances of the Ebne Sina hospital, **c** the ambulances of the Fatemeh Zahra health center and **d** the ambulances of the Payambaran hospital are not available

the ambulances dispatched to the demand locations according to the generated MWNVDs.

In VD_1, the number of demands is more than the ambulance numbers available in Sarem Specialist hospital. In this condition, the three wounded that have high priority are served first. The other three wounded wait until the ambulances become available again upon termination of their mission. When one of the ambulances have undertaken its mission, the high priority of these remained wounded are responded. Also, this trend is continued for the two remained wounded. The assignment process in VD_3 is similar to VD_1. Due to the fewer wounded than existing ambulances in VD_2 and VD_4, the wounded people get immediate medical assistance.

In the second and third types of the multi-agent rescue operation models, the location and the priority of the wounded are the same as the first type of the multi-agent rescue operation model. Four, two, five and one demands initially are located in VD_1, VD_2, VD_3 and VD_4 based on PSO-MWNVDs, respectively. Due to the more wounded than ambulances in VD_3, the re-allocation processing for Sarem Specialist, Ebne Sina and Payambaran hospitals were performed. After determining the new PSO-MWNVD for these three hospitals (Fig. 11c), the condition of the location of the remained three wounded against PSO-MWNVD are determined which are located in the PSO-MWNVD of the Payambaran hospital, Payambaran hospital and Ebne Sina hospital, respectively.

So, with this reallocation process, these five wounded persons are responded faster than the first type of multi-agent rescue operation model. In VD_1, VD_2 and VD_4, the ambulances are more than the wounded and the wounded who are located in theses VDs can receive medical assistance with no delay. After several minutes, a number of wounded send help demand to the coordination center agent. The
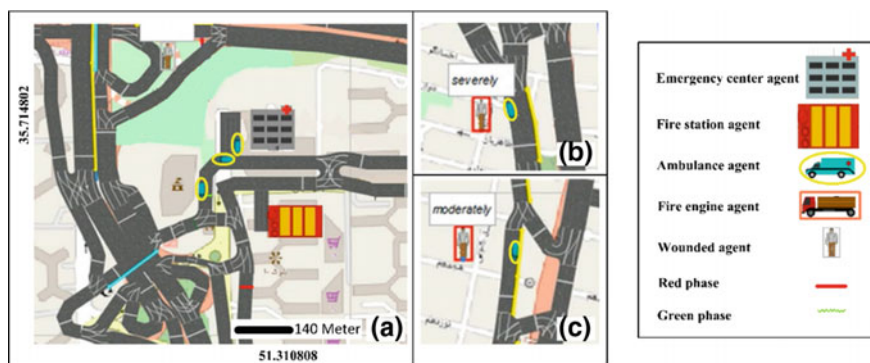
Fig. 12 The actions of the ambulance agent. **a** Assignment of the tasks to the ambulances located in the Sarem Special hospital, **b** Reaching the ambulance to the wounded locations with severe injury levels, **c** Reaching the ambulance to the wounded with moderate injury levels

assignment process is again performed for the new demands. Figure 12 shows the ambulances allocation and actions in Anylogic simulation software.

Figures 13 and 14 show the ambulances and fire engines tasks and actions in the three types of the multi-agent rescue operation models in Anylogic simulation software.

The third type of multi-agent rescue operation model has some facilities for decreasing delay of the emergency vehicles in intersections and increasing the survival chance of the injured in comparison to the second one. The time

Fig. 13 The actions of the ambulance and fire engine agents. **a** and **b** Updating of the ambulance route when faced with the blocked street in the second and third type of the multi-agent rescue operation model, **c** Resolving the blocked street by the fire engine in the first type of the multi-agent rescue operation model, **d** Resolving the blocked street by the fire engine in the second and third types of the multi-agent rescue operation models
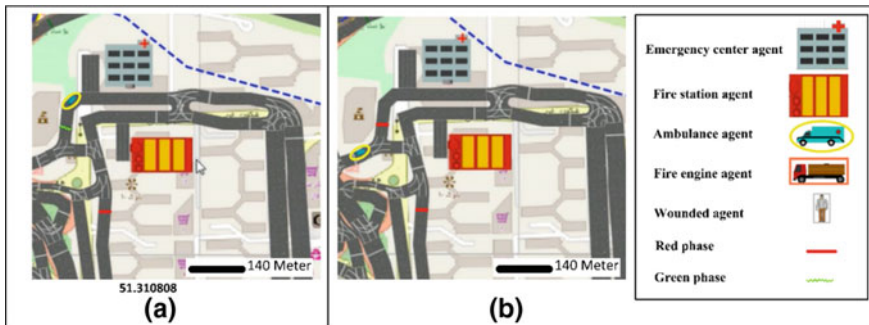
Fig. 14 The actions of the ambulance agent in the third type of the multi-agent rescue operation model. **a** The traffic light phase becomes green during the passage of the ambulance, **b** The traffic light phase becomes red after the passage of the ambulance

performance of the third type of the multi-agent rescue operation model has the better result in comparison to other models.

Mustafa (2013) has shown that if the ambulance sends patient data to the hospital prior his/her arrival, the treatment preparation in the hospital will expedite about two minutes. These results are applied in the implementation of this research.

The diagram of response time of the ambulances to the injured persons and the diagram of the duration time of the ambulance missions for the first, second and third types of the multi-agent rescue operation models are shown in Figs. 15 and 16, respectively. In Figs. 15 and 16, the ambulance response time to the wounded persons for the first, second and third types of the multi-agent rescue operation models are demonstrated in red, green and yellow colours, respectively.
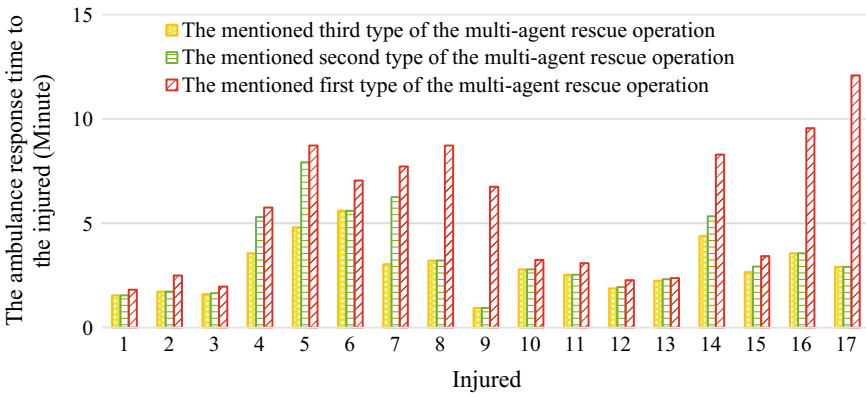
Fig. 15 The diagram of arrival time of the ambulances to the injured location
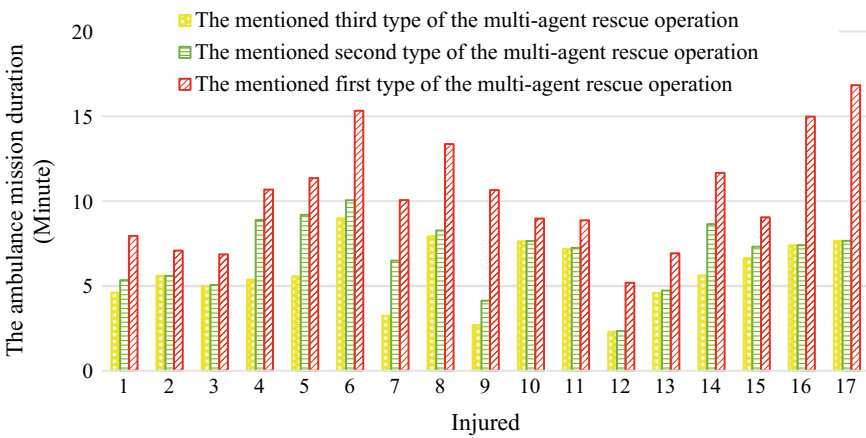
Fig. 16 The diagram of the ambulance mission time in order to respond to the injured

Table 1 The time improvement of the second and third types of rescue operation models compared to the first one

	The second type of the multi-agent rescue operation model compared to the first one	The third type of the multi-agent rescue operation model compared to the first one
The improvement of the average response time of the ambulances to the injured (%)	29.7	37.7
The improvement of the average of the ambulance mission duration (%)	32.6	42.5

According to the Table 1, the improvement of the average response time of the ambulances to the wounded persons and the average of the ambulance mission duration in the second and third types of the multi-agent rescue operation models in comparison to the first type of the multi-agent rescue operation model are computed as 29.7%, 32.6%, 37.7% and 42.5%, respectively.

5 Discussion

Using the Voronoi Diagram method to determine the service areas for each emergency center in many cases causes some emergency centers have the load more than their capacity and some of them have the shortage of the load, or if all of them have additional or lack of load, these amounts are not the same. Therefore, the PSO algorithm is used to solve these problems. The PSO-MWNVD algorithm improved the *Er* about 31% and decreased the *Er* to 6% at a relatively high speed. By applying the PSO on MWNVD in the second and third types of the multi-agent rescue operation models and wayfinding of emergency vehicles based on the minimum travel distance and time as well as utilizing smart city facilities, the ambulance performance for saving the injured is improved (Figs. 15 and 16). Updating the fire engine routes based on the blocked streets will prevent them from delaying. Therefore, the delivery of assistance to the wounded location will improve by removing obstacles quickly. Also, greening the traffic light in order to expedite the passage of the emergency vehicles from the intersections will cause the quick response to the injured and increase their survival probability. Therefore, consideration of the mentioned additional parameters in the third type of rescue operation model in comparison to the second one cause the average response time of the ambulances to the injured and the average of the ambulance mission duration decrease about 8 and 10% compared to the second one (Table 1).

6 Conclusion

Search and rescue of victims is an important issue in the disaster management. After occurring a disaster, the navigation of the first responders in the presence of obstacles and blocked streets for decreasing delay is necessary. Also, the efficient planning of appropriate allocation of the medical assistance to the disaster site is critical in response to the disaster.

In this study, the multi agent-based model for optimum allocation of the ambulances to the wounded locations according to the urban street network, population density, the number of ambulances exist in emergency centers, optimum wayfinding of emergency vehicles to the injured locations, the street blockage and smart city facilities to expedite the relief operation is proposed. The proposed rescue operation models using the multi agent-based model consists of coordination center, emergency centers, ambulances, fire stations, fire engines and the wounded agents.

After occurring the disaster, the wounded delivered their locations and initial symptoms to the coordination center agent. The rescue operation starts when the location and initial symptoms of the wounded are delivered to the coordination center agent. The severity levels of the patients' injury are directly relevant to the priority that should be given to each patient for receiving the medical assistance. The Bi-label Dijkstra algorithm is used for routing of the ambulances under the objective of minimizing travel length and time of the ambulances in the street network. The three types of multi-agent rescue operation models were implemented and their time performance for surviving the injured were compared. In the first one, the MWNVD allocation for determining the service areas of each emergency center is performed. After specifying the associated MWNVD for each wounded agent, the ambulance is delivered from the emergency center of the concerned MWNVD to the wounded agent location. In the case of high demand, if there is an available ambulance located in the emergency center, the allocation is performed, in order to prevent the injured remained helpless.

In the second type of the multi-agent rescue operation model, the PSO-MWNVD allocation specified the optimum service areas for the emergency centers. The ambulances routes are updated once facing with the blocked street. When the rescue operation workload exceeds the available ambulances of one or more emergency centers, the PSO-MWNVD allocation is performed again for another emergency centers as far as the new demanded wounded received medical assistance with no delay. Also, the information about the condition of the injured have been transferred to the hospitals prior to their arrival.

The third type of the multi-agent rescue operation model is similar to the second one with the difference that it has more smart facilities. Greening traffic lights when the passage of the emergency vehicles from the intersections and updating the route of the fire engine during its mission are considered in the third type of the rescue operation model compared to those of the second one. In PSO-MWNVD allocation, the partial difference between the estimated and expected population in VDs

decreased to 6%. While the mentioned difference computed as 37% in the MWNVD allocation. The implementation results of the multi-agent rescue operation models show that the second type of the multi-agent rescue operation model decreased the average response time of the ambulances to the injured and the average of the ambulance mission duration about 29.7 and 32.6% compared to those of the first one, respectively. Also, the average response time of the ambulances to the injured and the average of the ambulance mission duration improved about 37.7 and 42.5% in the third type of multi-agent rescue operation model compared to those of the first one.

Our future work will be focused on more facilities of the smart city for improving the relief operation such as using the social media in the disaster management. The implementation of the proposed model by using other agent-based software platforms such as GAMA, Agent Analyst, RoboCup and their comparative analyses can be considered. The navigation of relief groups among moving obstacles can be investigated in the proposed model. Also, considering more agents such as police forces and Red Crescent agents in the multi agent-based model will bring the implementation closer to the reality.

References

Alami-Kamouri S, Orhanou G, Elhajji, S (2017) Mobile agent service model for smart ambulance. In Cloud Infrastructures, services, and IoT systems for smart cities, Springer, pp 105–111

Alazawi Z, Alani O, Abdljabar MB, Altowaijri S, Mehmood R (2014) A smart disaster management system for future cities. In Proceedings of the 2014 ACM international workshop on wireless and mobile technologies for smart cities, ACM, pp 1–10

Andersson T, Varbrand P (2007) Decision support tools for ambulance dispatch and relocation. J Oper Res Soc 58(2):195–201

Aurenhammer F, Klein R (2000) Voronoi diagrams. Handb Comput Geom 5:201–290

Azimi S, Delavar MR, Rajabifard A (2017) Multi-agent simulation of allocating and routing ambulances under condition of street blockage after natural disaster. Paper presented at the international archives of the photogrammetry, remote sensing and spatial information sciences, SMPR and EOEC 2017, 7–10 Oct 2017

Azimi S, Delavar MR, Rajabifard A (2018) An optimized multi agent-based modeling of smart rescue operation, The International Archives of the Photogrammetry, Remote Sensing and Spatial Information Sciences, Paper presented at the 2018 GeoInformation for disaster management (Gi4DM), Istanbul, Turkey, 18–21 Mar 2018

Bae JW, Shin K, Lee HR, Lee HJ, Lee T, Kim CH, Cha WC, Kim GW, Moon IC (2018) Evaluation of disaster response system using agent-based model with geospatial and medical details. IEEE Trans Syst Man Cybern Syst 48:1454–1469

Bai Q (2010) Analysis of particle swarm optimization algorithm. Comput Inf Sci 3(1):180

Bakici T, Almirall E, Wareham J (2013) A smart city initiative: the case of Barcelona. J Knowl Econ 4(2):135–148

Bandara D, Mayorga ME, Mclay LA (2014) Priority dispatching strategies for EMS systems. J Oper Res Soc 65(4):572–587

Billhardt H, LujaKk M, Sanchez-Brunete V, Fernandez A, Ossowski S (2014) Dynamic coordination of ambulances for emergency medical assistance services. Knowl Based Syst 70:268–280

Bostick NA, Subbarao I, Burkle FM, Hsu EB, Armstrong JH, James JJ (2008) Disaster triage systems for large-scale catastrophic events. Disaster Med Public Health Preparedness 2(S1): S35–S39

Chavoshi SH, Delavar MR, Malek MR, Frank A (2008) Landmark-based simulation for agent Wayfinding after earthquake

Djahel S, Jabeur N, Barrett R, Murphy J (2015) Toward V2I communication technology-based solution for reducing road traffic congestion in smart cities. Paper presented at the International symposium on Networks, computers and communications (ISNCC), IEEE, 13–15 May 2015a

Djahel S, Smith N, Wang S, Murphy J (2015) Reducing emergency services response time in smart cities: An advanced adaptive and fuzzy approach. Paper presented at the 2015 IEEE First international smart cities conference (ISC2), 25–28 Oct 2015b

Engelbrecht AP (2006) Fundamentals of computational swarm intelligence. John Wiley and Sons

Fiedrich F, Gehbauer F, Rickers U (2000) Optimized resource allocation for emergency response after earthquake disasters. Saf Sci 35(1–3):41–57

Ghomian Z, Yousefian S (2017) Natural disasters in the Middle-East and North Africa With a focus on Iran: 1900 to 2015. Health Emerg Disasters Q 2(2):53–62

Gong Q, Batta R (2007) Allocation and reallocation of ambulances to casualty clusters in a disaster relief operation. IIE Trans 39(1):27–39

Haghani A, Hu H, Tian Q (2003) An optimization model for real-time emergency vehicle dispatching and routing. Paper presented at the transportation research board 82nd annual meeting, Washington, DC, 12–16 Jan 2003

Hawe GI, Coates G, Wilson DT, Crouch RS (2015) Agent-based simulation of emergency response to plan the allocation of resources for a hypothetical two-site major incident. Eng Appl Artif Intell 46:336–345

Hirokawa N, Osaragi T (2016) Access time of emergency vehicles under the condition of street blockages after a large earthquake. ISPRS Annals of the Photogrammetry, Remote Sensing and Spatial Information Sciences, Paper presented at the 1st international conference on smart data and smart cities, 7–9 Sep 2016

Hooshangi N, Alesheikh AA (2018) Developing an agent-based simulation system for post-earthquake operations in uncertainty conditions: a proposed method for collaboration among agents. ISPRS Int J Geo-Inf 7(1):27

Ibrion M, Mokhtari M, Parsizadeh F, Nadim F (2015) Timescape of the earthquake disasters in Iran: the intricacies of earthquake time and earthquake disaster risk reduction. Geografiska Annaler Ser A Phys Geogr 97(1):197–216

Imawan A, Indikawati FI, Kwon J, Rao P (2016) Querying and extracting timeline information from road traffic sensor data. Sensors 16(9):1340

Karimi F, Delavar M, Mostafavi M (2009) Space allocation of educational centers using multiplicatively weighted voronoi diagram. In WG II/2, II/3, II/4: Workshop on Quality, Scale and Analysis Aspects of City Models

Li D, Shan J, Shao Z, Zhou X, Yao Y (2013) Geomatics for smart cities-concept, key techniques, and applications. Geo-spatial Inf Sci 16(1):13–24

Li X, Zhao Z, Zhu X, Wyatt T (2011) Covering models and optimization techniques for emergency response facility location and planning: a review. Math Methods Oper Res 74(3): 281–310

Lopez B, Innocenti B, Busquets D (2008) A multiagent system for coordinating ambulances for emergency medical services. IEEE Intell Syst 23(5)

Mustafa A (2013) Wireless applications of GIS in dynamic platforms: a case study in laptops and mobile phones. PhD Thesis, Mangalore University, India

Okabe A, Boots B, Sugihara K, Chiu S (1992) Spatial tessellations: concepts and applications of Voronoi diagrams. Chichester, UK

Pyrga E, Schulz F, Wagner D, Zaroliagis C (2008) Efficient models for timetable information in public transportation systems. J Exp Algorithmics (JEA) 12:2–4

Reitsma R, Trubin S, Mortensen E (2007) Weight-proportional space partitioning using adaptive Voronoi diagrams. Geoinformatica 11(3):383–405

Rezayan H, Najian A (2008) Land use allocation optimization using advanced geographic information analyzes. World Appl Sci J 3:136–142

Rini DP, Shamsuddin SM, Yuhaniz SS (2011) Particle swarm optimization: technique, system and challenges. Int J Comput Appl 14(1):19–26

Roozemond DA (2001) Using intelligent agents for pro-active, real-time urban intersection control. Eur J Oper Res 131(2):293–301

Rusell S, Norvig P (2003) Artificial intelligent: a modern approach

Sang TX (2013) Multi-criteria decision making and task allocation in multi-agent based rescue simulation. PhD Thesis, Japan Graduate School of Science and Engineering, Saga University, Japan

Santosa B (2006) Tutorial Particle Swarm Optimization. Kampus ITS, Sukolilo Surabaya, p 66

Serafini P (1987) Some Considerations About Computational Complexity for Multi Objective Combinatorial Problems. Recent Advances and Historical Development of Vector Optimization. Springer, Berlin, Heidelberg:222–232

Talarico L, Meisel F, Sorensen K (2015) Ambulance routing for disaster response with patient groups. Comput Oper Res 56:120–133

Ticha HB, Absi N, Feillet D, Quilliot A (2017) A solution method for the Multi-destination Bi-objectives Shortest Path Problem. Ecole des Mines de Saint Etienne, CMP, Gardanne, France

Wang Y, Colledanchise M, Marzinott A, Ogren P (2014) A distributed convergent solution to the ambulance positioning problem on a streetmap graph. IFAC Proc Vol 47(3):9190–9196

Wang z, Zlatanova S (2016) Multi-agent based path planning for first responders among moving obstacles. Comput Environ Urban Syst 56:48–58

Wood L (1974) Spatial interaction and partitions of rural market space. Mag Econ Soc Geogr 65 (1):23–34

Yang XS (2010) Engineering optimization: an introduction with metaheuristic applications. John Wiley and Sons

Yue Y, Marla L, Krishnan R (2012) An efficient simulation-based approach to ambulance fleet allocation and dynamic redeployment. Paper presented at the AAAI on artificial intelligence, 22–26 Jul 2012

Zhuang J, Bier VM (2007) Balancing terrorism and natural disasters—defensive strategy with endogenous attacker effort. Oper Res 55(5):976–991

Part III
Landslide Monitoring

CitSci as a New Approach for Landslide Researches

Sultan Kocaman and Candan Gokceoglu

Abstract Landslide is a commonly and frequently observed disaster on the Earth both spatially and temporally. The landslide researches mainly aim at characterizing and understanding this process and the earth dynamics, and predicting their occurrence based on triggering factors, their spatial and temporal dimension, thus assess the hazard potential; and estimating the risks which they cause on the economy, environment, and lives. Due to the great variety and amount of data included in this field, it is crucial to form complete landslide databases both at regional level and worldwide. The main aim of this assessment is to bring new insights to the landslide data acquisition aspect by different users. The need of accurate and reliable geodata collection by ordinary people is inevitable for ensuring sufficient spatiotemporal density and distribution, thus forming extensive landslide databases and simulating and planning the future. With the developments in geoinformation technologies, as well as the transforming power of information and communication technologies (ICT) on the society, it became possible to use the citizen science (CitSci) methods in many scientific fields. It has as well enormous potential in landslide data collection, validation and interpretation, and thus contribute to landslide researches. In this review, the uncertainties lead by missing data and affecting quality of regional landslide assessments are discussed, and the potential of citizen science in landslide researches is described. The role of volunteer data is portrayed with specific examples from the literature. The levels of citizen contribution are depicted accordingly.

S. Kocaman · C. Gokceoglu (✉)
Department of Geomatics Engineering, Hacettepe University,
06800 Beytepe Ankara, Turkey
e-mail: cgokce@hacettepe.edu.tr

S. Kocaman
e-mail: sultankocaman@hacettepe.edu.tr

161

1   Introduction

With the rise of human population and climate change, the occurrence of the extreme weather events has increased considerably. Such events result in increases in the numbers and the severity of natural hazards such as flooding, wildfire, droughts, landslides etc. Among those, landslide is perhaps the most dangerous because it occurs frequently throughout the World and cause serious economic losses and also life threatening situations.

Nowadays, almost all extreme events are being recorded with the help of the developments in ICT, which also assist disaster-related studies. Cutter et al. (2015) have stated that the annual global economic losses from geophysical, hydro-meteorological and climatological events could double from 2005 levels to 2030 and exceed US$300 billion; and climate change, globalization, technological change, urbanization and political and economic instability risk more lives and assets. For sustainable societies, improved disaster-risk management and resilience is essential and an important focus both at local and global level. United Nations (UN) adopted 17 Goals (aka 2030 goals), on September 25th 2015 at the Summit to end poverty, protect the planet and ensure prosperity for all as part of a new sustainable development agenda (UN Sustainable Development Goals 2018). With these goals, all countries will mobilize efforts to end all forms of poverty, fight inequalities and tackle climate change, while ensuring that no one is left behind.

CitSci is an emerging research field and a scientific approach, which investigates the fundamentals of the participation of ordinary people and non-professionals to scientific processes at various levels (e.g. data collection, interpretation, analysis, quality control, hypothesis generation and testing, etc.). This encourages democratic engagement of people and increase public awareness for solving up-to-date problems of societies, thus lets the societies to deal with complex modern problems. There is a growing public interest for research projects involving CitSci (Silvertown 2009); and it can be critical to achieve the aims of especially earth and ecosystem-related research projects and also to achieve the sustainability goals. The number of CitSci projects running in these domains, especially in environmental monitoring, biodiversity research, urban studies, etc. have increased rapidly during the last decades. The trends in open science and open data; the increase in the availability and the variety of open educational resources; and the policy changes supporting open government data in many countries can help to increase public awareness in CitSci projects and thus achieve the 2030 Goals.

The developments in geospatial technologies have a significant and bidirectional role in CitSci projects. While providing the necessary tools and infrastructure for different CitSci themes, the geoinformation science benefits significantly from the geodata collected by volunteers. Goodchild (2007) has coined the term Volunteer Geographical Information (VGI) and underlined that people are not only consumers of maps but also producers. Every human can be considered as a sensor for our environment and forms the network of human sensors with over 6 billion components, where each has an intelligent synthesizer and interpreter of local

information. The VGI provides an effective use of this network, enabled by Web 2.0 and the technology of broadband communication (Goodchild 2007). In their extensive literature review, See et al. (2016) have listed the other frequently used terms for VGI, such as geographic citizen science, crowdsourced geographic information, mashup, neogeography, web mapping, participatory sensing, etc. Haworth and Bruce (2015) have stated that disaster management is also an important area in which VGI has value.

Kocaman et al. (2018) has listed the potential application areas of CitSci for disaster management, inspired by the categories and potential indicators to climate change and impacts and responses as summarized in the National Climate Assessment Report (2011). These application areas are modified here and categorized as pre-, during- and post-disaster (Fig. 1). Each of these stages can be explained with specific examples, although the list can easily be extended with further use cases.

For example, as a pre-disaster stage contribution, the volunteers can help with the planning, geomorphological characterization, production of disaster susceptibility maps, and lifeline and infrastructure site selection. Capacity building, increasing public awareness, ensuring comprehensive environmental monitoring and protection are also key benefits of pre-disaster stage. Examples to the environment-related CitSci projects implemented in the last two decades can be given from meteorological measurements by volunteers through recording the temperature, precipitation or extreme weather events (World Meteorological Organization 2001); air pollution monitoring (Scott and Barnett 2009); biodiversity monitoring (Firehock and West 1995; Sorte et al. 2016; Singh et al. 2018), etc. Recently large-scale projects, which combine CitSci with landslide hazard assessments (Research Councils UK 2018; Landslide EVO 2018; USGS Landslide Hazards Program 2018), have also been initiated.

Pre-disaster	During-disaster	Post-disaster
➢ Suitable site selection	➢ Application of emergency plans	➢ Damage assessment
➢ Risk assessment	➢ Application of evacuation plans	➢ Monitoring long-term effects
➢ Capacity building	➢ Data collection and validation	➢ Cost assessment
➢ Early-warning system	➢ Aid provision	➢ Performance assessment
➢ Planning		
➢ Education		

Fig. 1 Potential contributions of CitSci in natural disaster management (modified after Kocaman et al. 2018)

At the post-disaster stage, the immediate contributions can be categorized as preparation and implementation of rescue and evacuation plans, mapping of transportation status, schools, hospitals, and other public buildings (Kocaman et al. 2018). For the long term, the monitoring of post-disaster effects on the environment, preparation of damage maps, performance assessment of the susceptibility methods and mitigation plans, and preparation of cost inventories can be listed.

The use of CitSci and VGI during disasters have also been increasing significantly. The first examples can be given from Haitian Earthquake in 2010, where web-based mapping services have been used for Haiti relief effort (Zook et al. 2010). The Ushahidi platform was developed to map the post-election violence in Kenya in 2008 (https://www.ushahidi.com/). The Peta Jakarta Project (www.peta-jakarta.org, Holderness and Turpin 2017), has been developed as a close collaboration of university, local government and social media (Twitter). An earthquake damage reporting system developed by Liang et al. (2017) let the citizens to collect after-earthquake field observations for ground damages, such as surface fault rupture, landslide-triggered dam or lake, rock fall, liquefaction, etc.

Apart from the disaster risk, CitSci can contribute to geoscience researchers in general, although examples of using volunteer data in geosciences are limited in the literature. Lewis and Park (2018) investigated the usability of social media videos (You Tube) in physical geographical processes and concluded that VGI and CitSci have advanced academic and public understanding of geographical and ecological processes.

Although landslide is an ordinary earth surface process, it has become among the most disruptive disasters, due to the increases in human population and anthropogenic activities, as well as the lack of proper planning and analysis of its effects. Landslides cause serious harmful and destructive effects on the environment, e.g. the quality of surface waters; agricultural activities; forests; man-made structures, e.g. roads, railways, buildings, infrastructures, lifelines; economy and human lives. The characterization and prediction stages of landslides are quite complex due to the nature of the phenomena. Therefore, the landslide researches deal with a great variety and quantity of data in four dimensions, i.e. 3D geolocation and time as the fourth dimension. All components related to the earth surface characteristics and processes, anthropogenic activities and triggering elements are involved in these data. Among them, the most important and commonly available or used ones are the geomorphological and geotechnical data, soil type, land use (e.g. agricultural activities, urban and rural set-ups, industrial zones, mining, etc.), land cover (e.g. vegetation types, forests, buildings, roads, etc.), seismicity, meteorological events, man-made structures and economic investments (e.g. transportation, schools, hospitals, factories, bridges, etc.), information about past landslides, and most importantly the number of inhabitants or the size of the population.

With the advancements in geoinformation technologies, i.e. data acquisition techniques, e.g. terrestrial data collection using hand-held devices and smartphones, spaceborne and airborne images; storage and management of large datasets in spatially enabled database management systems; presentation of the data to the public via web- and mobile-GIS (geographical information systems) using proper

geo-visualization approaches; it has become possible to form complete landslide databases both at regional level and worldwide. Although major issues such as the integration of multi-platform data with varying quality, interoperability between different software and databases, differences in terminologies, language barriers, the need of new policies at governmental level and worldwide, and the availability of trained users still exist, the future is quite promising in this field.

The landslide researches can also benefit from CitSci, as described in the following sections in detail. To start with, landslide susceptibility mapping and hazard assessment can be carried out with higher accuracy and reliability with the provision of more on-site data and uncertainties can be reduced in this way. On the other hand, the risk assessment and management stages, which are performed after the hazard determination can also benefit from CitSci as categorized in Fig. 1. As an example, the landslide reporter website, launched on March 22, 2018 by NASA, aims at building a global landslide inventory based on the data collected by citizen scientists, and this ongoing activity emphasizes the importance of volunteer data collection for this purpose (NASA Landslide Reporter 2018). The characterization and the determination of the runout distances after a landslide is an example of post-disaster assessments, and this distance can be predicted using the information from locals and past cases. One example for runout distance assessment is given by Ocakoglu et al. (2002), where the velocity and the distance of a major landslide have been assessed with the observations of local eyewitnesses. In addition, they have explained the mechanism of the landslide with these observations together with the topography, morphology and land cover. The prediction of the runout distance at the pre-disaster stage would affect the infrastructure and construction planning at regional level, and also would be useful for evacuating people at the during- or post-disaster stage.

The main goals of this study are; (a) to discuss the importance of the spatially and temporally dense and accurate data for landslide researches; (b) and to introduce the need of using *citizen science* methods for coping with the uncertainties caused especially by the lack of reliable temporal data. The importance and the different aspects of landslide researches, and the state-of the art and future challenges in this field are provided in Sect. 2. In Sect. 3, potential of CitSci for landslide researches are analyzed in detail and a scheme for different levels of participation and engagement is proposed. The last Section discusses how to realize the potential and identify the open issues briefly.

2   Aspects of Landslide Researches

Landslide is perhaps one of the most complex phenomena in the nature and due to its complexity, still extensive studies and analyses on large-scale databases are required to understand this natural process clearly. Statistics from The Center for Research on the Epidemiology of Disasters (CRED) show that 17% of all fatalities from natural hazards worldwide were caused by landslides (Lacasse et al. 2010).

However, according to Foster et al. (2012), landslides have often been undervalued due to their local character.

A massive landslide induced by a 7.7 magnitude earthquake has occurred on May 31, 1970 in Peru (Keefer et al. 1978). A large mass of ice and rock flew from Mount Huascaran, and covered the towns of Yungay and Ranrahirca at the velocities of 280–400 km per hour. Within 4 min, the landslide had killed almost 18,000 people. However, another major landslide occurred in the same area just 8 years before (year 1962), which caused loss of 5000 lives (Schuster and Fleming 1986). This deadly example is a significant one for site selection and by increasing the public awareness, such situations can hopefully be reduced.

A major example on the economic impacts of landslides can be given from Panama Canal, where landslides were a dominant aspect of the construction of the Canal. They resulted in 40 million m^3 of additional excavation and they were a major factor in the bankruptcy of the French enterprise (Berman 1995). Large numbers and sizes of slope failures occurred during the construction, and shortly after the opening, two large landslides closed the Canal for almost a year (Berman 1995). The Canal has been partially obstructed several times due to landslides, and the impact goes beyond the repair costs and the delayed transits.

A typical example of landslide losses from Turkey was presented by Can et al. (2005), which was the result of an extreme rainfall that caused also flooding by the second day. Thousands of shallow earthflow landslides occurred during the rainfall and this event caused 10 deaths, extensive damage to both public and private property, and cost social and economic disruption (Can et al. 1999). The total economic cost was estimated as 500 million US Dollars and the affected area and population were 37,000 km^2 and 2.2 million, respectively. In addition, a considerable amount of forest area was destroyed. Such meteorological events are frequent in the Black Sea Region of Turkey. For example, in 1955 another flooding event was also recorded in the region but historical data about the landslides are not available. In the future, this type of rainfalls is very likely to occur in the region. When considering the principle "the past is the key to the future", future landslides are also very likely to occur under such conditions, which leads to past and present instability (Can et al. 2005).

The landslide researches in the literature involve different aspects. Gokceoglu and Sezer (2009) have scanned the landslide literature in 2009 and performed a keyword analysis to investigate the possible trends in the international landslide studies. They have found out that the most frequently used key words by that time were: *landslide*, *debris flow*, *landslide hazard*, *GIS*, *slope stability, rock fall, earthquake, landslide susceptibility, rainfall, tsunami, landslide risk,* and *natural hazard*. The increasing trend in the regional landslide susceptibility and hazard assessments is an obvious output of the study. Innovative researches on the assessment of landslide risk, prediction of runout and time of landslides, and early warning systems are expected. Several properties and time of landslides should be known for better understanding the anatomy and triggering mechanisms of landslides. From the most frequently used key words, one can categorize the different aspects as:

- Landslide anatomy or characterization (i.e. landslide inventory or the earth surface state at time t_0)
- Susceptibility mapping tools and methods (GIS, data types, techniques)
- Hazard assessments (effects of triggering and conditioning factors on landslides, such as earthquake, rainfall, slope stability at time t_n)
- Risk assessments (elements at risk, hazard level)

To reduce the losses caused by landslides, regional landslide characterization based on the regional assessments of susceptibility, hazard and risks are of crucial importance. The management of risks, disasters or also the land requires the knowledge on the probability of spatial (defined as susceptibility) and temporal (defined as hazard) occurrence of landslides. Existence of both the spatial and temporal data are mandatory for correct characterization and for accurate modeling. The rise of citizen science is a great opportunity to understand this complexity and develop suitable methods to be use it.

2.1 Landslide Risk Management

The regional landslide risk management process is simply depicted in Fig. 2. The process has five major steps, from landslide inventory mapping to risk management. Although landslide triggering time and estimation of the runout distance can be performed probably only by using citizens' observations, each step given in Fig. 2 should be analyzed separately to find out the parts that citizens can contribute optimally and to identify the most suitable methods for volunteer data collection, quality control and analysis. Often contributions of local people play a major role for the characterization of the landslides and further analysis of the events. From the experiences in the literature, a systematic approach can be defined for utilizing citizen science in regional landslide risk management process.

Assessment of the landslide susceptibility is the first stage of landslide mitigation efforts. Endeavors to produce representative landslide susceptibility maps have increased especially during the last two decades. The landslide susceptibility mapping methods can basically be classified into two main groups, namely heuristic and data-driven (automatic) mapping. Great difficulties are being encountered while producing heuristic landslide susceptibility maps, which bring up severe uncertainties in the resulting maps. Among those, subjectivity, lack of expertise and knowledge on map preparation, the need of enormous effort can be listed as major factors. In addition, the production of the landslide susceptibility map by heuristic approach is an extremely exhaustive process. Due to these reasons, automatic landslide susceptibility mapping has become more attractive. However, automatic landslide susceptibility mapping requires a robust mapping approach and high-quality inventory data.

| Landslide inventory |

Landslide conditioning parameters

| Susceptibility assessment |

Landslide triggering time

| Hazard assessment |

Element at risk, run out distance

| Risk assessment |

| Risk management |
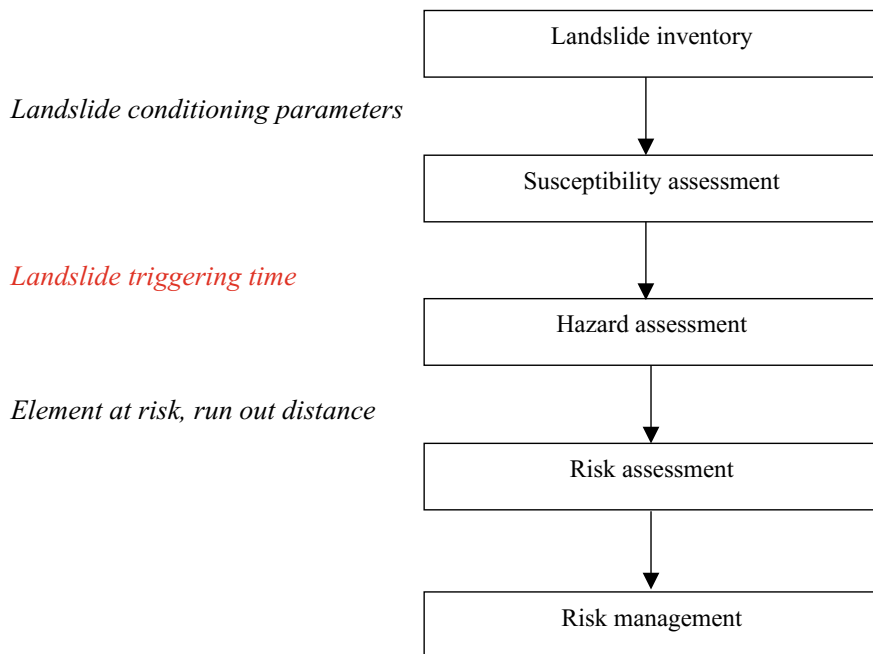
Fig. 2 A simple representation of regional landslide risk management stages with LS-CitSci approach

The second stage of regional landslide characterization is the assessment of landslide hazard. Landslide hazard can basically be defined as the occurrence probability of the landslides in a given period. The exact time of occurrence is crucial for computation of landslide probability, thus hazard determination. Under the assumption of having high quality data for meteorological phenomenon and earthquakes, which are the most important triggering factors of landslides, the exact time of landslide occurrence is the most important parameter for accurate linking of these data. The main obstacle in determination of the landslide hazard is knowing the exact time of occurrence of the past events. Additionally, some shallow landslides or flows may lose their features and traces in a short time. Some typical examples for such type landslides from Buyukkoy near Rize Province of Turkey are given in Fig. 3 (Nefeslioglu and Gokceoglu 2011). From the Fig. 3, it can be seen that the earth surface characteristics change in a short time, which may make it impossible to detect the landslide by post-event observations, such as by using aerial or satellite images, etc.

The risk assessment and management stages are performed after the hazard determination. Prediction of the runout distance, which involves the direction, displacement and the magnitude of the landslide, is crucial for land and disaster management as well. Infrastructure and construction planning at regional level should be performed based on this data, as well as disaster management during and
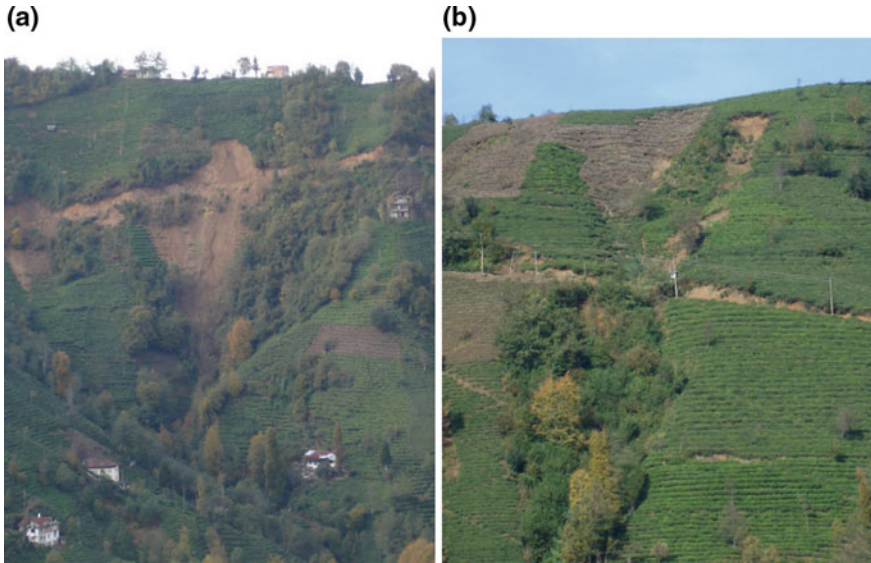
Fig. 3 Typical views of the earthflows occurred in Buyukkoy Region; **a** fresh, and **b** a few years old (Nefeslioglu and Gokceoglu 2011)

after the landslide event such as evacuation of people. The runout distance can best be modeled using the data of past landslides, and the morphology, topography and the land cover of the region.

Methods used for landslide susceptibility, hazard and risk mapping have been improved drastically with the developments of GIS, and other geospatial and computing technologies. Most of the zoning studies are qualitative in nature, although more recently there have been examples of quantifying the hazard by assigning a temporal probability to the potential landslides and quantifying the risks for existing development (JTC-1 Joint Technical Committee on Landslides and Engineered Slopes 2008). When producing landslide susceptibility maps, the conditioning or preparatory factors are employed. Landslide conditioning factors such as geological, geomorphological and environmental parameters are mainly static. However, when assessing landslide hazard, the triggering factors and their threshold values must be known. In general, landslide triggering factors are earthquake, rainfall and anthropogenic effects (excavation, surcharge or change in hydrologic conditions etc.). Anthropogenic effects are local and it is possible to work on these effects by geotechnical and analytical approaches. However, earthquake and rainfall, depending on their magnitude, intensity and duration, can influence large regions. The following assumptions are considered for landslide susceptibility zonation (Varnes 1984; Hutchinson 1995):

a. landslides will always occur in the same geological, geomorphological, hydrogeological and climatic conditions as in the past,

b. the main conditions that cause landsliding are controlled by identifiable physical factors,

c. the degree of susceptibility can be evaluated, and

d. all types of slope failures can be identified and classified.

As can be seen from these assumptions, when producing landslide susceptibility maps, the spatial distribution of landslides must be known. A classification of methods for the landslide susceptibility assessment is given by Aleotti and Chowdhury (1999) and a slightly modified version is provided in Fig. 4.

Qualitative methods are usually not preferred since they are time consuming, subjective, and labor intensive processes, and require high level of expertise. On the contrary, the quantitative methods have become much more attractive especially in the last two decades. It is possible to add several extra methods to the classification
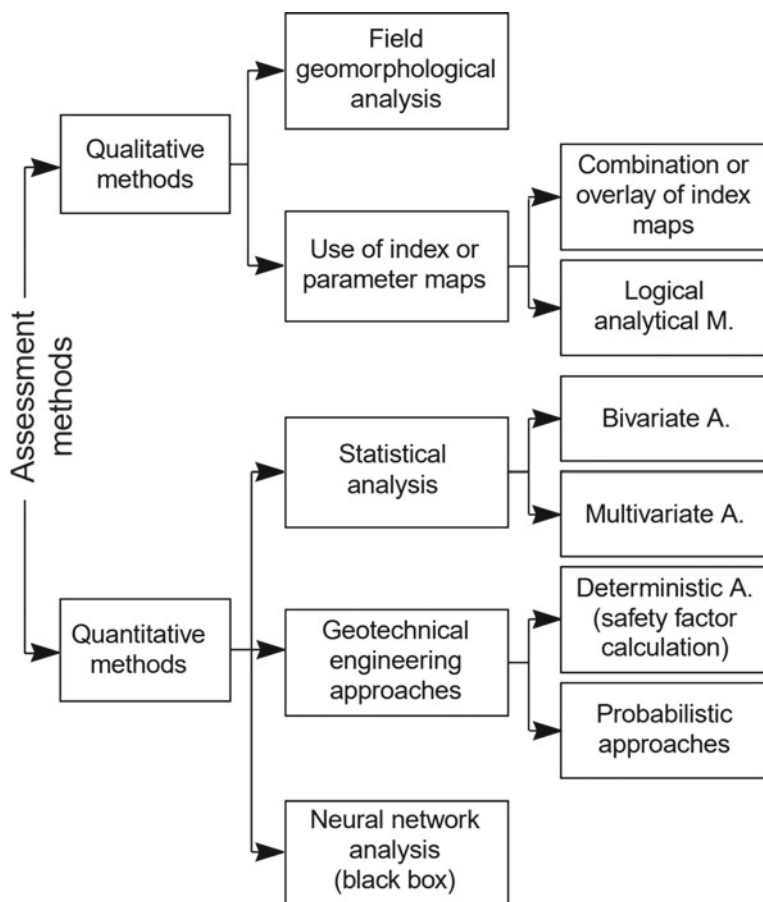

Fig. 4 Classification of the methods employed for landslide susceptibility assessments (modified after Aleotti and Chowdhury 1999)

given by Aleotti and Chowdhury (1999). An important aspect of all new qualitative methods is that they require high quality spatial data. Deep-seated landslides have several clear features, which can be observed in field or on aerial photos. Also, these features can be visible for a long time. However, to determine the location and the features of shallow landslides can be problematic in a short time (see Fig. 3). For this reason, to provide high quality spatial data for landslide susceptibility maps of shallow failures can sometimes be a big problem.

If reliable spatial data are not available, any landslide susceptibility map produced by automatic or data-driven method is open to discussion because it contains several uncertainties. Additionally, time of occurrence of a shallow of deep-seated landslide is extremely important for the assessment of landslide hazard. This data is necessary to assess the threshold values triggering landslides for a region and a described condition. Consequently, these data should be collected from large areas and in rural regions and it is almost impossible to collect these data without the observations of humans.

A schematic presentation of the landslide risk assessment procedure is given in Fig. 5 (van Westen et al. 2008). Landslides are conditioned by various geological, geomorphological and environmental factors while they are triggered by rainfall and earthquake. When producing landslide susceptibility maps, the conditioning factors are employed and they are mainly static. Determination of landslide conditioning factors to be used in production of landslide susceptibility map depends on the type and magnitude of landslides observed in the area. When considering the nature of the conditioning parameters, it can be said that the conditioning parameters are mainly time-independent. However, a complete risk assessment requires landslide hazard assessment and determination of the elements at risk.

2.2 Volunteer Data Use Cases for Landslide Risk Management

From Fig. 5, it can clearly be seen that the types of spatial data cover an extensive variety and they can neither be collected nor processed by a single stakeholder group. The time dimension of all datasets are important and these datasets can be produced or updated at different periods of time. Landslide databases contain the essential knowledge for hazard modeling, damages on buildings and infrastructure, mitigation, and research needs (Jaeger et al. 2018). Since landslides are local phenomena and linked with other hazards such as heavy rainfall, floods, etc.; comprehensive databases are required to assess the losses sourced from them (Valenzuela et al. 2017). Even for small to mid-size regions, they can be generated with great efforts.

In their study, Grahn and Jaldell (2017) have assessed the data availability Scandinavian countries for the development of landslide fatality curves. In northern Philippines, Nolasco-Javier and Kumar (2018) used media and reports to extract the
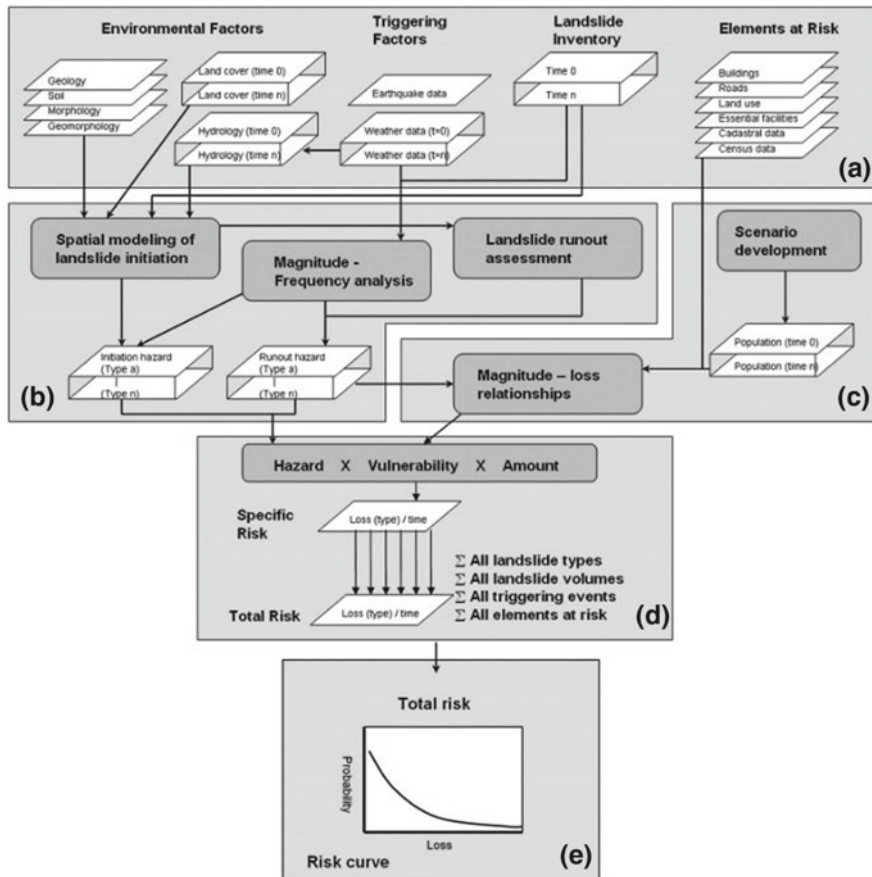
Fig. 5 Schematic representation of the landslide risk assessment procedure. **a**: Basic data sets required, both of static, as well as dynamic (indicated with "time…") nature, **b**: Susceptibility and hazard modeling component, **c**: Vulnerability assessment component, **d**: Risk assessment component, **e**: Total risk calculation in the form of a risk curve (van Westen et al. 2008)

rainfall threshold for shallow landslides and they have performed interviews with locals and government personnel. In addition, the have carried out field observations for the landslide occurrence time. Another example can be found from New Zealand (Rosser et al. 2017), where automated data-upload routines and mobile applications have been seen as future work to get help from people for landslide reports. In Italy, Salvati et al. (2018) established a database to collect fatalities caused by floods and landslides, where they used interviews of eyewitnesses, newspaper articles, reimbursement requests filed by survivors, and official government reports. In Indonesia, Samodra et al. (2018) used the observations of eyewitnesses to form the landslide inventory in a part of the country. In Uganda, Masaba et al. (2017) considered the results of interviews of the locals to discuss the

landslide disaster risk reduction efforts. In Fiji, more than 150 debris flows occurred near Ba river in 2012; and the villagers reported that it happened at around 2–3 a.m. (Stephens et al. 2018). In northern Iceland, the triggering factors of the Móafellshyrna debris slide have been explained by using witness reports and field observations together with the data from weather stations, seismometers (Saemundsson et al. 2018). The first signs (a new tension crack) of the catastrophic rockslope failure occurred in Preonzo in 2012, have been noticed by local farmers 1989 and these reports provided serious benefits (Loew et al. 2017). Such studies show that the observations of multiple stakeholders are crucial to compile complete and comprehensive databases.

The observations of local eye-witnesses also help to explain the mechanism of a complex landslides. An example can be given from the Dagkoy Region near Zonguldak Province, Turkey, where the sliding blocks and runout distance could be depicted with the help of locals (Fig. 6). The dislocation of the buildings (e.g. the mosque) due to the landslide and its rotational movements can be observed in the Fig. 6. The velocity of the landslide was also calculated by using these observations (Ocakoglu et al. 2002).

Fig. 6 Restoration of the sliding blocks in Dagkoy Region, Zonguldak. Note the trend of transverse cracks and rotation (HF: Hazelnut Field) (Ocakoglu et al. 2002)
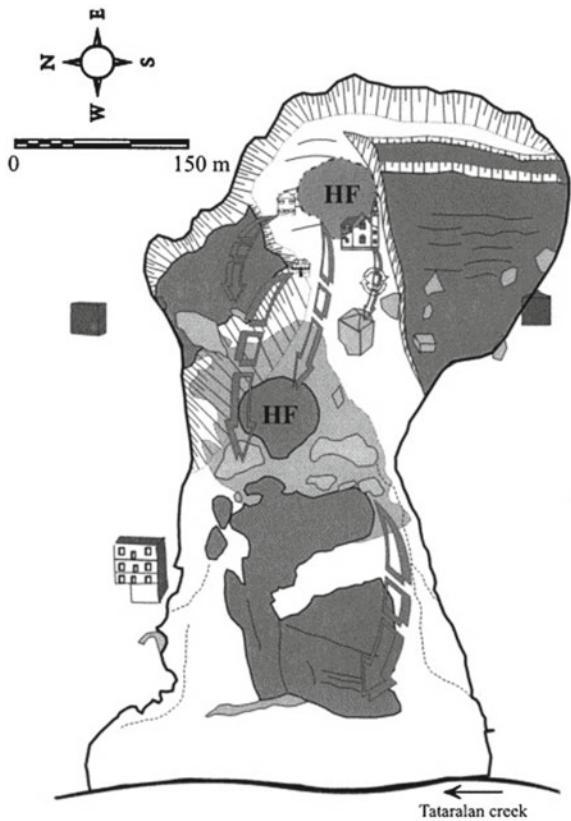
The majority of landslides occur in mountainous areas and the installation of necessary equipment to monitor the landslides and possible triggers is almost impossible in general. For this reason, many studies rely on the observations of local eye-witnesses. As an example, a deadly, large and complex landslide occurred in Kuzulu village (Sivas, Turkey) on March 17, 2005. The mechanism of this catastrophic landslide (Fig. 7) was investigated by in situ observations, morphometric and geological assessments and using the observations of local eye-witnesses by Gokceoglu et al. (2005). Especially, the velocity of landslides provides crucial information for the mechanism of complex and catastrophic movements, because such types of movements are the result of combination of several factors. The velocity of the earth-flow part of the Kuzulu landslide was an extremely fast one, which was approximately 6 m/s (Gokceoglu et al. 2005).

To make hazard assessment of shallow landslides, Nefeslioglu et al. (2011) have mapped the temporal and spatial distribution of shallow landslides in the catchment and they performed aerial-photo interpretations (Fig. 8). As can be seen from the Fig. 8, it is impossible to find exact time of occurrence by aerial photo interpretations and only a rough approximation of the time interval can be estimated. In addition to various data sources, Nefeslioglu et al. (2011) conducted field investigations in the year 2007 to map the recent shallow landslides, to georeference the movements published by the geological reports and to extract the exact date of certain failures by interviews with the local community. A conventional method for mapping the spatiotemporal distribution of the shallow landslides in the catchment is the use of existing aerial orthoimages and manual definition of them by human

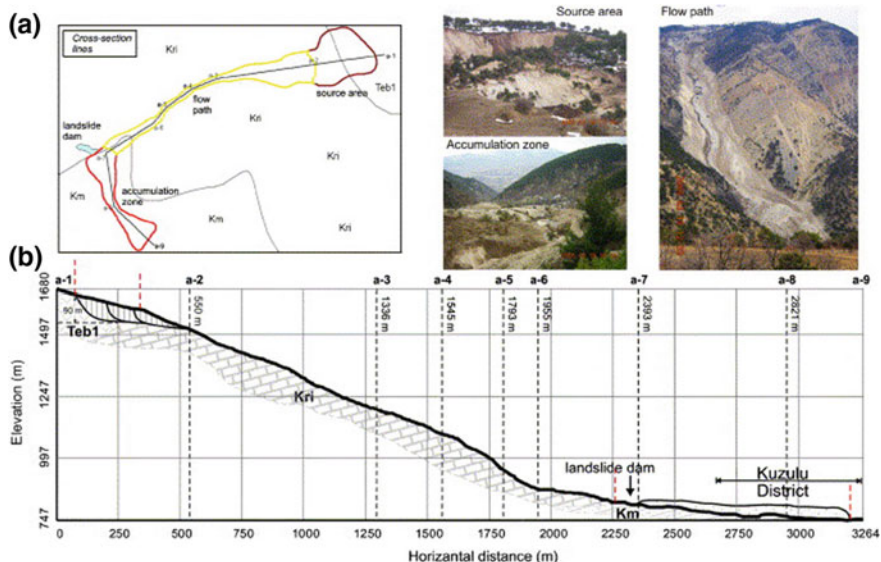

Fig. 7 Plan view and cross section showing the mechanism of the landslide, and photos from the source area, flow path, and accumulation zone of the Kuzulu landslide (Gokceoglu et al. 2005)

Fig. 8 Cumulative shallow landslide frequency (%) with respect to the anthropogenic activity observed in the catchment; the anthropogenic data were provided by TUIK (2006) (Nefeslioglu et al. 2011)
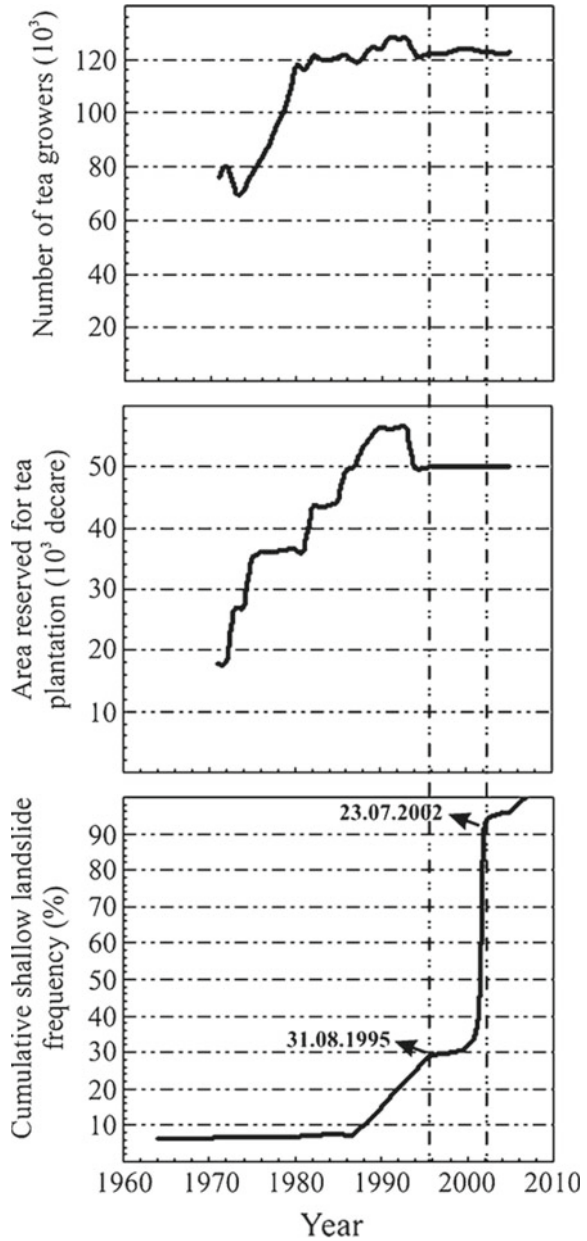
interpreters. Nefeslioglu et al. (2011) have assessed the spatial distribution using the aerial orthoimages at 10-year intervals, with additional field investigations to map the recent shallow landslides, to geolocate the movements published by the geological reports and also to determine the exact dates with the help of local community. Although 10-year temporal resolution and accuracy is not sufficient for performing the hazard assessment, it was the only possible method for that case study and no other solution for the given time frame was available.

As can be seen from the case studies summarized herein, the researchers rely heavily on the observations of local communities because these observations are highly valuable and sometimes even the only source of information to understand the mechanism of movements.

3 Potential of CitSci in Landslide Researches

Citizen science methods can provide the necessary means for a complete and accurate regional landslide characterization and risk management. Volunteers especially living in the region can help to assess the time and location of a landslide event by collecting timely accurate data. With the widespread use of mobile phones equipped with GNSS receivers, it is also possible to detect the location and thus provide the spatial aspect of the landslides with sufficient accuracy. It is evident that citizen science is one of candidates for reliable data support for landslide mitigation efforts. Although recent projects are being carried out by different organizations and research groups (Landslide EVO 2018; Research Councils UK 2018; USGS Landslide Hazards Program 2018), this is an emerging research and application area, where the contributions of citizens can have a huge impact on the theory and the practice. However, the use potential cannot be limited to the landslide characterization and risk management, and the contributions can be spread to more areas as described in the following section. In Sect. 3.2, the different levels of participation is described and in Sect. 3.3, the issues and open research questions in the field are given.

3.1 Fields of Citizen Contributions

The major fields where volunteers can contribute to landslide researches and risk management can be listed as following. However, it should be noted that these fields are not separated crisply from each other and they have mutual information and benefits.

- *spatial data collection* (to increase the accuracy, density, distribution, reliability)
- *temporal data collection* (for inventories, mitigation, characterization, mechanism explanation)

- *risk management and mitigation* (early warning, monitoring, etc.)
- *socioeconomic aspects* (site selection, economic impact assessment, saving human lives, educational, increasing awareness public and governmental, etc.)

Reliable spatial data is crucial for landslide susceptibility assessment. Especially, footprints of shallow landslides and some features of complex failures can be disappeared shortly by natural process. For this reason, some pictures and observations obtained from fresh surfaces are extremely useful for landslide researches. Additionally, zone of accumulation is easily eroded and removed by surface waters. This results in loss of some serious information about landslides. Volunteers can provide serious contribution to collect data from fresh failure surfaces and zone of accumulations without loss of information.

Temporal data collection is the basic element of hazard assessment. This data is necessary for determination of threshold of triggering event. Rainfall and earthquakes are the basic triggers for landslides and these events have returning period. Calculation of the returning periods of these events is possible and the degree of hazard for landslides can be determined if the thresholds are known. In addition, the velocity and movement mechanism can be explained clearly if the existing time and duration of landslide are known. This information can be used for early warning systems as well.

If the susceptible areas for landslides are known, it is possible to select suitable areas for infrastructures, settlement etc., and to develop effective engineering measures. Additionally, development of realistic and correct risk management plans is possible. All these efforts can provide serious economic benefits and prevent loss of lives. On the other hand, the produced information from collective efforts can be returned to local dwellings using CitSci tools to increase public awareness.

3.2 Levels of Citizen Participation and Engagement

The volunteers can participate to landslide researches for different levels. A generic typology pf participation for CitSci projects has been proposed by Haklay (2013). Here, a new scheme is proposed for the potential CitSci projects in the field of landslide researches. As shown in Fig. 9, the basic level of participation is the data collection, including spatial, temporal and semantic information. These data can be collected implicitly (e.g. soil movements in the north of nearby river three years ago) or explicitly (e.g. coordinates and area of a shallow landslide at a certain date and time). Applications and tools used to collect data can be developed with web and mobile interfaces to provide sufficient flexibility to the users. Volunteers from any background (e.g. school children, visitors, hikers, etc.) can participate at this level with necessary training of software or tool.

At the second level, volunteers can play a significant role in the validation and interpretation of the collected data. Quality control and quality assessment (QC & QA) is an issue for many CitSci projects, as mentioned in the following section.

---

1. Basic data collection (spatial, temporal, semantic)

implicit and explicit, web- and mobile-based

---

2. Data validation and interpretation (spatial, temporal, semantic)

Quality assessment, validation, basic interpretation of the collected data

---

3. Advanced interpretation

Data aggregation and enrichment, basic analysis of the results

---

4. Project and policy development and establishment of common sense/rules

Advanced analyses and reporting, design of LS-CitSci projects, capacity building initiatives, legal enforcements

Fig. 9 Levels of participation and engagement in LS-CitSci projects

The QC & QA can be performed automatically by designing specific algorithms and setting rules, as well as by manual checks by humans. In this level of participation, trained volunteers can do manual checks on the data while interpreting the results (e.g. assessing the type of the landslide or determining the location). Specific guidelines should be prepared by the researchers for helping the volunteers to understand and validate the data.

At level 3, advanced interpretation and analysis tasks can be performed by the volunteers. This can probably be done by well-educated users with some level of analytical skills and they should work in close collaboration with the professionals.

The last level involves advances analyses and reporting with the help of professionals, designing and managing local and regional CitSci projects by volunteers, help the trainers and contribute to the policy development at regional level.

Although fewer citizen scientists can take this role, it is pretty important as several projects are needed to be run to be able to collect and interpret the great amount of spatiotemporal data.

3.3 Issues for Citizen Participation

There are still several major issues regarding the citizen participation in scientific projects and disaster management as described by Kocaman et al. (2018). Similar issues exist for landslide risk management, which can be summarized as following:

Technical: The variety of applications and data sources may cause integration issues. These issues can be solved through ensuring interoperability standards in software and data by relying on Open Geospatial Consortium (OGC) standards (OGC 2018). Moreover, with the increase in the number of stakeholders, communication of these stakeholders may be an issue. The management of large data sets, their storage and analysis can also be complex. Interface design for the users from different backgrounds (educational, language, cultural barriers) are also important for landslide risk management applications.

Data quality: Data quality is an issue mentioned in almost all CitSci projects and it is one of the most important aspect of CitSci research. The quality of the data collected by citizens may be questionable, since they are collected by people with different backgrounds and motivation. The users may like to use different technological tools or they might perceive the measured phenomenon differently (Hollenstein and Purves 2014; Montello 2003). An additional user group may be required for data validation.

Education: Many CitSci projects require training of the volunteers at different levels depending on the required level of participation and the experiences of the users. Training materials should be prepared for the different user groups, different tasks, and be available online as well as on-site if needed. In addition, some users can be trained to be the trainers.

Legal: Risk management/insurance especially in the field work, ownership rights of the project data, outcomes and dissemination, responsibility issues in case of missing or false data are all situations in which legal guidance must be sought (Kocaman et al. 2018).

Motivation: Ensuring continuous motivation of the volunteers is still an active research agenda (Coleman et al 2009; Tang and Liu 2016). The citizen scientists can most likely be motivated by helping and protecting their environment, seeing the actual benefits, and believing that their data and efforts are useful for the purpose of the projects.

Management: Just like many other disasters, governments and local authorities play the most significant for the management. The policies, availability of open government data, and coordination activities of the governments are extremely important for successful landslide risk management.

4   Conclusions and Discussions

The endeavors for regional landslide characterization, i.e. landslide susceptibility mapping, hazard and risk assessment, have been increasing and are of great importance for the risk and disaster management. The density (frequency) and the quality of spatial and temporal data required for the regional landslide characterization should be high to reduce the uncertainties and provide accurate models. Concluding from the case studies in this paper, researchers rely heavily on the observations of local communities for collection of these data, which sometimes are even the only available data for performing the analyses and identifying the processes. However, the temporal and spatial accuracy of the given data are usually low as they are based on vague statements of eye-witnesses.

With the development of mobile and geospatial technologies and the rise of citizen science, the data needed for regional landslide assessment and risk management can be collected more frequently and accurately. A systematic approach for identifying the gaps and particular fields where citizens can provide their contributions in this process should be performed. Afterwards appropriate tools, e.g. mobile apps, do-it-yourself kits, etc., and methods for the quality control and analysis of the contributions should be developed for the optimal use of citizen science in regional landslide assessment and risk management.

Collecting data with conventional methods is expensive and sometimes open to some errors sourced from operational difficulties. In addition, to apply a cross-check process on the data collected with conventional methods is almost impossible. Use of CitSci has serious advantageous to eliminate these problems because it is possible to collect much more data and observations from the same event and/or location. Another chance is the enormous development of artificial intelligence methods. Accumulation of gigantic data can be processed easily by artificial intelligence methods and it is possible to check the data quality and to extract meaningful inferences from huge data accumulation. Consequently, use of CitSci and artificial intelligence together for landslide researches is open new and big horizons for explanation of landslide mechanisms and prevention of losses sourced from landslides.

References

Aleotti P, Chowdhury R (1999) Landslide hazard assessment: summary review and new perspectives. Bull Eng Geol Env 58:21–44
Berman G (1995) Landslides on the Panama Canal. In: Miller RL, Escalante G, Reinemund JA, Bergin MJ (eds) Energy and mineral potential of the central American-Caribbean region. Circum-Pacific Council for Energy and Mineral Resources Earth Science Series, vol 16. Springer, Heidelberg
Can T, Duman TY, Emre O, Alkan M (1999) Investigation of earthflows occurred in May 1998 in the western Black Sea region. In: Proceedings of 3rd national symposium on landslides, 13–15 May, Cukurova University, Adana, p. 7 (in Turkish)

Can T, Nefeslioglu HA, Gokceoglu C, Sonmez H, Duman TY (2005) Susceptibility assessments of shallow earth flows triggered by heavy rainfall at three catchments by logistic regression analyses. Geomorph 72:250–271

Coleman D, Georgiadou Y, Labonte J (2009) Volunteered Geographic Information: the nature and motivation of producers. Int J Spat Data Infrastr Res 4:332–358

Cutter SL, Ismail-Zadeh A, Alcantara-Ayala I, Altan O, Baker DN, Briceño S, Gupta H, Holloway A, Johnston D, McBean GA, Ogawa Y, Paton D, Porio E, Silbereisen RK, Takeuchi K, Valsecchi GB, Vogel C, Wu G (2015) Global risks: Pool knowledge to stem losses from disasters. Nature 522:277–279. https://doi.org/10.1038/522277a

Firehock K, West J (1995) A brief history of volunteer biological water monitoring using macroinvertebrates. J North Am Benthol Soc 14(1):197–202

Foster C, Pennington CVL, Culshaw MG et al (2012) The national landslide database of Great Britain: development, evolution and applications. Env Earth Sci 66:941–953. https://doi.org/10.1007/s12665-011-1304-5

Gokceoglu C, Sezer E (2009) A statistical assessment on international landslide literature (1945–2008). Landslides 6:345–351. https://doi.org/10.1007/s10346-009-0166-3

Gokceoglu C, Sonmez H, Nefeslioglu HA, Duman TY, Can T (2005) The 17 March 2005 Kuzulu landslide (Sivas, Turkey) and landslide-susceptibility map of its near vicinity. Eng Geo 81:65–83

Goodchild M (2007) Citizens as sensors: the world of volunteered geography. GeoJournal 69:211–221

Grahn T, Jaldell H (2017) Assessment of data availability for the development of landslide fatality curves. Landslides 14:1113–1126. https://doi.org/10.1007/s10346-016-0775-6

Haklay M (2013) Citizen science and volunteered geographic information: overview and typology of participation. In: Crowdsourcing geographic knowledge, pp 105–122. Springer, Dordrecht. https://doi.org/10.1007/978-94-007-4587-2_7

Haworth B, Bruce E (2015) A review of volunteered geographic information for disaster management. Geogr Compass 9:237–250. https://doi.org/10.1111/gec3.12213

Holderness T, Turpin E (2017) PetaJakarta.org: assessing the role of social media for civic co-management during monsoon flooding in Jakarta, Indonesia. White Paper. SMART Infrastructure Facility, University of Wollongong ISBN: 978-1-74128-249-8)

Hollenstein L, Purves R (2014) Exploring place through user-generated content: using Flickr tags to describe city cores. J Spatial Inf Sci 1:21–48

Hutchinson JN (1995) Landslide hazard assessment. In: Proceedings of VI International symposium on landslides, Christchurch, vol 1, pp 1805–1842

Jaeger D, Kreuzer T, Wilde M, Bemm S, Terhorst B (2018) A spatial database for landslides in Northern Bavana: a methodological approach. Geomorph 306:283–291. https://doi.org/10.1016/j.geomorph.2015.10.008

JTC-1 Joint Technical Committee on Landslides and Engineered Slopes (2008) Guidelines for landslide susceptibility, hazard and risk zoning, for land use planning. Eng Geo 103:85–98

Keefer DK, Wieczorek GF, Harp EL, Tuel DH (1978) Preliminary assessment of seismically induced landslide susceptibility. In: Proceedings of 2nd international conference on microzonation for safer construction—research and application, San Francisco, Nov 1976, pp 279–290

Kocaman S, Anbaroglu B, Gokceoglu C, Altan O (2018) A review on citizen science (CitSci) applications for disaster management. Int Arch Photog Rem Sens Spatial Inf Sci XLII-3/W4:301–306. https://doi.org/10.5194/isprs-archives-xlii-3-w4-301-2018

Lacasse S, Nadim F, Kalsnes B (2010) Living with landslide risk. Geotech Eng J SEAGS & AGSSEA 41:4

Lewis QW, Park E (2018) Volunteered geographic videos in physical geography: data mining from YouTube. Ann Am Assoc Geogr 108(1):52–70. https://doi.org/10.1080/24694452.2017.1343658

Liang WT, Lee JC, Chen KH, Hsiao NC (2017) Citizen earthquake science in Taiwan: From science to Hazard mitigation. J Disaster Res 12(6):1174–1181. https://doi.org/10.20965/jdr.2017.p1174

Loew S, Gschwind S, Gischig V, Keller-Signer A, Valenti G (2017) Monitoring and early warning of the 2012 Preonzo catastrophic rockslope failure. Landslides 14:141. https://doi.org/10.1007/s10346-016-0701-y

Landslide EVO (2018). http://www.iiasa.ac.at/web/home/research/researchPrograms/RISK/Landslide-EVO.html. Accessed 10 Feb 2018

Masaba S, Mungai DN, Isabirye M, Nsubuga H (2017) Implementation of landslide disaster risk reduction policy in Uganda. Int J Disaster Risk Reduct 24:326–331. https://doi.org/10.1016/j.ijdrr.2017.01.019

Montello DR, Goodchild MF, Gottsegen J, Fohl P (2003) Where's downtown? Behavioral methods for determining referents of vague spatial queries. Spatial Cog Comp 3(2–3):185–204. https://doi.org/10.1080/13875868.2003.9683761

National Climate Assessment Report (2011) Climate change impacts and responses. NCA Report Series, vol. 5c, April 28–29, Washington D.C., USA

NASA Landslide Reporter (2018). https://pmm.nasa.gov/landslides/report.html. Accessed 21 Aug 2018

Nefeslioglu HA, Gokceoglu C (2011) Probabilistic risk assessment in medium scale for rainfall induced earthflows: Catakli catchment area (Cayeli, Rize, Turkey). Math Probl Eng 1–21. Article ID 280431

Nefeslioglu HA, Gokceoglu C, Sonmez H, Gorum T (2011) Medium scale hazard mapping for shallow landslide initiation: the Buyukkoy catchment area (Cayeli, Rize, Turkey). Landslides 8:459–483

Nolasco-Javier D, Kumar L (2018) Deriving the rainfall threshold for shallow landslide early warning during tropical cyclones: a case study in Northern Philippines. Nat Hazards 90 (2):921–941. https://doi.org/10.1007/s11069-017-3081-2

Ocakoglu F, Gokceoglu C, Ercanoglu M (2002) Dynamics of a complex mass movement triggered by heavy rainfall: a case study from NW Turkey. Geomorph 42(3):329–341. https://doi.org/10.1016/S0169-555X(01)00094-0

OGC (2018). http://www.opengeospatial.org/docs/is. Accessed 21 Aug 2018

Research Councils UK (2018). http://gtr.rcuk.ac.uk/projects?ref = NE%2FP000452%2F1. Accessed 10 Feb 2018

Rosser B, Dellow S, Haubrock S, Glassey Ph (2017) New Zealand's national landslide database. Landslides 14:1949. https://doi.org/10.1007/s10346-017-0843-6

Saemundsson T, Morino C, Kristinn HJ, Conway SJ, Pétursson HG (2018) The triggering factors of the Móafellshyrna debris slide in Northern Iceland: intense precipitation, earthquake activity and thawing of mountain permafrost. Sci Total Env 621:1163–1175. https://doi.org/10.1016/j.scitotenv.2017.10.111

Salvati P, Petrucci O, Rossi M, Bianchi C, Pasqua AA, Guzzetti F (2018) Gender, age and circumstances analysis of flood and landslide fatalities in Italy. Sci Total Env 610–611:867–879

Samodra G, Chen G, Sartohadi J, Kasama K (2018) Generating landslide inventory by participatory mapping: an example in Purwosari Area, Yogyakarta, Java. Geomorph 306:306–313. https://doi.org/10.1016/j.geomorph.2015.07.035

Schuster RL, Fleming RW (1986) Economic losses and fatalities due to landslides. Bull Assoc Eng Geol 23(1):11–28

Scott D, Barnett C (2009) Something in the air: civic science and contentious environmental politics in post-apartheid South Africa. Geoforum 40(3):373–382

See L, Mooney P, Foody G, Bastin L, Comber A, Estima J, Fritz S, Kerle N, Jiang B, Laakso M, Liu HY, Milčinski G, Nikšič M, Painho M, Pődör A, Olteanu-Raimond AM, Rutzinger M (2016) Crowdsourcing, citizen science or volunteered geographic information? The current state of crowdsourced geographic information. ISPRS Int J Geo-Inf 5:55

Silvertown J (2009) A new dawn for CitSci. Trends Eco Evol 24:467–471

Singh P, Saran S, Kumar D, Padalia H, Srivastava A, Kumar AS (2018) Species mapping using citizen science approach through IBIN portal: use case in foothills of Himalaya. J Indian Soc Rem Sens 46(10):1725–1737. https://doi.org/10.1007/s12524-018-0833-8

Sorte FAL, Fink D, Hochachka WM, Kelling S (2016) Convergence of broad-scale migration strategies in terrestrial birds. Proc R Soc B 283(1823):20152588. https://doi.org/10.1098/rspb.2015.2588

Stephens M, Lowry JH, Ram AR (2018) Location-based environmental factors contributing to rainfall-triggered debris flows in the Ba river catchment, northwest Viti Levu Island. Fiji. Landslides 15:145. https://doi.org/10.1007/s10346-017-0918-4

Tang Z, Liu T (2016) Evaluating Internet- based public participation GIS (PPGIS) and volunteered geographic information (VGI). Env Plan Man J 59:1073–1090

UN Sustainable Development Goals (2018). http://www.un.org/sustainabledevelopment/sustainable-development-goals/. Accessed 15 Feb 2018

USGS Landslide Hazards Program (2018). https://landslides.usgs.gov/. Accessed 15 Feb 2018

van Westen CJ, Castellanos Abella EA, Sekhar LK (2008) Spatial data for landslide susceptibility, hazards and vulnerability assessment: an overview. Eng Geo 102:112–131. https://doi.org/10.1016/j.enggeo.2008.03.010

Valenzuela P, Domínguez-Cuesta MJ, García MAM, Jiménez-Sánchez M (2017) A spatio-temporal landslide inventory for the NW of Spain: BAPA database. Geomorph 293:11–23. https://doi.org/10.1016/j.geomorph.2017.05.010

Varnes DJ (1984) IAEG commission on landslides: landslide hazard zonation—a review of principles and practice. UNESCO, Paris, p 63

World Meteorological Organisation (2001) Volunteers for weather, climate and water, Geneva, Switzerland, WMO No. 919

Zook M, Graham M, Shelton T, Gorman S (2010) Volunteered geographic information and crowdsourcing disaster relief: a case study of the Haitian Earthquake. World Med Health Policy 2(2): Art. 2. https://doi.org/10.2202/1948-4682.1069

Geospatial-Based Slope Mapping Studies Using Unmanned Aerial Vehicle Technology

Ahmad Razali Yusoff, Norhadija Darwin, Zulkepli Majid, Mohd Farid Mohd Ariff, Khairulnizam Mohd Idris and Mohd Azwan Abbas

Abstract Unmanned Aerial Vehicle (UAV) is one of the geospatial-based data acquisition technologies which acquire data within a short period for slope mapping studies. Geospatial-based UAV mapping are widely used in many applications, specifically for scientific and mapping research. The capabilities of rapid data acquisition and accessibility to slope risk area are several advantages of using UAV technology. However, the accuracy that influences the output of slope mapping studies using UAV technology need to be considered such as flying altitude and selection of the optimum numbers of Ground Control Points (GCPs). This study focuses on the reviews of geospatial-based UAV mapping, others geospatial-based technologies as well as accuracy assessment of its output. Several considerations were discussed in the production of slope map using UAV technology namely determining the optimum number of GCPs and flying altitudes, as well as evaluating of UAV images. This study presents the production of high resolution slope map area that has been conducted at Kulim, Kedah, Malaysia as the slope location

A. R. Yusoff (✉)
Faculty of Built Environment and Surveying, Department of Geoinformation,
Universiti Teknologi Malaysia, Skudai, Johor, Malaysia
e-mail: ahmadrazali89@gmail.com

N. Darwin · Z. Majid · M. F. M. Ariff · K. M. Idris
Geospatial Imaging and Information Research Group, Faculty of Built Environment
and Surveying, Universiti Teknologi Malaysia, Skudai, Johor, Malaysia
e-mail: norhadija2@utm.my

Z. Majid
e-mail: zulkeplimajid@utm.my

M. F. M. Ariff
e-mail: mfaridma@utm.my

K. M. Idris
e-mail: khairulnizami@utm.my

M. A. Abbas
Faculty of Architecture Planning and Surveying, Centre of Study for Surveying Science
and Geomatic, Universiti Teknologi MARA, Shah Alam, Malaysia
e-mail: mohdazwanabbas@gmail.com

185

prone to landslide occurrences. Multi-rotor UAV known as DJI Phantom 4 was used for collecting the high resolution images with various flying altitudes. The result of X, Y and Z coordinates show that the accuracy is influenced by the flying altitude of UAV. As for flying altitude is increased, the accuracy of slope mapping is improved. Moreover, the analysis indicated that the slope area coverage and the number of tie point increases as the UAV altitude level also increases.

1 Introduction

Geospatial is defined as the relative position of objects on the earth's surface (Collin English Dictionary 2012). All related earth surface measurement including drone mapping and monitoring are classify as geospatial-based work. Drone or Unmanned Aerial Vehicle (UAV) normally attached with set of digital camera that can record the scene or object of interest. Photogrammetry offers advance mapping technology to measure and produce 2-Dimension (2D) and 3D geospatial-based mapping without touching the object.

According to Forlani et al. (2015), photogrammetry can be define as a science of extracting metric information which is position of image surface points. One of major use of photogrammetry is to measure object or scene from images taken at long distance by UAV. There are many UAV photogrammetric applications being used recently, for instance; topography, crop monitoring, coastal monitoring, landslide monitoring. Geospatial-based slope mapping is one part of the applications that can be employed by UAV. But how does the accuracy of altitude level affect the accuracy of slope map? This study will elaborate the analysis of the three different altitude levels.

2 Slope Monitoring

A slope area is associated with the height of an area where as it becomes higher thus the steeper is the gradient. The risk of landslides may occur when the height of the slopes increases and becomes unstable (Knapen et al. 2006). Landslide is one of the disasters related with unstable land condition that can lead to property damage and death. Landslide is a geological incident which includes most of the earth's movements, such as falling rocks (Hungr et al. 1999; Trappmann et al. 2014), and slope failures (Arnold et al. 2015; Hori and Tamate 2018).

There are several factors that causes landslides such as: (a) gravity acts on the slope (Reis et al. 2016); (b) erosion by rivers, glaciers, or sea waves which produce steep slopes (Blyth and de Freitas, 2017); (c) sloping rock or land slopes due to saturation by heavy rain; (d) an earthquake that produces tensions causing weak slopes to collapse; (e) volcanic eruptions produce ash, heavy rain, and trash flow; (f) tremors from machines, traffic, explosives, even thunder may trigger tremendous

Fig. 1 Example of landslide area

collapse; (g) extreme weight resulting from the accumulation of rain or snow, stacks of rocks or ores, from garbage dumps, or man-made structures that put pressure on weak to heavy cracks and other structures; (h) Groundwater pressure acts to make the slope unstable on shallow soils, deep-rooted plantings that bind colluvium to base stones. These factors can affect a slope condition in long-term if not monitored regularly. The main thing that needs to be done is monitoring the slope area that prone to landslide incidence (Fig. 1 shows example of landslide area at Johor, Malaysia).

3 Geospatial-Based Slope Mapping

Geospatial-based Slope mapping is one of the approaches to monitor slope area where the generated maps can be combined with geology inputs and environmental engineering of an area. The slope map is intended to be frequently produced for landslide mapping as a reference material for stakeholders such as developers, researchers and local authorities. There are several technologies that have been used for Geospatial-based monitoring and mapping of slope area such as satellite imagery (Bagnardi et al. 2016), Light Ranging and Radar (LiDAR) (Dunham et al. 2017), Terrestrial Laser Scanner (TLS) (Francioni et al. 2014; Tahar 2015), manned aircraft, Total Station, Mobile Laser Scanner (MLS) (Michoud et al. 2015), Global Positioning System (GPS) and drone. Table 1 shows the summary of the comparison between these technologies.

Table 1 The summary of the comparison from various geospatial-based technologies

Technology	Flight planning	Flight restriction	Cost estimation	Production rate	Coverage area	Accuracy
Satellite imagery	–	Tropical region cover with cloud	Up to ten thousand	Depend on satellite	Large area	Up to m
LiDAR	More complex	Less impact from weather	Up to hundred thousand	Can be automated, faster	Large area and not practical for small area	Up to cm and can be mm
TLS	No	No	Up to hundred thousand	Can be automated and faster	Limited coverage	Up to cm
Manned aircraft	Overlap and side lap need to be considered	Must fly during day time and need clear sky	Up to hundred thousand	Time consuming	Large area and not practical to cover small area	Up to cm
Total station	No	No	Up to thousand	Time consuming	Limited coverage	Up to mm
MLS	No	No	Up to hundred thousand	Can be automated and faster		Up to cm
GPS	No	No	Up to thousand	Can be automated and faster	Limited coverage	Up to mm
Drone/ UAV	Overlap and side lap need to be considered	Fly during day, clear sky time and under cloud	Up to thousand	Can be automated and rapid	Cover small and large area based on endurance	Up to cm

All these technologies have its specific capabilities and limitations which were used to produce slope map. For example, satellite imagery has potential for covering large area with different image resolution, however, most of the images in tropical region are covered with cloud (Al-Tahir et al. 2011). For LiDAR technology and manned aircraft, both requires huge budget reaching up to hundred thousand Dollars but provide accurate map. Meanwhile, total station required a lot of time and manpower from fieldwork until map production (Tahar 2015). Furthermore, this technique only measure bearing and distance on the earth's surface which impractical for performing fast and cost saving projects. Figure 2 shows the platforms and sensors that usually used for slope and landslide survey, which were used by Geospatial Imaging and Information Research Group (Gi2RG), Universiti Teknologi Malaysia (UTM), Johor, Malaysia.

Small rotary UAV

Fixed-wing UAV

Multi-rotar UAV

Terrestrial laser scanning

Mobile LiDAR sensor

Fig. 2 Platforms and sensors that usually used for slope and landslide survey

Moreover, laser scanning either mobile or terrestrial are techniques used for obtaining 3D coordinate data and capable to scan high-density data of an object or surfaces. GPS is used for obtaining 3D coordinates with accurate result but limited in mapping application. Presently, UAV is often used and become more popular as a monitoring and mapping application since it can provide map data in a short time. UAV applications recently have widely been used in many studies. Table 2, Figs. 3, and 4 shows UAV-based application and other sensors that used by many researches that utilize UAV and other sensors for slope and landslide survey and mapping.

Initially, the UAV was introduced for military and surveillance purposes. With the advancement of technology and instrumentation surveying, the importance of using UAV has been seen by researchers, surveyors and practitioners. By using photogrammetry concept, mapping application can provide up to sub-centimeter accuracy. Photogrammetry concept has been introduced since 1990 which divided into close range, aerial and terrestrial photogrammetry.

UAV photogrammetry was introduced by Henri Eisenbess in year 2009 through his study for capturing images of cultural heritage using close range photogrammetry concept. As one of the geospatial data acquisition technologies, UAV can be used to monitor the slope of the area experiencing instability. It is believed that this technology can be used in producing high resolution images and also can speed up the process of getting information on the incident.

In producing slope mapping, the most important part is getting the accurate result for detecting the changes of the slope area. According to Tahar (2013), number of ground control points and flying altitudes are the most important aspect need to be consider during data acquisitions. These two aspects can influence the accuracy of the produced map. Therefore, this study presents the production of high

Table 2 Some research utilize UAV and other sensors for slope and landslide survey and mapping

Published article	Drone	Photogrammetry	LiDAR	Total station	GPS
Lucieer et al. (2014)	/	/			/
Uysal et al. (2015)	/	/			/
Kršák et al. (2016)	/	/		/	
Kumar et al. (2018)	/	/			/
Tung et al. (2018)	/	/			/
Fuad et al. (2018)	/		/		/
Fugazza et al. (2018)	/	/	/		/
Rossi et al. (2018)	/	/			/
Agüera-Vega et al. (2017)	/	/		/	/
Francioni et al. (2018)	/	/	/		/
Yeh et al. (2018)	/	/			/
Xiang et al. (2018)	/	/			/
Cahyono and Zayd (2018)	/	/		/	/
Zieher et al. (2018)	/	/	/		/

Fig. 3 Total station in slope
model study

Fig. 4 GPS survey used for
landslide mapping

resolution slope map using UAV technology. The research involved the following steps, (i) preparation of field work (i.e. determination of the flying altitude) and the flight mission; (ii) processing and evaluating of UAV images, and (iii) production of slope map.

4 Applications of UAV

UAV technology become popular all over the world due to its rapid development and people awareness on the importance of UAV usage especially among surveyors, researchers, government agencies and other organizations. An aerial image is an output obtained from UAV technology which used in the field of mapping and remote sensing. Digital camera or any sensors attached to UAV used for capturing object on the earth's surface accordance to the flight path. Digital camera can be attached either in horizontal or vertical based on the purposes of study.

There were several studies have been conducted in mapping and monitoring using UAV such as cultural heritage (Eisenbeiss et al. 2005), urban planning (Spatalas et al. 2006), 3D modelling (Remondino et al. 2011), coastal (Darwin et al. 2014; Gonçalves and Henriques 2015), landslide (Everaerts 2008), river mapping (Ahmad et al. 2013; Alho et al. 2009) and others.

The advantage of UAV is able to mount different types of sensors and items for various applications. In addition, the use of UAV reduces human risk, cost and manpower which are suitable for project that involve with risky or disaster areas. UAV also is widely used in the agricultural sector to evaluate the soil conditions, identifying pests that attack soil, soil mapping or spreading seeds, pesticides and water (Krishna 2016). All UAV applications either in mapping or non-mapping fields requires different method, accuracy and standard of procedure.

5 Accuracy Assessment of UAV Mapping Studies

Some researches applied the mapping technique for specific purposes while other researches were done to determine the behaviour of the data collection and result obtained. Some studies focuses in different level mapping accuracy, UAV camera calibration, and also the effect of the Ground Control Point (GCP) distribution and numbers. Below are some studies and findings that have been done for UAV mapping application including slope mapping.

Throughout the research have been done by Agüera-Vega et al. (2017), the Ground Control Points (GCPs) affects the mapping accuracy and the findings are to choose 15 GCPs rather than 20 GCPs as the accuracy are quiet similar at 120 altitude level, and the map accuracy are increase from 4 GCPs until 15 GCPs. The optimum number for the research is 15 numbers of GCPs.

There are also other research from Udin and Ahmad (2014), based on the finding for experiment done at altitude levels of 40, 60, 80, and 100 m, sub-meter accuracy achieved by the (Root Men Square Error) RMSE value decreases when the altitude levels or flying altitude increased.

There also researches have been done to assess the calibration altitude levels for photogrammetric UAV mapping such as by Yusoff et al. (2017). Based on the finding, the optimum calibration parameters is at 25 m camera distance for the best mapping accuracy at 1.5, 15 and 25 m UAV mapping. The camera distance for calibration and UAV mapping are correlated and the optimum camera parameters are needed for high accurate mapping.

Based on Tahar (2013), the photogrammetric block for GCPs configuration shows the mapping accuracy behavior in order to produce the best photogrammetric products. In the study, two main photogrammetric results were produced namely digital orthophoto and digital elevation model. The result stated that various configurations recorded coefficient percentage of more than 97% accuracy for the six configurations. The research concluded that GCPs affected the photogrammetric block to acquire the accurate photogrammetric results such as slope mapping using photogrammetric drone. In this study, eight and nine CCPs configurations are the best configurations.

6 Significant of Study

Some applications do not concern with the accuracy and only require the overview of the area. Moreover, most of the projects are handled by UAV mapping practitioner usually involves small areas where the use of UAV technology is practical. Geospatial-based high resolution aerial images also can be obtained using UAV technology where it can fly with low flying altitude and under cloud cover.

7 Study Area

The study area is situated in Kulim, Kedah, Malaysia (Fig. 5) where three different altitude levels and numbers of GCPs were performed. The main factor for this research was conducted at Kulim, Kedah, Malaysia due to the condition of slope in that area is prone to the landslide incidences. The geospatial-based slope mapping produced in this study based on the data collection conducted in November 2017.

Fig. 5 Study area site at Kulim, Kedah, Malaysia

8 Instrumentations

8.1 DJI Phantom 4

Rotary wing UAV known as DJI Phantom 4 was used in this study. DJI Phantom 4 was equipped with gimbal, vision system, camera, remote controller, charger, live view and intelligent flight battery. This DJI Phantom 4 has an advanced stereo Vision Positioning System (VPS) which make it able to fly precisely, easier and safer without satellite positioning. Table 3 shows details specification of DJI Phantom 4.

8.2 Camera

In this study, digital camera was used and attached at the DJI Phantom 4. The camera has a megapixel of 12.4 and other specification as shown in Table 4. It has four (4) blades in which two blades rotate in clockwise direction and another two blades rotate in counter-clockwise direction. The DJI Phantom 4 is more stable and safe to be used for outdoor and indoor activities, especially in the urban area and it

Table 3 DJI Phantom 4 specification

Specification	Detail
Weight	1380 g
Diagonal size	350 mm
Max ascent speed	S-mode: 6 m/s
Max descent speed	S-mode: 4 m/s
Max speed	S-mode: 20 m/s
Max tilt angle	S-mode: 42° A-mode: 35° P-mode: 15°
Max angular speed	S-mode: 200°/s A-mode: 150°/s
Max service ceiling above sea level	19685 feet (6000 m)
Max wind speed resistance	10 m/s
Max flight time	Approx. 28 min
Operating temperature range	32° to 104°F (0° to 40 °C)
Satellite positioning systems	GPS/GLONASS
Hover accuracy range	Vertical: ±0.1 m (with Vision Positioning) ±0.5 m (with GPS positioning) Horizontal: ±0.3 m (with Vision Positioning) ±1.5 m (with GPS Positioning)

is capable to capture images from certain altitude. Figure 6 show DJI Phantom 4 with remote controller and camera attached.

8.3 Global Positioning System (GPS)

Based on the article by Geomatics World (2017), generally, there are three methods on ways to achieve high geospatial-based accuracies for UAV mapping:

1. Combining image data with Ground Control Points (GCPs)
2. Correcting position information by means of post-processing kinematic (PPK) systems
3. Correcting position information by means of real-time kinematic (RTK) systems

In this study, static observation of GPS was used for ground control points (GCPs) establishment. This observation technique only takes around 20–30 min per point. In addition, this technique can provide millimeter accuracy for absolute orientation or exterior orientation and to perform aerial triangulation. This GPS instruments is the combination of a compact form factor, revolutionary universal tracking technology, and multiple communication methods. The Topcon GR-5

Table 4 Camera specification

Specification	Detail
Sensor	1/2.3" CMOS Effective pixels:12.4 M
Lens	FOV 94° 20 mm (35 mm format equivalent) f/2.8 focus at ∞
ISO range	100–3200 (video) 100–1600 (photo)
Electronic shutter speed	8 - 1/8000 s
Image size	4000 × 3000
Still photography modes	Single shot Burst shooting: 3/5/7 frames Auto exposure bracketing (AEB): 3/5 bracketed frames at 0.7 eV Bias Timelapse HDR
Video recording modes	UHD: 4096 × 2160 (4 K) 24/25p 3840 × 2160 (4 K) 24/25/30p 2704 × 1520 (2.7 K) 24/25/30p FHD: 1920 × 1080 24/25/30/48/50/60/120p HD: 1280 × 720 24/25/30/48/50/60p
Max video bitrate	60 Mbps
Supported file systems	FAT32 ($\leq$ 32 GB); exFAT (>32 GB)
Photo	JPEG, DNG (RAW)
Video	MP4, MOV (MPEG-4 AVC/H.264)
Supported SD cards	Micro SD Max capacity: 64 GB Class 10 or UHS-1 rating required
Operating temperature range	32° to 104°F (0° to 40 °C)

Fig. 6 DJI Phantom 4

receiver is the most popular and versatile option for high precision GNSS reliability where it capable to tracking GPS, GLONASS, BeiDou, Galileo, QZSS constellations. Figure 7 shows the static GPS observation using Topcon GR-5.

Fig. 7 CPs establishment
through GPS observation

9 Research Methodology

In this study, the research methodology involves three main phases, namely data
acquisition, data processing and data analysis. The DJI Phantom 4 was flown at
three different flying altitudes such as 20, 40 and 60 m. Figure 8 shows the research
method is done.

Minimum of five (5) GCPs numbers is required for the image processing soft-
ware. The details explanations of fieldwork preparation, processing and evaluating
UAV images and production of Slope Map are discussed in the next sub sections.

10 Preparation of Field Work and the Flight Mission

Image acquisition is an important step that needs to be completed in order to get the
best aerial images. The flight planning needs to be settled before capturing the aerial
images. Several considerations need to be clarified during flight planning such as
flying altitude, coverage of the study area, focal length, scale, percentage of the end
and side lap. In real site image acquisition, the important part depends on weather
and time taken for aerial images on the study area which could affect the brightness
of images. For the two real sites of study area, the best time to acquire aerial images
is about from 8.00 am until 11.30 am in the morning.

Two people were put in-charge during the flight mission namely the pilot and the
ground crew. In this study, autonomous micro rotary wing UAV for image
acquisition was implemented for flight mission and landing. In the autonomous
mode, micro rotary wing UAV received input from laptop or mission planner via
radio modem and was flown based on the starting waypoints until the end of
waypoints. However, an operator must be alert at all time to avoid accident during
the flight mission (Tahar 2013).

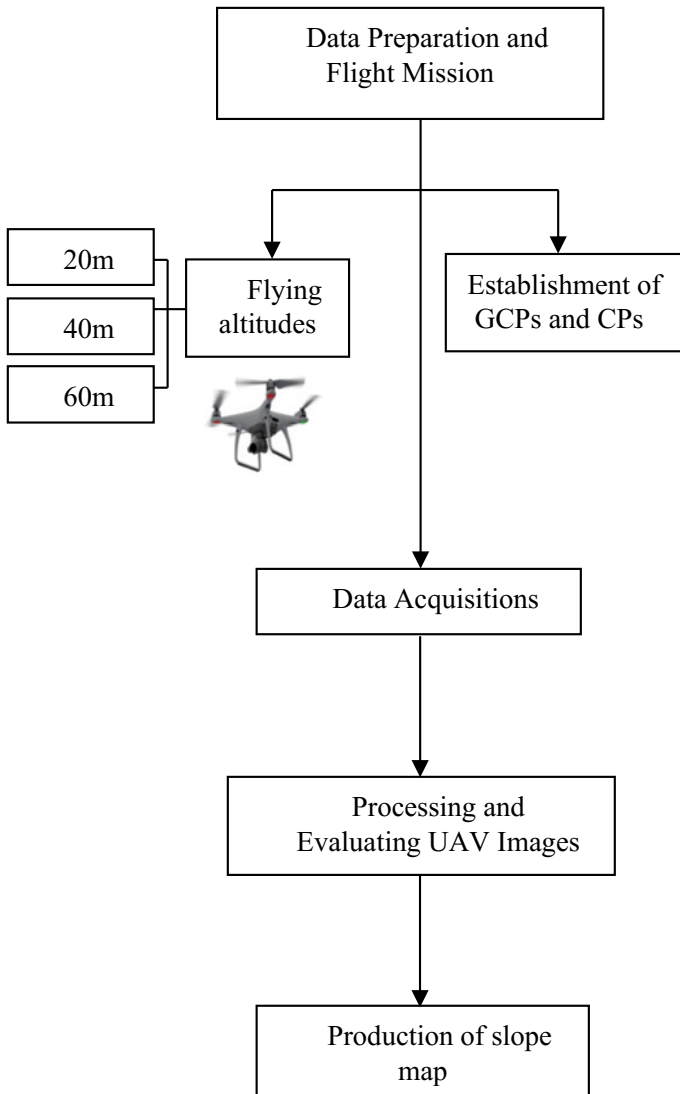**Fig. 8** Research methodology

11 Processing and Evaluating of UAV Images

Data processing was carried out after the required data were acquired successfully. In this study, the data processing involved the following; (a) The collected data were processed by using ArcGIS software to produce map either in softcopy or/and hardcopy; (b) The GCPs and CPs obtained from ground survey measurement (i.e.

Fig. 9 Distribution of GCPs and CPs of the slope area

total station and GPS rapid static technique) were processed to obtain the 3D coordinates of these points. Figure 9 shows the distribution of GCPs and CPs of the slope area.

12 Production of Geospatial-Based Slope Mapping

This stage was conducted after performing the processing and evaluating of UAV images. There are two geospatial-based slope mapping produced in this study namely, orthophoto and (Digital Elevation Model) DEM mapping of slope area. Figures 10, 11 and 12 shows the produced orthophoto based on three different flying altitudes. Meanwhile, Figs. 13, 14 and 15 shows the produced DEM based on three different flying altitudes.
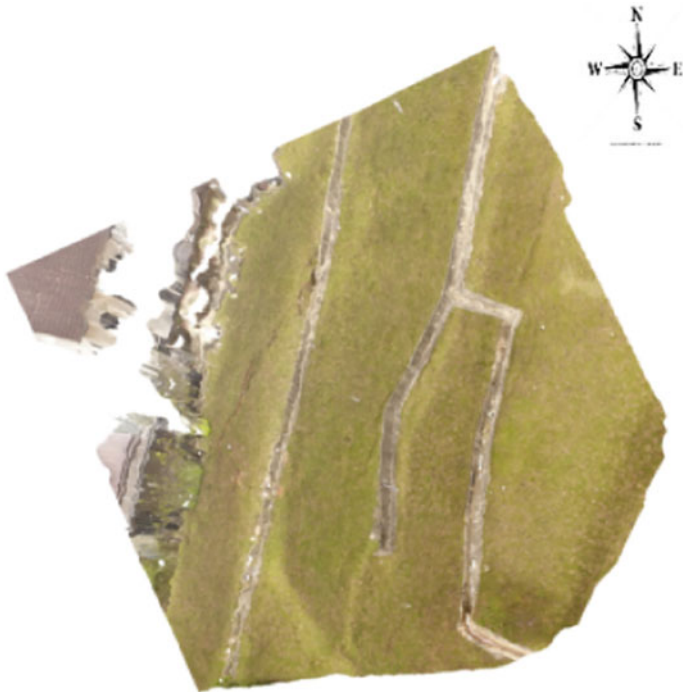
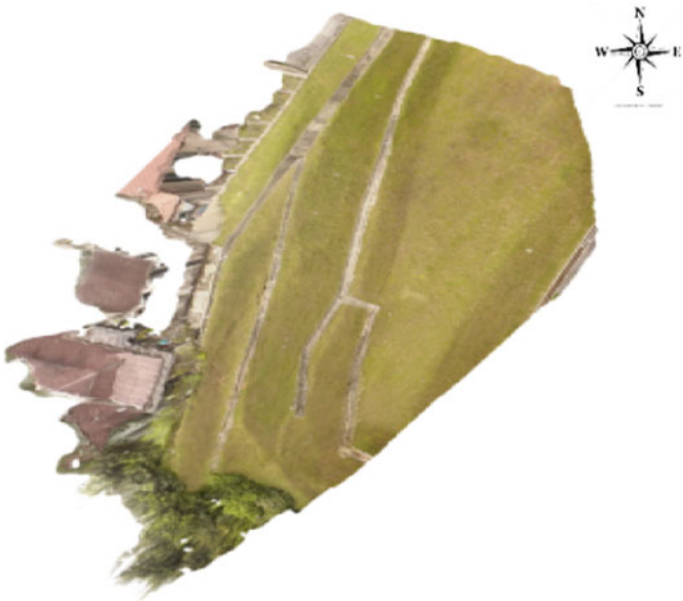**Fig. 10** Orthophoto for flying altitude of 20 m

Fig. 11 Orthophoto for flying altitude of 40 m

Fig. 12 Orthophoto for flying altitude of 60 m

13 Result and Analysis

There are two main results produced in this study, namely orthophoto and digital elevation model (DTM). Both of the results contains horizontal and height coordinates which can be used to give information of movement points of the slope area. Orthophoto and DEM results contain X, Y and Z coordinates. Figures 10, 11 and 12 illustrates the orthophoto of the produced slope area after through image processing step. Orthophoto specifically contain horizontal coordinate which gives provides clear images with high resolution and up-to-date information; in other words, data on demand can be produced by using the micro UAV.

Meanwhile, Figs. 13, 14 and 15 shows the DEM of the slope area which gives height information where the brown and magenta colour represents the highest and lowest value for three different flying altitudes respectively. The DEM shows the different highest and lowest value.

The lowest value of the slope area are 56.849 m, 56.363 m and 46.472 m at 20 m, 40 m and 60 m flying altitudes, respectively. Whereas, the highest value of the slope area are 84.042 m, 72.104 m and 68.804 m at 20 m, 40 m and 60 m flying altitudes, respectively. Based on Fig. 16, it was identified that the flying altitudes influenced the error of the aerial images. The error of the map is decreased when the flying altitudes increased. It represents all the error of X, Y and Z below
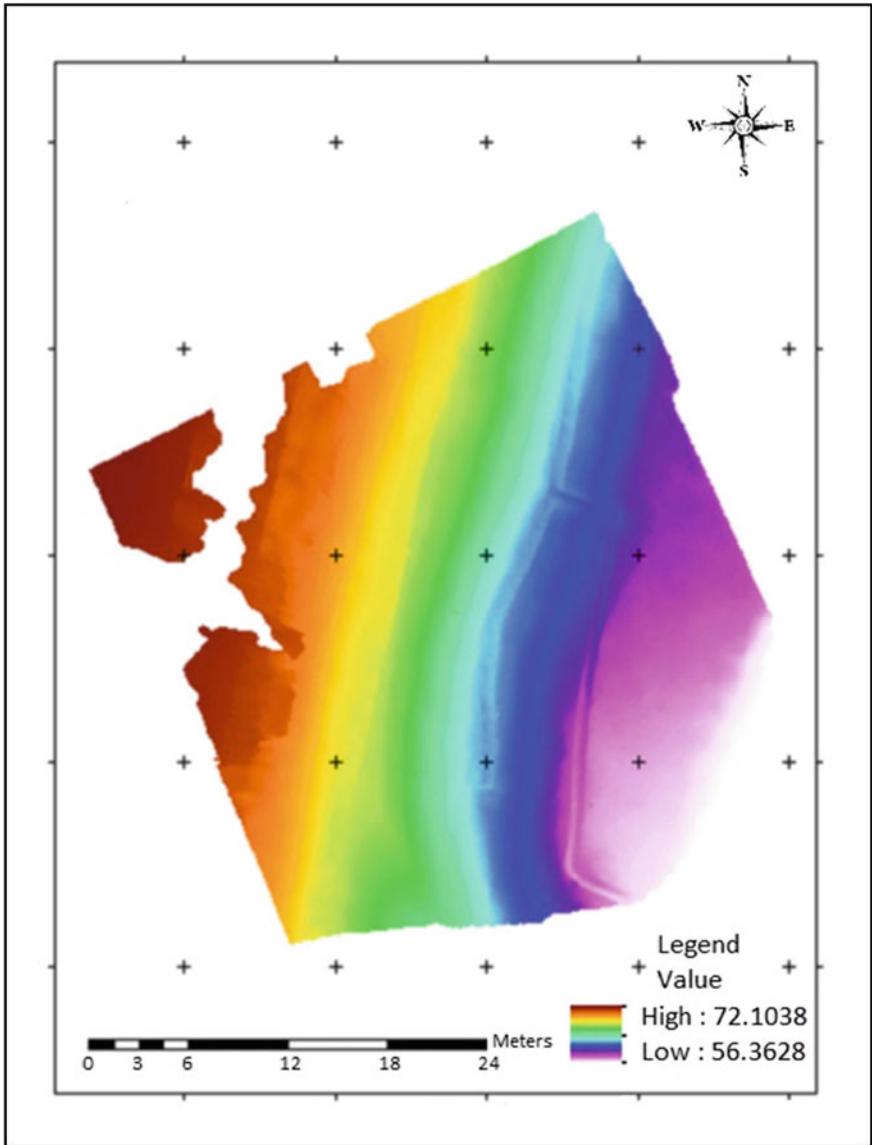
Fig. 13 DEM for flying altitude of 20 m

one (1) meter. Figure 17 shows the relationships between number of tie points, coverage area and flying altitudes. The coverage area and number of tie point increases when the flying altitude increases.
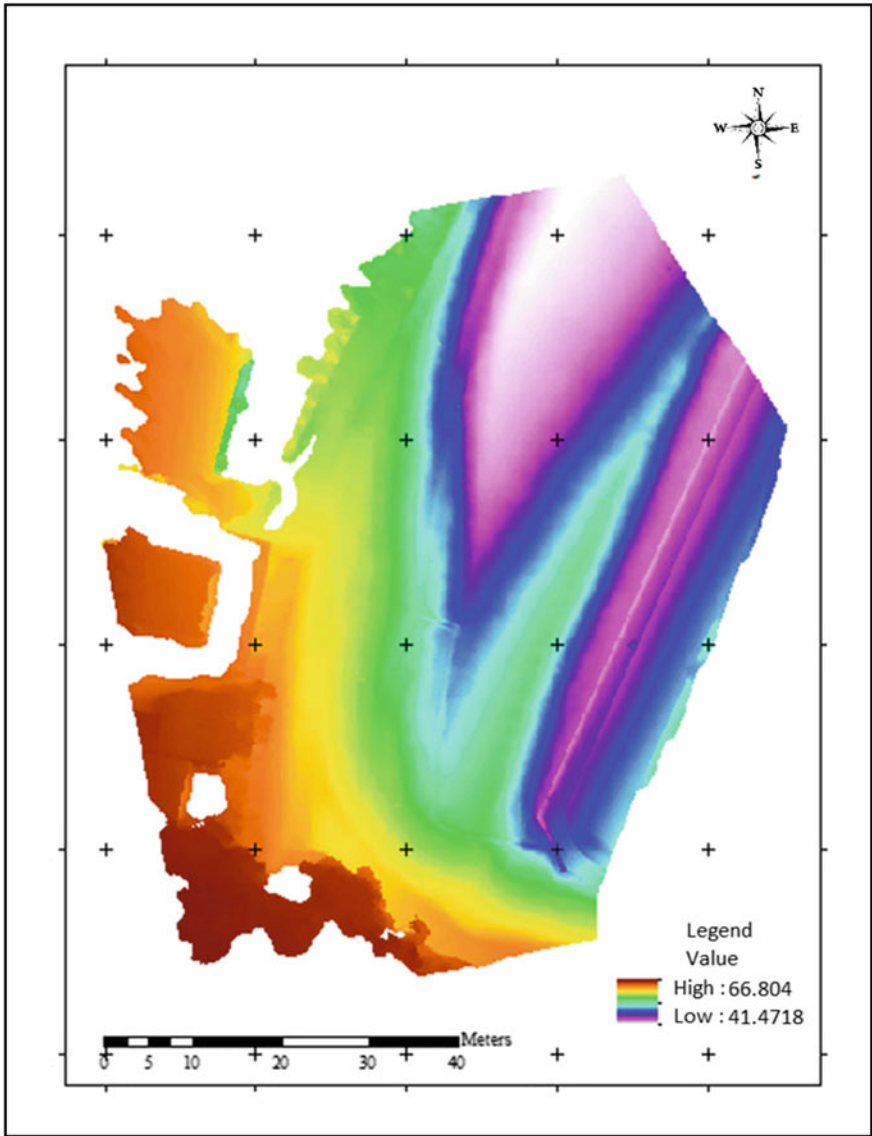
Fig. 14 DEM for flying altitude of 40 m

Fig. 15 DEM for flying altitude of 60 m

	20	40	60
X (m)	0.106784	0.132373	0.076634
Y (m)	0.132298	0.274654	0.072325
Z (m)	0.189065	0.151966	0.116996
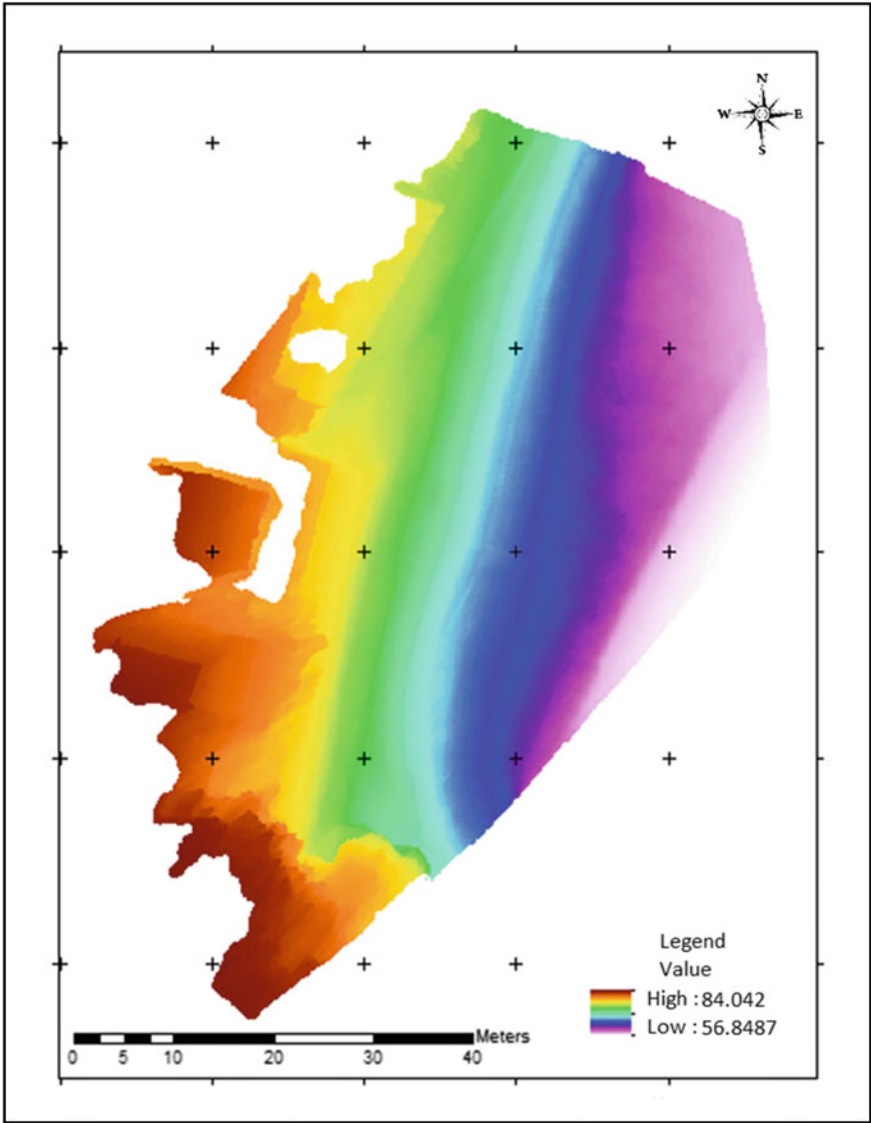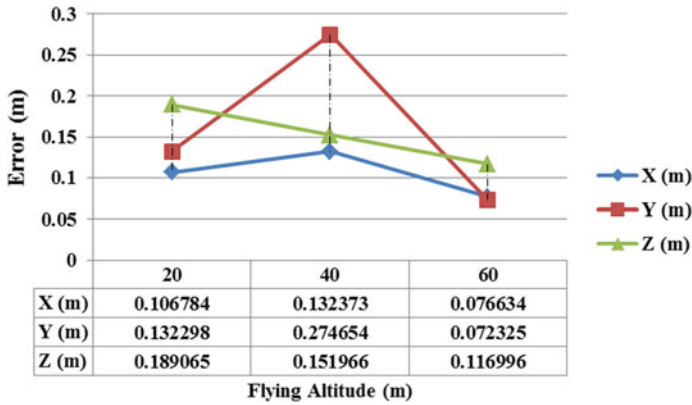
Fig. 16 Error at different flying altitudes
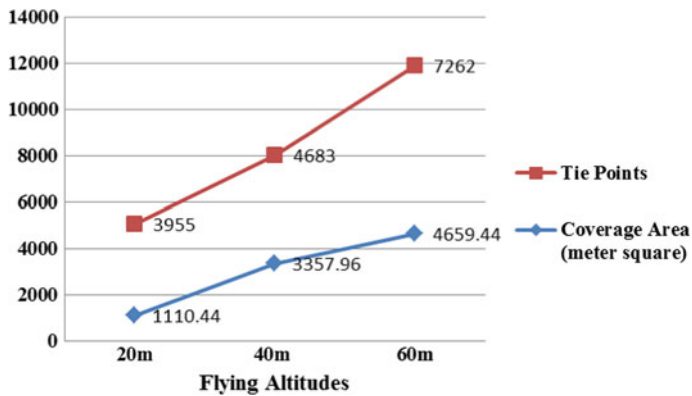
Fig. 17 Numbers of tie points and coverage area at three different altitudes

14 Conclusion

As conclusion, this study has successfully evaluated the orthophoto and DEM accuracy based on different flying altitudes using UAV technology to produce slope map. It also demonstrates the capability of UAV technology to fly at three different altitudes over the study area. Three different flying altitudes were performed, namely 20, 40, and 60 m. Throughout the study investigation, the overall error of X, Y and Z value at different altitudes for the study area are at centimeter level.

Different flying altitudes have influence on the error of X, Y and Z which means the higher the altitudes, the smaller will be the error of coordinates obtained. In addition, the analysis showed that the coverage of slope area and number of tie point increases when the flying altitude increases. Subsequently, this practical study

contributed to the slope work activities where the specific requirements for flying altitudes have been clearly stated. It is recommended in future studies will expand the analysis using UAV attached with multi sensor such as LiDAR, thermal camera, and infrared to capture slope data.

References

Agüera-Vega F, Carvajal-Ramírez F, Martínez-Carricondo P (2017) Assessment of photogrammetric mapping accuracy based on variation ground control points number using unmanned aerial vehicle. Measurement 98:221–227

Ahmad A, Tahar KN, Udin WS, Hashim KA, Darwin N, Hafis M (2013) Digital aerial imagery of unmanned aerial vehicle for various applications. In: 2013 IEEE international conference on control system, computing and engineering (ICCSCE), pp 535–540

Alho P, Kukko A, Hyyppa H, Kaartinen H, Hyyppa J, Jaakkola A (2009) Application of boat-based laser scanning for river survey. Earth Surf Proc Land 34(13):1831–1838

Al-Tahir R, Arthur M, Davis D (2011) Low cost aerial mapping alternatives for natural disasters in the caribbean. FIG Working Week 2011, Bridging the gap between cultures. Marrakech, Morocco

Arnold L, Wartman J, Massey C, MacLaughlin M, Keefer D (2015) Insights into the seismically-induced rock-slope failures in the Canterbury region using the discrete element method. Paper presented at the 6th international conference on earthquake geotechnical engineering, pp 1–4

Bagnardi M, González PJ, Hooper A (2016) High-resolution digital elevation model from tri-stereo Pleiades-1 satellite imagery for lava flow volume estimates at Fogo Volcano. Geophys Res Lett 43(12):6267–6275

Blyth FGH, de Freitas M (2017) A geology for engineers. CRC Press

Cahyono A, Zayd R (2018) Rapid mapping of landslide disaster using UAV-photogrammetry. Paper presented at the journal of physics: conference series, p 012046

Collin English Dictionary (2012) Complete & unabridged 2012 digital edition

Darwin N, Ahmad A, Zainon O (2014) The potential of unmanned aerial vehicle for large scale mapping of coastal area. Paper presented at the IOP conference series: earth and environmental science, p 012031

Dunham L, Wartman J, Olsen MJ, O'Banion M, Cunningham K (2017) Rockfall activity index (RAI): a lidar-derived, morphology-based method for hazard assessment. Eng Geol 221:184–192

Eisenbeiss H, Lambers K, Sauerbier M, Zhang L (2005) Photogrammetric documentation of an archaeological site (Palpa, Peru) using an autonomous model helicopter. In: International archives of photogrammetry, remote sensing and spatial information sciences, vol 34, no 5, p C34

Everaerts J (2008) The use of unmanned aerial vehicles (UAVs) for remote sensing and mapping. In: The international archives of the photogrammetry, remote sensing and spatial information sciences, vol 37, pp 1187–1192

Forlani G, Roncella R, Nardinocchi C (2015) Where is photogrammetry heading to? State of the art and trends. Rendiconti Lincei 26(1):85–96

Francioni M, Salvini R, Stead D, Litrico S (2014) A case study integrating remote sensing and distinct element analysis to quarry slope stability assessment in the Monte Altissimo area, Italy. Eng Geol 183:290–302

Francioni M, Salvini R, Stead D, Coggan J (2018) Improvements in the integration of remote sensing and rock slope modelling. Nat Hazards 90(2):975–1004

Fuad N, Ismail Z, Majid Z, Darwin N, Ariff M, Idris K (2018) Accuracy evaluation of digital terrain model based on different flying altitudes and conditional of terrain using UAV LiDAR technology. Paper presented at the IOP conference series: earth and environmental science, p 012100

Fugazza D, Scaioni M, Corti M, D'Agata C, Azzoni RS, Cernuschi M (2018) Combination of UAV and terrestrial photogrammetry to assess rapid glacier evolution and map glacier hazards. Nat Hazards Earth Syst Sci 18(4):1055–1071

Geomatics World (2017) UAV Monitoring of coastal erosion. https://www.geomatics-world.co.uk/content/article/uav-monitoring-of-coastal-erosion. Accessed 25 Sept 2018

Gonçalves J, Henriques R (2015) UAV photogrammetry for topographic monitoring of coastal areas. ISPRS J Photogram Remote Sens 104:101–111

Hori T, Tamate S (2018) Monitoring Shear strain in shallow subsurface using mini pipe strain meter for detecting potential threat of slope failure. Geotech Test J 41(2)

Hungr O, Evans S, Hazzard J (1999) Magnitude and frequency of rock falls and rock slides along the main transportation corridors of southwestern British Columbia. Can Geotech J 36(2):224–238

Knapen A, Kitutu MG, Poesen J, Breugelmans W, Deckers J, Muwanga A (2006) Landslides in a densely populated county at the footslopes of Mount Elgon (Uganda): characteristics and causal factors. Geomorphology 73(1–2):149–165

Krishna K R (2016) Push button agriculture: Robotics, drones, satellite-guided soil and crop management. CRC Press

Kršák B, Blišťan P, Pauliková A, Puškárová P, Kovanič Ľ, Palková J (2016) Use of low-cost UAV photogrammetry to analyze the accuracy of a digital elevation model in a case study. Measurement 91:276–287

Kumar NS, Ismail MAM, Sukor NSA, Cheang W (2018) Geohazard reconnaissance mapping for potential rock boulder fall using low altitude UAV photogrammetry. Paper presented at the IOP conference series: materials science and engineering, p 012033

Lucieer A, Jong SM, Turner D (2014) Mapping landslide displacements using structure from motion (SfM) and image correlation of multi-temporal UAV photography. Prog Phys Geogr 38(1):97–116

Michoud C, Carrea D, Costa S, Derron M-H, Jaboyedoff M, Delacourt C (2015) Landslide detection and monitoring capability of boat-based mobile laser scanning along Dieppe coastal cliffs, Normandy. Landslides 12(2):403–418

Reis A, Araújo E, Silva C, Cruz A, Gorini C, Droz L (2016) Effects of a regional décollement level for gravity tectonics on late Neogene to recent large-scale slope instabilities in the Foz do Amazonas Basin, Brazil. Mar Pet Geol 75:29–52

Rossi G, Tanteri L, Tofani V, Vannocci P, Moretti S, Casagli N (2018) Multitemporal UAV surveys for landslide mapping and characterization. Landslides 1–8

Remondino F, Barazzetti L, Nex F, Scaioni, M, Sarazzi D (2011) UAV photogrammetry for mapping and 3d modeling–current status and future perspectives. In: International archives of the photogrammetry, remote sensing and spatial information sciences, vol 38, no 1, p C22

Spatalas S, Tsioukas V, Daniil M (2006) The use of remote controlled helicopter for the recording of large scale urban and suburban sites. In: Proceedings of the scientific conference. Culture of representation, Xanthi, Greece

Tahar K (2013) An evaluation on different number of ground control points in unmanned aerial vehicle photogrammetric block. Int Arch Photogramm Remote Sens Spat Inf Sci 40:93–98

Tahar KN (2015) Investigation on different scanning resolutions for slope mapping studies in cameron highlands, Malaysia. Arabian J Sci Eng 40(1):245–255

Trappmann D, Stoffel M, Corona C (2014) Achieving a more realistic assessment of rockfall hazards by coupling three-dimensional process models and field-based tree-ring data. Earth Surf Proc Land 39(14):1866–1875

Tung WY, Nagendran SK, Ismail MAM (2018) 3D rock slope data acquisition by photogrammetry approach and extraction of geological planes using FACET plugin in CloudCompare. Paper presented at the IOP conference series: earth and environmental science, p 012051

Udin W, Ahmad A (2014) Assessment of photogrammetric mapping accuracy based on variation flying altitude using unmanned aerial vehicle. Paper presented at the IOP conference series: earth and environmental science, p 012027

Uysal M, Toprak Polat N (2015) DEM generation with UAV photogrammetry and accuracy analysis in Sahitler hill. Measurement 73:539–543

Xiang J, Chen J, Sofia G, Tian Y, Tarolli P (2018) Open-pit mine geomorphic changes analysis using multi-temporal UAV survey. Environ Earth Sci 77(6):220

Yeh F-H, Huang C-J, Han J-Y, Ge L (2018) Modeling slope topography using unmanned aerial vehicle image technique. Paper presented at the MATEC web of conferences, p 07002

Yusoff AR, Ariff MFM, Idris KM, Majid Z, Chong AK (2017) Camera calibration accuracy at different UAV flying heights. In: The international archives of photogrammetry, remote sensing and spatial information sciences, vol 42, p 595

Zieher T, Toschi I, Remondino F, Rutzinger M, Kofler C, Mejia-Aguilar A, Schlögel R (2018) Sensor-and scene-guided integration of TLS and photogrammetric point clouds for landslide monitoring. In: International archives of the photogrammetry, remote sensing & spatial information sciences, vol 42, no 2

Remote Sensing Techniques in Disaster Management: Amynteon Mine Landslides, Greece

Aikaterini Karagianni, Ilias Lazos and Alexandros Chatzipetros

Abstract Natural or man-made disasters are phenomena that can affect large areas and have many environmental, societal and economic impacts. Landslides are among the major disasters of large scale that may affect the natural environment as well as urban areas, often causing massive destruction, loss of property, or even fatalities worldwide. Developing tools that are effective for disaster management is imperative to monitor and mitigate their effect. Satellite data and remote sensing techniques, combined with geological data and studies can provide valuable information regarding monitoring of natural hazards in general and especially of landslides. This chapter concerns the ex ante and ex post study of a complex set of landslides that occurred in the lignite mine of Amynteon in north-western Greece (June 2017). Weakened material cohesion due to fragmentation, further degraded by mining activities and hydrogeological factors led to the catastrophic event. The landslide occurred in along the south faces of the mine, resulting to extended collapses, destruction of mining machinery, evacuation of the adjacent Anargyri village and a big financial impact. Landsat 8 and Sentinel-2 satellite data acquired before and after the event are being used. Digital image processing techniques are applied for change detection. In addition, geological data are being used to provide information about the geological background of the area and landslides vulnerability. Visual interpretation of the area affected by the landslides is also being done, contributing to the overall study.

A. Karagianni (✉)
Laboratory of Photogrammetry – Remote Sensing, School of Civil Engineering,
Faculty of Engineering, Aristotle University of Thessaloniki, Thessaloniki, Greece
e-mail: aikateck@civil.auth.gr

I. Lazos · A. Chatzipetros
Laboratory of Geology and Palaeontology, School of Geology,
Aristotle University of Thessaloniki, Thessaloniki, Greece
e-mail: ilialazo@geo.auth.gr

A. Chatzipetros
e-mail: ac@geo.auth.gr

1 Introduction

Natural or man-made disasters are phenomena that can affect large areas and have many environmental, societal and economic impacts (van Westen 2000). Landslides are among the major disasters of large scale that may affect the natural environment as well as urban areas. The occurrence of destructive landslide phenomena is frequent worldwide, causing radical changes in the wider area, related to geomorphological, environmental, societal and economic factors (Metternicht et al. 2005).

Landslide hazard of an area is an essential parameter in the overall assessment of the geological-geotechnical suitability of this area. Activation of landslide phenomena is connected to a variety of endogenous and exogenous factors. Most land slopes have reached a state of equilibrium as it has been formed during the geological evolution of the slopes (discharges due to erosion, change in material properties, old movements, etc.).

Mass movements are the result of many and complex processes that present a dynamic development and cause significant environmental degradation. The extent and rate of environmental impacts range from the morphological evolution of the surface due to geodynamic erosion processes to the local and rapid change of topographic data of an area, caused by a landslide. According to their characteristics (materials involved and mode of movement), landslides can be classified in various types that often determine the study approach.

Landslides are primarily associated with mountainous regions. However, they can also occur in areas of generally low relief as cut-and-fill failures (roadway and building excavations), collapse of mine-waste piles (especially coal), river bluff failures, lateral spreading landslides and a wide variety of slope failures associated with quarries and open-pit mines (USGS 2018).

Monitoring landslide activity over extensive areas occurs as an important aspect at the management of natural hazards and risk. Detection and monitoring of landslide areas, in order to understand their dynamics, could provide useful information regarding negative effects reduction (Gili et al. 2000). Especially in areas of natural resources extraction, studying of these phenomena is quite important and necessary as it is connected to a combination of factors and impacts (Paull et al. 2006).

Landslide monitoring could be accomplished by several methods (Hervás et al. 2003). Among the used methods, satellite data and remote sensing techniques can be proven of particular importance as they provide wide coverage of the affected areas, high frequency data and information about non-visible spectral regions (Mantovani et al. 1996; Scaioni et al. 2014; Joyce et al. 2009). Additional geological data can provide information about the geological background of the area contributing in landslide disaster management studies (Scaioni et al. 2014).

In general, remote sensing data offer valuable information during various phases of a landslide study as: detection and classification of landslides, monitoring the activity of existing landslides, analysis and prediction in space and time of slope

failures (Mantovani et al. 1996). Particularly in landslide monitoring, a wide range of satellite remote sensing techniques in combination with more traditional or recently developed methods can be applied to obtain useful data (aerial or terrestrial photogrammetry, Global Position System for location determination, thermal infrared data for soil moisture conditions monitoring in relation to landslide movements, etc.).

Regarding monitoring of landslides in mine areas, remote sensing data are able to provide information on changes in local environments in a cost effective way. Furthermore, this type of data has been successfully used in several cases of mining sector studies as investigating geological hazards or monitoring the environmental impact of mining (Wang et al. 2013; Paull et al. 2006; Li et al. 2015; Dong et al. 2009). In combination with other forms or sources of data (e.g. geological data, terrestrial imagery, precipitation data sets, surface displacement measurements), remote sensing data may contribute to the assessment of changes in land cover, the extent of the physical impact of mining operations (e.g. infrastructure, mining pits, sedimentation), the effects of migration and settlement dynamics, etc. (Paull et al. 2006). Satellite images offer quick and concise views of a potential geological hazard area, composing a large database that presents the dynamic changes caused by landslide phenomena and thus can be a valuable and efficient tool in mine monitoring (Wang et al. 2013).

The case study presented in this chapter concerns a large scale landslide phenomenon that took place in June 10, 2017 in the lignite mine of Amynteon, region of Western Macedonia in Greece, leading to the destruction of a large part of the mine, cancelation of mining activities, partial destruction and evacuation of the adjacent Anargyri village and multiple socio-economic impacts. Landsat 8 and Sentinel-2 satellite data acquired before and after the event are being used. Digital image processing techniques are applied for change detection and visual interpretation of the area affected by the landslides is also being done. In addition, an overview of the geological structure and the tectonic setting of the active faults of the area, as well as the landslide type and its triggering factors are presented.

2 Study Area

Study area is located in the north-western part Greece, region of Western Macedonia, in medium-high altitude (600 m) and concerns the lignite mine of Amynteon. The mine is located between lakes Vegoritis and Chimaditis, close to the town of Amynteon. The smaller village of Anargyri is located on the southwest side of the mine. Figure 1 presents the location of the study area in Greece (red dot), as well as a satellite image of the mine from Google Earth (2018).
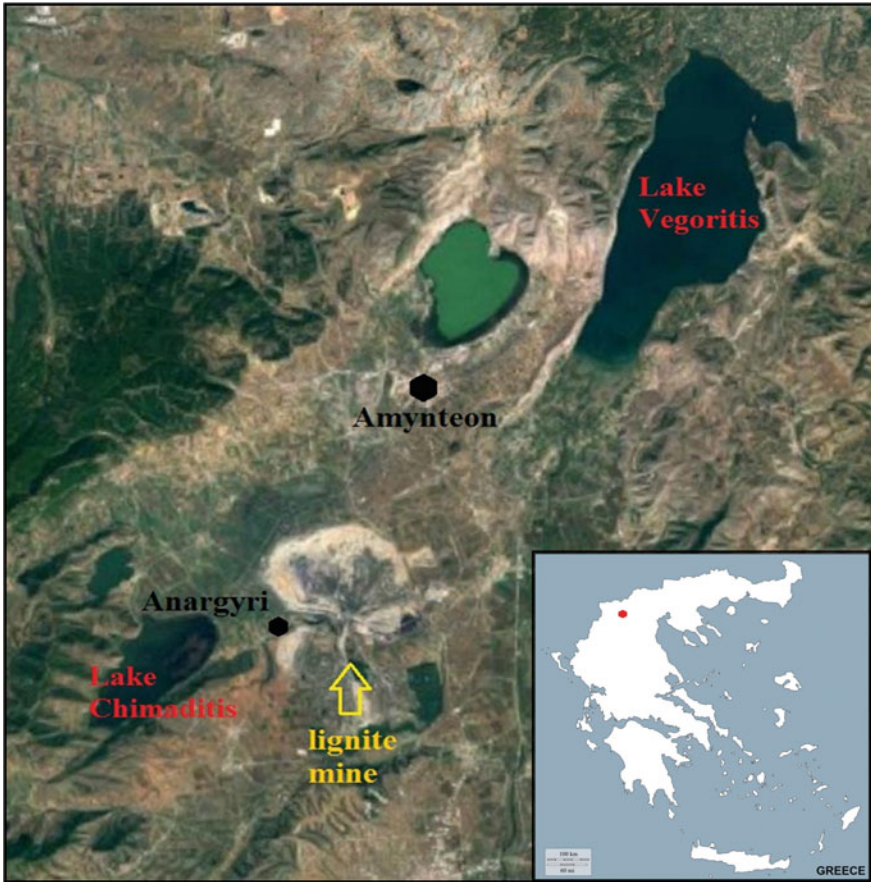
Fig. 1 Location of the study area in Greece (red dot) and satellite image of the mine from Google Earth

3 Geological and Structural Setting

3.1 Geological Setting

The bedrock of the broader area is comprised mainly of Pelagonian geological zone and, covering a much smaller area, Subpelagonian rocks. In general terms, Palaeozoic metamorphic rocks are overlain either stratigraphically or tectonically by younger Mesozoic and Tertiary rocks (Mountrakis 1986). The bedrock is unconformably covered in places by post-alpine sedimentary formations, while Upper Quaternary deposits (mainly alluvium and scree) cover locally both of them. The Pelagonian bedrock is mainly structured in four distinct units (Mountrakis 1986; Pavlides and Mountrakis 1987): (a) Palaeozoic crystalline rocks, including

granite intrusions and Permian-Triassic metaclastic sequences, (b) Triassic-Jurassic carbonates, which constitute the main part of the bedrock in the study area, (c) ophiolites and associated sediments, overthrusting Pelagonian zone and (d) Middle-Late Cretaceous transgressive sediments. Most of the study area is covered by mainly lacustrine Middle Pliocene–Lower Pleistocene sediments. The Pliocene formation comprises of three main horizons: the lower one is dominated by conglomerate, containing ophiolitic clasts, red clay and marls. A middle horizon comprises of fine-grained sediments, mainly white marl, with thin lignite-bearing layers. The uppermost horizon contains alternations of white marl and marly limestone with occasional sandy layers. The total thickness of the Pliocene deposits is more than 700 m at the central part of the basin. The Lower Pleistocene sequence is rather cohesive and consists of red clays with gravel parts at its lower part and red clay and breccia at its upper one (Pavlides and Mountrakis 1987).

3.2 Structural Setting

The area of NW Greece has been subjected to several deformations, which caused continuous geomorphological changes and a variety of tectonic structures (active or not). Successive deformation phases affected in various ways the geotectonic evolution of the area, forming its current structure (Kilias and Mountrakis 1989). The first major deformation phase is associated with the thrusting of Axios (Vardar) and Subpelagonian ophiolites. They overthrust the Pelagonian carbonates and are associated with the destruction of the Axios and Subpelagonian-Pindos oceans. This phase is imprinted on the schistosity and folding and is characterized by abundant ophiolitic mélange (Figs. 2 and 3). The Upper Cretaceous–Upper Eocene compressional phase formed NW-SE trending folds and thrusts. This imbrication caused widespread inversions, especially along the western Pelagonian margin. The major folding resulted in the formation of NW–SE trending anticline and syncline structures.

An ENE-WSW trending extensional event during the Lower Oligocene formed the molassic Mesohellenic Trench (Figs. 4 and 5). The detachment faults of this phase affected the ophiolite masses under semi-ductile conditions, causing their displacement to approximately their current location. The 40-km-wide Mesohellenic Trench is developed in a NNW-SSE direction, transversely to the direction of Lower Oligocene extension, constituting the most recent and extensive molassic trench of Greece, while the sedimentation went on from Oligocene to Upper Miocene. During the Middle–Upper Miocene, an E-W compressional phase caused the formation of N-S trending ophiolite imbrications, as well as strike-slip faults of WNW–ESE strike. A significant number of them were reactivated as normal faults during the subsequent extensional neotectonic phases. The compressional deformation was completed during the Upper Miocene by the last NNE-SSW trending phase. This phase formed E-W reverse faults in the ophiolitic masses and reactivated of the inherited strike-slip faults.

Fig. 2 Ophiolitic mélange of the broader area, derived from the Axios and Subpelagonian-Pindos oceans destruction (later generation quartz veins crisscross the rock mass)

Fig. 3 Characteristic example of a slickenside in the broader area (successive stages of brittle, semi-brittle & ductile deformation are evident throughout the ophiolitic mass)

Fig. 4 Molassic formations (alternations of sandstones and marls) of the Mesohellenic Trench of the broader area

Fig. 5 Reverse fault in the molassic formations of the Mesohellenic Trench

3.3 Neotectonic Setting

Two main neotectonic extensional phases affected the broader NW Greece area (Pavlides 1985; Pavlides and Mountrakis 1987). The first one, during Upper

Miocene–Pliocene, created or reactivated NW-SE trending normal faults, which formed large grabens of the same direction. A constant NE-SW directed extensional stress field affected the entire interior Aegean region. The last deformation phase during the Quaternary is still active. This NNW-SSE trending extension caused the formation or reactivation of significant NE-SW to E-W striking normal faults. They caused the fragmentation of the large grabens into smaller transverse sub-basins. This extensional phase is currently active and its faults played the most important role in the neotectonic evolution of the area. Several of these NE-SW to ESE-WNW striking faults have been active during the Neogene-Quaternary and are located within the large basins of the area (Florina, Amynteon–Ptolemais and Kozani ones). One of the most important faults in the area is the Aliakmon one, a segment of which was activated during the May 13th, 1995 Kozani-Grevena Mw 6.6 earthquake (Pavlides et al. 1995; Chatzipetros 1998). Nevertheless, several earthquakes of smaller magnitude have been recorded in the broader area (Tsapanos 2005). Figure 6 presents the Neotectonic faults and epicenter locations of earthquake events within the time period 1800–2007 into the broader area (modified from Tsapanos 2005). Several microseismic events are recorded in the close area of the main active tectonic structures.
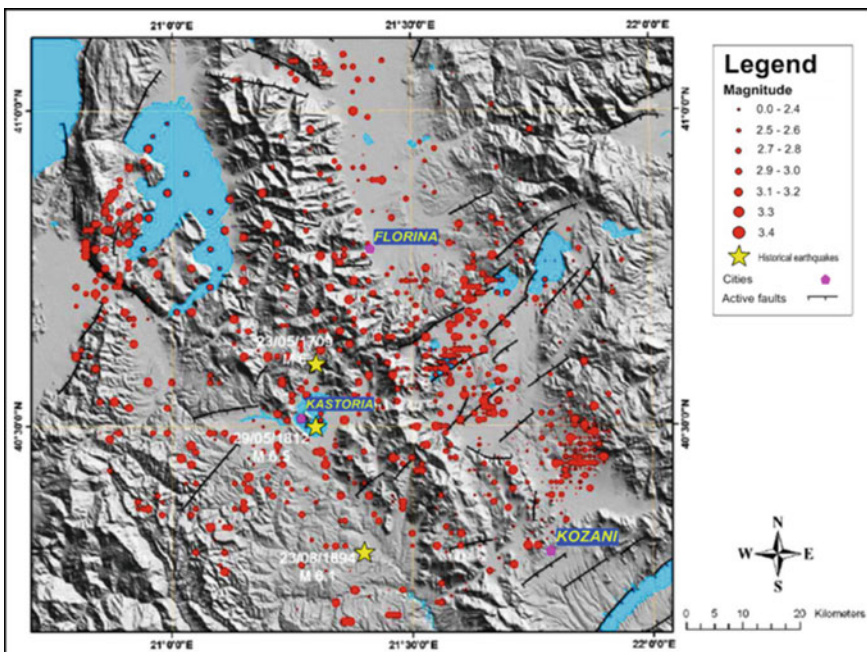
Fig. 6 Neotectonic faults and epicenter locations of earthquake events within the time period 1800–2007 into the broader area (modified from Tsapanos 2005)

3.4 Active Faults of the Study Area

The broader Ptolemais basin, where the lignite mine of Amynteon is located, is characterized by six major active fault zones (Fig. 7). They are Komnini-Asvestopetra (possibly extended to Pyrgi village), Emporion-Perdika, Anargyri (or Chimaditida-Anargyri), Perea-Maniaki, Vegora (or Vegoritida-AgiosPanteleimon) and Nymfeon-Xino Nero-Petres Lake (Pavlides 1985). The Amynteon mine landslide is associated to Anargyri and Vegora active faults. Nevertheless, a multitude of secondary faults also affect the area of the mine and might have contributed to the weakening of the rock/soil mass (see Tzampoglou and Loupasakis 2018 and references therein).

3.4.1 Anargyri Fault

Anargyri fault is one of the major faults of Amynteon-Ptolemais basin and defines the southern shore of Chimaditida Lake (Pavlides 1985). It is of N60E strike and dips to the NW. It forms the Chimaditida Lake graben, which is the most recent (Quaternary) graben of the basin. Based on drilling data from the lignite-bearing sediments, the estimated fault throw is 130 m. The Anargyri fault affects the entire Pliocene-Quaternary sequence.
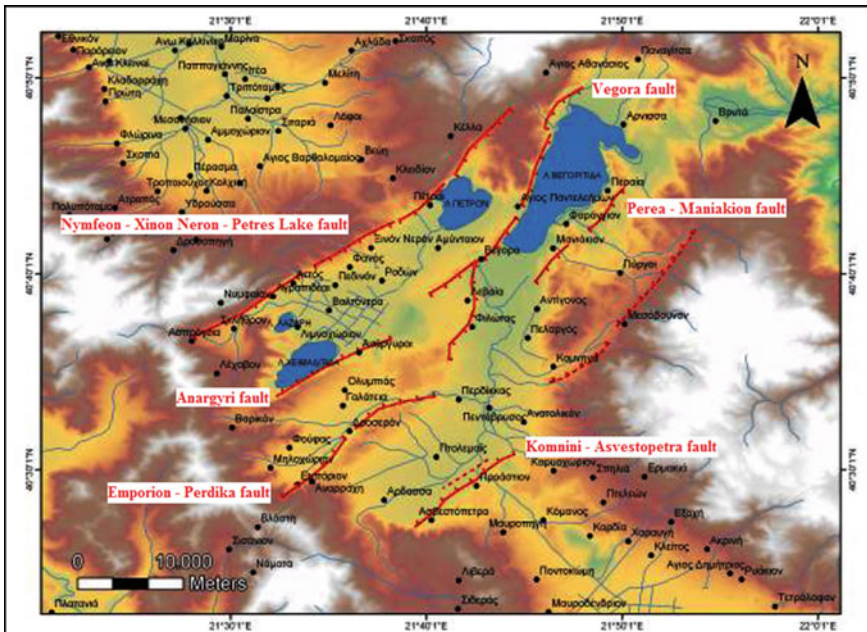
Fig. 7 Simplified structural map of the study area (modified from Pavlides, 1985)

3.4.2 Vegora Fault

Vegora fault is a major normal fault along the western shore of Vegoritida Lake, with a NE-SW strike (between 30° and 40°), while the estimated dip angle is 60° SE (Pavlides 1985). The total length of Vegora fault is 20 km, and it deforms the Mesozoic Pelagonian carbonates, forming the Vegoritida Lake graben. A SW extension of this fault zone extends into the Pliocene and Quaternary sediments of Ptolemais basin, while the fault throw is estimated between 200 and 500 m. It is also considered an active fault, as it deforms very recent scree that overlies the fault slickenside.

3.5 Interpretation of the Tectonic Setting of the Amynteon Lignite Mine Area

The interaction of both the Anargyri and Vegora faults affects the Amynteon lignite mine area, leading to complicated deformation of the lignite-bearing formations, forming a transitional transfer zone.
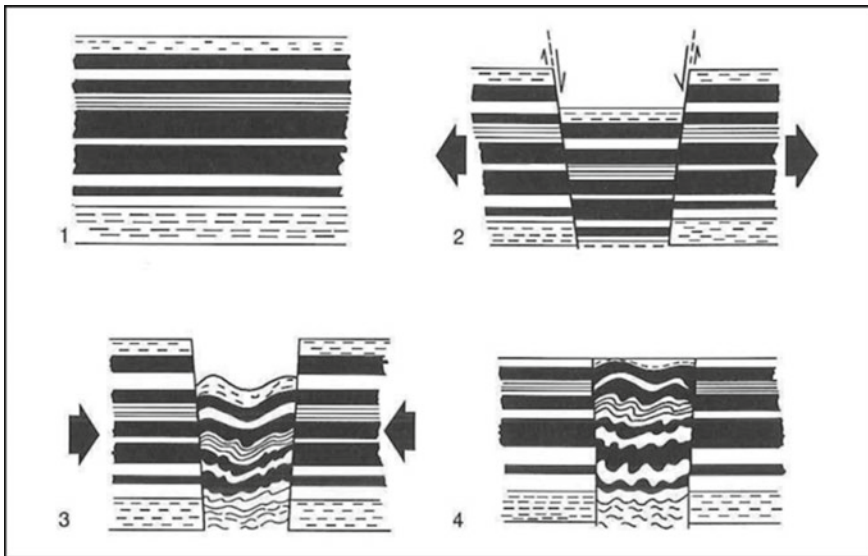
Fig. 8 Schematic representation of the subsequent stages of a pincée structure: (1) Deposition of horizontal beds, (2) Graben formation (extensional stage), (3) Folding of the graben formations (compressional stage), (4) Final form due to erosion (modified from Pavlides 1985)

Furthermore, various tectonic structures are observed within the mine. The most important of them are normal faults, which are dominant, but also bed-parallel slip, anticlines, reverse faults, folds and grabens. All these structures can be produced by the interplay of localized extensional and compressional tectonic processes, often forming what is known as pincée structures. A pincée structure is characterized by the formation of a graben in an initial stage (extensional stage), while a subsequent compressional one, which can be very weak, folds the formations within the graben (Fig. 8).

4 The Amynteon Mine

Amynteon mine is one of the main lignite mining areas in the broader Ptolemais basin coal field. Mining produces lignite which is used for power production in the adjacent Amynteon coal power plant. Throughout the years, the mine has experienced successive expansions both horizontally, as well as vertically. This was necessary in order to respond to increased demand, as well as to follow the coal seams that are being displaced by numerous faults.

Figure 9 presents a typical excavation front, exhibiting a very complex faulting pattern, causing the lignite seams and the intercalated marl to fracture and be deformed by occasionally large displacements. This multifractured nature of the sequence might have played a role in reducing the cohesiveness of the material and hence facilitated the landslide.

Fig. 9 Typical excavation front of the Amynteon lignite mining area

5 The Amynteon Mine Landslides

Landslides are some of the most important destructive phenomena and are caused by both natural and man-made factors. Landslides are classified into several types, the main ones being (a) rotational, (b) translational, (c) block slide, (d) rockfall, (e) toppling and (f) creep. The Amynteon lignite mine landslide shows characteristics of a rotational landslide. According to U.S. Geological Survey (USGS 2018),
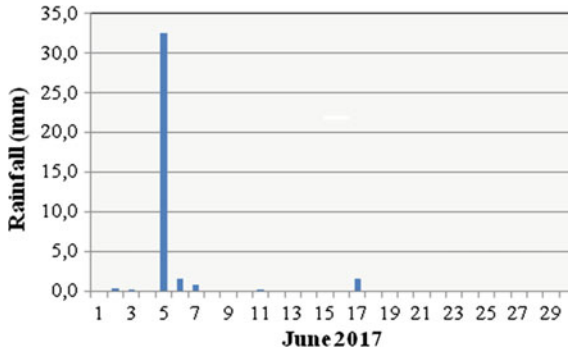
Fig. 10 Rainfall during June 2017

Fig. 11 General view of the June 10, 2017 Amynteon mine landslide

rotational landslide is a slide in which the surface of rupture is curved concavely upward and the slide movement is roughly rotational about an axis that is parallel to the ground surface and transverse across the slide. Furthermore, this type of landslide is observed mainly into soil masses, while other landslide types (block slide, rockfall and topple) are common in cohesive rock formations.

The exact failure factors have not been determined yet and are subject to ongoing modelling (e.g. Tzampoglou and Loupasakis 2017a, b; 2018; Dimitrakopoulos and Koumantakis 2017), as well as investigation by expert panels appointed by the Ministry of Infrastructure, Transport and Networks and the owner of the mine (Public Power Company S.A.). It is possible that the Plio-Pleistocene sedimentary sequence in Amynteon mine acted as a soil mass, due to the intense fragmentation caused by extensive faulting and jointing associated to the transfer zone between Anargyri and Vegora faultzones. These faults affected the lignite bearing formations, causing poor cohesion and leading to the formation of a multifragmented mass. Furthermore, it is

Fig. 12 Ground rupture at Anargyri village due to the landslide

possible that human factors affected the initiation of the landslide. The deep exca-
vation at the foot of the mining fronts and the simultaneous deposition of material at
the mine's upper part may have charged the upper excavation area, while the stability
at the lower part was reduced. Initial signs of failure (e.g. creep, surface ruptures, etc.)
caused halting of mining activity at this sector and removal of machinery. Finally, a
few days before the main landslide a rather extreme rain event was recorded
(36.2 mm of precipitation) during a normally dry period. Figure 10 presents a dia-
gram based on rainfall data of the area during June 2017 (Interactive database
Meteosearch 2018).

The landslide effects covered a large area and caused damages in the order of
several hundreds of millions of Euros, due to loss of exploitable lignite deposits,
destruction of mining machinery and equipment, halting of works and significant
damages to the nearby Anargyri village, a large part of which was preventively
evacuated (Figs. 11 and 12). Compensation of properties and public infrastructure
damaged during the landslide will also add further to the total cost.

6   Satellite Data

The constant evolution of technology in remote sensing and Earth observation
provide continuous information, several times under the policy of free data. The
available satellite data have significantly increased over the past years, offering
various possibilities for a high number of applications.

The data employed for this case study concern Landsat 8 and Sentinel-2 satellite
imagery acquired before and after the catastrophic event, providing the ability to
detect the landslide and monitor the affected area, highlighting also the changes.

6.1   Landsat 8 Satellite Data

Landsat 8 was launched on February 11, 2013 and carries two instruments: The
Operational Land Imager (OLI) sensor and the Thermal Infrared Sensor (TIRS).
These sensors both provide improved signal-to-noise (SNR) radiometric perfor-
mance, quantized over a 12-bit dynamic range (4096 potential grey levels in an
image compared with only 256 grey levels in previous 8-bit instruments). Improved
signal to noise performance enables better characterization of land cover state and
condition (Landsat 8 Mission 2018).

Satellite data acquired from Landsat 8 consist of eleven spectral bands with a
spatial resolution of 30 m for Bands 1–7 and 9. The resolution for Band 8
(panchromatic) is 15 m and for Bands 10, 11(thermal bands) is 100 m. Among the
eleven spectral bands, Landsat 8 includes one band that measures the near infrared
(Band 5-NIR) and two bands that cover different slices of the shortwave infrared
(Bands 6 and 7-SWIR).

Landsat 8 satellite data could be a useful tool for monitoring and analysing the territory, as their spectral capabilities give the opportunity to identify the extent of the landslide and provide additional information about the landslide location and the affected area in general.

The image data that have been used in this study were downloaded free of charge from USGS EarthExplorer (2018). They were acquired at 2017-05-02 (path: 185, row: 32) and 2017-06-26 (path: 184, row: 32) before and after the landslide event respectively, with level processing 1T–Standard Terrain Correction (systematic radiometric and geometric accuracy) and projection information: UTM, zone 34, spheroid and datum WGS 84. The images have excellent quality (image quality: 9).

6.2 Sentinel-2 Satellite Data

Sentinel-2 mission consists of two polar-orbiting satellites (Sentinel-2A and Sentinel-2B) providing high-resolution optical imagery for land monitoring. The full mission specification of the twin satellites flying in the same orbit but phased at 180°, is designed to give a high revisit frequency of 5 days at the Equator. Among the mission objectives is the disaster relief support and change detection maps (Sentinel-2 Mission 2018).

Sentinel-2A was launched on June 23, 2015 while Sentinel-2B on March 07, 2017. Both satellites are equipped with the MSI (Multispectral Imager) instrument that offers high-resolution optical images. Sentinel-2 mission, as Landsat 8, is provided on board with an optical-multispectral high resolution sensor that operates on/covering 13 different bands: four visible and near-infrared bands with a spatial resolution of 10 m (bands 2, 3, 4, 8), six red edge and shortwave infrared bands with a spatial resolution of 20 m (bands 5, 6, 7, 8A, 11, 12) and three atmospheric correction bands with a spatial resolution of 60 m (bands 1, 9, 10). Sentinel data products are available to all users and can be accessed free of charge (free, full and open data policy adopted for the Copernicus programme) through the Copernicus Open Access Hub (2018).

The image data that have been used in this study derive from Sentinel-2A (S2A_MSIL2A) and were acquired at 2017-06-01 and 2017-06-21 respectively with level processing 2A. The Level-2A products provide Bottom of Atmosphere (BOA) reflectance images derived from the associated Level-1C products. Each Level-2A product is composed of 100×100 km^2 tiles in cartographic geometry (UTM/WGS84 projection).

7 Digital Image Processing

As a result of the several sensors that satellite platforms are equipped with, the obtained data are available in digital form. Digital images of spectral reflectance data give us the advantage to apply computer analysis techniques to extract information. Every discrete picture element (pixel) of a digital image is represented by a digital number (DN) which depicts the average radiance of relatively small area within a scene. Smaller numbers indicate low average radiance. Digital image processing is based on these numbers and includes computer based procedures that concern four basic operations: image rectification and restoration, image enhancement, image classification and data merging (Lillesand and Kiefer 1987).

Image rectification and restoration include operations dealing with correction and calibration of distorted images in order to achieve a more faithful representation of the original scene (e.g. radiometric and geometric corrections). This type of restoration preprocessing depends on the type of image format, the initial condition of the image and its level processing, as well as the information of interest and the composition of the image scene. These operations prepare data for subsequent analysis, although might not be necessarily applied in all case, as systematic errors can be removed before they reach the user (Navi 2017).

Image enhancement includes operations to improve the interpretability of an image for a particular application, by increasing the apparent contrast among various features in the scene. Accentuation of the contrast can increase the amount of information that can be visually interpreted (Lillesand and Kiefer 1987). Enhancement techniques are often used for feature extraction, making important features more interpretable to the human eye (ERDAS Field Guide 2013). Depending on the data, objectives, expectations and interpreter's background, several enhancement techniques can be applied to derive useful information from images by studying and locating areas or objects on the ground.

Image classification includes quantitative techniques that can be applied to automatically interpret digital image data. During this process, individual pixels are evaluated and assigned to an information category replacing the image data file with a matrix of specific classes. Each pixel is characterized by its spectral signature, which is determined by the relative reflectance in different wavelength bands. Thus, multispectral classification is an information extraction process that analyses these signatures and assigns pixels to classes based on similar signatures.

Data merging includes procedures to combine image data for a given area with other data sets for the same area. Regarding satellite imagery, image fusion is the combination of two or more different images to form a new image by using a certain algorithm. The image resulting from this process contains more information than the original. Specifically, fusion of a multispectral image of relatively low spatial resolution with a high resolution panchromatic image is called pan-sharpening and it is an important issue for a number of remote sensing applications of large scale (Zhang 2004). Several image fusion techniques have been developed trying to combine spectral information of the multispectral image with spatial information of

the panchromatic image. Depending on the application, as well as on the computer-based analysis that will follow (e.g. classification), attention should be paid in the selected fusion method in order to obtain better preservation of the spectral characteristics (Karagianni and Lazaridou 2017).

Visual analysis is also a key element in the interpretation of the initial satellite data, as well as in every step of digital image processing and often depends on the techniques to be followed. Different land cover features (water, soil, vegetation, concrete, snow, etc.) reflect visible and infrared light in different ways. Interpretation of optical images requires the knowledge of the spectral reflectance patterns of various materials (natural or man-made) covering the surface of the earth.

To detect and delineate the area affected by the landslide in this case study, several methods can be applied. Initially, different color composites can be used to highlight several features in the landscape and reveal the bare ground or vegetation allowing the interpreter to detect the presence of landslides. Spectral bands capture energy in different parts of the electromagnetic spectrum. Using different band combinations certain features will contrast greatly with their surroundings, enabling better delineation (Scaioni et al. 2014).

Further digital image processing techniques (spectral enhancement, pan-sharpening, image algebra, etc.) can be applied for change detection and direct landslide monitoring (Hervás et al. 2003; Joyce et al. 2009; Scaioni et al. 2014). Visual interpretation of images (before or/and after digital processing) taken at different times can also contribute to the qualitative analysis of change detection (Scaioni et al. 2014) and is being done on the base of geometric (shape, size, etc.) and radiometric (tone-color, texture) characteristics. Optical data can provide good results due to spatial resolution and sensor look angle (although misclassification in other areas of bare ground may appear) (Joyce et al. 2009; van Westen 2000).

The software that was used for digital processing of the satellite imagery is ERDAS Imagine 2011 and SNAP (Sentinel Application Platform) freely distributed by ESA (STEP-Scientific Toolbox Exploitation Platform 2018).

7.1 Landsat 8 Image Processing

Digital processing of Landsat 8 data included layerstacking of the downloaded data, subsetting the scene to the study area, spectral enhancement performing principal components analysis (PCA) and image fusion (pan-sharpening) using Wavelet transform.

As a first step, various color composites can be used to visualize the information in the bands of the acquired images. In this study, the band combinations that were considered the most effective for a qualitative approach of the landslide detection were the following: the Natural Color Composite 4-3-2 (Red: Band 4, Green: Band 3, Blue: Band 2) and the Color Composite 6-3-2 (Red: SWIR1-Band 6, Green: Band 3, Blue: Band 2). These band combinations were applied at the images
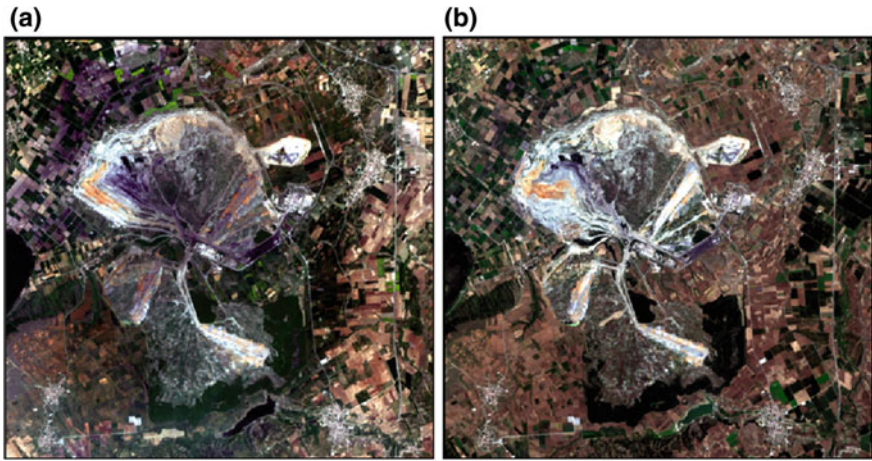
Fig. 13 Study area in Natural Color Composite (4-3-2) before (**a**) and after (**b**) the landslide
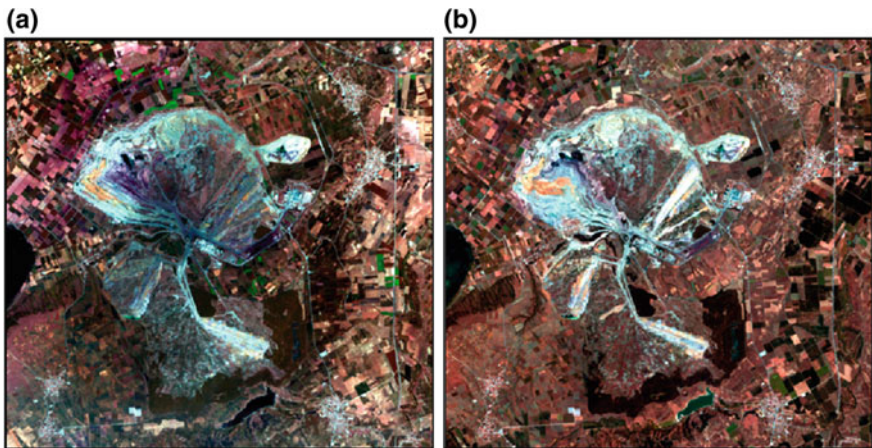
Fig. 14 Study area in Color Composite (6-3-2) before (**a**) and after (**b**) the landslide

acquired before (02-05-2017) and after (26-06-2017) the event and were visually compared.

In the Natural Color Composite 4-3-2 (Fig. 13) ground features appear in colors similar to their appearance to the human visual system. The landslide area is detected in the left part of the mine and the slope deformations are visible. In the Color Composite 6-3-2 (Fig. 14), the landslide area is also detected and clearly highlighted, as the shortwave infrared band (SWIR1) that were used in this combination is suitable for discerning differences in bare earth, indicating wet and dry areas in a scene.

Further digital processing concerned spectral enhancement of the satellite images, applying principal components analysis (PCA). This statistical method of data compression allows redundant data to be compacted into fewer bands. Dimensionality of the data set is reduced by projecting the data along new non-correlated axes. The bands of PCA data (principal components-PCs), are non-correlated and independent, therefore are often more interpretable than the source data (ERDAS Field Guide 2013, Deng et al. 2008). Although there are n output bands in a PCA, the first few bands account for a high proportion of the variance in the data. This image enhancement technique is useful for compressing data into fewer bands and can be used to give satisfactory results in change detection analysis, as in several applications appears to be better than classification comparison approach for change detection (Gupta et al. 2013).

There are several ways to apply PC transformation for change detection (Deng et al. 2008). In this study, to detect changes that appeared after the landslide, Landsat 8 images of two different times were both transformed into new PCA images applying PC transformation and were compared visually (Fig. 15). Most of the variance of the dataset is found on the first components. Therefore, the first three images are presented (3 principal components: PC1, PC2, PC3) as they provide most of the information contained within the dataset. The results were evaluated visually.

Areas affected by the landslide are evident in all three components. In PC1 pair of images the landslide area appears in lighter shades of grey while built up areas and water regions are also highlighted. In PC2 pair of images landslide area appears in darker shades and vegetation regions are discernible. In PC3 pair of images the 'boundaries' of the lignite mine are delineated and especially the landslide area in the left part of the mine (lighter shades of grey) where a shape disturbance is detected.

To exploit the panchromatic band of Landsat 8 (spatial resolution: 15 m) image fusion (pan-sharpening) was performed in order to delineate the landslide area in more detail. Various methods have been developed for image fusion. In this study, Discrete Wavelet transform (DWT) was chosen as in several cases seem to preserve better the spectral characteristics of the original multispectral image and can be more effective for further digital processing (Karagianni and Lazaridou 2017; Gungor and Shan 2004).

Wavelet methods belong in the broader category of Multiple Resolution Analysis (MRA) methods. In wavelet fusion, a high resolution panchromatic image is first decomposed into a set of low resolution panchromatic images using corresponding wavelet coefficients (spatial details) for each level. Individual bands of the multispectral image then replace the low resolution panchromatic image at the resolution level of the original multispectral image. The high resolution spatial detail is injected into each multispectral band by performing a reverse wavelet transform on each multispectral band using the corresponding wavelet coefficients (Zhang 2004).

The pansharpened images are presented in Fig. 16 focusing in the affected area (left part of the mine) and are evaluated visually, as well as quantitatively.
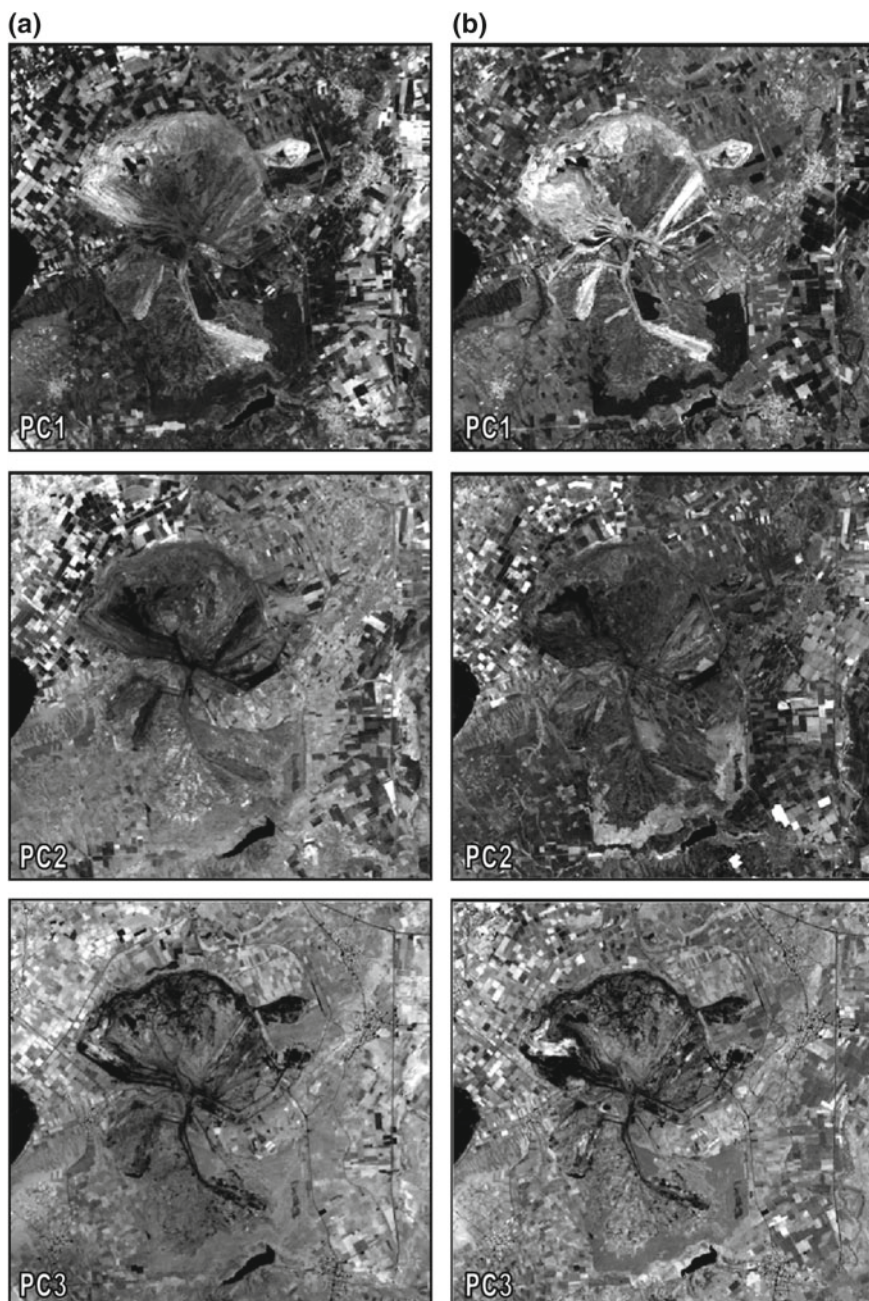
Fig. 15 PCA images of the study area before (**a**) and after (**b**) the landslide
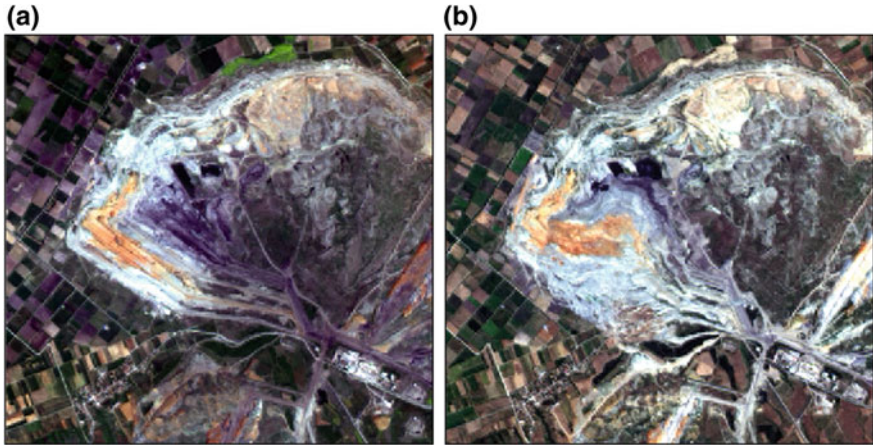
Fig. 16 Pansharpened images of the study area in Natural Color Composite (4-3-2) before (**a**) and after (**b**) the landslide

As is presented in Fig. 16, the spatial resolution of the images after pan-sharpening is improved and the landslide area is distinguished in more detail. In addition, there is a minimum color distortion regarding the original multispectral images. Therefore, the resulted images are suitable for change detection as spectral information is maintained while at the same time spatial resolution is increased.

In order to evaluate quantitatively the pansharpened images for both dates, the correlation coefficients among the Landsat 8 multispectral bands before and after pan-sharpening were calculated. The results are presented in Table 1, indicatively

Table 1 Correlation coefficients among the Landsat 8 multispectral bands before and after pan-sharpening (for both dates and indicatively for bands 2, 3, 4)

02-05-2017		Band 2	Band 3	Band 4
Band 2	Before	1	0.964	0.878
	After	1	0.963	0.877
Band 3	Before	0.964	1	0.940
	After	0.963	1	0.939
Band 4	Before	0.878	0.940	1
	After	0.877	0.939	1
26-06-2017		Band 2	Band 3	Band 4
Band 2	Before	1	0.974	0.899
	After	1	0.973	0.898
Band 3	Before	0.974	1	0.945
	After	0.973	1	0.944
Band 4	Before	0.899	0.945	1
	After	0.898	0.944	1

for bands 2, 3, 4. An acceptable fusion approach should not present considerable changes in the correlation of the corresponding bands (Gungor and Shan 2004). As shown in Table 1, the correlation among all bands is subject to minor changes after applying Wavelet transform. In addition, high spectral value preservation is observed, as values are close to +1.
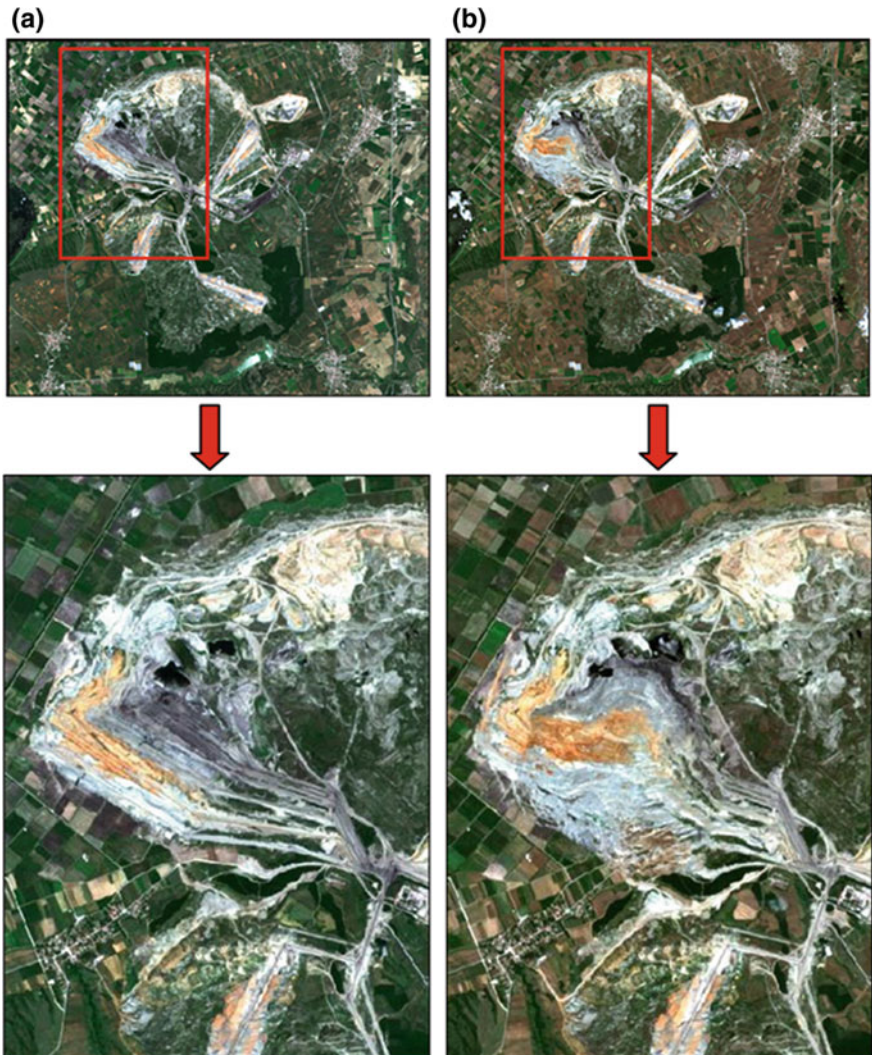
Fig. 17 Sentinel-2A images of the study area in Natural Color Composite (4-3-2) before (**a**) and after (**b**) the landslide

7.2 Sentinel-2A Image Processing

Digital processing of Sentinel-2A data included resembling at 10 m, layerstacking of the downloaded data, subsetting the scene to the study area and image algebra technique implementation (image difference) to detect the changes.

Figure 17 presents the study area before and after the landslide in Natural Color Composite (4-3-2), as well as a second pair of subsets that focuses on the left area of the mine where the landslide occurred (red rectangle in the first pair of images).

Visual interpretation of Sentinel-2 images could prove to be more effective than interpretation of Landsat 8 images due to higher spatial resolution of the former (10 m vs. the 30 m of Landsat 8). In addition, relevant indicators as texture, vegetation density, land use, cracks, surface disturbance or scarp visibility could be used to detect the presence of landslides. As shown in the second pair of images in Fig. 17 the affected area is clearly detected and difference in texture as well as surface disturbance are also evident.

To exploit further the high spatial resolution that Sentinel-2 offers (10 m after resampling), as well as the processing level of the data (L2A data are atmospherically corrected) an image algebra change detection technique (image difference) was applied to detect spectral reflectance differences between the two images.

Image difference is an image-to-image comparison and can be used for change analysis with images that depict the same area at different points in time. This process computes the differences between two images, highlighting change that

Fig. 18 Resulted image after applying 'image difference'

exceeds a user-specified threshold (ERDAS Field Guide 2013). The first image (before the event) is subtracted from the second image (after the event). Any changes in brightness values over time are reflected in the resulted grayscale image. Selecting a threshold value to express the changes in brightness as a percent, increases or decreases in brightness values that are greater than this threshold will be highlighted in certain color. Familiarity with the study area could help to place the critical threshold properly between true changes and spurious changes. The final product is a thematic image.

The resulted thematic image after applying image difference in Sentinel-2A images is presented in Fig. 18. The red color represents the changes detected in brightness values (increases or decreases) regarding the images that are compared (before and after the landslide). The processing was limited in an area of interest according to the previous findings (landslide area detection in the left part of the lignite mine).

8 Discussion–Conclusions

Natural or man-made disasters are phenomena that can affect large areas and have many impacts (environmental, societal and economic). Landslides are among the major disasters of large scale that may affect the natural environment as well as urban areas, often causing massive destruction, loss of property, or even fatalities worldwide. Developing tools that are effective for disaster management is imperative to monitor and mitigate their effect. Satellite data and remote sensing techniques, combined with geological data and studies can provide valuable information regarding monitoring of natural hazards in general and especially of landslides.

In this chapter, Landsat 8 and Sentinel-2 satellite data were used to study a complex set of landslides that occurred in the lignite mine of Amynteon in north-western Greece. The landslide occurred in along the south faces of the mine, resulting to extended collapses, destruction of mining machinery, evacuation of the adjacent Anargyri village and a big financial impact. Digital image processing techniques were applied for change detection in satellite data acquired before and after the event and geological data were also used to provide information about the geological background of the area and landslides vulnerability.

According to geological data, this is probably a multifactor event. It is possible that the multifragmented Plio-Pleistocene sedimentary sequence, due to the transfer zone between the Anargyri and Vegora marginal fault zones acted as a soil, instead of a rock, mass. These fault zones affected the lignite bearing formations, causing poor cohesion. Due to widespread fragmentation of the lignite-bearing sequence the mine landslide shows characteristics of a rotational landslide. It is also possible that human factors affected the initiation of the landslide. Hydrogeological factors that predated the event had already been identified in previous studies (e.g. Tzampoglou and Loupasakis 2016), while, a few days before the main landslide a heavy rainfall

was recorded during a normally dry period, possibly accelerating the already initiated earth mass movements.

Regarding digital processing of Landsat 8 data, different color composites along with spectral enhancement (principal components analysis-PCA) were used to detect the changes and delineate the landslide. Spectral capabilities of the data gave the opportunity to identify the location, as well as the extent of the landslide. Applying PCA, data were compressed into fewer bands and the resulted images (first three components) were visually interpreted giving satisfactory results in change detection analysis.

In order to delineate the landslide area in more detail a Wavelet transform was applied to combine the rich spectral context of the multispectral images with the high spatial resolution of the panchromatic image (pan-sharpening). The pan-sharpened images were effectively evaluated visually, as well as quantitatively. They can be photointerpreted easier than the original, while preservation of the spectral characteristics makes them suitable for change detection.

Sentinel-2A satellite data were also used as they were considered effective for change detection analysis due to high spatial resolution (higher than this of Landsat 8 data, even after pan-sharpening), data acquisition frequency and policy of free data (as Landsat 8 data). Visual interpretation of Sentinel-2 images provides more details about the affected area as differences in texture and surface disturbance are clearly detected.

To exploit further the high spatial resolution of Sentinel-2 atmospherically corrected data (Level-2 products) an image algebra technique (image difference) was applied to detect spectral reflectance differences between the two images. The resulted thematic image that reflects changes in brightness values of the pixels provides useful information about the parts of the lignite mine that are affected and could contribute further to landslide monitoring. Direct digital processing for change detection may limit the uncertainty of outputs, as well as the subjectivity and the strict dependency on human expertise that visual interpretation introduces.

Further processing extension could include a combination of SAR and optical data. SAR data could be a further step in digital processing (displacement calculations and volume estimation), especially in scenes where cloud cover impedes optical acquisition. Moreover, terrestrial laser scanning (TLS) systems could be used to generate 3D point clouds and DEMs of the area contributing to landslide monitoring. Complementary ground-based techniques could also be used to acquire precise information on displacement or deformation at specific locations, especially near residential areas and road infrastructure.

References

Chatzipetros A (1998) Palaeoseismological and morphotectonic study of the Mygdonia, Eastern Halkidiki and Kozani-Grevena active fault systems. PhD thesis, Aristotle University of Thessaloniki (in Greek)

Copernicus Open Access Hub (2018). https://scihub.copernicus.eu. Accessed 23 Sept 2018

Deng JS, Wang K, Deng YH, Qi GJ (2008) PCA-based land-use change detection and analysis using multitemporal and multisensor satellite data. Int J Remote Sens 29(16):4823–4838

Dimitrakopoulos D, Koumantakis I (2017) Hydrodynamic regime of Amynteon basin. Influence of open lignite mines. Paper presented at the 11th international hydrogeological congress of Greece, Athens, Greece, 4–6 Oct 2017

Dong Y, Fu B, Ninomiya Y (2009) Geomorphological changes associated with underground coal mining in the Fushun area, northeast China revealed by multitemporal satellite remote sensing data. Int J Remote Sens 30(18):4767–4784

EarthExplorer (2018). http://earthexplorer.usgs.gov. Accessed 23 Sept 2018

ERDAS Field Guide™ (2013) Intergraph Corporation, Erdas Inc., U.S.A 405, 440–445, 453–454

Gili JA, Corominas J, Rius J (2000) Using Global Positioning System techniques in landslide monitoring. Eng Geol 55(3):167–192

Google Earth (2018). https://www.google.com/intl/el/earth. Accessed 23 Sept 2018

Gungor O, Shan J (2004) Evaluation of satellite image fusion using wavelet transform. Paper presented at the XX th ISPRS Congress, Istanbul, Turkey, 12–23 July 2004

Gupta RP, Tiwari RK, Saini V, Srivastava N (2013) A simplified approach for interpreting principal component images. Adv Remote Sens 2:111–119

Hervás J, Barredo JI, Rosin PL, Pasuto A, Mantovani F, Silvano S (2003) Monitoring landslides from optical remotely sensed imagery: the case history of Tessina landslide, Italy. Geomorphology 54:63–75

Interactive database Meteosearch (2018). http://meteosearch.meteo.gr/data/amyntaio/2017-06.txt. Accessed 23 Sept 2018

Joyce KE, Belliss SE, Samsonov SV, McNeill SJ, Glassey PJ (2009) A review of the status of satellite remote sensing and image processing techniques for mapping natural hazards and disasters. Prog Phys Geogr 33:183–207

Karagianni A, Lazaridou M (2017) Fusion of multispectral and panchromatic satellite images in environmental issues. Int J Eng Res Appl 7(7):47–50

Kilias A, Mountrakis D (1989) The tectonic nappe of Pelagonian zone: tectonics, metamorphism and magmatism. Bull Geol Soc Greece 23:29–46 (in Greek)

Landsat 8 Mission (2018). http://landsat.usgs.gov/landsat8.php. Accessed 23 Sept 2018

Li Y, Zhao H, Fan J (2015) Application of remote sensing technology in mine environment monitoring. Paper presented at the international conference on engineering technology and application (ICETA), Taipei, Taiwan, 22–24 April 2015

Lillesand TM, Kiefer RW (1987) Remote sensing and image interpretation, 2nd edn. John Wiley and Sons, New York

Mantovani F, Soeters R, Van Westen CJ (1996) Remote sensing techniques for landslide studies and hazard zonation in Europe. Geomorphology 15:213–225

Metternicht G, Hurni L, Gogu R (2005) Remote sensing of landslides: an analysis of the potential contribution to geo-spatial systems for hazard assessment in mountainous environments. Remote Sens Environ 98:284–303

Mountrakis D (1986) The pelagonian zone in Greece: a polyphase-deformed fragment of the cimmerian continent and its role in the geotectonic evolution of the eastern Mediterranean. J Geol 94:335–347

Navi K (2017) Satellite image processing. In: Proceedings of the fourth international conference on signal processing, communication and networking (ICSCN), Chennai, India, 16–18 March 2017

Paull D, Banks G, Ballard C, Gillieson D (2006) Monitoring the environmental impact of mining in remote locations through remotely sensed data. Geocarto Int 21:33–42

Pavlides S (1985) Neotectonic evolution of Florina–Vegoritida–Ptolemais basin. PhD thesis, Aristotle University of Thessaloniki (in Greek)

Pavlides S, Mountrakis D (1987) Extensional tectonics of northwestern Macedonia, Greece, since the Late Miocene. J Struct Geol 9:385–392

Pavlides SB, Zouros NC, Chatzipetros AA, Kostopoulos DS, Mountrakis DM (1995) The 13 May 1995 western Macedonia, Greece (Kozani-Grevena) earthquake; preliminary results. Terra Nova 7:544–549

Scaioni M, Longoni L, Melillo V, Papini M (2014) Remote sensing for landslide investigations: an overview of recent achievements and perspectives. Remote Sens 6:5909–5937

Sentinel-2 Mission (2018). https://sentinel.esa.int/web/sentinel/missions/sentinel-2. Accessed 23 Sept 2018

STEP-Scientific Toolbox Exploitation Platform (2018). https://step.esa.int. Accessed 23 Sept 2018

Tsapanos T (2005) Seismicity and seismic hazard in western Macedonia. Bull Geol Soc Greece 37:232–244

Tzampoglou P, Loupasakis C (2016) New data regarding the ground water level changes at the Amyntaio basin–Florina Prefecture, Greece. Bull Geol Soc Greece 50:1006–1015

Tzampoglou P, Loupasakis C (2017a) Mining geohazards susceptibility and risk mapping: the case of the Amyntaio open-pit coal mine, West Macedonia, Greece. Environ Earth Sci 76:542

Tzampoglou P, Loupasakis C (2017b) Updated ground water piezometry data of the Amyntaio sub-basin and their effect on the manifestation of the land subsidence phenomena. Paper presented at the 11th international hydrogeological congress of Greece, Athens, Greece, 4–6 Oct 2017

Tzampoglou P, Loupasakis C (2018) Evaluating geological and geotechnical data for the study of land subsidence phenomena at the perimeter of the Amyntaio coalmine, Greece. Int J Min Sci Technol 28:601–612

USGS (2018) U.S. Geological Survey. https://pubs.usgs.gov. Accessed 23 Sept 2018

van Westen C (2000) Remote sensing for natural disaster management. Int Arch Photogramm Remote Sens XXXIII(Part B7):1609–1617

Wang Q, Guo H, Chen Y, Lin Q, Li H (2013) Application of remote sensing for investigating mining geological hazards. Int J Digit Earth 6(5):449–468

Zhang Y (2004) Understanding image fusion. Photogramm Eng Remote Sens 657–661

Part IV
Natural Disasters

Structure-From-Motion Photogrammetry to Support the Assessment of Collapse Risk in Alpine Glaciers

Marco Scaioni, Luigi Barazzetti, Vasil Yordanov, Roberto S. Azzoni, Davide Fugazza, Massimo Cernuschi and Guglielmina A. Diolaiuti

Abstract The application of Structure-from-Motion (SfM) Photogrammetry with ground-based and UAV camera stations may be exploited for modelling the topographic surface of Alpine glaciers. Multi-temporal repeated surveys lead to geometric models that may be applied to analyze the glacier retreat under global warming conditions. Thanks to the integration of point clouds obtained from ground-based and UAV imaging platforms, a complete 3D reconstruction also including vertical and sub-vertical surfaces may be achieved. These 3D models may be also exploited to understand the precursory signals of local collapse that might represent a risk for tourists and hikers visiting glaciers. In this paper a review on the application of SfM Photogrammetry in the field of glaciological studies is reported. The case of Forni Glacier in the Italian Alps is presented as emblematic study. Photogrammetric data sets obtained from measurement campaigns carried out in

M. Scaioni (✉) · L. Barazzetti
Department of Architecture, Built Environment and Construction Engineering (DABC),
Politecnico di Milano, Milan, Italy
e-mail: marco.scaioni@polimi.it

L. Barazzetti
e-mail: luigi.barazzetti@polimi.it

V. Yordanov
Polo Territoriale di Lecco, Politecnico di Milano, Milan, Italy
e-mail: vasil.yordanov@mail.polimi.it

R. S. Azzoni · G. A. Diolaiuti
Department of Environmental Science and Policy (DESP),
Università degli studi di Milano, Milan, Italy
e-mail: robertosergio.azzoni@unimi.it

G. A. Diolaiuti
e-mail: guglielmina.diolaiuti@unimi.it

D. Fugazza
Department of Earth Sciences "Ardito Desio", Università degli studi di Milano, Milan, Italy
e-mail: davide.fugazza@unimi.it

M. Cernuschi
Agricola 2000 S.C.P.A, Tribiano, MI, Italy
e-mail: massimo.cernuschi@gmail.com

2014, 2016, 2017 and 2018 have been processed using a common workflow. Attention is paid to a few crucial aspects, such as image orientation and calibration, dense surface matching, georeferencing and data fusion. In the end, the use of output point clouds to evaluate the risk of collapse in the Forni Glacier is addressed.

1   Introduction

Global warming has resulted in severe and diffuse melting processes in the cryosphere (Kerr 2012). Alpine glaciers may be considered as the most vulnerable areas that have shown the most evident effects (Gobiet et al. 2014). By comparing the extension of continental glaciers during the last one hundred years, the glacier retreat is generally impressive. In addition, local collapsing processes have affected the terminus areas of several Alpine glaciers, very often with a very fast dynamics that led to the quick loss of important ice volumes. In the case of glaciers that are visited by tourists and mountain hikers, these local phenomena may have severe consequences on humans (Carey et al. 2015).

As thoroughly discussed in (Fugazza et al. 2018), *cryospheric hazards* include ice-avalanches from hanging glaciers (see Fig. 1), detachment of seracs, debris flows caused by the mobilization of accumulated loose sediments, water outburst that might originate from the breaching of moraines, ice-dammed lakes or collapsing englacial/subglacial systems. These processes are in general directly or indirectly accelerated under climate change forcing. In the former case, the development of proglacial moraine-dammed lakes or ice avalanches can be accounted for (see, e.g., Gobiet et al. 2014). In the latter, the retreat of permafrost

Fig. 1 Example of an ice avalanche from a hanging section of a glacier captured by the authors on Forni Glacier, Rhaetian Alps (see Sect. 3)

and glaciers may result in slope instability and in different types of landslides (see, e.g., Fey et al. 2017; Albers et al. 2017).

Moreover, glacier downwasting may affect water resources (Kääb et al. 2005b) with consequences on the local agriculture, industry and economy. The increase of glacier-related risk may have a negative influence on the tourism industry (Palomo 2017). In Fig. 2, some significant photos depicting typical risk situations that are becoming more and more frequent in places that may be easily reached by tourists and hikers are reported. These images also highlight the lack of awareness of some people visiting glacier and periglacial areas, who are not able to understand the potential risk and to maintain adequate safety measures.

Understanding under where and when a local collapse in the ice bulk may happen is not a trivial task. On one side, the direct inspection by experts who have experience of those collapsing processes in a specific region is the most valuable method to recognize the precursory signals of forthcoming collapses. On the other hand, the local reconnaissance is not always possible. Different types of sensing technologies may contribute to understand the evolution of local collapses, even though they cannot be used to establish an autonomous decision support system. The judgement by experts is always required. However, observations could help to

Fig. 2 Two dangerous situations for people (including kids) visiting a glacier. In both cases, a sudden collapse of the ice vault or surface would involve human beings in the area

obtain a complete picture of the local conditions, including *digital surface models* (DSM) from photogrammetric and laser scanning techniques, ice-penetrating data, rheological and weather records, and measurement of sub-glacial water flow. In particular, the integration of surface and subsurface surveying and inspections is expected to provide a better support to the hydraulic and structural modelling, as already achieved in other fields of the Geosciences, see Longoni et al. (2012).

Among different types of observations from Remote Sensing (Rutzinger et al. 2018), DSM's play a paramount role because they help evaluate glacier thickness and volume variation, and to identify those areas where geomorphological and dynamical changes are expected (Kääb et al. 2005a). Provided that images at sufficient *ground sample distance* (GSD) are available, these may help the recognition of those typical hints of potential collapses, such as circular crevasses, sub-vertical ice walls, thin ice vaults and the like. The necessary GSD prevents the use of medium-resolution satellite images (e.g., ASTER, Landsat and Sentinel series), which are suitable for regional-scale mapping. Some authors have demonstrated that HR/VHR (high-resolution/very high-resolution) imagery may be exploited for investigating the majority of cryospheric hazards, see Kääb et al. (2005b) and Quincey et al. (2005). On the other hand, the analyses at the scale of single glaciers require higher resolution than the one that may be obtained only from specific airborne or ground missions employing Photogrammetry (image-based) or Laser Scanning (range-based). In addition, HR/VHR images may suffer from cloud cover and bad atmospheric conditions, that may result in difficulties in retrieval of suitable data sets.

It's out of the scope of this article to focus on pros *vs* contras of Photogrammetry (Luhmann et al. 2013) and Laser Scanning (Heritage 2009), which also depend on the specific application, see Chandler and Buckley (2016) and O'Banion et al. (2018). Photogrammetry, with the development of easy and accurate self-calibration techniques (Luhmann et al. 2016), Structure-from-Motion (SfM) for automatic image orientation (Barazzetti et al. 2009) and dense surface matching (Remondino et al. 2014) for detailed 3D reconstruction, has demonstrated to be a successful technique to be widely applied in the Geosciences (Eltner et al. 2016), among which high-mountain research (Remondino et al. 2014) and Glaciology (Piermattei et al. 2015, 2016). Nowadays, the term SfM Photogrammetry has become a synonym of the full automatic process leading to object reconstruction, not only limited to the orientation stage as in its origin (Hartley and Zisserman 2003).

A further help to the diffusion of SfM Photogrammetry has been the development of small UAV (Unmanned Aerial Vehicles or *drones*, see Sect. 2) for data acquisition (Santangelo et al. 2018). Regardless of the platform for image acquisition, ground-based or UAV Photogrammetry is quite flexible and does not call for the use of heavy equipment such in the case long/very-long range terrestrial laser scanners are used (see Fig. 3).

In the next Sect. 2, a review of the state-of-the-art of SfM Photogrammetry for application to glaciers is reported. In the following Sect. 3, a case study where the application of this technique has been carried to the study of changes of a glacier and to analyze the possible risks related to downwasting is presented and discussed.

Fig. 3 TLS acquisition at Forni Glacier (Raethian Alps, Italy) based on a *long-range terrestrial laser scanner* Riegl LMS-Z420i. Even though modern long-range and very long-range TLS have a smaller size and weight, they are still difficult to be carried and operated in high-mountain environment
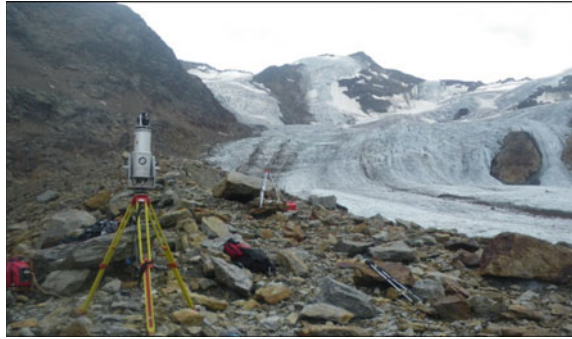
2 SfM/UAV Photogrammetry in Glacier Studies

As already highlighted in Sect. 1, SfM Photogrammetry (Westoby et al. 2012; Granshaw 2018b) has given new popularity to the image-based reconstruction techniques after a period when Terrestrial Laser Scanning (TLS) seemed to become the main approach for 3D surface reconstruction. This success has been also supported by a large development of the applications in the domain of Geosciences, as widely reviewed in Eltner et al. (2016) and, recently, in O'Banion et al. (2018). But it is the combination of SfM and UAV's—also often referred to with many other acronyms, see the interesting discussion in Granshaw (2018a)—that transformed the photogrammetric technique in a competitive approach with respect to TLS for 3D reconstruction in the mountain environment (Ryan et al. 2015) and to face with emergency surveying during geohazards (Giordan et al. 2018). In addition to the lower cost, the SfM and UAV coupling allows to overcome the problems of occlusions and may simplify data acquisition in complex terrains as well, see Chandler and Buckley (2016). The road map to this success has been completed by the availability of several software packages implementing SfM in a user-friendly environment while keeping low-cost or also the availability of software from the open source community (Gonzalez-Aguilera et al. 2018).

Beyond the abovementioned reviews, different technical aspects about the use of integrated SfM/UAV Photogrammetry in Geosciences can be found in the literature: problems related to camera set up (Mosbrucker et al. 2017; O'Connor et al. 2017), mission planning (Pepe et al. 2018), direct georeferencing (Carbonneau and Dietrich 2017; Dall'Asta et al. 2017), evaluation of the accuracy using a theoretical framework (James et al. 2017) or an empirical approach (O'Banion et al. 2018), analysis of multi-temporal surveying reproducibility (Clapuyt et al. 2016).

In the field of *glaciological studies*, the potential of SfM/UAV Photogrammetry is documented in several applications. Glaciers in different areas of the Earth could be mapped, such as Svalbard Glaciers (Norway—Solbø and Storvold 2013), Fountain Glacier in Bylot Island (Canada—Whitehead et al. 2013), Forni Glacier in Raethian Alps (Italy—Fugazza et al. 2015, 2018), debris-covered Lirung glacier (Himalaya, Nepal—Immerzeel et al. 2014), calving dynamics at Store Glacier

(Greenland—Ryan et al. 2015), ice cliffs at Kilimanjaro Mount (Kenya—Winkler et al. 2012), and Gran Sommetta Glacier in Aosta Valley (Italy—Dall'Asta et al. 2017). The same approach may be used for mapping periglacial areas or moraines, as described in Tonkin et al. (2014), or to measure snow depth (Bühler et al. 2015). UAV's may be used also to operate other types of remote sensing techniques, as discussed in Bhardwaj et al. (2016). In Kraaijenbrink et al. (2016) the emphasis is given to the application of *object-based image analysis* (OBIA) obtained from SfM/ UAV Photogrammetry to map and characterize surface features (ponds, ice cliffs) on Langtang debris-covered glacier in Nepal.

For some applications the individual use of SfM Photogrammetry from ground-*based stations* may suffice to obtain the reconstruction of the glacier surface. This especially holds in the case of small glaciers (Piermattei et al. 2015, 2016) and where the local topography allows to set up a suitable network geometry from the ground (Gómez-Gutiérrez et al. 2014, 2015). In Fugazza et al. (2018) the integration of UAV/SfM and ground-based SfM Photogrammetry has been carried out to obtain a more complete 3D reconstruction of an Alpine glacier, as also shown in next Sect. 3.

3 A Case Study: The Forni Glacier in Raethian Alps, Italy

3.1 Case Study Presentation

A typical case where a rapid retreat is occurring with the development of local collapse processes in the ice-tongue terminus is given by the *Forni Glacier*, which is located in the Raethian Alps within the Ortles Cevedale mountain group. The glacier is included in the National Stelvio Park (Northern Italy). It is one of the major valley glaciers in the Italian Alps, which is currently suffering from intense ablation processes. The latest Italian Glacier Inventory (Smiraglia et al. 2015) reported the total glacier area as 11.34 km^2, an altitudinal range between 2501 and 3673 m a.s.l., and a North-North-Westerly aspect. Since this inventory was based on 2007 data, the successive separation of the multiple ice tongues, the loss of ice bulk at global level and the retreat resulted in a reduction of the reported extension. These are progressive processes that have been active in the latest decades but recently they have been showing a rapid acceleration. Just to give an idea of the magnitude of the retreat process, during the Little Ice Age (LIA), which approximately extended between 1500 and 1850 A.D., Forni Glacier spanned over an area of 17.80 km^2 (Diolaiuti and Smiraglia 2010). On the other hand, some sectors of the lower part of glacier's main tongue are undergoing a local disruption process entailing first the formation of circular crevasses, to be followed by their collapse and the formation of large exposures of bedrock, see Fig. 4.

Other similar processes are documented in the literature (Albers et al. 2017). Such local processes are quite fast to develop: from their preliminary events to the full ice collapse the process may take less than one year. Monitoring the ice

Fig. 4 Examples of local collapses in the terminus area of Forni Glacier. From top to bottom: collapse of circular crevasses in 2016; the same process on the opposite side of the ice tongue in the end of Summer 2017 (after formation) and one year after (August 2018); the remaining right part of the glacier front after the creation of the discontinuity shown above

degradation process from a quantitative and qualitative point-of-view is of great importance to understand the related dynamics and to apply rigorous numerical models. While the analysis of archive maps, medium resolution satellite images and *digital elevation models* (DEM) may provide an overview of the long-term processes, as shown in Fig. 4, the application of close-range sensing techniques (Remondino et al. 2014) from ground-based and UAV stations offers the unprecedented opportunity to operate a 4D reconstruction of the glacier geometry at

both global and local levels. Recent research on this glacier can be found in Fugazza et al. (2015, 2016, 2018).

In the latest years, the melting process at Forni Glacier has resulted in the formation of some circular deep crevasses on the surface of the terminal ice tongue. Due to the contemporary erosion of subglacial water, large areas have collapsed resulting in the formation of huge craters in the ice tongue, see Fig. 4. The event occurred at the end of Summer 2017 (see Figs. 4 and 5) partially interrupted the active ice flow on the right hydrographic flank of the terminus, speeding up the melting process of this portion of the glacier.

In Fig. 5 a series of medium resolution satellite images (Sentinel 2A/2B) over the area of Forni Glacier has been used to provide an overview of the evolution of the retreat in the period that is considered here. Despite of the quite large GSD (10 m), these images allow to understand the formation and development of the local collapses close to the terminus of the glacier tongue.

In order to carry out a detailed analysis of the dynamic development of this glacier, the authors have decided to start some observation campaigns during the summer period, when the glacier is easier to be accessed and the melting process reaches its fastest rate. Missions using drones have been operated in 2014, 2016, 2017 and 2018. Starting in 2016, close-range photogrammetric surveys were accomplished from ground stations, in order to integrate some better views of vertical and subvertical facies that cannot be completely seen from vertical photos captured by drones. As reported in Fugazza et al. (2018) a comparative study between long-range TLS, UAV and terrestrial photogrammetry, was operated during the 2016 campaign. The results published there demonstrated that the integration of photogrammetry from both platforms may lead to adequate results for the purpose of this study, avoiding the necessity of using a TLS for the study of the ice tongue area. The DEM's derived from the interpolation of point clouds could be used for analyzing the rate of glacier retreat, the ice volume thickening and the consequent loss of water equivalent volume. The point clouds could be exploited for a better detection of the collapsed areas and to locate those regions where new forthcoming failures may be predicted.

In the next subsections, some aspects related to photogrammetric data acquisition at Forni Glacier case study are reported and discussed.

3.2 Photogrammetric Data Acquisition

3.2.1 UAV Missions

Four UAV missions covering the glacier terminus were operated from 2014 to date. The main technical features of these missions are reported in Table 1. The first survey covered both the terminus of the central and eastern ablation tongue of the glacier (see Fugazza et al. 2015). It was flown on 28th August 2014 using a SenseFly SwingletCam fixed wing aircraft at a relative flying height of
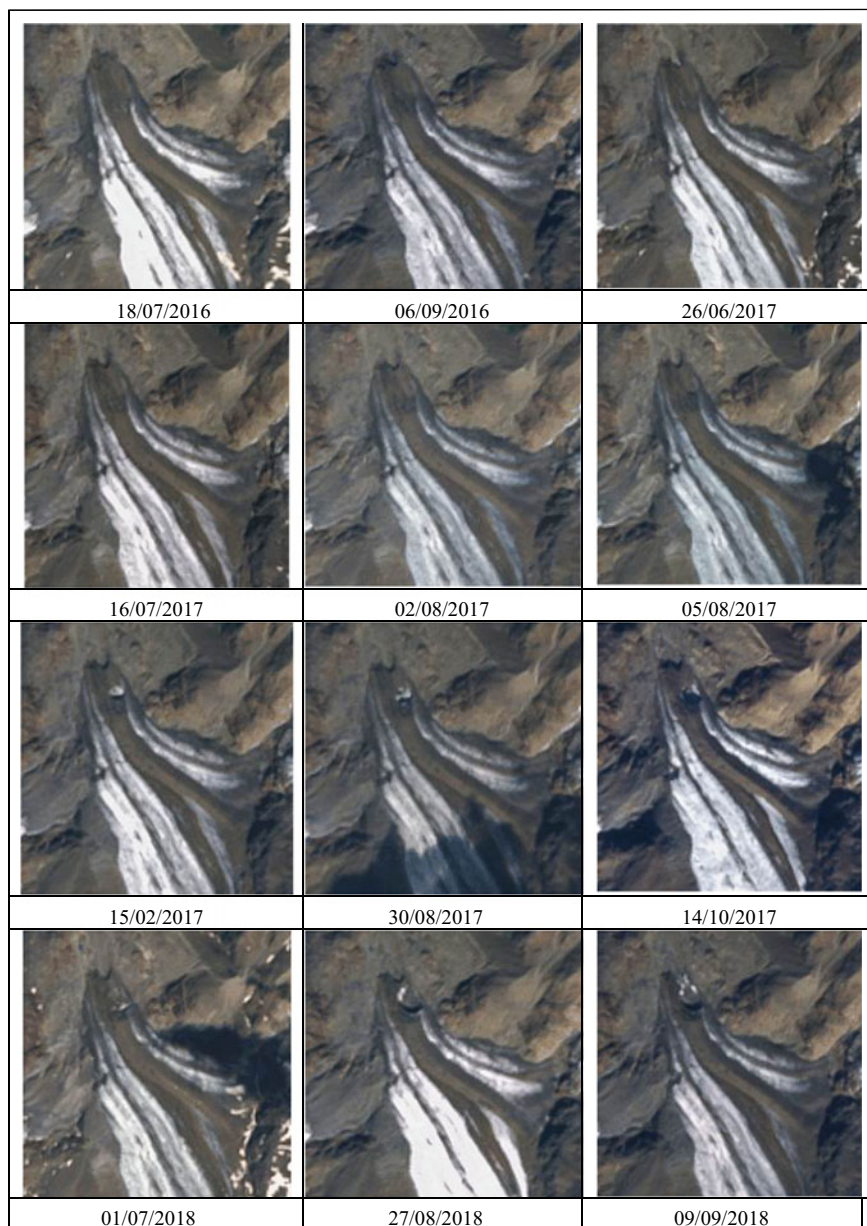
Fig. 5 Patches from Sentinel 2A/2B medium resolution satellite images (GSD = 10 m) depicting the dynamical evolution of the Forni Glacier's tongue from summer 2016 to summer 2018

Table 1 Main technical features of UAV mission at Forni Glacier from 2014–2018

UAV platform type	Time	UAV model	Camera model	Sensor size (pixels/mm)	Focal length (mm)	Avg. GSD (cm)	# GCP's
Fixed wing	08/2014	SwingletCam (SenseFly)	Canon IXUS 127 HS	4608 × 3456 6.16 × 4.62	4.3	12	0
Multicopter	08/2016	Customized quadcopter	Canon PowerShot ELPH 320 HS	4608 × 3456 6.16 × 4.62	4.3	6	8
Multicopter	10/2017	Customized quadcopter	Canon PowerShot ELPH 320 HS	4608 × 3456 6.16 × 4.62	4.3	5	5
Multicopter	08/2018	Customized quadcopter	Canon PowerShot ELPH 320 HS	4608 × 3456 6.16 × 4.62	4.3	6	6

approximately 380 m above the average glacier surface. The resulting average GSD was 12 cm. No *ground control points* (GCP's) were deployed during this flight. The only information available for absolute georeferencing were the 291 camera-pose locations obtained from the onboard navigation-grade GNSS (Global Navigation Satellite System) sensor. The uncertainty of this type of positioning could be estimated in the order of ±2 m.

The second flight was operated across two days (30th August and 1st September 2016), see Fugazza et al. (2018). The drone employed in this mission was a customized quadcopter, flown at a low relative altitude of 50 m with respect to the topographic surface (average GSD = 6 cm). Eight GCP's were deployed on the glacier terminus and in the periglacial area in front of it. GCP coordinates were measured by using a GNSS/RTK (Real-Time Kinematic) sensor.

The third flight was operated on 25th October 2017 in order to reconstruct the glacier topography after the collapse occurred at the end of summer, see Fig. 4. The drone employed in this mission was a customized quadcopter. A GSD = 5 cm was achieved. A set of 5 GCP's measured using GNSS/RTK were used for georeferencing. The RMSE (Root Mean Square Error) on these residuals was evaluated as 7 cm.

A fourth flight was carried out during August 2018, but at the moment of writing the processing has not been completed yet.

3.2.2 Terrestrial Photogrammetric Campaigns

Three photogrammetric campaigns using digital cameras for the acquisition of images from ground-based stations around the glacier tongue have been accomplished up until today. The main characteristics of these blocks are shown in Table 2, while the locations of camera stations are illustrated in Fig. 6.

Table 2 Main technical features of terrestrial photogrammetric blocks captured at Forni Glacier from 2016–2018 (CST = camera stations)

Time	Camera model	Sensor size (pixels/mm)	Focal length (mm)	#GCP's
08/2016	Nikon D700	4256 × 2823/36 × 24	50	7
09/2017	Nikon D700	4256 × 2823/36 × 24	35	0
08/2018	Nikon D700	4256 × 2823/36 × 24	50	3 + 28 CST's

The first block was captured concurrently to the 2016 UAV mission. A block of 134 images captured using an SLR (single lens reflex) camera Nikon D700 equipped with 50 mm lens was obtained to cover the glacier terminus including the rock flanks, a part of the periglacial area, and the ending part of the central moraine over the main glacier tongue. The criterion applied for establishing the camera stations was to explore as many positions as possible from which the targeted region could be observed from multiple, redundant viewpoints. In particular, to optimize the SfM process for automatic image orientation, an attempt to find a trade-off between long baselines with convergent images (providing a better geometric intersection of corresponding rays) and short-baselines with parallel images (helping the image-matching process adopted for image orientation and surface reconstruction), see Wenzel et al. (2013). Seven natural features were selected as GCP's on the glacier front for georeferencing of terrestrial block. Their coordinates in the mapping reference frame were measured using a theodolite equipped with a reflector-less rangefinder. The position and heading of the theodolite stations in the geodetic reference frame was found using GNSS/RTK.

During September 2017, a new photogrammetric survey from ground-based stations was repeated after the impressive collapse shown in Fig. 4. A Nikon D700 camera equipped with 35 mm lens was adopted in such a case with the purpose of shortening the acquisition distance. This solution was necessary because of the geometric constraints imposed by the new collapse. Due to some technical problems, no measurements for absolute georeferencing could be obtained from this campaign.

The third available photogrammetric survey was operated at the beginning of August 2018. In such a case, the same SLR camera Nikon D700 equipped with a 50 mm lens was used. The location of a subset of camera stations were measured using GNSS/RTK to establish the ground reference datum. Additionally, a few rock features were also measured by GNSS/RTK to be recognized in photos and used as standard GCP's.

3.3 Photogrammetric Data Processing

The processing of all photogrammetric blocks from either terrestrial or UAV imaging platforms has been carried out by applying the same processing workflow.
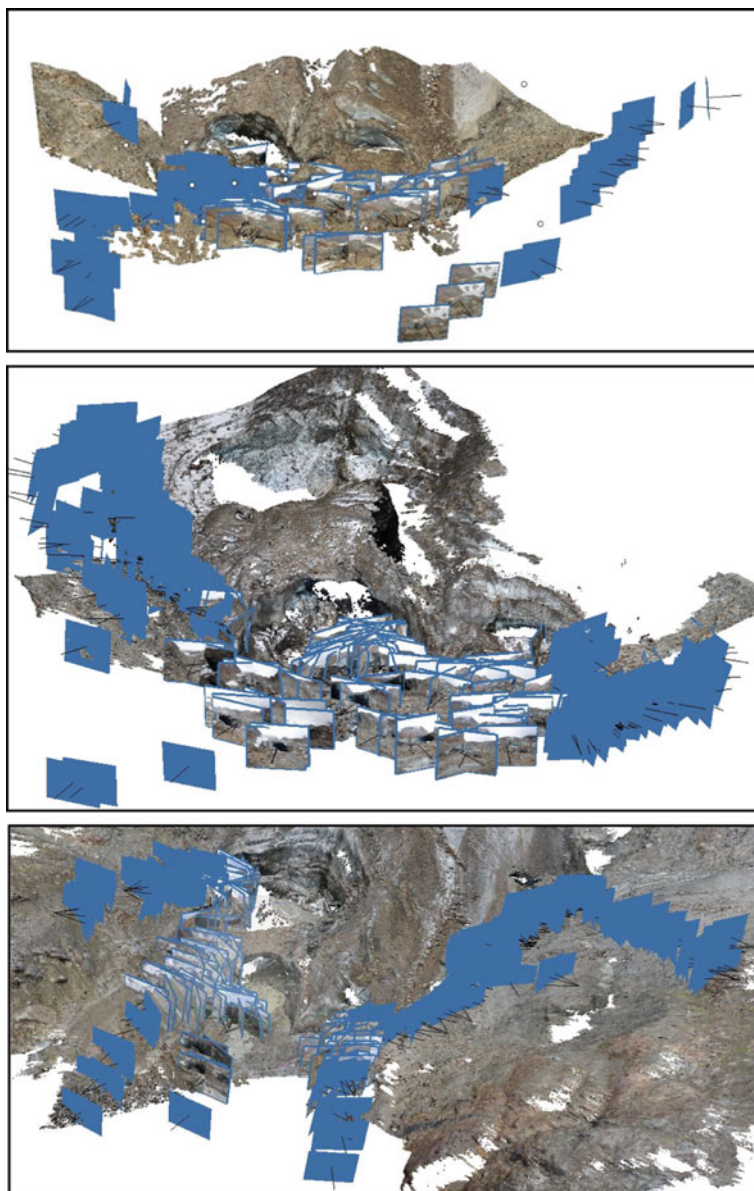
Fig. 6 Camera stations (blue rectangles) after exterior orientation of terrestrial photogrammetric networks accomplished in 2016 (at the top), in 2017 (in the middle), and in 2018 (at the bottom)

Table 3 Main properties of SfM processing with Agisoft Photoscan (r) Professional of the photogrammetric blocks captured at Forni Glacier in the period 2014–2018

| Imaging platform (UAV/ Terrestrial)	Time (month/ year)	#oriented photos	Image RMS residuals (pix)	Processing "Accuracy" level		Final point cloud size (#10^6 points)
				EO	Dense matching	
UAV (fixed wing)	08/2014	86	0.5	High	High	55.7
Terrestrial	08/2016	134	0.8	Highest	High	27.7
UAV (multicopter)	08/2016	288	2.0	Highest	High	75.1
Terrestrial	09/2017	232	0.4	Highest	High	29.5
UAV (multicopter)	10/2017	161	1.4	Highest	High	55.7
Terrestrial	08/2018	291	0.4	Highest	High	70.0

Each block has been independently processed. Agisoft Photoscan® Professional ver. 1.4.0 (in the following referred to as "APP"—www.agisoft.com) has been used for photogrammetry processing based on SfM and dense matching. The fusion of data sets captured at the same epoch has been carried out on the final point clouds in CloudCompare environment (www.cloudcompare.org). More details about the different processing stages are described in the following paragraphs. In Table 3, some basic properties of different processing steps adopted with these blocks are reported.

3.3.1 Sensors Calibration and Orientation

First, *tie points* (TP's—Hartmann et al. 2016) have been extracted and matched using feature-based matching (FBM—Barazzetti et al. 2009). In Fig. 7, a typical distribution of feature points extracted as candidates for the FBM are displayed. Among these, blue points are those that have been successfully matched in other images and consequently they may play as TP's in successive bundle-block adjustment (BBA). As can be clearly seen, discarded feature points (grey circles) are mainly located on the background and on the water surfaces. Since TP's on these areas are not likely to be selected a mask could be applied to avoid it. On the other hand, this kind of filtering operation is difficult to automate, and masking should be manually applied to each photo. To escape this time-consuming operation, masking has not been considered, but we relied on the sufficient robustness of the TP set to discard points in unwanted areas. Barring a few exceptions, this strategy worked well, as shown in the example displayed in Fig. 7.

The BBA implemented in APP provided the exterior orientation (EO) of the images, the ground coordinates of TP's, and camera calibration parameters. APP is able to compute all the approximate values of the unknown parameters needed to

Fig. 7 Example of feature points extracted on one image from terrestrial block captured in 2016: blue points represent TP's that have been matched in at least another image; grey points are features points that have not been successfully matched
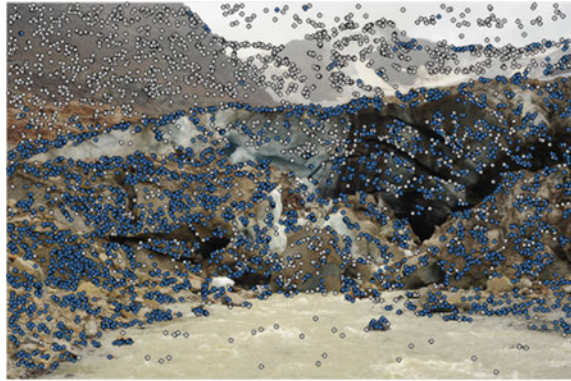
instantiate the BBA, though providing initial values may speed up processing. This option has been followed in the case of the UAV blocks, since the GNSS onboard sensors recorded the position of each shot at navigational accuracy (approximately ±2 m). In such a case, GNSS coordinates were used to instantiate the datum for the initial BBA. In the case of terrestrial blocks, no approximate values were available to help BBA processing. Anyway, the procedure could automatically derive the final EO parameters by using an internal strategy based on a preliminary SfM procedure carried out on subsampled images. Initial EO obtained this way was than used to instantiate the final processing. APP allows to define the level of accuracy (see Table 3). In most cases, the highest level has been selected ("Very-high accuracy") in order to better define the EO of each block, which may guarantee a geometric stability to next processing steps. This level corresponds to processing the images at full resolution.

In the case of UAV blocks (2014, 2016, 2017) all the images could be processed at the same time, after discarding a few photos with significant shadows or wrong expositions (e.g., due to clouds). In the case of terrestrial blocks collected in 2016 and 2017, the direct processing of all the images together was not possible. Consequently, the block from 2016 was initially split into two sub-blocks (referred to as "chunks" in APP jargon) to be independently oriented. The block from 2017 required the subdivision in four sub-blocks. The standard procedure to join sub-blocks should be based on the use of a sufficient number of GCP's (Barazzetti et al. 2011), solution that could not be applied in such a case. Then sub-blocks were successfully merged using an automatic function implemented in APP with the purpose of aligning overlapping "chunks." A critical analysis of this problem led to the conclusions that in the case of complex, large blocks, the overlaps between photos covering surfaces with a different spatial orientation should receive much attention during data acquisition. Thanks to this lesson learnt, the terrestrial block surveyed during August 2018 could be entirely oriented in a single step. In previous papers, some aspects such as the image configuration for the terrestrial blocks have been discussed, see Corti (2017), Fugazza et al. (2018), Scaioni et al. (2017). In Fig. 6 the camera poses for the terrestrial blocks are depicted.

3.3.2 Ground Control

In order to make sound comparisons among multi-temporal data sets, an external datum has been defined per each photogrammetric block. The planimetric datum adopted for georeferencing all mapping products in this part of Italy is ITRS2000/UTM 32 N.

Thanks to the measurements of static GNSS baselines with respect to permanent stations located at a distance inferior to 30 km, the accurate position of one or more GNSS/RTK master station in ITRS2000/UTM 32 N reference system was found. From here, differential corrections were broadcasted via radio-link to correct the position of a rover station used to determine the coordinates of targets to be used as GCP's in UAV projects. In other cases, the GNSS/RTK rover was used to measure directly the camera stations of photogrammetric blocks, or some vertices from which thodolite measurements could be operated. In the case of terrestrial blocks, either targets and natural features were used as GCP's.

Since GNSS processing could provide ellipsoidal elevations, each project needed to be transformed into orthometric heights. In order to have a standard procedure for determining local geoid ondulation and due to the limited size of the area where the glacier terminal tongue spanned over, a unique constant value was selected. The constant ondulation was computed with the help of the official software Verto 3, distributed by the Italian mapping agency (IGMI).

When enough GCP's were available, these have been directly included in the BBA implemented in APP to establish the geodetic *datum*. GCP's can be included as weighted pseudo-observations, contributing this way to adjust possible geometric deformations of the block. In fact, in most SfM software packages, GCP's are only used to compute a general 3D similarity transformation to better fit GCP coordinates in object space to corresponding coordinates derived from space intersection. In general, a limited number (less than ten) GCP's were available per each project. Average residuals on GCP's resulted in the order of few tens of centimetres. These results are aligned with the ones obtained in similar projects on other glaciers (see, for example, Piermattei et al. 2015, 2016).

In the case of missing sufficient GCP's, some alternative procedures were applied to align a block with respect to another one already georeferenced in ITRS2000/UTM 32 N. When two blocks collected at the same time (or at short time gap) had to be oriented, they were first imported into the same APP project as "chunks." Then the procedure for merging "chunks" on the basis of FBM was applied. This was the case, for instance, of the terrestrial block collected in 2017, for which it was not possible to measure any GCP's due to the time shortage during data acquisition campaign. In such a case, the UAV block flown during the same year was used as reference for co-registration, since in the case of this block a consistent set of GCP's was available.

On the other hand, in the case of the co-registration of blocks captured in different years, the same procedure could not be used because of the impressive changes of the local surface. Indeed, it is really difficult to find persistent features to be used for co-registration when a full year has passed: in addition to the ice flow

and melting, also the periglacial area in front of the glacier may undergo dramatic changes, while the surface texture may be completely altered due to the action of atmospheric agents. In such a case, the 3D coordinates of GCP's can be derived by spatial intersection from the already oriented images of the block to be used as reference. These "photogrammetric" GCP's should be selected in correspondence of selected features that may be easily recognized at both epochs in stable areas (for example on the rocks outside the glacier tongue). The number of these GCP's should be sufficient to guarantee a stable geometry in the registration process, and to maintain enough precision. In the case the identification of "photogrammetric" GCP's is difficult, another approach consists in including some images from the block to be registered into the reference block. Once this new data set is oriented using SfM, the image coordinates of "photogrammetric" GCP's can be measured in the same images for the both blocks. Than the EO of the reference block will be used to compute the object coordinates of GCP's to be used for co-registration of the other block (Scaioni et al. 2017).

3.3.3   3D Reconstruction Using Dense Surface Matching

A dense matching technique has been adopted for deriving the point cloud describing the surface of the region of interest. The "Build Dense Cloud" function implemented in APP has been used to this purpose. In Table 3 the main input parameters and some characteristics of the output point clouds are shown for all data sets. In all of them, the total number of images could be processed at the same time starting from the EO and camera calibration parameters that had been previously computed. The "High" accuracy level has been set up, which is based on subsampled images at half the original resolution. As discussed in Scaioni et al. (2017), the use of the images at full resolution ("Very-high" accuracy level) entails an impressive growth of processing time and computing resources, which is not counterbalanced by the increase of quality in the final point cloud. In addition, the size of this may become too large so that a successive decimation filtering might be necessary to handle such a huge data set. The final point clouds have been automatically assigned colors to points by using RGB information from images.

3.4   *Data Fusion*

Point clouds from "terrestrial" and "UAV" blocks collected during 2017 campaigns are displayed in Fig. 8 to show differences. Similar figures may be retrieved in Fugazza et al. (2018) to show the same point clouds but from 2016 campaigns. In Fig. 9, a quantitative comparison between these point clouds is also reported. This has been carried out in CloudCompare environment using M3C2 function (Lague et al. 2013).
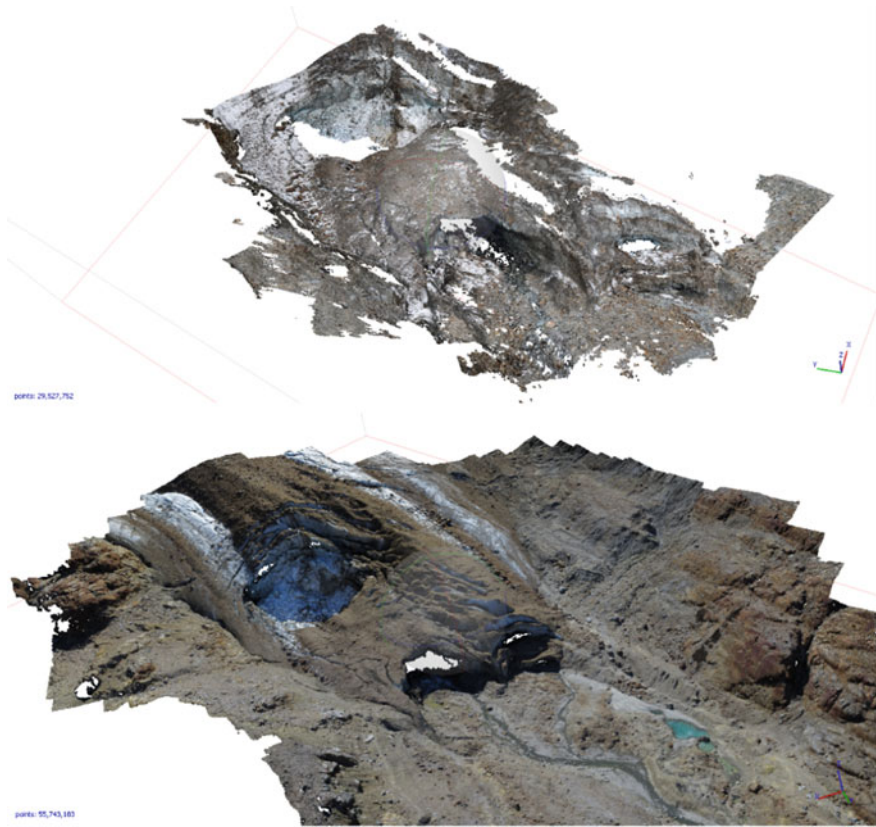
Fig. 8 Point clouds obtained from "terrestrial" (at the top) and "UAV" (at the bottom) blocks captured in 2017

While for some applications a single point cloud per epoch (from UAV or from ground-based stations) may suffice, the data fusion of both may lead to a more complete 3D reconstruction. Thanks to previous georeferencing into the same reference system, point clouds could be directly merged. Afterwards, the resulting data sets were subsampled at 20 cm spatial resolution to obtain complete 3D reconstruction of the entire ice tongue of the Forni Glacier in 2016 and 2017, see Figs. 10 and 11, respectively. RGB information of points in overlapping areas has been also averaged. Indeed, due to the large size of the merged point clouds, to the high point density in the overlapping regions, and the possible presence of small misalignments at local level, subsampling allowed overcoming all these drawbacks. Furthermore, the resulting point clouds were easier to handle.
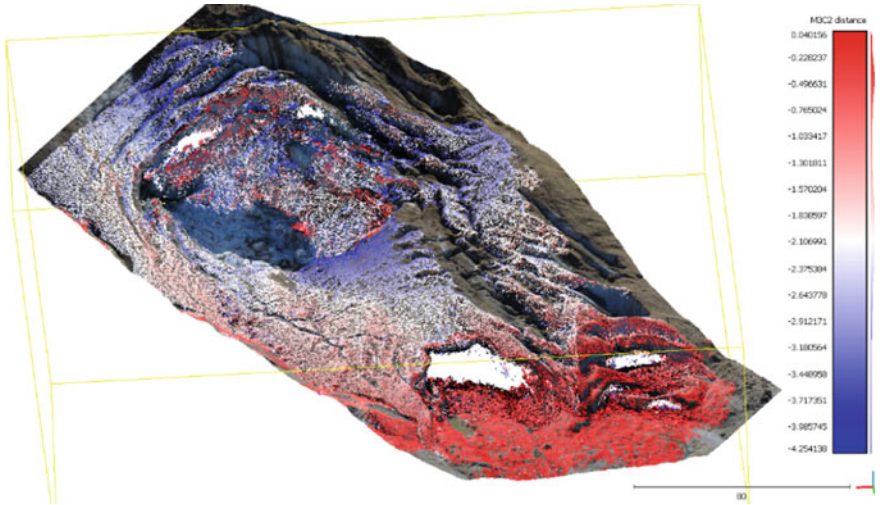
Fig. 9 Comparison between point clouds obtained from "terrestrial" and "UAV" blocks captured in 2017 (see Fig. 8). Grey areas are those where no overlap exists

Fig. 10 Point cloud obtained from the fusion of "terrestrial" and "UAV" blocks captured in 2016

The integration of a point cloud obtained from airborne vertical images to another one from ground-based camera stations, allows to improve the reconstruction of surfaces with different spatial orientation such as those typical of a glacier terminus.

Fig. 11 Point cloud obtained from the fusion of "terrestrial" and "UAV" blocks captured in 2017

3.5 Results and Discussion

The point cloud obtained by merging terrestrial and UAV blocks captured in 2016 (Fig. 10) covers the full terminus of the Forni Glacier. In addition, no holes or major occlusions can be noticed. By looking at 3D geometry, the presence of surface features is easy to detect. The presence of a large collapsed area (Summer 2016) on the left hydrographic side of the glacier can be observed.
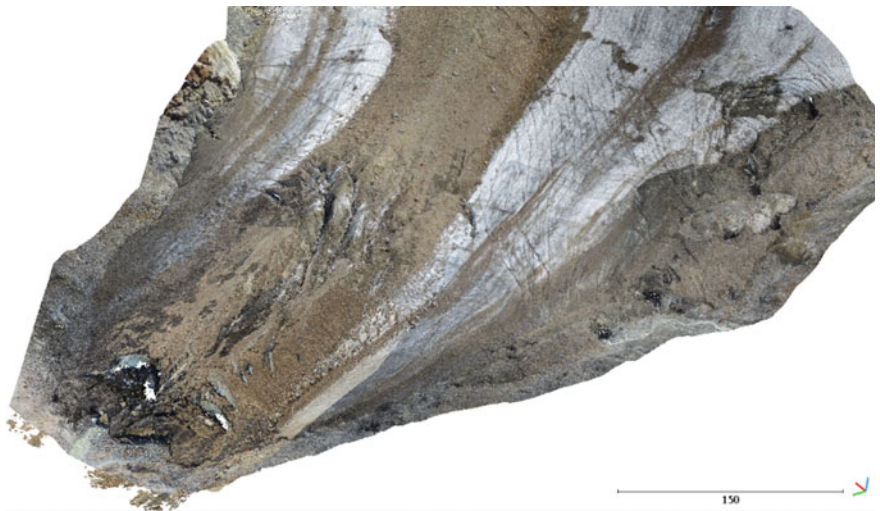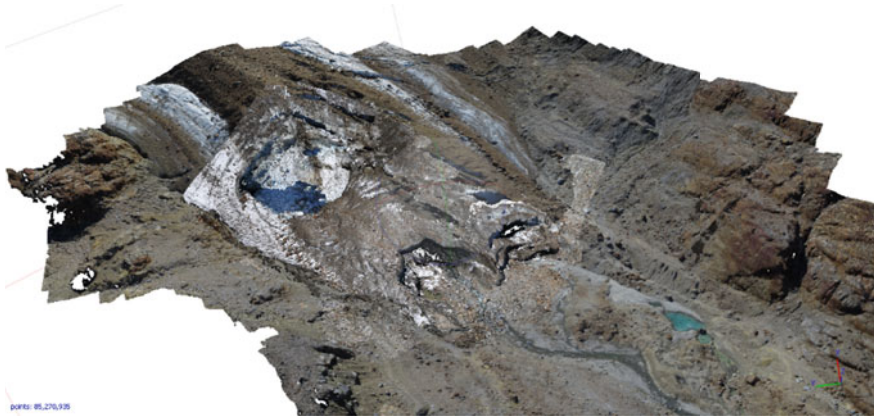
The point cloud derived from terrestrial and UAV blocks surveyed during September 2017 (Fig. 11) has a smaller spatial coverage. It should be also remarked that the complexity of the glacier topography was higher in 2017, due to the large area that collapsed in the end of summer, and the major fragmentation of the terminus. Anyway, these events are clearly visible in the point cloud, also because data acquisition was designed for their specific documentation.

By looking at point clouds from 2016 and 2017, a first impressive change concerned the interannual retreat of the glacier front. The average value distance between the medial part of the front was 38 m. The observed shape of the front is quite similar in both years, with the terminus split in two longitudinal sectors by the medial supraglacial moraine. In both sectors, water may flow out from the glacier, where it is excavating subglacial tunnels. The thinning of the vault of a portion of the right tunnel was probably the causative reason of the collapse occurred in the end of summer 2017. This resulted in the formation of a big crater, which also had the effect of breaking the ice flow on the terminal part of the corresponding longitudinal sector, close to the glacier front. The lack of ice input will speed up the melting process of this part of the terminus.

In August 2018 the "terrestrial" point cloud shows a progress in the retreat of the glacier front, while the collapsed area continued to grow. It is interesting to notice that the water flow has now completely switched to the right hydrographic side, since no water is flowing out from the left side.

During each summer, the terminus of Forni Glacier is visited by many hikers and tourists. On one hand, tracks to reach some mountain peaks in the nearby go through the terminus. On the other hand, the short walking distance from Branca Hut, which may be also reached using a car service, brings hundreds of tourists every day to the terminus. The easy access allows also non-experts and children to visit this area. Consequently, big collapses like the ones discussed in this paper, and other of minor magnitude, may have serious consequences on people visiting the glacier.

The availability of 3D models obtained from photogrammetric surveys may help understand those areas where collapses are foreseen, and consequently to limit the access to the glacier. In particular, these 3D models may help obtain a three-dimensional view of the problems, and to realize which is the effective region involved. In addition, the use of stereo-visualization and virtual-reality techniques may help better understand the glacier morphology without a direct inspection of the site.

Of course, this type of information may be integrated by on-site reconnaissance and other investigations (weather conditions, precipitations, ice penetrating radar, hydraulic flow measurements, etc.).

Another option to consider consists in the installation of fixed cameras to record a continuous documentation of melting events. Thanks to suitable locations of at least two cameras, the stereo-reconstruction by using dense matching techniques could be operated (see Roncella and Forlani 2015). Terrestrial photogrammetric blocks could be exploited to help find the optimal positions for those camera stations, by means of some network simulations to evaluate the completeness and the accuracy of the obtainable point clouds.

Of course, in the future the availability of several 3D models that will be likely captured at least on an yearly basis is expected to provide a very detailed description of the ongoing processes. A better understanding on how they may dynamically evolve since the appearance of precursory signals on the glacier surface and whether there are some parameters that may be related to them, will potentially lead to a more precise forecasting of collapses and then to assess the risk for those people who visit the glacier. To this purpose, the repetition of more data acquisition campaigns during the same summer (e.g., on a monthly-basis), may provide unprecedented information to understand these rapid melting processes, to be generalized to other case studies as well.

4 Conclusions

The application of 'Structure-from-Motion' (SfM) Photogrammetry from ground-based and UAV imaging platforms has been evaluated for monitoring changes of mountain glaciers. In this paper the focus has been given on the assessment of the risk of collapses, which may potentially result in casualties among people who visit some glaciers. Even though the specific analyses for the

evaluation of the risk have not been directly in the scope of the paper, the availability of detailed 3D models of the glacier surface has been highlighted as a potential source of information for this type of investigations.

The paper has specifically dealt with the case study of Forni Glacier, where the risk is quite relevant under current global warming conditions and accelerated melting. In such a case, the use of SfM Photogrammetry has been demonstrated to be quite supportive, since the analysis and comparison of 3D models allowed to extract useful information to detect potential collapses.

Close-range surveys from drones and ground-based imaging platforms are supposed to be repeated in the future for both long-term (annual basis) and short-term (monthly basis, only during summer), to better depict global and local phenomena contributing to the acceleration of the glacier ablation process. Since a measurement campaign requires time, suitable weather conditions, and a team of people, the organization of multiple expeditions is in general a non-trivial task. For this reason, on one side the installation of a permanent camera system for both visual analysis and 3D reconstruction is envisaged. On the other side, SfM Photogrammetry is now mature to be implemented within Citizen Science initiatives, for instance. People may be trained on how and where images should be collected, while the processing stage may be left to experts. As proposed in Albers et al. (2017), some apps may be also developed to guide users to capture the images following a precise scheme and to obtain redundant data acquisition.

References

Albers B, De Lange N, Xu S (2017) Augmented citizen science for environmental monitoring and education. Int Arch Photogramm Remote Sens Spatial Inf Sci 42(2/W7):1–4. https://doi.org/10.5194/isprs-archives-xlii-2-w7-1-2017

Barazzetti L, Forlani G, Remondino F, Roncella R, Scaioni M (2011) Experiences and achievements in automated image sequence orientation for close-range photogrammetric projects. In: Videometrics, range imaging, and applications XI. International Society for Optics and Photonics, paper no. 80850F. https://doi.org/10.1117/12.890116

Barazzetti L, Remondino F, Scaioni M (2009) Combined use of photogrammetric and computer vision techniques for fully automated and accurate 3D modeling of terrestrial objects. In: Videometrics, range imaging, and applications X. International Society for Optics and Photonics, paper no. 74470 M. https://doi.org/10.1117/12.825638

Bhardwaj A, Sam L, Martín-Torres FJ, Kumar R (2016) UAVs as semote sensing platform in glaciology: Present applications and future prospects. Remote Sens Env 175:196–204. https://doi.org/10.1016/j.rse.2015.12.029

Bühler Y, Marty M, Egli L, Veitinger J, Jonas T, Thee P, Ginzler C (2015) Snow depth mapping in high-Alpine catchments using digital photogrammetry. Cryosphere 9:229–243. https://doi.org/10.5194/tc-9-229-2015

Carbonneau PE, Dietrich JT (2017) Cost-effective non-metric photogrammetry from consumer-grade SUAS: implications for direct georeferencing of structure from motion photogrammetry. Earth Surf Proc Land 42(3):473–486. https://doi.org/10.1002/esp.4012

Carey M, Mcdowell G, Huggel C, Jackson J, Portocarrero C, Reynolds J M, Vicuña L (2015) Integrated approaches to adaptation and disaster risk reduction in dynamic socio-cryospheric systems. In: Shroder JF, Haeberli W, Whiteman C (eds) Snow and ice-related hazards, risks and disasters. Academic Press, Elsevier, pp 219–261. https://doi.org/10.1016/B978-0-12-394849-6.00008-1

Chandler JH, Buckley S (2016) Structure from motion (SfM) photogrammetry vs terrestrial laser scanning. In: Carpenter MB, Keane CM (eds) Geoscience handbook 2016: AGI data sheets, 5th edn. American Geosciences Institute, Alexandria (Virginia-USA), p 4

Clapuyt F, Vanacker V, Van Oost K (2016) Reproducibility of UAV-based earth topography reconstructions based on structure-from-motion algorithms. Geomorph 260:4–15. https://doi.org/10.1016/j.geomorph.2015.05.011

Corti M (2017) Analysis of multiple data sources for topographic reconstruction of Forni Glacier (Rhaetian Alps, Italy). Dissertation, Politecnico di Milano, MSc on Civil Engineering for Risk Management

Dall'Asta E, Forlani G, Roncella R, Santise M, Diotri F, Di Cella UM (2017) Unmanned aerial systems and DSM matching for rock glacier monitoring. ISPRS J Photogramm Remote Sens 127:102–114. https://doi.org/10.1016/j.isprsjprs.2016.10.003

Diolaiuti G, Smiraglia C (2010) Changing glaciers in a changing climate: How vanishing geomorphosites have been driving deep changes in mountain landscapes and environments. Geomorphologie: relief, processus, environnement 16(2):131–152. https://doi.org/10.4000/geomorphologie.7882

Eltner A, Kaiser A, Castillo C, Rock G, Neugirg F, Abellán A (2016) Image-based surface reconstruction in geomorphometry–merits, limits and developments. Earth Surf Dyn 4:359–389. https://doi.org/10.5194/esurf-4-359-2016

Fey C, Wichmann V, Zangerl C (2017) Reconstructing the evolution of a deep seated rockslide (Marzell) and its response to glacial retreat based on historic and remote sensing data. Geomorphology 298:72–85. https://doi.org/10.1016/j.geomorph.2017.09.025

Fugazza D, Senese A, Azzoni RS, Smiraglia C, Cernuschi M, Severi D, Diolaiuti GA (2015) High-resolution mapping of glacier surface features. The UAV survey of the Forni glacier (Stelvio National Park, Italy). Geogr Fis Din Quat 38:25–33. https://doi.org/10.4461/GFDQ.2015.38.03

Fugazza D, Senese A, Azzoni RS, Maugeri M, Diolaiuti GA (2016) Spatial distribution of surface albedo at the Forni glacier (Stelvio National Park, Central Italian Alps). Cold Reg Sci Technol 125:128–137. https://doi.org/10.1016/j.coldregions.2016.02.006

Fugazza D, Scaioni M, Corti M, D'agata C, Azzoni RS, Cernuschi M, Smiraglia C, Diolaiuti GA (2018) Combination of UAV and terrestrial photogrammetry to assess rapid glacier evolution and map glacier hazards. Nat Hazard Earth Sys Sci 18:1055–1071. https://doi.org/10.5194/nhess-18-1055-2018

Giordan D, Hayakawa Y, Nex F, Remondino F, Tarolli P (2018) The use of remotely piloted aircraft systems (RPASS) for natural hazards monitoring and management. Nat Hazard Earth Sys Sci 18:1079–1096. https://doi.org/10.5194/nhess-18-1079-2018

Gobiet A, Kotlarski S, Beniston M, Beniston M, Heinrich G, Rajczak J, Stoffel M (2014) 21st Century climate change in the European Alps—A review. Sci Total Environ 493:1138–1151. https://doi.org/10.1016/j.scitotenv.2013.07.050

Gómez-Gutiérrez Á, De Sanjosé-Blasco JJ, De Matías-Bejarano J et al (2014) Comparing two photo-reconstruction methods to produce high density point clouds and DEMs in the Corral del Veleta rock glacier (Sierra Nevada, Spain). Remote Sens-Basel 6(6):5407–5427. https://doi.org/10.3390/rs6065407

Gómez-Gutiérrez Á, De Sanjosé-Blasco JJ, Lozano-Parra J, Berenguer-Sempere F (2015) Does HDR pre-processing improve the accuracy of 3d models obtained by means of two conventional SfM-MVS software packages? The case of the Corral del Veleta rock glacier. Remote Sens-Basel 7(8):10269–10294. https://doi.org/10.3390/rs70810269

Gonzalez-Aguilera D, López-Fernández L, Rodriguez-Gonzalvez P, Hernandez-Lopez D, Guerrero D, Remondino F, Menna F, Nocerino E, Toschi I, Ballabeni A (2018) Graphos–open-source software for photogrammetric applications. Photogramm Rec 33:11–29. https://doi.org/10.1111/phor.12231

Granshaw SI (2018a) RPV, UAV, UAS, RPAS … or just drone? Photogramm Rec 33:160–170. https://doi.org/10.1111/phor.12244

Granshaw SI (2018b) Structure from motion: origins and originality. Photogramm Rec 33:6–10. https://doi.org/10.1111/phor.12237

Hartley R, Zisserman A (2003) Multiple view geometry in computer vision. Cambridge University Press, Cambridge

Hartmann W, Havlena M, Schindler K (2016) Recent developments in large-scale tie-point matching. ISPRS J Photogramm 115:47–62. https://doi.org/10.1016/j.isprsjprs.2015.09.005

Heritage GL, Large AGR (eds) (2009) Laser scanning for the environmental sciences. Wiley, Chichester, p 302

Immerzeel WW, Kraaijenbrink PDA, Shea JM, Shrestha AB, Pellicciotti F, Bierkens MFP, De Jong SM (2014) High-resolution monitoring of Himalayan glacier dynamics using unmanned aerial vehicles. Remote Sens Environ 150:93–103. https://doi.org/10.1016/j.rse.2014.04.025

James MR, Robson S, Smith MW (2017) 3-D uncertainty-based topographic change detection with structure-from-motion photogrammetry: Precision maps for ground control and directly georeferenced surveys. Earth Surf Proc Land 42:1769–1788. https://doi.org/10.1002/esp.4125

Kääb A, Huggel C, Fischer L, Guex S, Paul F, Roer I, Salzmann N, Schlaefli S, Schmutz K, Schneider D (2005a) Remote sensing of glacier-and permafrost-related hazards in high mountains: an overview. Nat Hazard Earth Sys Sci 5:527–554. https://doi.org/10.5194/nhess-5-527-2005

Kääb A, Reynolds JM, Haeberli W (2005b) Glacier and permafrost hazards in high mountains. In: Huber UM, Bugmann HKM & Reasoner MA (eds) Global change and mountain regions. Advances in Global Change Research, Vol 23. Springer, Dordrecht, p 225. https://doi.org/10.1007/1-4020-3508-X_23

Kerr RA (2012) Experts agree global warming is melting the world rapidly. Science 338 (6111):1138. https://doi.org/10.1126/science.338.6111.1138

Kraaijenbrink P, Shea J, Pellicciotti F, De Jong S, Immerzeel W (2016) Object-based analysis of unmanned aerial vehicle imagery to map and characterise surface features on a debris-covered glacier. Remote Sens Environ 186:581–595. https://doi.org/10.1016/j.rse.2016.09.013

Lague D, Brodu N, Leroux J (2013) Accurate 3D comparison of complex topography with terrestrial laser scanner: application to the Rangitikei Canyon (N-Z). ISPRS J Photogramm 82:10–26. https://doi.org/10.1016/j.isprsjprs.2013.04.009

Longoni L, Arosio D, Scaioni M, Papini M, Zanzi L, Roncella R, Brambilla D (2012) Surface and subsurface non-invasive investigations to improve the characterization of a fractured rock mass. J Geophys Eng 9:461. https://doi.org/10.1088/1742-2132/9/5/461

Luhmann T, Fraser C, Maas H-G (2016) Sensor modelling and camera calibration for close-range photogrammetry. ISPRS J Photogramm 115:37–46. https://doi.org/10.1016/j.isprsjprs.2015.10.006

Luhmann T, Robson S, Kyle S, Boehm J (2013) Close-range Photogrammetry and 3D Imaging. Walter de Gruyter, p 684

Mosbrucker AR, Major JJ, Spicer KR, Pitlick J (2017) Camera system considerations for geomorphic applications of SfM photogrammetry. Earth Surf Proc Land 42:969–986. https://doi.org/10.1002/esp.4066

O'Banion MS, Olsen MJ, Rault C, Wartman J, Cunningham K (2018) Suitability of structure from motion for rock-slope assessment. Photogramm Rec 33:217–242. https://doi.org/10.1111/phor.12241

O'Connor J, Smith MJ, James MR (2017) Cameras and settings for aerial surveys in the geosciences: optimising image data. Prog Phys Geog 41:325–344. https://doi.org/10.1177/0309133317703092

Palomo I (2017) Climate change impacts on ecosystem services in high mountain areas: a literature review. Mt Res Dev 37:179–187. https://doi.org/10.1659/MRD-JOURNAL-D-16-00110.1

Pepe M, Fregonese L, Scaioni M (2018) Planning airborne photogrammetry and remote-sensing missions with modern platforms and sensors. Eur J Remote Sens 51:412–435. https://doi.org/10.1080/22797254.2018.1444945

Piermattei L, Carturan L, Guarnieri A (2015) Use of terrestrial photogrammetry based on structure-from-motion for mass balance estimation of a small glacier in the Italian Alps. Earth Surf Proc Land 40:1791–1802. https://doi.org/10.1002/esp.3756

Piermattei L, Carturan L, De Blasi F, Tarolli P, Fontana GD, Vettore A, Pfeifer N (2016) Suitability of ground-based SfM-MVS for monitoring glacial and periglacial processes. Earth Surf Dynam 4:325–443. https://doi.org/10.5194/esurf-4-425-2016

Quincey D, Lucas R, Richardson S, Glasser N, Hambrey M, Reynolds J (2005) Optical remote sensing techniques in high-mountain environments: application to glacial hazards. Prog Phys Geog 29:475–505. https://doi.org/10.1191/0309133305pp456ra

Remondino F, Spera MG, Nocerino E, Menna F, Nex F (2014) State of the art in high density image matching. Photogramm Rec 29:144–166. https://doi.org/10.1111/phor.12063

Roncella R, Forlani G (2015) A fixed terrestrial photogrammetric system for landslide monitoring. In: Scaioni M, (ed) Modern technologies for landslide monitoring and prediction, Springer, Cham. https://doi.org/10.1007/978-3-662-45931-7_3

Rutzinger M, Bremer M, Höfle B, Hämmerle M, Lindenbergh R, Oude Elberink S, Pirotti F, Scaioni M, Wujanz D, Zieher T (2018) Training in innovative technologies for close-range sensing in alpine terrain. ISPRS Ann Photogramm Remote Sens Spatial Inf Sci 4(2):239–246. https://doi.org/10.5194/isprs-annals-iv-2-239-2018

Ryan JC, Hubbard AL, Box JE, Todd J, Christoffersen P, Carr JR, Holt TO, Snooke NA (2015) UAV photogrammetry and structure from motion to assess calving dynamics at store glacier, a large outlet draining the Greenland ice sheet. Cryosphere 9:1–11. https://doi.org/10.5194/tc-9-1-2015

Santangelo M, Alvioli M, Baldo M, Cardinali M, Giordan D, Guzzetti F, Marchesini I, Reichenbach P (2018) Brief communication: Remotely piloted aircraft systems for rapid emergency response: road exposure to rockfall in Villanova di Accumoli (Central Italy). Nat Hazard Earth Sys Sci. https://doi.org/10.5194/nhess-2018-177 Accessed 18 Oct 2018

Scaioni M, Corti M, Diolaiuti G, Fugazza D, Cernuschi M (2017) Local and general monitoring of Forni glacier (Italian alps) using multi-platform structure-from-motion photogrammetry. Int Arch Photogramm Remote Sens Spatial Inf Sci 42(2/W7):1547–1554. https://doi.org/10.5194/isprs-archives-xlii-2-w7-1547-2017

Smiraglia C, Azzoni RS, D'agata C, Maragno D, Fugazza D, Diolaiuti GA (2015) The evolution of the Italian glaciers from the previous data base to the new Italian inventory. Preliminary considerations and results. Geogr Fis Din Quat 38:79–87. https://doi.org/10.4461/GFDQ.2015.38.08

Solbø S, Storvold R (2013) Mapping Svalbard glaciers with the cryowing UAS. Int Arch Photogramm Remote Sens Spatial Inf Sci 40(1/W2):373–377. https://doi.org/10.5194/isprsarchives-XL-1-W2-373-2013

Tonkin TN, Midgley NG, Graham DJ, Labadz J (2014) The potential of small unmanned aircraft systems and structure-from-motion for topographic surveys: a test of emerging integrated approaches at CWM Idwal, North Wales. Geomorph 226:35–43. https://doi.org/10.1016/j.geomorph.2014.07.021

Wenzel K, Rothermel M, Fritsch D, Haala N (2013) Image acquisition and model selection for multi-view stereo. Int Arch Photogramm Remote Sens Spatial Inf Sci 40(5/W1):251–258. https://doi.org/10.5194/isprsarchives-XL-5-W1-251-2013

Westoby MJ, Brasington J, Glasser NF, Hambrey MJ, Reynolds J (2012) 'Structure-from-Motion' Photogrammetry: a low-cost, effective tool for Geoscience applications. Geomorph 179:300–314. https://doi.org/10.1016/j.geomorph.2012.08.021

Whitehead K, Moorman B, Hugenholtz C (2013) Brief communication: low-cost, on-demand aerial Photogrammetry for glaciological measurement. Cryosphere 7:1879–1884. https://doi.org/10.5194/tc-7-1879-2013

Winkler M, Pfeffer WT, Hanke K (2012) Kilimanjaro ice cliff monitoring with close range photogrammetry. Int Arch Photogramm Remote Sens Spatial Inf Sci 39(B5):441–446. https://doi.org/10.5194/isprsarchives-XXXIX-B5-441-2012

Pre- and Post-Fire Comparison of Forest Areas in 3D

Devrim Akca, Efstratios Stylianidis, Daniela Poli, Armin Gruen,
Orhan Altan, Martin Hofer, Konstantinos Smagas,
Victor Sanchez Martin, Andreas Walli, Elisa Jimeno
and Alejandro Garcia

Abstract A satellite processing platform for high resolution forest assessment (FORSAT) was developed. It generates the digital surface models (DSMs) of the forest canopy by advanced processing of the very-high resolution (VHR) optical satellite imagery and automatically matches the pre- and post-fire DSMs for 3D change detection. The FORSAT software system can perform the following tasks: pre-processing, point measurement, orientation, quasi-epipolar image generation, image matching, DSM extraction, orthoimage generation, photogrammetric restitution either in mono-plotting mode or in stereo models, 3D surface matching, co-registration, comparison and change detection. It can thoroughly calculate the planimetric and volumetric changes between the epochs. It supports most of the VHR optical imagery commonly used for civil applications. Capabilities of

D. Akca (✉)
Isik University, Istanbul, Turkey
e-mail: akca@isikun.edu.tr

E. Stylianidis
Aristotle University of Thessaloniki, Thessaloniki, Greece
e-mail: sstyl@auth.gr

D. Poli
4DiXplorer AG, Zurich, Switzerland
e-mail: daniela@4dixplorer.com

A. Gruen
ETH Zurich, Switzerland/4DiXplorer AG, Zurich, Switzerland
e-mail: agruen@geod.baug.ethz.ch; agruen@4dixplorer.com

O. Altan
Istanbul Technical University/Ekinoks Surveying Software Engineering Ltd,
Istanbul, Turkey
e-mail: oaltan@itu.edu.tr; altan@ekinoks3d.com

M. Hofer · A. Walli
GeoVille Information Systems GmbH, Innsbruck, Austria
e-mail: hofer@geoville.com

A. Walli
e-mail: walli@geoville.com

FORSAT have been tested in two real forest fire cases, where the burned areas are located in Cyprus and Austria. The geometric characteristics of burned forest areas have been identified both in 2D plane and 3D volume dimensions, using pre- and post-fire optical image data from different sensors. The test studies showed that FORSAT is an operational software capable of providing spatial (3D) and temporal (4D) information for monitoring of forest fire areas and sustainable forest management. Beyond the wildfires, it can be used for many other forest information needs.

1 Introduction

Deforestation is one of the major sources of carbon emission which threatens the global climate targets. Several satellites and sensors have been used to monitor deforestation areas. The Advanced Very High Resolution Radiometer (AVHRR) on board the NOAA-series satellites (Di Maio Mantovani and Setzer 1997), JERS-1 (Almeida-Filho et al. 2005), MODIS on-board the NASA EOS satellites (Anderson et al. 2005), ASTER (Haboudane and Bahri 2008), Formosat-2 (Baillarin et al. 2008), PALSAR on-board ALOS (Isoguchi et al. 2009) constitute a small set of examples.

Low to medium resolution level optical images present drawbacks for operation in the moist tropics and in all weather conditions, synthetic aperture radar (SAR) data might be seen as an alternative (Santos et al. 2008; Solberg et al. 2013). Applications of SAR data to map deforestation are generally based on the assumption that undisturbed forests consistently exhibit higher radar backscatter than deforested areas. Depending on the stage of the deforestation process (slashing, burning and terrain clearing), this assumption is not always valid, and deforested areas may display a stronger radar return backscatter than primary forest (Almeida-Filho et al. 2007). Especially, new deforested areas are not unequivocally detected in some cases (Almeida-Filho et al. 2009).

With over 30 years of directly comparable satellite observations, now freely available and new imagery being added to the archive every day, Landsat time

K. Smagas
GeoImaging Ltd, Nicosia, Cyprus
e-mail: kostas@geoimaging.com.cy

V. S. Martin · E. Jimeno · A. Garcia
Ingeniería Y Soluciones Informáticas S.L., Seville, Spain
e-mail: vsanchez@isoin.es

E. Jimeno
e-mail: elisa.jimeno@isoin.es

A. Garcia
e-mail: agarcia@isoin.es

series legacy affords novel opportunities for ecosystem mapping, environmental monitoring and comparative ecology (Pasquarella et al. 2016). It has been used to understand the space-time dynamics of deforestation over large areas, but at moderate resolution (Alves 2002; Ichii et al. 2003; Bodart et al. 2011; Souza et al. 2013).

Measuring the areal extent of deforestation for other than localized areas requires the use of fine resolution satellite data. An accurate determination of deforestation is very difficult to achieve by a random sampling analysis of Landsat or similar resolution data unless a very high percentage of the area to be studied is sampled (Tucker and Townshend 2000). The very high resolution (VHR) satellite imagery is an alternative and effective solution (Mora et al. 2013). Availability and metric capability of the VHR satellite imagery is given in Remondino (2011) and Sefercik et al. (2013).

Conventional forest inventory contains extensive field work to collect data of coverage, specie, height, volume, health, damage, change, deforestation, etc. It is expensive and time consuming (Eva et al. 2010; Koch 2010). Although the traditional forest inventory methods are the most accurate, they are neither agile nor economic. Alternative management strategies are required (Mondal et al. 2010). The Global Forest Watch (GFW) is one of the example of the worldwide responses to this demand, which is an open-source web application to monitor global forests in near real-time (http://www.globalforestwatch.org). It is an initiative of the World Resources Institute (WRI) with partners including Google, Esri and many other academic, non-profit, public and private organizations. The Global Forest Observations Initiative (GFOI) is another international collaboration to support countries to develop their national forest monitoring systems (http://www.gfoi.org/). The satellite data primarily comes from USGS Landsat series, and EU Copernicus Programme ESA Sentinel-1 radar and Sentinel-2 optical series. Japan (JAXA), Brazil (INPE), China (CRESDA), France (CNES), Italy (ASI), Canada (CSA) and Germany (DLR) provides additional contributions.

Deforestation is caused by ever-increasing activities of the growing human population (Pahari and Murai 1999), its density (Svancara et al. 2009) and agricultural colonisation (Millington et al. 2003). Their effects are seen in long terms. On the other hand, the forest fire, which is another main cause of deforestation, is a rapid event whose effects are seen in very short terms (Lee 2008). A rapid, effective and economic way of change detection is required in order to understand the pre- and post-fire changes of forest areas. The VHR satellite imagery which allows stereo and triplet acquisitions at very fine spatial resolutions offers less expensive, faster and more agile remote sensing capacities than the alternative technologies, thereby providing an optimum solution for such change detection tasks. Additional advantages are no overflight permissions needed, an optimum ground coverage capacity versus spatial resolution, and repetition of image acquisitions on a certain area of interest until cloud coverage is free. FORSAT (a satellite processing platform for high resolution forest assessment) is an operational software system designed to fulfil these special requirements in the forestry sector, which was originally a research and development project funded by Eurostars

(https://www.eurostars-eureka.eu/) and the European Commission. It is a standalone satellite-based monitoring capacity specifically for 3D forest cover mapping and change detection applications. Moreover, it is a processing platform, where high performance and well-studied methods of the terrestrial and airborne techniques are coupled with the spaceborne VHR image data, to obtain a single source forest information system.

The FORSAT software can generate digital surface models (DSM) of forest canopy in high resolution and accuracy. By comparing pre- and post-fire DSMs, the system allows automatic 3D change detection of forest and non-forest areas along with change both in area and volume dimensions.

In the next section, state-of-the-art methods for forest fire prediction, detection, monitoring and measurement are reviewed. In the third section, the FORSAT methodology is presented with its algorithmic details. Performance of the FORSAT software was tested by executing case studies at two forest fire areas located in Cyprus and Austria. The experimental results have proved that public bodies and private organisations can use the VHR satellite data for many forest information needs. In the fourth section, the results achieved on the test cases are reported and discussed. The final conclusions are given in the fifth section.

2 Forest Fire Prediction, Detection, Monitoring and Measurement

Thanks to the rising public awareness and comprehensive forest protection programs, the global vegetation showed a remarkable greening (+0.28% per year) over browning (−0.14% per year) based on the Moderate Resolution Imaging Spectroradiometer (MODIS) vegetation index data from 2011 to 2015 (Zhang et al. 2017). The forest fire is one of the major threats that attenuate this global greening trend. Human-started fires represent the vast majority of wildfires whose distance from built-up areas becomes closer-and-closer by the time (Mancini et al. 2018).

The susceptibility of forest fires increases with direct human activities, road accessibility, forest fragmentation, habitat loss and similar causes (Mancini et al. 2018; Silva Junior et al. 2018). This list can be extended. All these factors together with meteorological data (Yu et al. 2017), weather variables (Sun and Zhang 2018), surface temperature and water content (Abdollahi et al. 2018) and elevation data (Adelabu et al. 2018) can be appropriately combined to establish forest fire prediction and forecasting models. The fire danger forecast module of the European Forest Fire Information System (EFFIS), is an active web-based system all year around, generates daily maps of 1 to 10 days of forecasted fire danger level using numerical weather predictions (http://effis.jrc.ec.europa.eu/).

Such models support risk assessment and mitigation, decision making and fire management activities (Altan et al. 2013; Nyongesa and Vacik 2018).

Early detection of forest fires is of vital importance as it saves critical times for fire extinguishing activities. The human visualization system is not optimally suited for fire detection. Smoke occlusion heavily limits flame visibility and low flames can be difficult to see. Thermal infrared (TIR) and near-infrared (NIR) sensors mitigate these affects and are widely used for fire detection (Burnett and Wing 2018). The satellite platforms offer wider field-of-view (FOV) at reasonable cost and with flexible operational capabilities. The satellite sensors that are widely used in fire detection are the Advanced Spaceborne Thermal Emission and Reflection Radiometer (ASTER), EO-1 Advanced Land Imager (ALI), Advanced Very High Resolution Radiometer (AVHRR), Moderate Resolution Imaging Spectroradiometer (MODIS), Landsat 7 Enhanced Thematic Mapper Plus (ETM+) and Landsat 8 Operational Land Imager (OLI). All of them are owned by NASA except the AVHRR by NOAA (Camaro et al. 2013).

MODIS offers several data products. Among them, the MODIS Thermal Anomalies/Fire products (https://modis.gsfc.nasa.gov/data/dataprod/) are the most used products to monitor and to detect hotspots and burned areas worldwide (Justice et al. 2002a, b). The product includes fire occurrence (day/night), fire location, the logical criteria used for the fire selection, detection confidence, Fire Radiative Power and numerous other layers describing fire pixel attributes. The product distinguishes between fire, no fire and no observation statuses. The embedded fire detection strategy is based on absolute detection (when the fire strength is sufficient to detect) and on detection relative to its background. An improved fire hotspot detection algorithm was proposed by Giglio et al. (2003) which uses a contextual algorithm exploiting the observations from several MODIS channels. The Fire Information for Resource Management System (FIRMS) is a web application that delivers global MODIS hotspots and fire locations in an easy to use format (http://earthdata.nasa.gov/data/near-real-time-data/firms).

The GOFC/GOLD (Global Observations of Forest and Land Cover Dynamics) is a project to provide a forum for international information exchange, observation and data coordination, and a framework for establishing the necessary long-term monitoring systems. The web site (http://gofc-fire.umd.edu/projects/index.php) lists several active fire detection and monitoring systems.

Numerous fire detection algorithms have been developed using the MODIS fire products (Giglio et al. 2016). The MODIS products are not only used for detecting wildfires but also for tree cover loss caused by illegal clearing, interdict deforestation and other reasons (Wheeler et al. 2018).

The Visible Infrared Imaging Radiometer Suite (VIIRS) aboard the Suomi National Polar–orbiting Partnership (Suomi-NPP) satellites, the Spinning Enhanced Visible and InfraRed Imager (SEVIRI) on board the Meteosat Second Generation (MSG) satellites, the Advanced Baseline Imager (ABI) on board the Geostationary Operational Environmental Satellite-R Series (GOES-R) and the Visible and Infra-Red Radiometer (VIRR) on board the Chinese FengYun-3C satellite are also used for active fire detection (Schroeder et al. 2014; Filizzola 2016; Koltunov et al. 2016; Lin et al. 2018).

Satellite sensors are feasible sources to be used for on-instant (or near real-time) monitoring of forest fires. NASA's Aqua satellite, carrying a MODIS sensor, captured the several parallel fires of California in a single scene on July 29, 2018. More than 85,541 hectares were burned, and eight civilians died. The second-deadliest wildfire in the 21st century, happened in Attica, Greece, in July 2018, was imaged by GeoEye-1 satellite. Ninety-nine people were dead and thousands of homes were destroyed. Planet, a Californian company, operates 130+ PlanetScope Dove, 13 SkySats and 5 RapidEye satellites to monitor the ground in near real-time, which are also frequently used to monitor active forest fires (https://www.planet.com/). USA Wildfires interactive map, which is an ESRI Storymap (https://storymaps.esri.com/stories/usa-wildfires/), shows location, magnitude and status of active fires raging across the United States. It is a good example of internet-based mapping applications which is used for near real-time monitoring of forest fires.

Burn severity metrics are useful indicators to assess the post-fire conditions in terms of forest damage and loss (Navarro et al. 2017). At least two images capturing the pre- and post-fire status are required, which would be SAR (Addison and Oommen 2018), VHR optical (Meng et al. 2017) or medium resolution multi-spectral (Edwards et al. 2018; Fernandez-Garcia et al. 2018) images. If mapped with appropriate cartographic techniques, the burn severity provides valuable information to forest managers for their restoration efforts in terms of post-fire recovery, regeneration and vegetation succession (Ryu et al. 2018; Vega et al. 2018; Li et al. 2018). The geomatics (geo-spatial) platforms, sensors and techniques offer a wide variety of solutions for rapid mapping of natural hazards including the wildfires (Toschi et al. 2017; Toschi et al. 2018). The primary focus is on the most recent satellites (Colson et al. 2018) and unmanned aerial vehicle (UAV) platforms (GW website 2018). The Global Ecosystem Dynamics Investigation (GEDI), pronounced like "Jedi" of Star Wars fame, will be the first space-borne laser instrument to measure the height, density and structures of forests in high resolution and three dimensions (https://gedi.umd.edu/). The expected launch to the International Space Station (ISS) is in late 2018. Although NASA has other space-borne LiDAR missions such as the ICESat (Ice, Cloud and land Elevation Satellite) and CALIPSO (Cloud-Aerosol Lidar and Infrared Pathfinder Satellite Observation), the GEDI will be the first to provide laser ranging of Earth's forests.

After the forest fire lasts, the burned area should be estimated and mapped in order to derive the canopy cover change (McCarley et al. 2017; Cabral et al. 2018; Garcia-Lazaro et al. 2018; Krasovskii et al. 2018). This is predominantly accomplished with either multi-spectral remote sensing data or through ground-based field sampling plots (McCarley et al. 2017). The main emphasis is given to the performance of several parametric and non-parametric classifiers (Ramo et al. 2018). The temporal dimension of post-fire changes is also attributed by analysing the data in time series (Tian et al. 2018; Mayr et al. 2018). The output is typical 2D map depicting the post-fire effects, since the standard burnt area products deal with area computation, which are usually given in hectare units (Soto-Berelov et al. 2018).

Even though the spatial dimension of forest fire changes is relatively less studied, the burned volume would give much more valuable information than the burned area. Volume computation requires more effort both in data and processing aspects (Cailliez 1992). It is actively used in many scientific studies from static object modelling to dynamic flow measurements (Schanz et al. 2018). Limited number of studies has been performed for the forest (or deforestation) volume computation. In a few number of studies, forest volume is conventionally predicted by interpolation methods (Xu et al. 2018).

The FORSAT methodology follows an alternative approach, in which the pre- and post-fire forest surfaces are modelled by generating DSMs derived from the VHR satellite images. The fire related changes are analysed through the comparison of pre- and post-fire DSMs. This operation is known as DSM of difference (DoD), where cell-by-cell subtraction (or other kind of operations) is performed to calculate the total volumes of change (Cucchiaro et al. 2018). If the image data of several epochs are available, temporal-spatial analysis can also be done as time-series, thus allowing 4D analysis and interpretation capabilities.

3   FORSAT Methodology

The FORSAT software allows processing the satellite imagery and extracting meaningful and quantitative information about forests, such as area and volume measurements of deforestation or regeneration of a forest. The software architecture comprises four building blocks for (1) pre-processing, (2) geo-referencing, (3) DSM generation and (4) 3D co-registration and comparison.

Each block is tightly coupled in a software suite framework. The FORSAT software suite is not a monolithic system, that is, every core module works independently but related to each other at the same time. It uses a graphical user interface (GUI) which eases users to work with the software (Fig. 1).

The entire system is an effective combination of two main tasks. The first one is dedicated to the geometric and radiometric processing of satellite imagery and 2D/3D information extraction, that is: radiometric pre-processing, image and
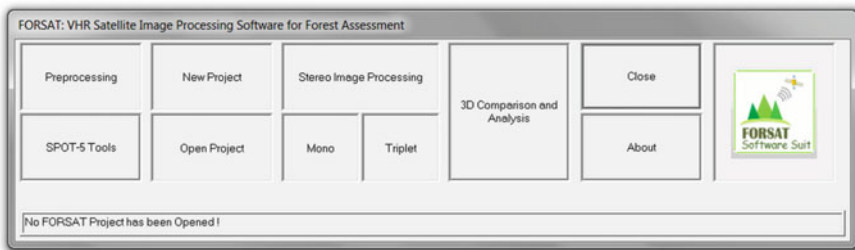

Fig. 1 The graphical user interface of the FORSAT software

ground point measurement and sensor orientation, quasi-epipolar image derivation, image matching, DSM extraction, ortho-rectification, and 3D vector measurement.

This unit supports most of the VHR optical imagery commonly used for civil applications, for example IKONOS, GeoEye-1, WorldView-1/2, SPOT-5/6/7, Pleiades-1A/1B, and it can be easily updated to similar images from future missions.

The second task is dedicated to 3D surface comparison for change detection. It allows the users to import DSMs and digital terrain models (DTMs), to align them using an advanced 3D surface matching technique, and to calculate the 3D volume differences.

The technical approach comprises a bunch of interconnected algorithms whose details are given in Poli (2005), Zhang (2005) and Akca (2007) all of which are the doctoral theses performed at the photogrammetry group of ETH Zurich. Later on, these algorithms were commercialized by 4DiXplorer AG (www.4dixplorer.com), an ETH spin-off company located in Zurich. The FORSAT software is a specialization of these base algorithms to forestry applications, and distributed by 4DiXplorer AG.

3.1 Pre-processing

The VHR satellite images are provided together with their metadata by the vendors. Before applying the algorithms for the geo-referencing of the images, some operations are required in order to prepare the input data. The pre-processing includes both the analysis of the metadata files for the extraction of the required information and the radiometric improvement of the images in order to facilitate the point measurements (Poli 2007).

The performance of the image matching and feature extraction procedures depends on the quality and quantity of information carried out by the images. Compared to the traditional scanned 8-bit/pixel images, digital imagery from linear array sensors has better radiometric performance e.g. higher dynamic range and signal-to-noise ratio. Most of the linear array sensors have the ability to provide high quality digital images. However, some radiometric problems still have to be considered: poor image contrast, the image blur problems mainly caused by CCD line jitter, kappa jitter and motion blur and deficiencies of the lens system, image noise, and radiometric problems caused by the variations in the sensor view angle, the sun angle, shadowing, and the seasonal and the atmospheric conditions. These problems are usually beyond the control of the users. However, they have to be restored as much as possible. In order to reduce the effects of such radiometric problems and optimise the images for subsequent feature extraction and image matching step, the image pre-processing methods have to be employed (Zhang 2005). While the gamma correction, contrast enhancement, histogram equalisation are trivial applications and can be found in many standard image processing software, FORSAT uses the Wallis filter, because it is a specific and powerful
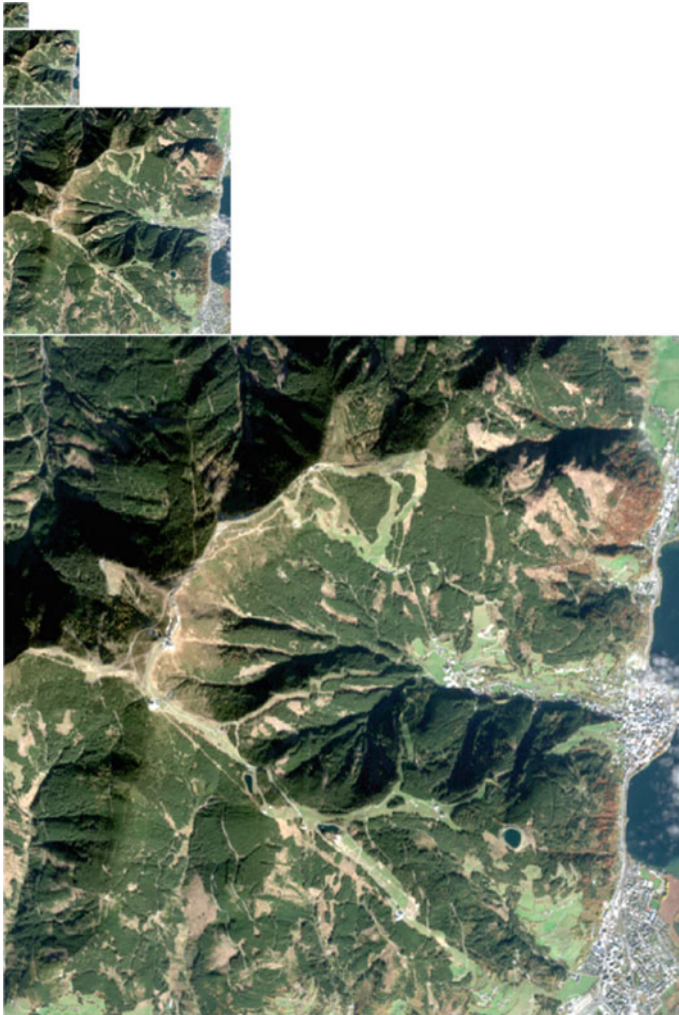
Fig. 2 An image pyramid starting from the original resolution level 0 through the levels 1, 2 and 3 by reducing the image size by factor 3 at each consecutive level

algorithm (Wallis 1976). The filter forces the mean and standard deviation of an image to given target values.

At present, many of the modern matching algorithms are based on the image pyramids (Fig. 2). An image pyramid is a multi-resolution representation of the original image. It is used to speed-up the image matching computation in a coarse-to-fine hierarchical approach while at same time keeping the finest spatial resolution of the final DSM output.

With coarse-to-fine hierarchical strategy based on image pyramid representation, the matches obtained at a coarse resolution are used to guide and limit the search space for the matching of finer-resolution features. The usual way is to start matching at a low resolution pyramid level, where the influence of image noise is reduced and coarse approximate values are sufficient to stay within the pull-in range of the matching procedure. In addition, the regions of interest for correspondence analysis in levels of higher resolution can be found in the low resolution images at low cost because irrelevant details are no longer available there. The computations are usually performed successively on each level of the hierarchy using the results of the higher level as approximate information (Ackermann and Hahn 1991; Zhang and Gruen 2006). The FORSAT software generates the image pyramids at the end of the pre-processing step, starting from the original resolution images. Each pyramid level is generated by multiplying a generating kernel and reduces the resolution by factor 3.

3.2 Geo-referencing

The FORSAT software uses the rational function model (RFM), a well-known non-rigorous (generalised) orientation method based on the rational polynomials functions. A RFM is the ratio of two polynomials derived from the rigorous sensor model and the corresponding terrain information, which does not reveal the sensor parameters explicitly. In most cases, the VHR satellite images are supplied with only rational polynomials coefficients (RPCs) instead of rigorous sensor model parameters.

The RFM is computed based on a rigorous sensor model (Fig. 3). With the given parameters of the rigorous model and by projecting evenly distributed image points into the object space, multiple-layer 3D object points can be computed and used as virtual (fictitious) control points. The control points are created based on the full extent of the image and the range of elevation variation in the object space. The entire range of elevation variation is sliced into several layers. Then, the RPCs are calculated by a least squares adjustment with these virtual control points (Tao and Hu 2001).

Grodecki and Dial (2003) proposed a block adjustment method for the VHR satellite imagery where the geo-referencing accuracy of the RFM is improved by use of a few numbers of control points. This RPC block adjustment method was implemented in the FORSAT software. It can run for stereo, triplet and block image configurations.
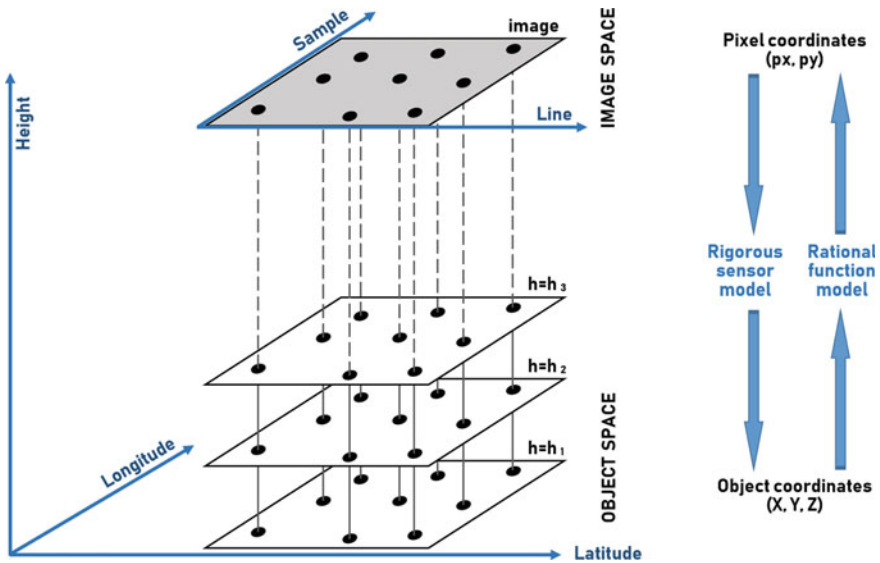
Fig. 3 The RPC computation

3.3 DSM Generation

The automated DSM generation was performed using a modified version of the multiple primitive multi-image matching (MPIM) method introduced by Zhang and Gruen (2004), Zhang (2005) and Zhang and Gruen (2006). In order to achieve successful and reliable results, the method matches a dense pattern of features with an appropriate matching strategy, making use of all available and explicit knowledge, concerning sensor model, network structure, image content and geometrical constraints such as the epipolar geometry constraint. The approach combines area-based matching (ABM) and feature-based matching (FBM), matching parameter self-tuning, generation of more redundant matches and a coarse-to-fine hierarchical matching strategy (Zhang et al. 2006; Baltsavias et al. 2007). The workflow is given schematically in Fig. 4.

After the pre-processing of the original images and production of the image pyramids, the area based and the feature based matching methods are run in parallel. Starting from the low-density features on the images with the low resolution, the matching procedure progressively approaches finally on the original resolution images. Since all the matching procedures are based on the concept of multi-image matching (two-fold and three-fold images) guided from the object space, any number of images could be processed simultaneously. The triangulated irregular network (TIN) is reconstructed from the matched features on each level of the
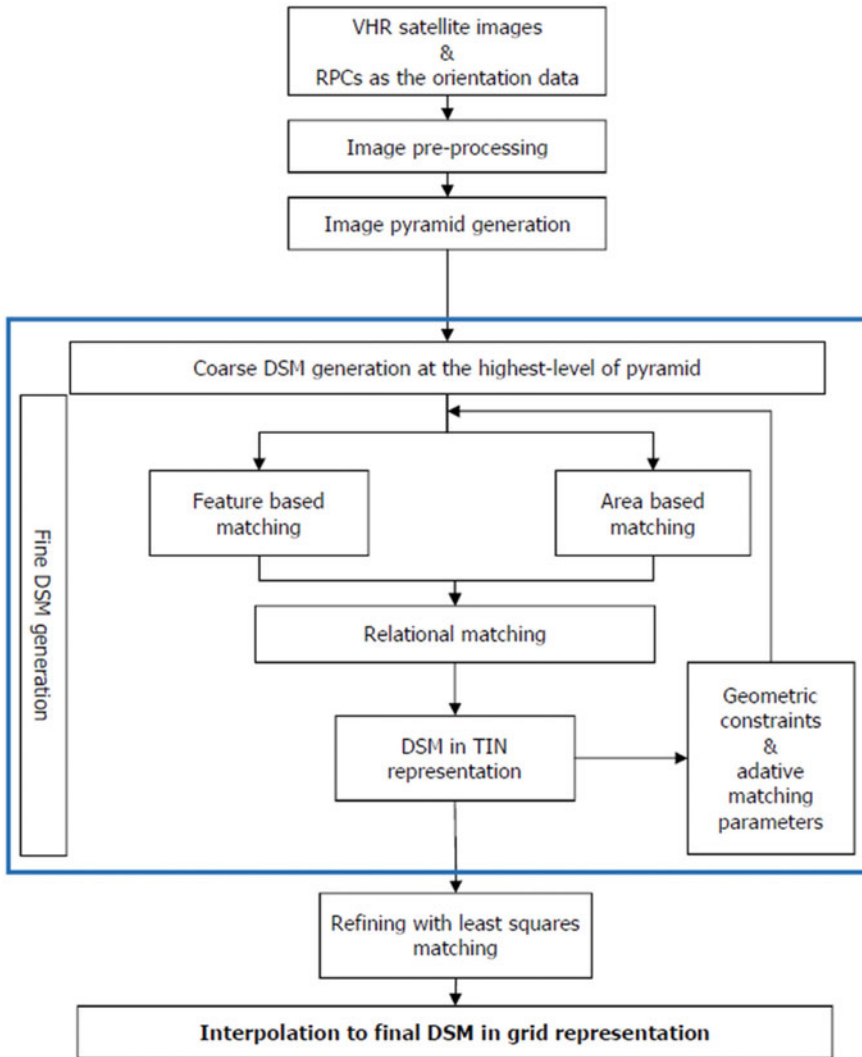
Fig. 4 Automated DSM generation in the FORSAT software

pyramid using the Delaunay triangulation method, which in turn is used in the subsequent pyramid level for the approximations and adaptively computation of the matching parameters. Finally, the least squares matching methods are used to achieve more precise matches for all the features and to identify some false matches.

The entire system consists of three mutually connected sub-systems: the image pre-processing module, the MPIM module and the refined matching module. The image pre-processing module is used to reduce the effects of the radiometric

problems and optimise the images for subsequent feature extraction and image matching procedure. A combined matching process (point matching, edge matching and relational matching processes) goes through all the image pyramid levels in the MPIM module and generates good enough approximations for the refined matching module. In the final refined matching module, the least squares matching methods are performed only on the original resolution images to achieve sub-pixel accuracy for all matched features obtained in the MPIM module (Zhang 2005).

3.4 3D Co-registration and Comparison

The co-registration is crucially needed wherever spatially related data sets, described as surfaces, have to be aligned to each other for comparison. Examples can be found in medicine, computer graphics, animation, cartography, virtual reality, industrial inspection and quality control, change detection, spatial data fusion, cultural heritage, photogrammetry, etc. Since DSMs represent the object surface, the problem can be defined as a surface co-registration problem. There have been some studies on the co-registration of DSMs for control information and for change detection tasks. This work is known as the digital elevation model (DEM) matching (Ebner et al. 1988; Rosenholm and Torlegard 1988; Mitchell and Chadwick 1999). This method basically estimates the 3D similarity transformation parameters between two DEM patches, minimising the sum of the squares of the elevation differences (1D along the z-axes). The 1D elevation differences may not truly represent the surface-to-surface distance where terrain is complex with steep changes and undulations.

For quality evaluation of DSMs, often a reference DSM is interpolated in the DSM to be checked. This approach is suboptimal (Gruen et al. 2004; Akca et al. 2016), since:

(1) at surface discontinuities surface modelling errors may lead to large height differences although the measurements are correct (Fig. 5a) and
(2) if the reference frames of the two DSMs differ (e.g. shifts and tilts), then again large differences occur, especially at discontinuities although the heights may be correct (Fig. 5c).

These shortcomings can be overcome by employing the approach where the shortest 3D (Euclidean) distance between each reference point and the produced DSM is used (Gruen and Akca 2005; Akca 2010; Akca et al. 2010). See Fig. 5b and Fig. 5d. Although the co-registration of surfaces is a very actively working area in many disciplines, we notice that a contribution that responds favourably to the following aspects is needed:
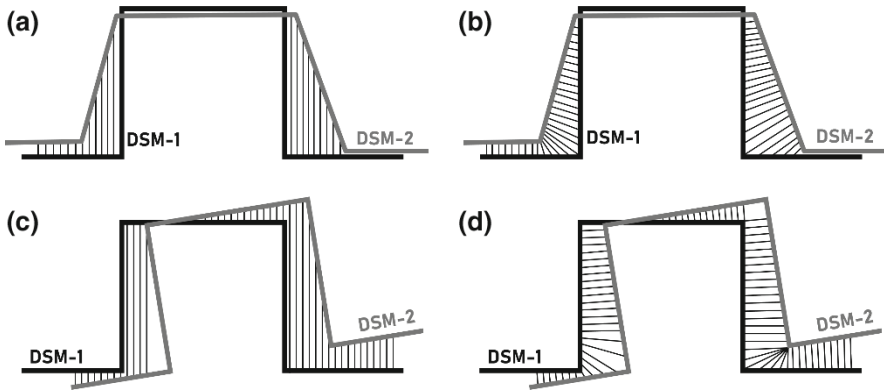
Fig. 5 The sub-optimality of 1D height differences **a** and **c** with respect to the 3D spatial distances **b** and **d** in case of surface modelling errors and reference frame differences (translation and rotation), respectively

(1) co-registration capability with higher order spatial transformation models,
(2) co-registration and comparison of full 3D surfaces (as opposed to 2.5D),
(3) a rigorous mathematical formulation for high accuracy demands,
(4) a flexible model for further algorithmic extensions,
(5) mechanisms and statistical tools for internal quality control, and
(6) capability of matching of data sets in different quality and resolution.

As a consequence, a fully satisfying general solution was implemented in the FORSAT software. We opted for the least squares 3D surface matching (LS3D) method (Gruen and Akca 2005; Akca 2007, 2010). The LS3D method is a rigorous algorithm for the matching of overlapping 3D surfaces and/or point clouds. It estimates the transformation parameters of one or more fully 3D surfaces with respect to a template surface, using the generalised Gauss–Markov model, minimising the sum of the squares of the Euclidean distances between the surfaces. This formulation gives the opportunity to match arbitrarily oriented 3D surfaces, without using explicit tie points. It is a powerful method whose accuracy and precision potential is directly dependent on the quality of the input data. Details of the procedure can be found in Akca and Gruen (2005; 2007). Several applications ranging from 3D modelling (Akca et al. 2006, 2007; Akca 2012) to geomorphology (Akca and Seybold 2016) showed the benefits of the method. The 3D co-registration and comparison module of the FORSAT software is a specialised implementation of the LS3D method.

3.5 Change Detection

Pre- and post-fire DSMs are matched with the co-registration module of the FORSAT software. Once the DSM pair is aligned and overlaid, the two surfaces form many interconnected or separated 3D manifolds (shapes). At each grid cell location, the surface elements are compared and the grid cell is assigned to any of those three states: decrease, no change and increase. Since the grid cell dimensions and surface-to-surface distances are known, the area and volume values are computed by summation the information of all grid cells.

Any spatial deviation larger than ±3 m between the DSMs is regarded as a "change" (fire induced decrease or vegetation growth based increase). This value is the mean a priori accuracy of the used DSMs according to our internal tests with VHR satellite images. The mean DSM generation accuracy of the FORSAT system is about 2–3 times of the ground sampling distance (GSD) of the used imagery. The spatial deviations less than ±3 m are labelled as "no change" class.

The gross errors due to image matching, triangulation and reconstruction problems produce abrupt changes on the DSM surface. Any spatial deviation larger than ±20 m are regarded as the gross error, excluded from the computation, and labelled as "no data". Although they are excluded in the computations, they are kept in the visualizations.

The selection of the threshold numbers as less than or greater than ±3 and ±20 m will accordingly change the ratio of Type-I and II errors. They can be tuned depending on the data type.

3.6 Error Assessment

Three classes "decrease in height", "no change" and "increase in height" are identified in the change detection step. In each test site, externally derived ground truth in the form of check points or polygons are used to perform the error assessment.

A sample point (or polygon) is classified as a true positive (TP), if the detection result corresponds to the reference data. A false positive (FP) error is a false detection where the detection result does not conform to the reference data (Shufelt 1999; McKeown et al. 2000). It is also known as Type-I error or commission error. A false negative (FN) error is a missed detection where an actual class in the reference data is omitted in the detection. It is also known as Type-II error or omission error.

Three commonly used metrics, the correctness, completeness and quality (Heipke et al. 1997; Rutzinger et al. 2009), are used for the evaluation of the results.

Correctness is the percentage of truly detected classes in the sample points, also referred to as users' accuracy (Foody 2002). It is relevant to the FP errors.

$$Correctness_i = (TP)_i / \left[(TP)_i + \sum(FP)_j\right] \tag{1}$$

Completeness is the percentage of truly detected classes in the reference points, also referred to as producers' accuracy (Foody 2002). It is relevant to the FN errors.

$$Completeness_i = (TP)_i / \left[(TP)_i + \sum(FN)_j\right] \tag{2}$$

Quality is the overall accuracy which takes into account both the correctness and completeness, also referred to percentage correct (Foody 2002).

$$Quality = \sum(TP)_i / \left[\sum(TP)_i + \sum(FP)_{ij} + \sum(FN)_{ij}\right] \tag{3}$$

The correctness and completeness metrics are computed for each of those three classes, individually. Quality is a single metric for the entire test site, given in the cells located at lower right corners of Tables 1 and 2.

Table 1 Confusion matrix of the Cyprus test site

		Ref. Decrease	Ref. No change	Ref. Increase	Row $\sum$	Correct. (%)
Det.	Decrease	40	44	1	85	47.1
Det.	No change	14	83	3	100	83.0
Det.	Increase	1	5	9	15	60.0
	Column $\sum$	55	132	13	200	
	Complet.	72.7%	62.9%	69.2%		66.0

Ref. Reference data, *Det.* Detection data, *Row* $\sum$ Row total, *Column* $\sum$ Column total

Table 2 Confusion matrix of the Austria test site

		Ref. Decrease	Ref. No change	Ref. Increase	Row $\sum$	Correct. (%)
Det.	Decrease	19	1	0	20	95.0
Det.	No change	5	92	3	100	92.0
Det.	Increase	0	57	23	80	28.8
	Column $\sum$	24	150	26	200	
	Complet.	79.2%	61.3%	88.5%		67.0

Ref. Reference data, *Det.* Detection data, *Row* $\sum$ Row total, *Column* $\sum$ Column total

4 Experimental Results

4.1 Cyprus Test Site

The climate of Cyprus is characterised by mild and rain-laden winters as well as dry and hot summers. Due to its climate conditions it is predestined for the breakout of forest fires. The high risk for forest ecosystems is also boosted through human interventions. The forest fire of Saittas, raged in 2007, was defined as a test site. The reason for this decision was the disastrous impact of the fire to the local vegetation which is still visible despite the long period of years between the event and image acquisition. The area of interest (AOI) covers an area of about 45 km^2 and includes the city of Pelentri in the Limassol district. There was an Ikonos stereo pair from October 2001 available which was used for the calculation of the pre-fire DSM. For the generation of the post-fire DSM a Pléiades stereo pair acquired in July 2014 was used.

The historic DSM (Fig. 6a) and the recent DSM (Fig. 6b) were generated using the FORSAT software. The both DSMs have a resolution of 2.0 m.

The change analysis was performed with "3D Comparison and Analysis" module of the FORSAT software. The effect of the forest fire of year 2007 can be seen in the west part of the change map (see the largest blue circle in Fig. 7 and enlarged 3D view in Fig. 8a). Furthermore, there are smaller burned areas near Pelentri in the north-east of the AOI (see the blue circle in the north-east of Fig. 7 and enlarged view in Fig. 8b). The decreased forest areas in the south-east of the AOI are man-made changes (Fig. 8c).

Figure 9 visualises the percentage of fire-affected vegetation cover in the AOI. It can be seen that conifer forest with nearly 70% is the most affected vegetation by the forest fire in 2007, followed by bushes and shrubs with 9.5% and tree cultivations with 9.2%.
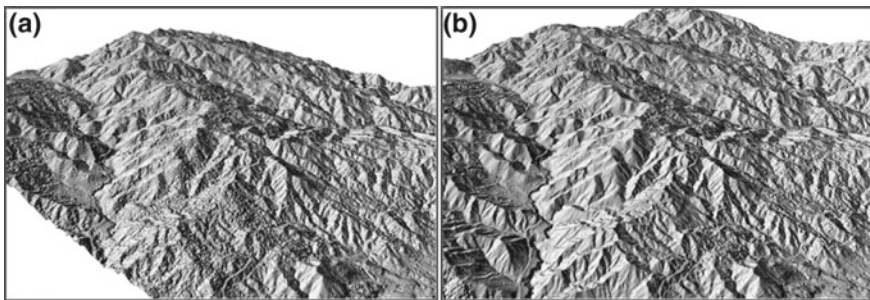
Fig. 6 **a** Ikonos DSM of October 2001, **b** Pléiades DSM of July 2014
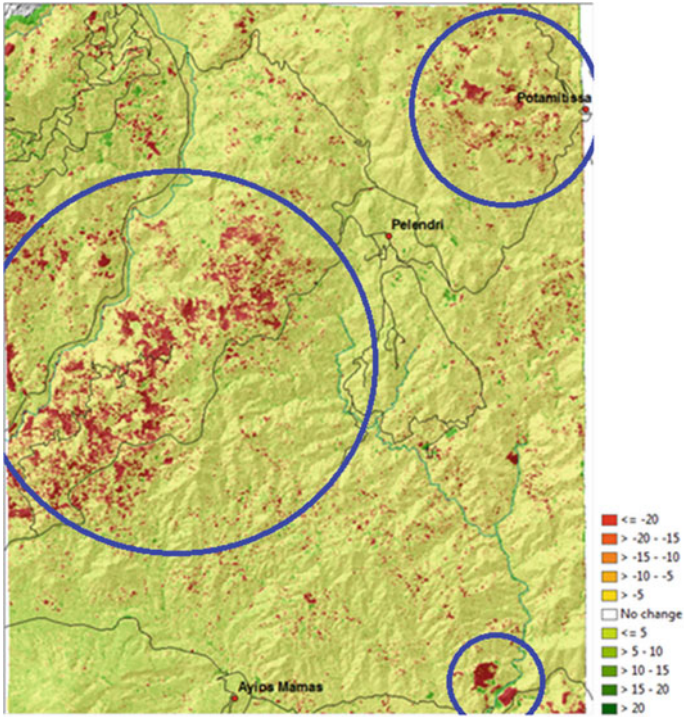
Fig. 7 Change map between pre-fire DSM and post-fire DSM in Cyprus
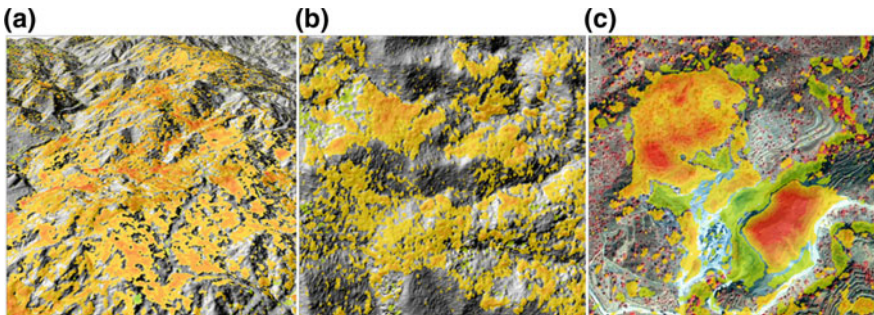
Fig. 8 Zoom into Fig. 7 **a** 3D view of the largest circle region in the centre, **b** the north-east circle region, **c** the south-east small circle region

Figure 10 shows that more than half (54.6%) of the broadleaved forest area, 47.5% of conifer forest and more than a third (36.0%) of the undefined (forest) area were affected by the decrease in height. We noticed that the forest has still not recovered from the fire in 2007.
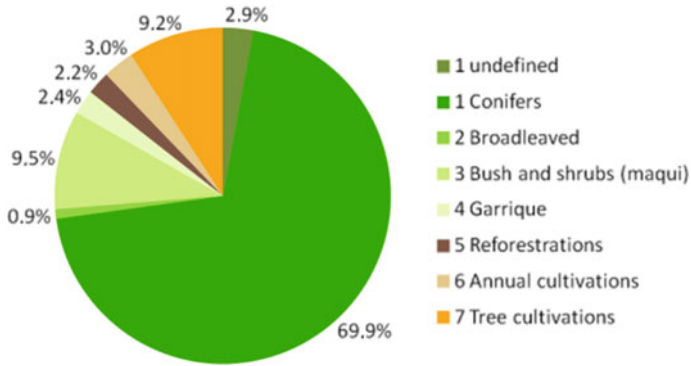
Fig. 9 Percentage of fire-affected vegetation cover in the area of interest
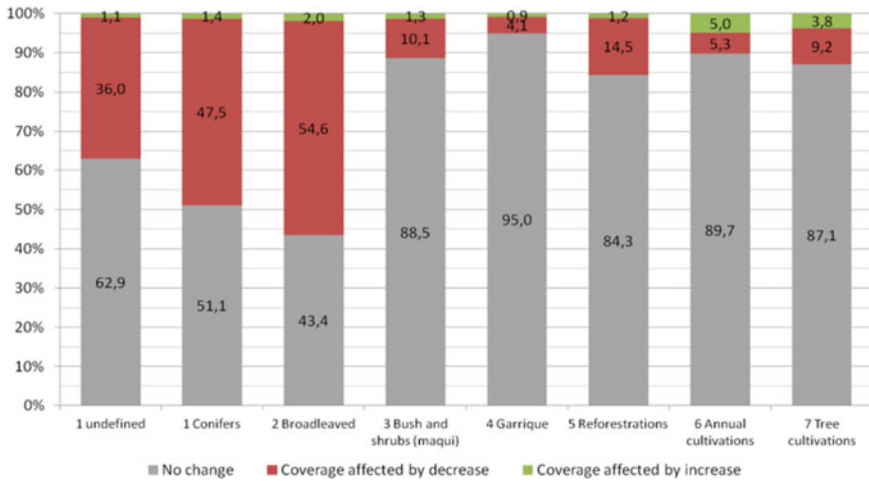
Fig. 10 Change in area (percentage) of fire effected forest vegetation

Figure 11 visualizes the change in volume in fire-affected vegetation cover based on comparison of the DSMs of 2001 and 2014. It illustrates that there is a large decrease (approx. 13 million m^3) of conifer forest. However, this class has also the highest volume increase (365,892 m^3), but it has to be noted that conifer forest cover almost 70% of the whole fire-affected area. Other land cover classes with a volume decrease of nearly 200,000 m^3 and more are undefined forest, broadleaved forest, tree cultivations as well as bush and shrubs (maqui). Besides conifer forest only tree cultivations have a volume increase of more than 100,000 m^3. An interesting fact is that the land cover class annual cultivations decreases the area, but increases the volume in total.
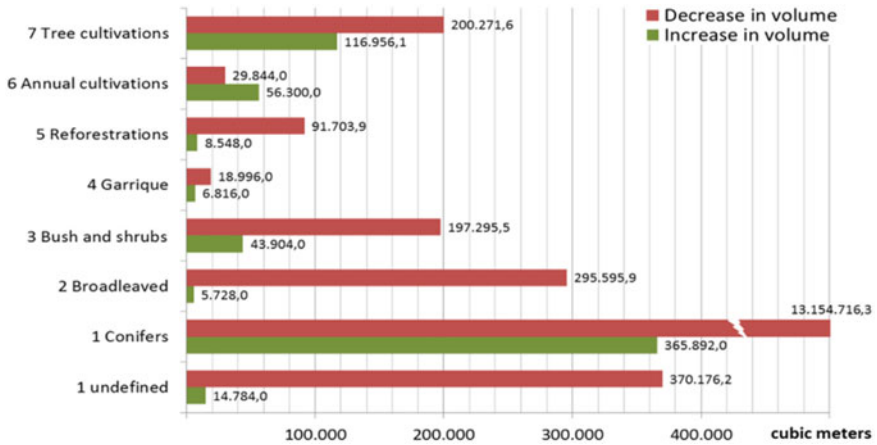
Fig. 11 Change in volume (m3) of fire effected forest vegetation

Fig. 12 Forest fire near Absam, Tyrol, Austria

In order to perform the error assessment, 85, 100 and 15 samples were randomly selected in the detected "decrease in height", "no change" and "increase in height" classes, respectively. Their actual states were manually investigated on the available aerial and satellite images. The results are presented in a confusion matrix (Table 1). The overall accuracy is 66.0%. There is a tendency towards overestimation of both of the change classes, whilst the "no change" class is underestimated. The "no change" class interferes with the both change classes. This is because of the image matching errors and modelling problems especially at the abrupt surface discontinuities, shadow and cloud coverages. This fact is especially significant in the "decrease in height" class in which 44 FPs were detected mistakenly, although they belong to the "no change" class in reality.

4.2 Austria Test Site

Monitoring of forest areas in terms of quantifying changes over time is a crucial topic in Austria. Strong winds cannot only cause direct damages, but also lead to threats concerning the break out and spreading of forest fires. Fires are great dangers for forests and subsequently for humans as the forests have a protection function for inhabited areas regarding other natural hazards like avalanches, landslides or rock falls. Due to the forest fire event near Absam in Tyrol (Austria), which started on 20-th of March 2014 and raged about two days, the corresponding burned area was selected as a test site (Fig. 12).

The AOI covers about 62 km^2 and includes the burned area from the afore-mentioned forest fire as well as the eastern suburbs of Innsbruck. Hence, the test site includes a variety of landscapes like mountains, dense urbanised areas surrounded by intensive agriculture as well as rural areas.

The pre-fire data, which dates back to 2006/2007, is a 1.0 m resolution DSM derived from an airborne LiDAR flight (Fig. 13a). A set of Pléiades triplet images was acquired in June 2014 and used to represent the post-fire situation. The Pléiades triplet was processed using the FORSAT software and a 1.0 m resampled DSM was generated (Fig. 13b).

The optical instrument of Pléiades has 70 cm resolution and offers three-fold images of the same scene from the along track trajectory of the platform. The three rays of the same object point increase the system redundancy, and so also the reliability. The LiDAR DSM and Pléiades DSM were co-registered and compared using the LS3D algorithm of the FORSAT software. The result of the 3D change analysis is given in Fig. 14.
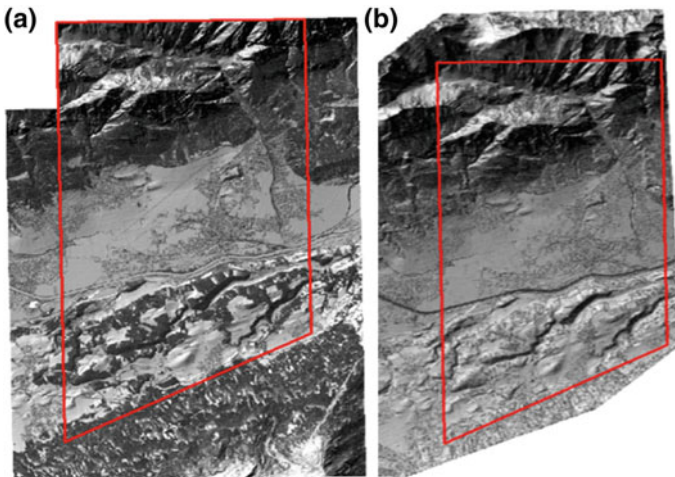
Fig. 13 **a** Historical LiDAR DSM of 2006/2007, **b** recent Pléiades DSM of 2014

Fig. 14 The 3D Change analysis. Red colour deforestation and green for growth of the vegetation
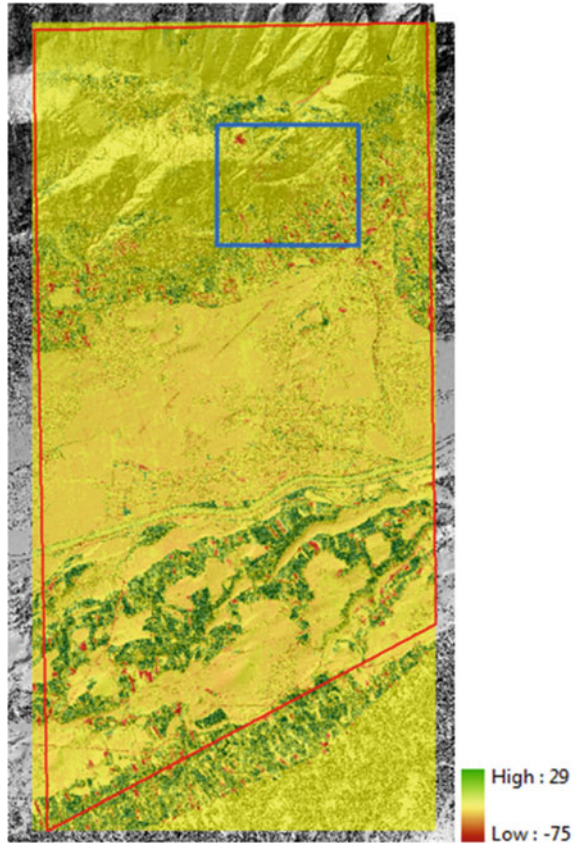
The occasional clear-cuts and storm damages in the north and the vegetation growth in the south are dominating patterns. The enlarged view of the forest fire, delineated with the blue rectangle, is given in Fig. 15a. The dark green region in the centre of the false colour composite image (Fig. 15b) is the fire affected area, which is shown in orange colour in its change DSM counterpart (Fig. 15a). The fire burned area was dominated by shrubs (proportionally shorter than trees) according to the reports of the Forest Department. This is the reason why the burned areas are not as dominant as the deforestation areas due to clear-cuts or storms such as the red plots in the upper left and lower right parts of Fig. 15a.

There are three classes in the test area: timber forest, shrubs and clear-cuts (Fig. 16). Timber forest is the dominating type with 81.3% coverage.

The forest map showing the boundaries of these three classes is obtained in vector format and overlaid with the change results given in Fig. 14. Thus, areal extends of change of each individual class are computed and given as percentage in Fig. 17.
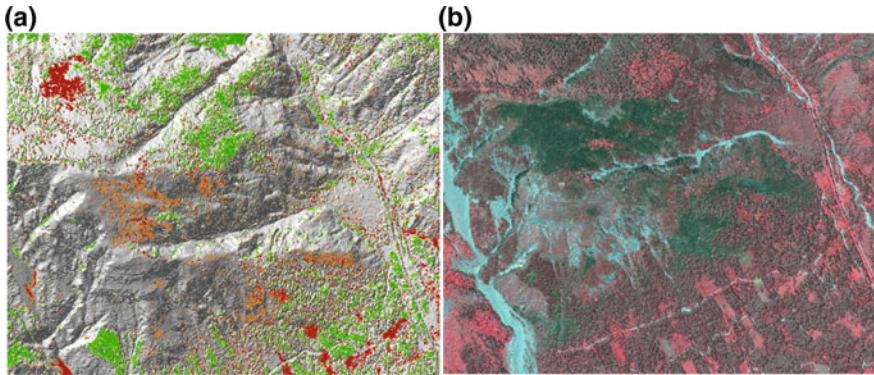
Fig. 15 **a** Enlarged view of the fire area which is shown as a blue rectangle in Fig. 14, **b** Pléiades (in June 2014) false colour composite of the same extend

Fig. 16 Percentage of forest map classes in the area of interest
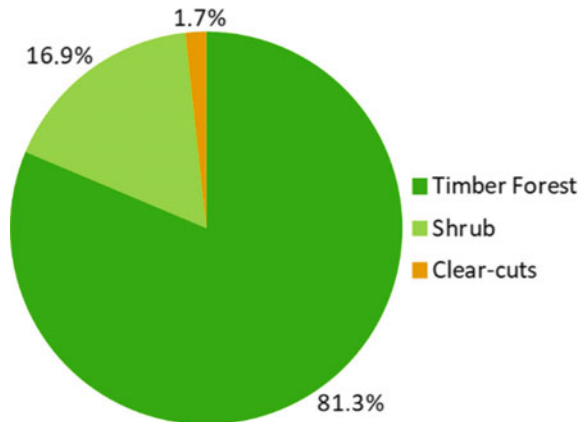
In spite of the forest fire, changes of shrubs are minor, and 99.1% area of the shrubs coverage remained unchanged. 17.5% area of the timber forest class increases in height, which is clearly visible as growth of the vegetation in the southern part of the test area (below green areas in Fig. 14).

The results of the volumetric comparison (Fig. 18) show that the trend is in the same direction with the area comparison, but the magnitude is overwhelmingly nonlinear. The timber forest class gained 17.7 million m^3 volume of stock whereas it lost 7.2 million m^3 due to deforestation. A detailed analysis of the burnt area, visualised in Fig. 15, shows a loss of volume caused by the fire in March 2014 of 41,800 m^3 shrubs and 40,100 m^3 timber forest.

20, 100 and 80 sample points to be used in the error assessment were randomly selected in the detected "decrease in height", "no change" and "increase in height"
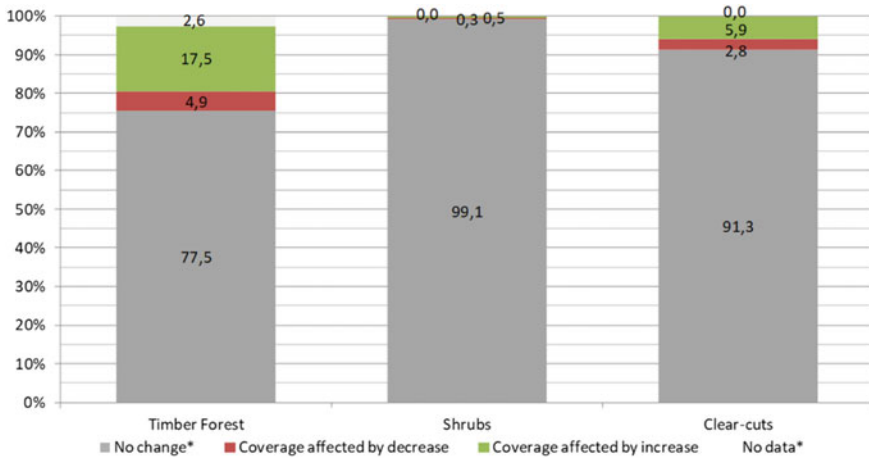
Fig. 17 Change in area (percentage) of each vegetation type
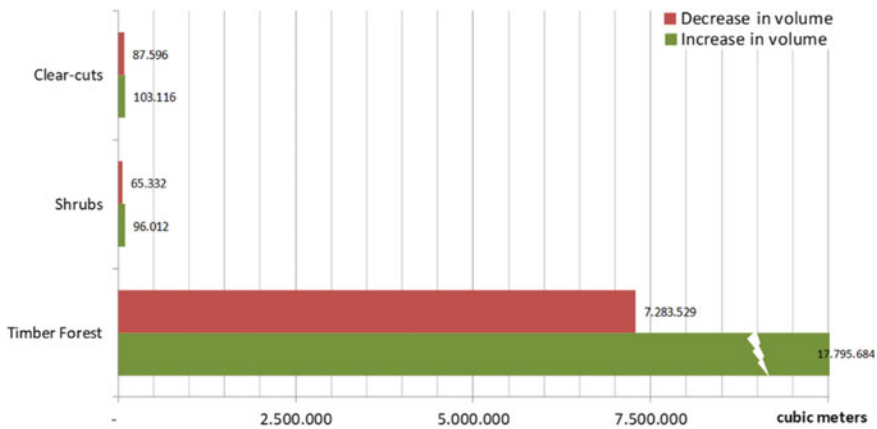
Fig. 18 Change in volume (m3) of each vegetation type

classes, respectively. Their actual states were manually investigated on the available historic orthophotos and actual satellite images. The results are presented in Table 2.

"Decrease in height" class is successfully detected in terms of both the correctness and completeness metrics. "Increase in height" class has the worst FP rate as 100%–28.8% = 71.2%, in contrast to the previous Cyprus test site. "Decrease" and "increase" in height classes do not significantly interfere to each other. "No change" class has the largest FN rate as 38.7%. The discrimination problems between the "no change" and "increase in height" classes degrade the overall accuracy, which is 67.0%.

5   Conclusions

Forest administrations give special attention to forest fires where post-disaster loss can rarely be gauged in a quick and economic way unless an appropriate technology is adopted. Determination of planimetric and volumetric changes between pre- and post-fire stages is in high demand. The FORSAT software was developed to meet the relevant demands. It is capable of providing spatial information for rapid monitoring of forest areas. The basic input data is the VHR satellite imagery. The software consists of mutually linked modules which are pre-processing, geo-referencing, DSM generation, and 3D comparison and analysis.

The pilot application studies demonstrate the capability of the FORSAT software especially for change analysis of the forest burnt areas. Special attention was paid to use combinations of different input data like stereo and triplet image data from different satellites as well as LIDAR point clouds. The results of the applications show the high potential of optical images from VHR satellite sensors for DSM generation on forest covers and that the FORSAT software is a powerful tool to extract value-added products related to forest and beyond. It provides an innovative approach by detecting changes from DEMs of different dates.

The results of FORSAT provide single source, flexible forest information solutions with a very competitive price versus quality ratio, allowing for new market entry in the forest sector. It can be used for various service applications related to forest as well as other topics.

References

Abdollahi M, Islam T, Gupta A, Hassan QK (2018) An advanced forest fire danger forecasting system: integration of remote sensing and historical sources of ignition data. Remote Sens 10:923. https://doi.org/10.3390/rs10060923

Ackermann F, Hahn M (1991) Image pyramids for digital photogrammetry. In: Ebner H, Fritsch D, Heipke C (eds) Digital photogrammetric systems. Wichmann, Karlsruhe, pp 43–58

Addison P, Oommen T (2018) Utilizing satellite radar remote sensing for burn severity estimation. Int J Appl Earth Obs Geoinf 73:292–299

Adelabu SA, Adepoju KA, Mofokeng OD (2018) Estimation of fire potential index in mountainous protected region using remote sensing. Geocarto International. https://doi.org/10.1080/10106049.2018.1499818

Akca D, Gruen A (2005) Recent advances in least squares 3D surface matching. In: Gruen A, Kahmen H (eds) Proceedings of the optical 3-D measurement techniques VII, Vienna, Austria, 3–5 October 2005, vol. II, pp 197–206

Akca D, Gruen A, Alkis Z, Demir N, Breuckmann B, Erduyan I, Nadir E (2006) 3D modeling of the Weary Herakles statue with a coded structured light system. Int Arch Photogramm Remote Sens Spat Inf Sci 36(5):14–19

Akca D (2007) Least Squares 3D surface matching. Ph.D. thesis, Institute of Geodesy and Photogrammetry, ETH Zurich, Switzerland, Mitteilungen Nr. 92, p 78. https://doi.org/10.3929/ethz-a-005461765

Akca D, Gruen A (2007) Generalized Least Squares multiple 3D surface matching. Int Archives Photogramm Remote Sens Spat Inf Sci 36(3/W52):1–7

Akca D, Remondino F, Novàk D, Hanusch T, Schrotter G, Gruen A (2007) Performance evaluation of a coded structured light system for cultural heritage applications. Proc. of SPIE-IS&T Electronic Imaging, Videometrics IX, San Jose, California, January 29–30. SPIE 6491:64910V-1–12

Akca D (2010) Co-registration of surfaces by 3D Least Squares matching. Photogramm Eng Remote Sens 76(3):307–318

Akca D, Freeman M, Sargent I, Gruen A (2010) Quality assessment of 3D building data. Photogram Rec 25(132):339–355

Akca D (2012) 3D modeling of cultural heritage objects with a structured light system. Mediterr Archaeol Archaeom 12(1):139–152

Akca D, Seybold HJ (2016) Monitoring of a laboratory-scale inland-delta formation using a structured-light system. Photogram Rec 31(154):121–142

Akca D, Stylianidis E, Smagas K, Hofer M, Poli D, Gruen A, Martin VS, Altan O, Walli A, Jimeno E, Garcia A (2016) Volumetric forest change detection through VHR satellite imagery. Int Archives Photogramm Remote Sens Spat Inf Sci 41(B8):1213–1220

Almeida-Filho R, Rosenqvist A, Shimabukuro YE, dos Santos JR (2005) Evaluation and perspectives of using multitemporal L-band SAR data to monitor deforestation in the Brazilian Amazonia. IEEE Geosci Remote Sens Lett 2(4):409–412

Almeida-Filho R, Rosenqvist A, Shimabukuro YE, Silva-Gomez R (2007) Detection deforestation with multitemporal L-band SAR imagery: a case study in western Brazilian Amazonia. Int J Remote Sens 28(6):1383–1390

Almeida-Filho R, Shimabukuro YE, Rosenqvist A, Sanchez GA (2009) Using dual-polarized ALOS PALSAR data for detecting new fronts of deforestation in the Brazilian Amazonia. Int J Remote Sens 30(14):3735–3743

Altan O, Backhaus R, Boccardo P, van Manen N, Tonolo FG, Trinder J, Zlatanova S (2013). The value of geoinformation for disaster and risk management (VALID), Joint Board of Geospatial Information Society (JB GIS), Copenhagen, ISBN 97887-90907-88-4

Alves DS (2002) Space-time dynamics of deforestation in Brazilian Amazonia. Int J Remote Sens 23(14):2903–2908

Anderson LO, Shimabukuro YE, Defries RS, Morton D (2005) Assessment of deforestation in near real time over the Brazilian Amazon using multitemporal fraction images derived from Terra MODIS. IEEE Geosci Remote Sens Lett 2(3):315–318

Baillarin F, Souza C, Gonzales G (2008) Use of Formosat-2 satellite imagery to detect near real time deforestation in Amazonia. IEEE International Geoscience & Remote Sensing Symposium (IGARSS'2008). https://doi.org/10.1109/IGARSS.2008.4779481

Baltsavias E, Kocaman S, Akca D, Wolff K (2007) Geometric and radiometric investigations of Cartosat-1 Data. ISPRS Workshop on high resolution earth imaging for geospatial information, Hannover, Germany, 29 May–1 June 2007

Bodart C, Eva H, Beuchle R et al (2011) Pre-processing of a sample of multi-scene and multi-date Landsat imagery used to monitor forest cover changes over the tropics. ISPRS J Photogramm Remote Sens 66:555–563

Burnett JD, Wing MG (2018) A low-cost near-infrared digital camera for fire detection and monitoring. Int J Remote Sens 39(3):741–753

Cabral AIR, Silva S, Silva PC, Vanneschi L, Vasconcelos MJ (2018) Burned are estimations derived from Landsat ETM+ and OLI data: comparing Genetic Programming with Maximum Likelihood and classification and regression trees. ISPRS J Photogramm Remote Sens 142:94–105

Cailliez F (1992) Forest volume estimation and yield prediction. FAO For Paper 22(1):98

Camaro W, Steffenino S, Vigna R (2013) Fire risk mapping and fire detection and monitoring. In: The value of Geoinformation for disaster and risk management (VALID), joint board of geospatial information society (JB GIS), Copenhagen, ISBN 97887-90907-88-4

Colson D, Petropoulos GP, Ferentinos KP (2018) Exploring the potential of Sentinels-1 & 2 of the Copernicus Mission in support of rapid and cost-effective wildfire assessment. Int J Appl Earth Obs Geoinf 73:262–276

Cucchiaro S, Cavalli M, Vericat D, Crema S, Llena M, Beinat A, Marchi L, Cazorzi F (2018) Monitoring topographic changes through 4D-structure-from-motion photogrammetry: Application to a debris-flow channel. Environ Earth Sci 77:632. https://doi.org/10.1007/s12665-018-7817-4

Di Maio Mantovani AC, Setzer AW (1997) Deforestation detection in the Amazon with an AVHRR-based system. Int J Remote Sens 18(2):273–286

Ebner H, Strunz G (1988) Combined point determination using digital terrain models as control information. Int Archives Photogramm Remote Sens 27(B11/3):578–587

Edwards AC, Russell-Smith J, Maier SW (2018) A comparison and validation of satellite-derived fire severity mapping techniques in fire prone north Australian savannas: extreme fires and tree stem mortality. Remote Sens Environ 206:287–299

Eva H, Carboni S et al (2010) Monitoring forest areas from continental to territorial levels using a sample of medium spatial resolution satellite imagery. ISPRS J Photogramm Remote Sens 65:191–197

Fernandez-Garcia V, Santamarta M, Fernandez-Manso A, Quintano C, Marcos E, Calvo L (2018) Burn severity metrics in fire-prone pine ecosystems along a climatic gradient using Landsat imagery. Remote Sens Environ 206:205–217

Filizzola C, Corrado R, Marchese F, Mazzeo G, Paciello R, Pergola N, Tramutoli V (2016) RST-FIRES, an exportable algorithm for early-fire detection and monitoring: description, implementation, and field validation in the case of the MSG-SEVIRI sensor. Remote Sens Environ 186:196–216

Foody GM (2002) Status of land cover classification accuracy assessment. Remote Sens Environ 80:185–201

Garcia-Lazaro JR, Moreno-Ruiz JA, Riano D, Arbelo M (2018) Estimation of burned area in the northeastern Siberian Boreal Forests from a long-term data record (LTDR) 1982-2015 time series. Remote Sens 10:940. https://doi.org/10.3390/rs10060940

Giglio L, Descloitres J, Justice CO, Kaufman YJ (2003) An enhanced contextual fire detection algorithm for MODIS. Remote Sens Environ 87:273–282

Giglio L, Schroeder W, Justice CO (2016) The collection 6 MODIS active fire detection algorithms and fire products. Remote Sens Environ 178:31–41

Grodecki J, Dial G (2003) Block Adjustment of High-Resolution Satellite Images Described by Rational Polynomials. Photogramm Eng Remote Sens 69(1):59–68

Gruen A, Poli D, Zhang L (2004) SPOT-5/HRS stereo images orientation and automated DSM generation. Int Archives Photogramm Remote Sens Spat Inf Sci 35(1):421–432

Gruen A, Akca D (2005) Least squares 3D surface and curve matching. ISPRS J Photogramm Remote Sens 59(3):151–174

GW website (2018) Insitu ScanEagle UAS helps suppress wildfires. https://www.geomatics-world.co.uk/content/news/insitu-scaneagle-uas-helps-suppress-wildfires. Accessed 09 Oct 2018

Haboudane D, Bahri EM (2008) Deforestation detection and monitoring in cedar forests of the Moroccan Middle-Atlas Mountains. IEEE International Geoscience & Remote Sensing Symposium (IGARSS'2007). https://doi.org/10.1109/IGARSS.2007.4423809

Heipke C, Mayer H, Wiedemann C, Jamet O (1997) Evaluation of automatic road extraction. Int Archives Photogramm Remote Sens 32(3–2W3):47–56

Ichii K, Maruyama M, Yamaguchi Y (2003) Multi-temporal analysis of deforestation in Rondonia state in Brazil using Landsat MSS, ETM+ and NOAA AVHRR imagery and its relationship to changes in the local hydrological environment. Int J Remote Sens 24(22):4467–4479

Isoguchi O, Shimada M, Uryu Y (2009) A preliminary study on deforestation monitoring in Sumatra island by PALSAR. IEEE International Geoscience & Remote Sensing Symposium (IGARSS'2009). https://doi.org/10.1109/IGARSS.2009.5417928

Justice CO, Townshend JRG, Vermote EF, Masuoka E, Wolfe RE, Saleous N, Roy DP Morisette JT (2002a) An overview of MODIS Land data processing and product status. Remote Sensing of Environment 83:3–15

Justice CO, Giglio L, Korontzi S, Owens J, Morisette JT, Roy D, Descloitres J, Alleaume S, Petitcolin F, Kaufman Y (2002b) The MODIS fire products. Remote Sens Environ 83:244–262

Koch B (2010) Status and future of laser scanning, synthetic aperture radar and hyperspectral remote sensing data for forest biomass assessment. ISPRS J Photogramm Remote Sens 65:581–590

Krasovskii A, Khabarov N, Pirker J, Kraxner F, Yowargana P, Schepaschenko D, Obersteiner M (2018) Forests 9:437. https://doi.org/10.3390/f9070437

Koltunov A, Ustin SL, Quayle B, Schwind B, Ambrosia VG, Li W (2016) The development and first validation of the GOES Early Fire Detection (GOES-EFD) algorithm. Remote Sens Environ 184:436–453

Lee H (2008) Mapping deforestation and age of evergreen trees by applying a binary coding method to time-series Landsat November images. IEEE Trans Geosci Remote Sens 46 (11):3926–3936

Li X, Zhang H, Yang G, Ding Y, Zhao J (2018) Post-fire vegetation succession and surface energy fluxes derived from remote sensing. Remote Sens 10:1000. https://doi.org/10.3390/rs10071000

Lin Z, Chen F, Niu Z, Li B, Yu B, Jia H, Zhang M (2018) An active fire detection algorithm based on multi-temporal FengYun-3C VIRR data. Remote Sens Environ 211:376–387

Mancini LD, Elia M, Barbati A, Salvati L, Corona P, Lafortezza R, Sanesi G (2018) Are wildfires knocking on the built-up areas door? Forests 9:234. https://doi.org/10.3390/f9050234

Mayr MJ, Vanselow KA, Samimi C (2018) Fire regimes at the arid fringe: A 16-year remote sensing perspective (2000–2016) on the controls of fire activity in Namibia from spatial predictive models. Ecol Ind 91:324–337

McCarley TR, Kolden CA, Vaillant NM, Hudak AT, Smith AMS, Wing BM, Kellogg BS, Kreitler J (2017) Multi-temporal LiDAR and Landsat quantification of fire-induced changes to forest structure. Remote Sens Environ 191:419–432

McKeown DM, Bulwinkle T, Cochran S, Harvey W, McGlone C, Shufelt JA (2000) Performance evaluation for automatic feature extraction. Int Archives Photogramm Remote Sens 33 (B2):379–394

Meng R, Wu J, Schwager KL, Zhao F, Dennison PE, Cook BD, Brewster K, Green TM, Serbin SP (2017) Using high spatial resolution satellite imagery to map forest burn severity across spatial scales in a Pine Barrens ecosystem. Remote Sens Environ 191:95–109

Millington AC, Velez-Liendo XM, Bradley AV (2003) Scale dependence in multitemporal mapping of forest fragmentation in Bolivia: implications for explaining temporal trends in landscape ecology and applications to biodiversity conservation. ISPRS J Photogramm Remote Sens 57:289–299

Mitchell HL, Chadwick RG (1999) Digital photogrammetric concepts applied to surface deformation studies. Geomatica 53(4):405–414

Mondal P, Southworth J (2010) Protection vs. commercial management: spatial and temporal analysis of land cover changes in the tropical forests of Central India. For Ecol Manage 259:1009–1017

Mora B, Wulder MA, White JC, Hobart G (2013) Modeling stand height, volume, and biomass from very high spatial resolution satellite imagery and samples of airborne LiDAR. Remote Sens 5:2308–2326

Navarro G, Caballero I, Silva G, Parra PC, Vazquez A, Caldeira R (2017) Evaluation of forest fire on Madeira Island using Sentinel-2A MSI imagery. Int J Appl Earth Observ Geoinf 58:97–106

Nyongesa KW, Vacik H (2018) Fire management in Mount Kenya: a case study of Gathiuru forest station. Forests 9:481. https://doi.org/10.3390/f9080481

Pahari K, Murai S (1999) Modelling for prediction of global deforestation based on the growth of human population. ISPRS J Photogramm Remote Sens 54:317–324

Pasquarella VJ, Holden CE, Kaufman L, Woodcock CE (2016) From imagery to ecology: leveraging time series of all available Landsat observations to map and monitor ecosystem state & dynamics. Remote Sens Ecol Conserv 2(3):152–170. https://doi.org/10.1002/rse2.24

Poli D (2005) Modelling of Spaceborne Linear Array Sensors. Ph.D. thesis, Institute of Geodesy and Photogrammetry, ETH Zurich, Switzerland, Mitteilungen Nr. 85, p 217

Poli D (2007) A Rigorous Model for Spaceborne Linear Array Sensors. Photogramm Eng Remote Sens 73(2):187–196

Ramo R, Garcia M, Rodriguez D, Chuvieco E (2018) A data mining approach for global burning area mapping. Int J Appl Earth Observ Geoinf 73:39–51

Remondino F (2011) Heritage recording and 3D modelling with photogrammetry and 3D scanning. Remote Sensing 3:1104–1138

Rosenholm D, Torlegard K (1988) Three-dimensional absolute orientation of stereo models using digital elevation models. Photogramm Eng Remote Sens 54(10):1385–1389

Rutzinger M, Rottensteiner F, Pfeifer N (2009) A comparison of evaluation techniques for building extraction from airborne laser scanning. IEEE J Sel Topics Appl Earth Observ Remote Sens 2(1):11–20

Ryu JH, Han KS, Hong S, Park NW, Lee YW, Cho J (2018) Satellite-based evaluation of the post-fire recovery process from the worst forest case in South Korea. Remote Sens 10:918. https://doi.org/10.3390/rs10060918

Santos JR, Mura JC, Paradella WP, Dutra LV, Goncalves FG (2008) Mapping recent deforestation in the Brazilian Amazon using simulated L-band MAPSAR images. Int J Remote Sens 29 (16):4879–4884

Schanz D, Huhn F, Schroeder A (2018) Large-scale volumetric flow measurement of a thermal plume using Lagrangian Particle Tracking (Shake-The-Box). In: Raffel M et al (eds) Particle Image Velocimetry, Springer, 606–610. https://doi.org/10.1007/978-3-319-68852-7_18

Schroeder W, Oliva P, Giglio L, Csiszar IA (2014) The new VIIRS 375 m active fire detection data product: algorithm description and initial assessment. Remote Sens Environ 143:85–96

Sefercik UG, Alkan M, Buyuksalih G, Jacobsen K (2013) Generation and validation of high-resolution DEMs from Worldview-2 stereo data. Photogramm Rec 28(144):362–374

Shufelt JA (1999) Performance evaluation and analysis of monocular building extraction from aerial imagery. IEEE Trans Pattern Anal Mach Intell 21(4):311–326

Silva Junior CHL, Aragao LEOC, Fonseca MG, Almeida CT, Vedovato LB, Anderson LO (2018) Deforestation-induced fragmentation increases forest fire occurrence in Central Brazilian Amazonia. Forests 9:305. https://doi.org/10.3390/f9060305

Solberg S, Astrup R, Weydahl DJ (2013) Detection of forest clear-cuts with Shuttle Radar Topography Mission (SRTM) and Tandem-X InSAR data. Remote Sensing 5:5449–5462

Soto-Berelov M, Jones SD, Clarke E, Reddy S, Gupta V, Felipe MLC (2018) Assessing two large area burnt area products across Australian Southern Forests. Int J Remote Sens 39(3):879–905

Souza CM, Siqueira JV, Sales MH et al (2013) Ten-year Landsat classification of deforestation and forest degradation in the Brazilian Amazon. Remote Sens 5:5493–5513

Sun P, Zhang Y (2018) A probabilistic method predicting forest fire occurrence combining firebrands and the weather-fuel complex in the northern part of the Daxinganling region. China For 9:428. https://doi.org/10.3390/f9070428

Svancara LK, Scott JM, Loveland TR, Pidgorna AB (2009) Assessing the landscape context and conversion risk of protected areas using satellite data products. Remote Sens Environ 113:1357–1369

Tao CV, Hu Y (2001) A Comprehensive Study of the Rational Function Model for Photogrammetric Processing. Photogramm Eng Remote Sens 66(12):1477–1485

Tian L, Wang J, Zhou H, Wang J (2018) Automatic detection of forest fire disturbance based on dynamic modelling from MODIS time-series observations. Int J Remote Sens 39(12):3801–3815

Toschi I, Remondino F, Kellenberger T, Streilein A (2017) A survey of geomatics solutions for the rapid mapping of natural hazards. Photogramm Eng Remote Sens 83(12):843–859

Toschi I, Allocca M, Remondino F (2018) Geomatics mapping of natural hazards: overview and experiences. Int Archives Photogramm Remote Sens Spat Inf Sci 42(3/W4):505–512

Tucker CJ, Townshend JRG (2000) Strategies for monitoring tropical deforestation using satellite data. Int J Remote Sens 21(6):1461–1471

Vega SGD, de las Heras J, Moya D (2018) Post-fire regeneration and diversity response to burn severity in pinus halepensis Mill. forests. Forests 9:299. https://doi.org/10.3390/f9060299

Wallis R (1976) An approach to the space variant restoration and enhancement of images. In: Proc of Symposium on Current Mathematical Problems in Image Science, Monterey, CA

Wheeler D, Guzder-Williams B, Petersen R, Thau D (2018) Rapid MODIS-based detection of tree cover loss. Int J Appl Earth Obs Geoinf 69:78–87

Xu C, Manley B, Morgenroth J (2018) Evaluation of modelling approaches in predicting forest volume and stand age for small-scale plantations forests in New Zealand with RapidEye and LiDAR. Int J Appl Earth Observ Geoinf 73:386–396

Yu B, Chen F, Li B, Wang L, Wu M (2017) Fire risk prediction using remote sensed products: a case of Cambodia. Photogrammetric Engineering and Remote Sensing 83(1):19–25

Zhang L, Gruen A (2004) Automatic DSM generation from linear array imagery data. Int Archives Photogramm Remote Sens Spat Inf Sci 35(B3):128–133

Zhang L (2005) Automatic Digital Surface Model (DSM) Generation from Linear array Images. Ph.D. thesis, Institute of Geodesy and Photogrammetry, ETH Zurich, Switzerland, Mitteilungen Nr.88, p 219. ISBN 3-906467-55-4

Zhang L, Gruen A (2006) Multi-image matching for DSM generation from IKONOS imagery. ISPRS J Photogramm Remote Sens 60:195–211

Zhang L, Kocaman S, Akca D, Kornus W, Baltsavias E (2006) Test and performance evaluation of DMC images and new methods for their processing. In: Proceedings ISPRS commission I symposium, Paris, 3–6 Jul 2006

Zhang Y, Song C, Band LE, Sun G, Li J (2017) Reanalysis of global terrestrial vegetation trends from MODIS products: browning or greening? Remote Sens Environ 191:145–155

Aerial Platform Reliability for Flood Monitoring Under Various Weather Conditions: A Review

Shazrizil Zakaria, Muhammad Razif Mahadi, Ahmad Fikri Abdullah and Khalina Abdan

Abstract Flood is an annual disaster in Malaysia, especially in the east coast region. Recently, other regions in Malaysia have experienced devastating flood as well. To monitor the flood extent, aerial monitoring approach is considered as one of the best measures. Compared to space borne remote sensing, aerial platforms are more reliable in obtaining real time data with higher spatial resolution. Among the obstacles in using space borne remote sensing approach are cloud coverage and revisit limitations, making it less desirable option for flood monitoring. In this chapter, a review of four types of aerial platforms that perform remote sensing task is presented, namely; rotary wings, fixed wings, blimps and helikites. The main criteria discussed in the review are payload capacity, endurance (flight duration), altitudes, tolerable wind speed, vertical take-off and landing ability, and the ability to perform under adverse weather, such as heavy precipitation and winds. From the findings, there are lack of studies that mentioned about the capability of aerial platform in rough weather conditions. Out of all four types of aerial platforms discussed, helikite is seen to be the most suitable device to fly in adverse weather. Nevertheless, the only drawback in using helikite is that it has mobility issue since it is tethered to the ground. Helikite application is suitable for small area coverage. As for future recommendations, the study to evaluate the helikite's reliability in performing such task has a great opportunity to be pursued further.

S. Zakaria (✉) · M. R. Mahadi · A. F. Abdullah · K. Abdan
Faculty of Engineering, Department of Biological and Agricultural Engineering,
Universiti Putra, Malaysia, 43400 Serdang, Selangor, Malaysia
e-mail: shazrizil@yahoo.com.my

M. R. Mahadi
e-mail: razifman@upm.edu.my

A. F. Abdullah
e-mail: ahmadfikri@upm.edu.my

K. Abdan
e-mail: khalina@upm.edu.my

1 Introduction

Natural disasters bring atrocious effect to the people around the world. In some cases, the physical extent of the disaster may escalate and become complex, causing sudden disruptions which makes it impossible for the affected community to react and respond accordingly. Efforts have been made by various parties to manage disasters in terms of response, damage assessments, and recovery after the disasters end. Recent studies shown that natural disasters, especially flood, will be more frequent because of the climate change effect (Erdelj et al. 2017). Compared to other natural hazard, flood is one of the most destructive natural disasters, which causes severe damages and kills more lives each year (Smith et al. 2014). As one of the measures to identify possible flood event and planning for actions, flood maps are put into use. Flood map, often referred to as flood risk or hazard map, is presented in graphical format that marks the areas with flood history, have potential of being flooded, or considered to be at risk of flooding. Among the features displayed by the maps are information such as flows, water levels, depths, and others. By utilizing flood maps, planning authorities assess useful information, such as to monitor flood direction as well as making flood damage assessment (Auynirundronkool et al. 2012).

As at current, flood mapping is considered important in organizing and coordinating emergency services' response during flood (Giustarini et al. 2015). To date, satellite remote sensing is considered as one of the best tools to acquire flood map information. In many countries, authorities have opted using airborne and satellite imagery to assist plans in the event of floods. However, several factors can cause difficulties to the system, such as shadow and layover effects, as well as cloud covers which complicate the detection of flood water pixels (Tanguy et al. 2017). Regrettably, satellite images are not consistently obtainable in real time. To solve this issue, in situ surveys are favoured in some occasions. Recent technologies in innovations such as unmanned aircraft system (UAS) or unmanned aerial vehicle (UAV) allows us to capture image and assessing the flood extent. Its characteristics such as flexibility, safe, easy to operate, and relatively low cost allow the unmanned aerial platforms to be utilized in disaster events (Xu et al. 2014). Unfortunately, most of small aerial platforms are inappropriate to lift heavy load in massive areas in a short time period. Furthermore, operational distance is only limited to the radio link range within 5 km with the ground control station as mentioned by Gonçalves and Henriques (2015).

Apart from that, studies by Díaz-Vilariño et al. (2016) also highlighted several criteria of limitations in its operational task namely; the altitude, endurance, range of controls, payload capacity, manoeuvrability, tolerable wind speed, and conditions of weather. To date, assessment of the image quality extracted from a non-metric camera mounted on aerial platform board in adverse weather was not one of the considerations (Kedzierski and Wierzbicki 2015). It is important to note that in aerial missions, there are possibilities that the weather and criteria limitations of aerial platforms may affect the data collection's reliability. Thus, the aim of this

study is to review existing unmanned aerial platforms, namely four major types; rotary wing, fixed wing, blimps, and helikite. This review puts consideration in the criteria of limitations and the operability of the platform under different weather conditions during disaster event, especially for flood monitoring.

2 Overview of Flood Monitoring

2.1 Flood in Malaysia

Flood is rather common and considered as the most significant natural hazard in Malaysia in terms of damage it does, occurrence frequency, area affected, flood duration as well as social economic impact (Roosli and Collins 2016). Malaysia has 189 river basins throughout the country, including in Sabah and Sarawak. In Malaysia, studies have shown that at least 3.5 million from its population reside on flood plains which expose them to flood probabilities (Mustaffa et al. 2014). Several factors are identified to be the potential cause of seasonal floods in Malaysia which among others are; increased number of development, changes in water collection and flows, substandard drainage system and most importantly the natural factors such as heavy monsoon rainfall, intense convection rain storms and other local factors (Mohd et al. 2016).

Among the country's worst case of flood history occurred in December 2014, in which a severe flood hit multiple states in the east coast of Malaysia such as Pahang, Terengganu, and Kelantan (Othman et al. 2016). About 3,390 people in Kelantan and 4,209 in Terengganu were temporarily evacuated. Prolonged rain had cause water level rose at most of the rivers beyond safety levees, forcing thousands people to be evacuated on the following day. The aftermath of flooding damages estimated reached up to 1 billion ringgits ($284 million USD). The last time the region experienced disastrous flood was in 2000 where 15 people killed and more than 10,000 people fled their homes (Ruiz Estrada et al. 2017). The affected victims were evacuated from their homes to designated temporary shelter facilities situated on higher grounds in each areas respectively (Aishah et al. 2015). A study by Abu Talib et al. (2018) mentioned that flood occurrence in Malaysia impacted the housing, health, education, and cultural heritage. The incident in Kelantan, for example caused physical destruction with total 14 casualties and temporal displacement of 158,476 victims.

Recent Malaysian Eleventh Plan (2016–2020) has stated three strategies under the sixth chapter; pursuing green growth for sustainability and resilience. The first strategy is by strengthening disaster risk management (DRM), by establishing DRM policy and institutional framework, improving disaster detection and response capacity, incorporating DRM into development plans and creating community awareness. Secondly, improving flood mitigation by generating new investments from flood mitigation projects, enhancing long-term planning and strengthening

flood forecasting and warning systems. Thirdly, enhancing climate change adaptation by developing a national adaptation plan, and strengthening resilience of infrastructure, natural buffers including water and agriculture (Rancangan Malaysia Kesebelas 2015).

The plan also emphasises on strengthening risk management during natural disaster through five phases; prevention, mitigation, preparedness, response and recovery. Other than that, numerous actions including regulations amendments, construct early warning and alert systems for disaster, mitigation structures, awareness campaigns, establish funds for national disaster relief, amend standard operating procedures, as well as collaboration with international organizations have been taken to upgrade emergency preparedness during natural disasters. Even though the Malaysian government already has procedures in place to handle flood disasters, there are still more opportunities to achieve better flood disaster management (Mohammed et al. 2018). Having mentioned that, this allows room of opportunities for research in the area of unmanned aerial platforms' application in disaster management.

2.2 Flood Monitoring and Mapping

In general, flood is caused by intense precipitation, and also known as the predominant cause of disruption in various sector, especially in transportation (Pregnolato et al. 2017). Currently, during the event of flood, the road assessment is made through assumptions of whether the road is either operational or blocked, without being backed up by real time observations. This method causes unnecessary disruptions and delay in resources management during flood. Based on the issue stated above, it is crucial to utilize a real-time flood extent map in managing and monitoring a disaster scenario. With the purpose of aiding the community in emergency planning, flood extent and hazard mapping is currently being developed and put into use, although it is still considered at an early stage (Zhang et al. 2015).

Near-real-time flood maps are essential to organize and synchronize emergency services' response actions during the events of flood (Shen et al. 2015). Chen et al. (2013) highlighted the issues and approaches in disaster management on the applications of UAV systems which are classified in different application domains within three main groups, namely; monitoring, response and forecast. Due to various reasons, current practises in disaster management programmes deploy resources and help from outside of the disaster zone. Unfortunately, this practise is prone to produce delay in disaster management as well as recovery efforts, which may cause a consequent loss of human lives and unnecessary waste of economic resources. Hence, it is deem important to note that mapping out disaster tendency and the availability of resources in advance is crucial to expedite damage recovery and at the same time prevent casualties (Mishra et al. 2012).

In common practise, flood mitigation approaches and planning are conducted based on the assessment of the flood occurrences in terms of location, magnitude

and distribution. Xiao et al. (2017) mentioned that flood hazard and risk analysis are mainly carried out with hydraulic model that simulate flood inundation extent, water depth and velocity. However, these modelling were often carried out from either space borne or satellite remote sensing data in testing condition, which means the data retrieved from the study was not real time and on certain circumstances, the data was affected by cloud covers.

Additionally, to gain a better accuracy output, flood modelling and flood monitoring should be carried out simultaneously (Tuna et al. 2012). This is due to the fact that flood modelling requires numerous amount of data and flood inventories such as extensive historical rainfall data, water level data, discharges and return period data, and others (Rollason et al. 2018). In most cases, insufficient amount of previous data (discharge and water level) becomes the prime barriers in predicting the water surface profile for water catchments. Apart from that, limited amount and the unmanaged conditions of some gauging stations along the river also contribute to the insufficient data collection of flood modelling (Mohammed et al. 2011). Hence, it is explicit to note that in order to achieve an ideal flood modelling, it requires integration of real time monitoring to gain accurate and reliable results.

It is a known fact that flood modelling approach may simulate and generate the flood extent map. To obtain more reliable and accurate results, the collected data must be combined with real time monitoring of flood. The quantification of dynamic and previously immeasurable hydraulic phenomena is now made possible through aerial image acquisition of flood occurrences. However, the possibility of this approach to provide dependable information on the hydraulic conditions during dynamic and high-energy flash floods has yet to be explored (Perks et al. 2016). In reality, it is insufficient to monitor flood events by relying solely on conventional rainfall stations and river water level stations because flood develop at space and time scales that conventional measurement methods by using samples of precipitation and river discharges are unable to be conducted effectively (Zoccatelli et al. 2010).

In view of that problem, hence, it is significant to have a more creative solution in flood monitoring such as aerial monitoring in order to obtain the flood extent map with time-step intervals, predict damages, and improve decision-making by emergency responders. To obtain aerial monitoring, aerial platform or UAVs can be utilized to carry small sensors for data acquisitions, which raises question of which aerial platforms are the most suitable for a real time flood monitoring under different weather conditions.

2.3 Unmanned Aerial Platforms

UAV or UAS is an unmanned aerial platform in the form of an aircraft that operates without a human pilot on board. The vehicle is controlled either autonomously or by an operator on the ground which enables it to be used to conduct aerial missions (Liu et al. 2014). Research by Visser et al. (2013) indicated that the UAV were

initially designed to regulate military communication for tasks such as spying and message deliveries. However, over the years, the UAV application has been gradually shifted to common usage such as to conduct researches as well as applications by civilians. Among popular applications of UAV are in the area of mapping, monitoring environmental changes, disaster response, exploration of resources, and others (Ludeno et al. 2018). UAV applications are rather favoured by many, compared to other flying vehicles and satellite remote sensing technology as they have two advantages to capture aerial photographs, namely; low cost and high mobility (Xiongkui et al. 2017).

In spite of that, UAV applications also have a number of environmental restrictions on their usage due to low flight stability especially under extreme weather conditions (Paneque-Gálvez et al. 2014). Analysing data collected through UAS or UAV can be meticulously conducted by professionals while at the same time reducing operational costs and safety, when paired with visual and audio recording, photography, or multi spectral imaging. The usage of UAS or UAV is also well known for its benefit in safety, economy and operational efficiency to carry out various kinds of surveying as well as monitoring applications (Rakha and Gorodetsky 2018).

Specifically, the unmanned aerial platforms are important because they have the capability to generate the information promptly whereby the data can be immediately conveyed to the coordination team, highlight the local assessment, effectively detect blocked areas as well as identification of secondary disasters, in which all the aforementioned benefits may help in increasing logistic efficiency during the disaster (Silva et al. 2017). In order to facilitate the need of the UAV in flood events, small sized UAVs are found to be more reliable in providing the researchers different views of the situation and also much easier method for remote sensing, especially if it is to be used in monitoring (Chao et al. 2010).

Additionally, the usage of UAV consumes less time than other techniques for data collection and therefore reduce the total costs (Martínez-carricondo et al. 2018). Apart from that, UAV imagery produces better results in terms of resolution and accuracy compared to satellite-derived products. Also, UAVs are found to be useful in situations where the use of other techniques to acquire data is unsafe (Agüera-vega et al. 2018).

It is also important to note that accurate imagery of the environment is essential to applications such as topographic modelling, mapping, environmental monitoring, and others. Recent advances in hardware and software technology development allows for more accurate results. The advantages of the new technology developments are utilization of low-cost digital cameras and navigation systems, but at the same time providing high scale, time efficient and low cost facility in aerial surveying, mapping and monitoring (Ajayi et al. 2018).

3   Aerial Platform Reviews

3.1   Rotary Wings

Rotary wings have a number of rotors installed on its body. For instance, a single rotor helicopter is a model with one rotor on top and one on its tail, while quad copter, hexacopter, octocopters are multi-rotors that are propelled by four, six, and eight rotors respectively (Mogili and Deepak 2018). Rotary wings are known for vertical take-off and landing (VTOL) capability, hovering and low speed manoeuvre. Since, they do not require a runway or any heavy facilities, the rotary wings are more preferred compared to fixed wings (Basset et al. 2014).

Furthermore, a rotary wing is capable of flying in windy conditions up to 50 kmh^{-1}. Not only it can perform static flights, which is appropriate to be used in monitoring process due to the hovering ability (Nonami et al. 2010), but it can also mount various camera instruments for aerial monitoring task (Delacourt et al. 2009). Over the years, different types of rotary wing UAV have been developed for photogrammetric data acquisition and topographic modelling (Coppa et al. 2009).

Most of the times, rotary wing UAVs can demonstrate slower cruising speed and relatively shorter flight durations (up to 50 min). The capability to hover at one fixed position enable them to hold a steady field of view for extensive time frame. Many organizations view the rotary wings as recommended device for monitoring because of their capability to circumnavigate in various angles without the necessity for a runaway in taking off and landing protocols (Brouwer et al. 2014). However, duration of rotary wings flight depends critically on both battery and payload weight. According to Uysal et al. (2015), the heavier the payload, the quicker the battery drains out. Apart from that, weather conditions such as strong winds also affect the endurance of the flights, which also cause the flight time to be shorten.

Daakir et al. (2017) presented a system consisting of a single-frequency GPS receiver coupled with a light photogrammetric quality camera embedded in a rotary wing UAV, which aimed to obtain high quality data for metrology applications. The sensors used are specifically designed to be used for close-range aerial image acquisition. Lever-arm calibration and time synchronization are performed on timely basis to maintain accuracy. The study also showed that an accuracy of a few centimetres could be reached by using the system which combined the usage of low-cost UAV and GPS module coupled with the home-made camera.

Connor et al. (2018) conducted work on aerial photogrammetry obtained using a rotary wing UAV which flew at low altitudes, merged with ground-based radiation mapping data acquired at an interim storage facility for wastes removal as part of the large-scale Fukushima clean-up program. The investigation was aimed to assess the extent of the remediation program at a specific site that still has the radiation contaminants. Based on the result, the researchers discover a powerful graphic confirming the elevated radiological intensity exists at the site containing the waste bags. The whole survey consumed less than one hour, and was subsequently post-processed using graphical information software to obtain the renderings. The

Table 1 Examples of rotary wing UAV

Model	Fazer R G2	DJI Inspire 2	DJI Matrice 200	DJI Matrice 600
No. of motors	1 (Single)	4 (Quad)	4 (Quad)	6 (Hexa)
Wingspan	3.15 m	0.63 m	0.887 m	1.668 m
Overall length	3.66 m	0.63 m	0.880 m	1.518 m
Cruise speed	70–80 kmh^{-1}	70–80 kmh^{-1}	70–80 kmh^{-1}	50–60 kmh^{-1}
Endurance	60 min (fuel)	27 min (battery)	24 min (battery)	18 min (battery)
Maximum altitude	2,800 m	4,500 m	3,000 m	2,500 m
Payload	35.0 kg	0.7 kg	1.6 kg	5.0 kg
Wind tolerable	20 ms^{-1}	10 ms^{-1}	12 ms^{-1}	8 ms^{-1}
Launch	Vertical	Vertical	Vertical	Vertical
Landing	Vertical	Vertical	Vertical	Vertical
Range of flight	30,000 m	7,000 m	7,000 m	5,000 m
Cost	$120,450	$2,999	$9,000	$5,500

conclusions of their study also deduced that the present monitoring methods of the storage facilities could be upgraded through the integration of UAVs within the existing standard protocol.

In general, integrated monitoring approach is proven to be able to provide a spatially detailed assessment by combining high resolution UAV remote sensing with rotary wing technology based on its ability to hover and agile manoeuvre (Filippo et al. 2017). Some examples of rotary wing UAVs are shown in Table 1.

3.2 Fixed Wings

Fixed wing UAV is very similar to a miniature airplane. This type of UAV has been known for its capability to fly for long durations and able to accelerate the speed up to 80 kmh^{-1}. With the combination of high speed and long endurance, fixed wing is a definite choice for photogrammetric mapping task in larger areas at high spatial resolution (Brouwer et al. 2014). According to previous studies, fixed wing UAVs have flown over cities and wetlands in order to assess damage level after natural disasters like earthquakes, hurricanes, and floods. As an example, a predator drone successfully produced infrared imagery which then allowed officials and relevant authorities to execute reasonable decisions in a disaster event as highlighted by Conniff and McClaran (2011).

High-resolution fixed wing UAV imagery was proposed by Feng et al. (2015) for urban flood mapping as the fixed wing works as an excellent platform for urban flood mapping which ensures accurate extraction results in dense urban landscapes during flood event. Technically, UAVs operate with the concept that their fixed wings use forward airspeed for lift generation. In cases of long flights duration, fixed wing is highly preferred as it is more energy efficient, but on the other hand, it

is also important to note that this concept does not permit hovering in the air (Gabrlik 2015).

Nowadays, fixed wings are commonly used for mapping, search, and rescue applications which need accurate tracking of inertial trajectories capabilities. Nevertheless, fixed wing platforms are sensitive to wind conditions that are prone to influence the vehicle inertial track. Based on this, it is possible that the trajectory tracking capability of the platform to be jeopardized, in cases where the embedded control system is not appointed as a wind disturbances (Brezoescu et al. 2015). Furthermore, unlike rotary wings, fixed wings require landing strips and trained pilots to operate the platform which necessitate the consideration of a spacious runaways.

According to Fan et al. (2017), even with autonomous flight features, it is still obligatory for fixed wings to have experts in landing and take-off since fixed wings are incapable to perform the vertical take-off and landing (VTOL). To date, the advantages of fixed wing platforms are only high lift-to-drag ratio, fuel-efficient flying, and high-speed flying, which make them a reasonable choice in aerial mapping. The obligations of having long runway and trained pilots to conduct take-off and landing, however, have turned the fixed wings as less recommendable option compared to rotary wings (Hong et al. 2013).

A study by Turner et al. (2016) have used a coastal engineering application of fixed wing UAV to represent the practical use and potential benefits of the surveying technology. In the span of two years of research, rapid post-storm deployment of UAV surveying was successfully integrated into an established four decades coastal monitoring program at Narrabeen Beach, Australia. Due to this, the scope of their research was extended to include detailed measurements of dune and beach surface erosion along the 3.5 km embayment at a spatial scale and temporal resolution that were unfeasible during previous research.

The survey data collected in that study were obtained using a fixed-wing, off-the-shelf, RTK-GPS UAV (SenseFly eBee-RTK) that was initially manufactured commercially for the professional survey purpose. The feature of the fixed wing was indeed applicable for the purpose of surveying with a wingspan of precisely below 1 m, weightage of 700 g, approximately 40 min flight-time per battery that enables coverage area of 2 km^2 during low wind conditions, or lesser areas in stronger wind condition of 45 kmh^{-1}. At present, the survey-grade UAV equipment are readily available off-the-shelf, complete with data processing and analysis tools for practicing coastal engineers, managers and researchers.

Apart from the regulatory constraints that determine their use, UAVs bring forth efficient and cost-effective survey tool for topographic mapping as well as measurement in the coastal zone. It is also sufficient to mention that the availability of off-the-shelf UAV survey systems combined with high-precision RTK-GPS positioning decreases the demand for any supplementary ground surveying equipment.

Other study by Iersel et al. (2018) aimed to assess multi-temporal high spatial-resolution imagery performance of the recorded dynamics in floodplain vegetation height and greenness which was collected with a UAV. In the study, field reference data on vegetation height were collected six times in a year at 28

field plots situated at a single flood plain along the Waal River, the main distributary of the Rhine River, Netherlands. The results proved high potential of using UAV-borne sensors in order to increase the classification accuracy of low floodplain vegetation along the area of the framework of floodplain mapping.

Fixed wing UAV has provided the community with a flexible, variety remote sensing tool with a wide range of payloads and applications. Of late, fixed wing UAV systems carry RGB, colour infrared, thermal infrared, spectrometers as well as LiDAR systems. Impressively, technical developments are changing rapidly which contribute to more diverse and wider coverage of UAV applications due to its cruising ability (Hemmelder et al. 2018). Table 2 shows some examples of other types of fixed wing UAV.

3.3 Blimps

Blimps or dirigibles are a form of light air vehicles which started as hot air balloons which later evolved to using lifting gas, tethered and un-tethered aerostats, airships, and novel buoyancy air vehicles in step with the advancement of new materials and technologies. Among the main advantage of blimps is that it is low in cost and energy consumption. Blimps have the capability to hover for a long period of time which cause their refuelling and operating costs to be much lower compared to conventional fixed-wing or rotary wings (Liao and Pasternak 2009).

In earlier days, low-level aerial photography was acquired using various kinds of unmanned platforms including small blimps (Tonkin et al. 2014). A blimp's lift generation mechanism uses light lifting gas which makes it different from other aerial platforms. Unfortunately, due to its frail structure and aerodynamic features, a blimp is incapable of withstanding strong winds during high wind condition, compared to other unmanned aerial platforms (Li et al. 2011).

Table 2 Examples of fixed wing UAV

Model	F-3	AIbird KC3000	F-5	Chilong
Wingspan	1.7 m	3.1 m	4.6 m	3.1 m
Overall length	0.9 m	1.9 m	2.8 m	2.1 m
Cruise speed	70–90 kmh^{-1}	110 kmh^{-1}	90 kmh^{-1}	90 kmh^{-1}
Endurance	90 min (battery)	8–10 h (fuel)	6 h (fuel)	4 h (fuel)
Maximum altitude	3,000 m	4,000 m	5,000 m	3,000 m
Payload	1.5 kg	2.0 kg	5.0 kg	5.0 kg
Wind tolerable	10 ms^{-1}	12 ms^{-1}	14 ms^{-1}	12 ms^{-1}
Launch	Catapult	Runaway	Runaway	Runaway
Landing	Belly/Catch Net	Runaway	Runaway	Runaway
Range of flight	3,000 m	60,000 m	30,000 m	30,000 m
Cost	$35,000	$47,000	$70,000	$60,000

Blimps float with the help of helium (gas with lower densities than air). The propulsion motor placed in separate nacelles in their gondola enables them to move. In order to allow asymmetric thrust to be applied for manoeuvring, the propulsion motor is mounted towards the sides of the envelope, located away from the centre line gondola (Abdul Kadir et al. 2012). Blimps can take off and land vertically without using runways (Al-Jarrah et al. 2013).

As for the dimension of the device, it is interesting to note that blimps come in various sizes; small ones for indoors applications, and large ones for outdoors applications. Blimp is also known to have lower resistance to wind. It is also relatively easy to be operated due to the reason that it operates with low flight speed as it is always in floating condition when filled with helium gas. Comparatively, the blimp is considered far more user friendly than any other types of UAV. The payload capacity of a blimp is however quite small depending on its size (Nitta et al. 2017).

Blimps are rather popularly used in a number of environmental remote sensing applications involving information collecting and interpreting process on land, oceans and the atmosphere. Among the example of the successful usage are; remote sensing towards the prediction of weather, tracking go of hurricanes, inspection of coastal dynamics, discoveries of pollutants, as well as mapping of coastal land that include forests, agriculture, tidal wetlands, and urban areas (Milstein 2011).

Conventionally, satellites are commonly used for remote sensing while aircrafts, in order to obtain similar observations are operated with human crew. However, both alternatives are not cost effective as satellites require a huge investment while manning aircrafts with human crew also adds to the initial cost of the project. Regrettably, blimps also have problems during flight, since they are very sensitive to winds (large problems arise with wind speeds higher than 10 kmh^{-1}). The best suitable application of small blimps is mainly for indoors usage. Some examples of blimps are shown in Table 3.

3.4   Helikites

Helikite is a device associating a combination of helium air balloon with kite as its wing which makes them lighter than any other air devices (Klemas 2011). Helium gas allows the balloon to launch easily even in windless weather conditions, while the kite feature works effectively in the presence of wind. To operate the device, it must be first lifted up in the air to achieve higher altitudes than the pure helium lift. Accelerating wind speed improves the helikite's lifting ability. Next, the wings which are attached to the balloon counteract any unstable characteristic of balloons and blimps in windy conditions, which consequently stabilize the helikite (Verhoeven et al. 2009).

Among the reasons why helikite is preferred to be used is because of its ease in lifting process since it can effortlessly carry payload in windless conditions. The reason behind the increment in payload capacity is the stabilization of the balloon

Table 3 Examples of blimps

Model	6 m RC Blimp	7 m RC Blimp	10 m RC Blimp	12 m RC Blimp
Wingspan	1.7 m	2.0 m	2.2 m	2.1 m
Overall length	6.0 m	7.0 m	10.0 m	12.0 m
Cruise speed	50 kmh^{-1}	50 kmh^{-1}	50 kmh^{-1}	60 kmh^{-1}
Endurance	60 min (battery)	60 min (battery)	60 min (battery)	70 min (battery)
Max altitude	100 m	150 m	300 m	400 m
Payload	2.0 kg	2.5 kg	5.0 kg	6.0 kg
Wind tolerable	5 ms^{-1}	5 ms^{-1}	7 ms^{-1}	10 ms^{-1}
Launch	VTOL	VTOL	VTOL	VTOL
Landing	VTOL	VTOL	VTOL	VTOL
Range of flight	100 m	150 m	300 m	400 m
Cost	$7,200	$8,800	$14,500	$35,000

by the kite section in windy conditions (Klemas 2013). On top of that, the cost of the helikite is considered low, which makes it one of the most cost effective UAV for any suitable types of aerial monitoring. The helikite is best known for its capacity in usage during multi-altitude and has high spatial resolution system (Marris 2013). For an example, the standard helikite is capable of flying up to an altitude of 1.2 km and at the same time carries a load of up to 5 kg. The latest invention of helikites comes with a diameter of 3 m, which makes them among the lightest aircraft balloons (Kushida et al. 2009). That being said, the stability of the helikite depends on the kite section which constantly prevents the helikite from getting bounced especially during windy conditions.

Helikites are mostly chosen for short time site-based monitoring because it can provide quick response to events and also due to its capability to acquire high temporal resolution imagery whereby the system is able to record images within desired time span (for example one day versus one week). The combination of helium balloon with non-metric digital singe reflex camera and additional surveying methods allows low altitude photogrammetry to be efficiently produced, resulting in the high quality outcome in mapping the selected small and medium size areas (less than 2.5 km^2) of interest (Mozas-Calvache et al. 2012). Conventionally, the images obtained using helikite often comes with irregular geometry, which has always been the main challenge. This is caused by wind effect and lack of flight control which generates high imprecision in camera sensors that cause the block pattern with irregular image.

One of the reasons why helikite is mostly favoured is because it can be modified according to required specifications. Sensors that can be fitted onto the helikite includes thermal infrared camera, digital camera, inertial measurement unit, GPS equipment and various other sophisticated equipment (Pereira et al. 2009). On top of the benefits listed above, it is also relatively straightforward and fast to deploy the helikite. Among successful application conducted using the helikite was the mapping of coastal plumes using temporal and spatial resolutions of the obtained

images. The images were utilized to analyse and study of the evolution of coastal plumes and wetland changes (Lechner et al. 2012).

White and Madsen (2016) presented a high-resolution aerial images using a helikite at 100 m altitude which were used to develop a detailed flooding model. The research took place at North Inlet estuary, South Carolina and derived a spatially comprehensive map of ecological zones at the headwaters of a small tidal marsh creek situated at a forest marsh boundary. In order to identify ecological zones, the researchers constructed photo mosaics obtained from helikite imagery over a 150 × 100 m area using automated, maximum likelihood classification. At the same time, by using imagery assessed by helikite and GPS, they also developed a digital terrain model with ±2 cm overall vertical accuracy, mainly from waterlines at known tide height. These methods are proven to be cost efficient and simple implementation methods for studying processes that take place in marsh where accessibility is strenuous. It is essential to note that their study have proven that balloon aerial photography is indeed an effective and inexpensive way to measure important time dependent processes in marshes such as flood that are currently understudied due inaccessible field conditions.

A study conducted by Al-Halbouni et al. (2017) presented the first low altitude (<150 m above ground) aerial photogrammetric survey using a helikite balloon at the sinkhole area of Ghor Al-Haditha, Jordan. The survey provided qualitative and quantitative analysis of a new, high resolution digital surface model (5 cm px^{-1}) and orthophoto of the area (2.1 km^2). The findings show that it is crucially important to rely on correct georeferencing and reliable subsequent DSM analysis for equal dispersed distribution of ground control points in the survey area. It is important to note that the high resolution DSM and geomorphological analysis are highly relevant for subsidence and sinkhole hazard as well as precursor assessment along the eastern coast of Dead Sea. Even though helikites are tethered to the ground, it is sufficient to mention that helikites satisfactorily assist in data acquisition for long term period monitoring due to the fact that they do not require

Table 4 Examples of helikite

Model	6 m^3 Skyhook	7 m^3 Skyhook	9 m^3 Skyhook	11 m^3 Skyhook
Wingspan	2.14 m	2.44 m	2.74 m	2.90 m
Overall length	3.35 m	3.5 m	3.57 m	3.66 m
Cruise speed	Tethered via dyneema cable from the ground			
Endurance	Depends on sensors and gimbal battery only			
Max altitude	1,500 m	1,600 m	1,700 m	1,800 m
Payload	2.7 kg	3.2 kg	4.0 kg	5.5 kg
Wind tolerable	17 ms^{-1}	17.89 ms^{-1}	18.77 ms^{-1}	17.89 ms^{-1}
Launch	VTOL	VTOL	VTOL	VTOL
Landing	VTOL	VTOL	VTOL	VTOL
Range of flight	Stationary at one hovering point (due to tethering)			
Cost	$2,500	$2,555	$3,000	$3,450

motorized power to lift compared to fixed wing and rotary wings, thus making it a high endurance and most suitable platform for monitoring. Table 4 shows some examples of helikites.

4 Aerial Platform Selection Criteria

From the overview of the literature, the comparison between UAVs are made and shown in the Table 5.

Depending on their sizes, most of the aerial platforms are capable to carry high capacity of payload. In terms of coverage area, fixed wing UAVs present the best option since they are equipped with greater cruising speed and endurance, allowing them to stay longer in the air and travel further for a data acquisition mission. Other types of UAV such as rotary wings and blimps have short durations of flying endurance and made worse with limited lifespan of batteries. Helikite however, has high endurance to fly as it uses helium as its lifting force which allows it to stay afloat longer compared to fixed wings UAV. From the finding, it is noted that most aerial platforms are incapable to operate in various weather condition as they have low tolerable wind speed resistance. Helikites however, has the all-weather operation capability.

Previous researches showed that fixed wing UAV has rigid wing constructed with predetermined air foil that allows the device to fly through the airlift concept, which happens due to the UAV forward movement. They have a simpler structure compared to rotary wings, requires uncomplicated repair work and maintenance process thus enabling fixed wing user to possess higher operational time with lower

Table 5 Comparison between aerial platform reviewed

Criteria	Rotary wings	Fixed wings	Blimps	Helikite
High payload capacity	√	√	√	√
Wide area coverage		√		
Extreme endurance		√		√
High altitude	√	√		√
All weather operation				√
Autonomous operation	√	√	√	
Easy operation	√		√	√
VTOL ability	√		√	√
Inexpensive cost	√		√	√
High wind tolerance				√
Suitable applications	Inspection Detection Surveying Mapping	Surveying Mapping	Monitoring Surveillance Inspection Detection	Monitoring Surveillance

operational cost than rotary wing user. Other than that, the simple structure of fixed wing design has proven to provide efficient aerodynamics, thus giving it long flight duration advantage which at the same time making it possible to execute surveying and mapping tasks on larger area. With that benefit, fixed wing is proven to be more suitable for aerial mapping than rotary wing UAV. However, it is also essential to note that fixed wings performance is restricted on its dependency on a runway or a launcher to facilitate take-off and landing, which eventually affect the payload weight that can be carried by the fixed wing UAV.

On the other hand, rotary wing does not require forward thrust in order to initiate the movement of the flight, although technically the rotary wing functionality is similar to the fixed wing. Instead, rotary wing flight movement is initiated by their rotor blades' constant rotation that creates the air movement over their air foil which generates the lift. Rotary wing UAV has more complicated mechanical structures than the fixed wing UAV. Furthermore, the rotor copter is known to have lower range of flight with most of them only have at most several minutes' flight time, depending on the load capacity. In spite of that, rotary wings have advantage on their capability for VTOL and landing protocols, as well as the ability in agile manoeuvring and hovering ability. Due to the fact that rotor copter is able to maintain visual on a specified target for a long time, they are highly recommended for conducting local inspection tasks. Moreover, the VTOL procedures was intentionally developed to solve problem faced by the fixed wing UAVs as they require runaway or launcher for take-off.

Blimp is known for its low-flying, short-endurance and slow moving feature, which is seemly to accommodate a monitoring platform at a target location intended for monitoring and surveillance. Among the advantages of using blimps is it does not require excess fuel or battery like other types of aircrafts to fly since it is operated using helium gas, which is lighter than air thus enabling the blimp to float using the buoyant force. The shape of the blimp is also proven to be the most economical and can be efficiently used because of its light condition, appropriate for wind conditions less than 10 kmh^{-1}. Due to the fact that the unmanned blimps cost less, they are more popular to be operated. In commercial use, the most used types are blimps with small-frontal aerial photography. The payload capacities depend on the size and type of the blimps. In terms of its stabilization during flights, it is achieved by using four rigid tail fins, and also with the help of multiple attachment points positioned along the keel, which helps to allow the fastening of the camera system weight up to 1.5 kilograms.

Helikite can easily carry payload in windless conditions. The functionality of helikite in windy conditions is based on the stabilization of the balloon by the kite section, which increases its payload capacity. Among the obvious benefit of helikites is low in price, making it a cost effective platform for aerial monitoring. Helikite is known for its durability since it is able to stay in the air for several weeks at a time. Recently, helikites are highly sought after in monitoring projects since they operate in various kind of severe weather conditions, be it windy, stormy or heavy rains. Further to that, helikites are also able to reduce camera shaking because their platforms are more stable. The position of steady camera is critical

during environmental monitoring because stability enhances quality and avoid the loss of expensive digital cameras as well as other equipment from falling. Apparently there is not much requirement for technical knowledge to operate helikites as it is known to be operable within minutes of training. Besides, safety precautions in using the helikites are quite minimal. As for the wind speed performance, while most UAV are only able to fly in windy conditions at 14 ms^{-1}, helikites can fly at up to 18 ms^{-1} wind condition.

5   Conclusions

The use of aerial platform technology coupled with remote sensors made it possible to achieve many tasks. The type of task or applications that suitable for an aerial mission is highly depends on the limitation criteria as been highlighted in this review. The reviews discussed in this paper also indicate that most of the studies did not investigate the capability and potentiality of aerial platforms specifically their performance under various weather conditions, such as heavy rainfall and windy condition. Thus it is important to highlight that it provides a gap to be explored in terms of which instrument or device is capable to be operated under such circumstances to acquire real time data within certain amount of period continuously. From the findings stated in this paper, the opportunity to explore the type of aerial platform that can perform under various weather conditions does exist and requires attention. Based on the results, the helikite is found to be suitable for the task of real time monitoring in various weather conditions due to its capability to operate under rough situations. However, it is also essential to note that helikite lacks in mobility and may only cover small area during its operation, but this would give higher spatial resolution and temporal data in a local area prone to the flood event. For future works, this research will seek on testing the reliability of helikite to perform in adverse weather condition.

References

Abdul Kadir H, Arshad MR, Husaini AB (2012) Modeling and control analysis of URRG monohull blimp. Proced Eng 41:216–223
Abu Talib IF, Takim R, Mohammad MF, Hassan PF (2018) Community empowerment through rehabilitation and reconstruction in social sector of Kuala Krai, Kelantan, Malaysia. Proced Eng 212:294–301

Agüera-vega F, Carvajal-ramírez F, Martínez-carricondo P, López JS, Mesas-carrascosa FJ, García-ferrer A, Pérez-porras FJ (2018) Reconstruction of extreme topography from UAV structure from motion photogrammetry. Measurement 121:127–138

Aishah TS, Wok S, Maznina A, Manaf A, Ismail R (2015) Exploring the use of social media during the 2014 flood in Malaysia. Proced Soc Behav Sci 211:931–937

Ajayi OG, Palmer M, Salubi AA (2018) Modelling farmland topography for suitable site selection of dam construction using unmanned aerial vehicle (UAV) photogrammetry. Remote Sens Appl Soc Environ 11:220–230

Al-Halbouni D, Holohan EP, Saberi L, Alrshdan H, Sawarieh A, Closson D, Walter T, Dahm T (2017) Sinkholes, subsidence and subrosion on the eastern shore of the Dead Sea as revealed by a close-range photogrammetric survey. Geomorphology 285:305–324

Al-Jarrah R, Jellal RA, Roth H (2013) Blimp based on embedded computer vision and fuzzy control for following ground vehicles. In: 3rd IFAC symposium on telematics applications, Seoul, 11–13 November 2013

Auynirundronkool K, Chen N, Peng C, Yang C, Gong J, Silapathong C (2012) Flood detection and mapping of the Thailand central plain using RADARSAT and MODIS under a sensor web environment. Int J Appl Earth Observ Geoinf 14:245–255

Basset P, Tremolet A, Lefebvre T (2014) Rotary wing UAV pre-sizing: past and present methodological approaches at Onera. Aerospace Lab(8):1–12

Brezoescu A, Lozano R, Castillo P (2015) Lyapunov-based trajectory tracking controller for a fixed wing unmanned aerial vehicle in the presence of wind. Int J Adapt Control Signal Process 29:372–384

Brouwer R, Schipper M, Rynne P, Graham F, Reniers J, MacMahan J (2014) Surfzone monitoring using rotary wing unmanned aerial vehicles. J Atmos Ocean Technol 32:855–863

Chao H, Cao Y, Chen Y (2010) Autopilots for small unmanned aerial vehicles: a survey. Int J Control Autom Syst 8(1):36–44

Chen D, Liu Z, Wang L, Dou M, Chen J, Li H (2013) Natural disaster monitoring with wireless sensor networks: A case study of data-intensive applications upon low-cost scalable systems. Mobile Netw Appl 18(5):651–663

Conniff R, McClaran R (2011) Drones are ready for takeoff. https://www.smithsonianmag.com/science-nature/drones-are-ready-for-takeoff-160062162/. Accessed 12 July 2017

Connor DT, Martin PG, Smith NT, Payne L, Hutton C, Payton OD, Yamashiki Y, Scott TB (2018) Application of airborne photogrammetry for the visualisation and assessment of contamination migration arising from a Fukushima waste storage facility. Environ Pollut 234:610–619

Coppa U, Guarnieri A, Pirotti F, Vettore A (2009) Accuracy enhancement of unmanned helicopter positioning with low-cost system. Appl Geomat 1(3):85–95

Daakir M, Pierrot-deseilligny M, Bosser P, Pichard F, Thom C, Rabot Y, Martin O (2017) Lightweight UAV with on-board photogrammetry and single-frequency GPS positioning for metrology applications. ISPRS J Photogramm Remote Sens 127:115–126

Delacourt C, Allemand P, Grandjean P, Deschamps A, Ammann J, Cuq V, Suanez S (2009) DRELIO: an unmanned helicopter for imaging coastal areas. J Coast Res 56:1489–1493

Díaz-Vilariño L, González-Jorge H, Martínez-Sánchez J, Bueno M, Arias P (2016) Determining the limits of unmanned aerial photogrammetry for the evaluation of road runoff. Measurement J Int Measurement Confed 85:132–141

Erdelj M, Król M, Natalizio E (2017) Wireless sensor networks and multi-UAV systems for natural disaster management. Comput Netw 124:72–86

Fan YM, Ding M, Cao YF (2017) Vision algorithms for fixed-wing unmanned aerial vehicle landing system. Sci China Technol Sci 60(3):434–443

Feng Q, Liu J, Gong J (2015) Urban flood mapping based on unmanned aerial vehicle remote sensing and random forest classifier: a case of Yuyao, China. Water 7:1437–1455

Filippo S, Gennaro D, Matese A, Gioli B, Toscano P, Zaldei A, Palliotti A, Genesio L (2017) Multisensor approach to assess vineyard thermal dynamics combining high- resolution unmanned aerial vehicle (UAV) remote sensing and wireless sensor network (WSN) proximal sensing. Sci Hortic 221:83–87

Gabrlik P (2015) The use of direct georeferencing in aerial photogrammetry with micro UAV. IFAC-PapersOnLine 48(4):380–385

Giustarini L, Vernieuwe H, Verwaeren J, Chini M, Hostache R, Matgen P, Verhoest NEC, de Baets B (2015) Accounting for image uncertainty in SAR-based flood mapping. Int J Appl Earth Observ Geoinf 34:70–77

Gonçalves JA, Henriques R (2015) UAV photogrammetry for topographic monitoring of coastal areas. ISPRS J Photogramm Remote Sens 104:101–111

Hemmelder S, Marra W, Markies H, Jong SM (2018) Monitoring river morphology and bank erosion using UAV imagery—A case study of the river Buëch, Hautes-Alpes, France. Int J Appl Earth Obs Geoinf 73:428–437

Hong S, Jeong J, Kim S, Suk J, Jung, JI (2013) Longitudinal flight dynamics of a single tilt-wing unmanned aerial vehicle. In: 19th IFAC symposium on automatic control in aerospace, Würzburg, 2–6 September 2013

Iersel W, Straatsma M, Addink E, Middelkoop H (2018) Monitoring height and greenness of non-woody floodplain vegetation with UAV time series. ISPRS J Photogramm Remote Sens 141:112–123

Kedzierski M, Wierzbicki D (2015) Radiometric quality assessment of images acquired by UAV's in various lighting and weather conditions. Measurement J Int Measurement Confed 76:156–169

Klemas V (2011) Remote sensing of wetlands: Case studies comparing practical techniques. J Coast Res 27(3):418–427

Klemas V (2013) Airborne remote sensing of coastal features and processes: an overview. J Coast Res 29(2):239–255

Kushida K, Yoshino K, Nagano T, Ishida T (2009) Automated 3D forest surface model extraction from balloon stereo photographs. Photogramm Eng Remote Sens 75(1):25–35

Lechner AM, Fletcher A, Johansen K, Erskine P (2012) Characterising upland swamps using object-based classification methods and hyper-spatial resolution imagery derived from an unmanned aerial vehicle. In: ISPRS annals of the photogrammetry, remote sensing and spatial information sciences, Melbourne, 25 August–01 September 2012

Li Y, Nahon M, Sharf I (2011) Airship dynamics modeling: A literature review. Prog Aerosp Sci 47:217–239

Liao L, Pasternak I (2009) A review of airship structural research and development. Prog Aerosp Sci 45:83–96

Liu P, Chen AY, Huang YN, Han JY, Lai JS, Kang SC, Wu TH, Wen MC, Tsai MH (2014) A review of rotorcraft unmanned aerial vehicle (UAV) developments and applications in civil engineering. Smart Struct Syst 13(6):1065–1094

Ludeno G, Catapano I, Renga A, Rodi A, Fasano G, Soldovieri F (2018) Assessment of a micro-UAV system for microwave tomography radar imaging. Remote Sens Environ 212:90–102

Marris E (2013) Fly, and bring me data: Unmanned aerial vehicles are poised to take off as popular tools for scientific research. Nature 498:156–158

Martínez-carricondo P, Agüera-vega F, Carvajal-ramírez F, Mesas-carrascosa F, García-ferrer A, Pérez-porras F (2018) Assessment of UAV-photogrammetric mapping accuracy based on variation of ground control points. Int J Appl Earth Obs Geoinf 72:1–10

Milstein M (2011) Unmanned aerial vehicles redefine the term non stop flight. https://www.airspacemag.com/flight-today/distance-runners-41727425/. Accessed 27 November 2017

Mishra V, Fuloria S, Bisht SS (2012) Enhancing disaster management by mapping disaster proneness and preparedness. Disasters 36(3):382–397

Mogili UR, Deepak BBVL (2018) Review on application of drone systems in precision agriculture. Proced Comput Sci 133:502–509

Mohammed N, Edwards R, Gale A (2018) Optimisation of flooding recovery for Malaysian universities. Proced Eng 212:356–362

Mohammed TA, Al-Hassoun S, Ghazali AH (2011) Prediction of flood levels along a stretch of the langat river with insufficient hydrological data. Pertanika J Sci Technol 19(2):237–248

Mohd T, Saraf MHM, Pin SFBC, Hasbullah MN (2016) Designing the invention house assessment form for Kuala Krai, Malaysia. Proced Social Behav Sci 234:317–325

Mozas-Calvache AT, Pérez-García JL, Cardenal-Escarcena FJ, Mata-Castro E, Delgado-García J (2012) Method for photogrammetric surveying of archaeological sites with light aerial platforms. J Archaeol Sci 39(2):521–530

Mustaffa CS, Marzuki NA, Ariffin MT, Salleh NA, Rahaman NH (2014) Relationship between social support, impression management and well-being among flood victims in Malaysia. Proced Soc Behav Sci 155:197–202

Nitta Y, Inai S, Matsumura K, Ishida M, Onai T, Nishitani A (2017) The visual inspection methodology for ceiling utilizing the blimp. Proced Eng 188:256–262

Nonami K, Kendoul F, Suzuki S, Wang W, Nakazawa D (2010) Fundamental modeling and control of small and miniature unmanned helicopters. Autonomous Fly Robots Unmanned Aer Vehicles Micro Aer Vehicles 17:33–61

Othman AZ, Dahlan A, Borhani SN, Rusdi H (2016) Post-traumatic stress disorder and quality of life among flood disaster victims. Proced Soc Behav Sci 234:125–134

Paneque-Gálvez J, McCall MK, Napoletano BM, Wich SA, Koh LP (2014) Small drones for community-based forest monitoring: An assessment of their feasibility and potential in tropical areas. Forests 5:1481–1507

Pereira E, Bencatel R, Correia J, Félix L, Gonçalves G, Morgado J, Sousa J (2009) Unmanned air vehicles for coastal and environmental research. J Coast Res 56:1557–1561

Perks MT, Russell AJ, Large ARG (2016) Technical note: Advances in flash flood monitoring using unmanned aerial vehicles (UAVs). Hydrology Earth Syst Sci 20(10):4005–4015

Pregnolato M, Ford A, Wilkinson SM, Dawson RJ (2017) The impact of flooding on road transport: A depth-disruption function. Transp Res Part D: Transp Environ 55:67–81

Rakha T, Gorodetsky A (2018) Review of unmanned aerial system (UAS) applications in the built environment: Towards automated building inspection procedures using drones. Autom Constr 93:252–264

Rancangan Malaysia Kesebelas (2015) Pursuing Green Growth for Sustainability and Resilience. Putrajaya

Rollason E, Bracken LJ, Hardy RJ, Large ARG (2018) The importance of volunteered geographic information for the validation of flood inundation models. J Hydrol 562:267–280

Roosli R, Collins AE (2016) Key lessons and guidelines for post-disaster permanent housing provision in Kelantan, Malaysia. Proced Eng 145:1209–1217

Ruiz Estrada MA, Koutronas E, Tahir M, Mansor N (2017) Hydrological hazard assessment: The 2014–15 Malaysia floods. Int J Disaster Risk Reduct 24:264–270

Shen D, Rui Y, Wang J, Zhang Y, Cheng L (2015) Flood inundation extent mapping based on block compressed tracing. Comput Geosci 80:74–83

Silva LDO, De Mello Bandeira RA, Gouvêa Campos VB (2017) The use of UAV and geographic information systems for facility location in a post-disaster scenario. Transp Res Proced 27:1137–1145

Smith MW, Carrivick JL, Hooke J, Kirkby MJ (2014) Reconstructing flash flood magnitudes using structure-from-motion: a rapid assessment tool. J Hydrol 519:1914–1927

Tanguy M, Chokmani K, Bernier M, Poulin J, Raymond S (2017) River flood mapping in urban areas combining Radarsat-2 data and flood return period data. Remote Sens Environ 198:442–459

Tonkin TN, Midgley NG, Graham DJ, Labadz JC (2014) The potential of Ssmall unmanned aircraft systems and structure-from-motion for topographic surveys: A test of emerging integrated approaches at Cwm Idwal, North Wales. Geomorphology 226:35–43

Tuna G, Mumcu TV, Gulez K, Gungor VC, Erturk H (2012) Unmanned aerial vehicle aided wireless sensor network deployment system for post-disaster monitoring. Commun Comput Inf Sci 304:298–305

Turner IL, Harley MD, Drummond CD (2016) UAVs for coastal surveying. Coast Eng 114:19–24

Uysal M et al (2015) DEM generation with UAV photogrammetry and accuracy analysis in Sahitler Hill. Measurement J Int Measurement Confed 73:539–543

Verhoeven GJJ, Loenders J, Vermeulen F, Docter R (2009) Helikite aerial photography—A versatile means of unmanned, radio controlled, low-altitude aerial archaeology. Archaeol Prospec 16(2):125–138

Visser F, Wallis C, Sinnott AM (2013) Optical remote sensing of submerged aquatic vegetation: opportunities for shallow clearwater sreams. Limnologica 43(5):388–398

White SM, Madsen EA (2016) Tracking tidal inundation in a coastal salt marsh with helikite airphotos: influence of hydrology on ecological zonation at Crab Haul Creek, South Carolina. Remote Sens Environ 184:605–614

Xiao Y, Yi S, Tang Z (2017) Integrated flood hazard assessment based on spatial ordered weighted averaging method considering spatial heterogeneity of risk preference. Sci Total Environ 599–600:1034–1046

Xiongkui H, Bonds J, Herbst A, Langenakens J (2017) Recent development of unmanned aerial vehicle for plant protection in East Asia. Int J Agric Biol Eng 10(3):18–30

Xu Z, Yang J, Peng C, Wu Y, Jiang X, Li R, Zheng Y, Gao Y, Liu S, Tian B (2014) Development of an UAS for post-earthquake disaster surveying and its application in Ms7.0 Lushan Earthquake, Sichuan. China. Comput Geosci 68:22–30

Zhang D, Quan J, Zhang H, Wang F, Wang H, He X (2015) Flash flood hazard mapping: A pilot case study in Xiapu River Basin. China. Water Sci Eng 8(3):195–204

Zoccatelli D, Borga M, Zanon F, Antonescu B, Stancalie G (2010) Which rainfall spatial information for flash flood response modelling? A numerical investigation based on data from the Carpathian Range, Romania. J Hydrol 394:148–161